2006

High resolution numerical simulations of lock-exchange gravity-driven flows

Seng Keat Ooi
University of Iowa

HIGH RESOLUTION NUMERICAL SIMULATIONS OF LOCK-EXCHANGE GRAVITY-DRIVEN FLOWS

by

Seng Keat Ooi

An Abstract

Of a thesis submitted in partial fulfillment
of the requirements for the Doctor of
Philosophy degree in Civil and Environmental Engineering
in the Graduate College of
The University of Iowa

May 2006

Thesis Supervisors: Associate Professor Larry J. Weber
Assistant Professor George Constantinescu

ABSTRACT

This dissertation focuses on the analysis of lock-exchange gravity-driven flows at high Grashof numbers using highly resolved numerical simulations and Large Eddy Simulation (LES) techniques. The present method uses a non-dissipative Navier-Stokes solver in which the sub-grid scale (SGS) viscosity and diffusivity are calculated dynamically. The use of LES allowed the study of these gravity current flows at Grashof numbers (Gr=10^9-10^{12}) much higher than those previously achieved using Direct Numerical Simulation (DNS). This is important because most practical applications of gravity current flows in river, coastal and ocean engineering occur at Grashof numbers much higher than the ones considered in previous DNS simulations and even in experimental laboratory studies. Three different Boussinesq compositional gravity-current configurations are examined in detail. The first configuration corresponds to the case of a lock exchange flow in an infinite channel in which the volume of the heavier lock fluid is infinite. The second configuration is the case in which the heavier lock fluid is finite (bottom propagating current). The third configuration corresponds to an intrusion current in which a certain amount of lock fluid is released into a two-layer ambient fluid. For all the configurations, it is found that the three-dimensional (3D) simulations correctly predict the main quantitative (e.g., front velocity at the different phases of the evolution of the current, bore velocity, etc.) and qualitative (e.g., formation of interfacial Kelvin-Helmholtz billows, their stretching and eventual break up into 3D turbulence) aspects of these flows observed in experimental investigations. The spatial and temporal bed shear stress distributions induced by the passage of bottom propagating currents are analyzed in detail, as accurate prediction of this quantity is essential in estimating the amount of sediment entrained by a compositional current propagating over a loose bed in river and coastal applications. Additionally, the energy budget, the distribution of the spanwise-averaged local dissipation rate and the streamwise

distributions of the local dissipation rate integrated over vertical planes are analyzed at different stages of the evolution of the current. All these quantities are practically impossible to be determined experimentally but essential in understanding the physics of the flow at the different stages of the evolution of the gravity current.

Abstract Approved: _____
Thesis Supervisor

_____
Title and Department

_____
Date

_____
Thesis Supervisor

_____
Title and Department

_____
Date

HIGH RESOLUTION NUMERICAL SIMULATIONS OF LOCK-EXCHANGE GRAVITY-DRIVEN FLOWS

by

Seng Keat Ooi

A thesis submitted in partial fulfillment
of the requirements for the Doctor of
Philosophy degree in Civil and Environmental Engineering
in the Graduate College of
The University of Iowa

May 2006

Thesis Supervisors: Associate Professor Larry J. Weber
Assistant Professor George Constantinescu

Graduate College
The University of Iowa
Iowa City, Iowa

CERTIFICATE OF APPROVAL

PH.D. THESIS

This is to certify that the Ph.D. thesis of

Seng Keat Ooi

has been approved by the Examining Committee
for the thesis requirement for the Doctor of Philosophy
degree in Civil and Environmental Engineering at the May 2006 graduation.

Thesis Committee: _____
Larry J. Weber, Thesis Supervisor

_____
George Constantinescu, Thesis Supervisor

_____
Robert Ettema

_____
Ching-Long Lin

_____
Jacob Odgaard

No bird soars too high if he soars with his own wings.
William Blake

ACKNOWLEDGMENTS

This dissertation would not be here without the assistance and suggestions of many people. Without the encouragement, guidance, support and patience of my advisors, Professors Larry Weber and George Constantinescu, this dissertation would not have reached this stage. I would also like to express my appreciation to Professors Robert Ettema, Jacob Odgaard and Ching-Long Lin for serving on my committee. Many thanks as well to the IIHR-Hydroscience and Engineering for providing financial support over the past five years.

As part of their collaborative effort with IIHR-Hydroscience and Engineering, the National Center for High-Performance Computing (NCHC) in Taiwan provided substantial computing time for the initial simulations. The final simulations were conducted on the IIHR Cluster during the initial break-in period of the cluster with assistance provided by Brian Miller and Mark Wilson.

I would also like to express my thanks to colleagues and friends at the laboratory, both past and present, who made life more fun and interesting at work. Many thanks go to my friends and community both in church and IVGCF for their support in love. Thank God for you all.

Finally, my wife, Po Li, without whose love, sacrifice, patience, care, persistence and editorial capabilities, this dissertation and the first step toward it may never have been taken.

ABSTRACT

This dissertation focuses on the analysis of lock-exchange gravity-driven flows at high Grashof numbers using highly resolved numerical simulations and Large Eddy Simulation (LES) techniques. The present method uses a non-dissipative Navier-Stokes solver in which the sub-grid scale (SGS) viscosity and diffusivity are calculated dynamically. The use of LES allowed the study of these gravity current flows at Grashof numbers (Gr=10^9-10^{12}) much higher than those previously achieved using Direct Numerical Simulation (DNS). This is important because most practical applications of gravity current flows in river, coastal and ocean engineering occur at Grashof numbers much higher than the ones considered in previous DNS simulations and even in experimental laboratory studies. Three different Boussinesq compositional gravity-current configurations are examined in detail. The first configuration corresponds to the case of a lock exchange flow in an infinite channel in which the volume of the heavier lock fluid is infinite. The second configuration is the case in which the heavier lock fluid is finite (bottom propagating current). The third configuration corresponds to an intrusion current in which a certain amount of lock fluid is released into a two-layer ambient fluid. For all the configurations, it is found that the three-dimensional (3D) simulations correctly predict the main quantitative (e.g., front velocity at the different phases of the evolution of the current, bore velocity, etc.) and qualitative (e.g., formation of interfacial Kelvin-Helmholtz billows, their stretching and eventual break up into 3D turbulence) aspects of these flows observed in experimental investigations. The spatial and temporal bed shear stress distributions induced by the passage of bottom propagating currents are analyzed in detail, as accurate prediction of this quantity is essential in estimating the amount of sediment entrained by a compositional current propagating over a loose bed in river and coastal applications. Additionally, the energy budget, the distribution of the spanwise-averaged local dissipation rate and the streamwise

distributions of the local dissipation rate integrated over vertical planes are analyzed at different stages of the evolution of the current. All these quantities are practically impossible to be determined experimentally but essential in understanding the physics of the flow at the different stages of the evolution of the gravity current.

TABLE OF CONTENTS

LIST OF TABLES

LIST OF FIGURES

LIST OF SYMBOLS

Alphabetical Symbols

C	non-dimensional concentration $((\overline{C}-\overline{C}_{\min})/(\overline{C}_{\max}-\overline{C}_{\min}))$
$\overline{C}$	dimensional concentration (density)
Δn	local grid spacing
Δn^{+}	local grid spacing in wall units
Δy_n	height of gravity current nose measured from bed
Δy_s	height of gravity current stagnation point measured from bed
E_d	time integral of total dissipation
E_k	total kinetic energy
E_{k0}	total initial kinetic energy
E_p	total potential energy
E_{p0}	total initial potential energy
Fr	Froude number of the front
g'	reduced gravity $(g(\overline{C}_{\max}-\overline{C}_{\min})/\overline{C}_{\min})$
Gr	Grashof number $((u_b h/v)^2)$
h	length scale; channel height
l	nondimensional streamwise distance indicating front position
R	initial aspect ratio of denser fluid (h/x_0)
Re_f	Reynolds number of the front
Sc	Schmidt number (υ/κ)
S_0	Incoming flow area
S_1	Surface area of lighter fluid trapped beneath the head
t	time
t_0	timescale
U_f	front velocity

U_{bore} bore velocity

u_b buoyancy velocity $(\sqrt{g'h})$

u_i velocity component in i direction

u_τ friction velocity

$\dot{V}_u$ light fluid flux underneath the front

$\dot{V}_0$ expected incoming flux of light fluid

x x distance

x_f front location measured from the end wall

x_b bore location measured from the end wall

x_i i coordinate

x_0 initial lock length

Greek Symbols

α_{SGS} sub-grid scale diffusivity

ε total dissipation

ε_0 viscous dissipation

ε_L local dissipation rate

ε_R difference between the density of the lock fluid and the mean density of the ambient fluid

ε_t sub-grid scale (SGS) dissipation

ε^{23} streamwise distribution of dissipation

ε_t^{23} streamwise distribution of SGS dissipation

ε^{13} vertical distribution of dissipation

ε_t^{13} vertical distribution of SGS dissipation

ε_{12}^{13} vertical distribution of wall-normal gradient dissipation

κ molecular diffusivity

ν	molecular viscosity
ν_{SGS}	sub-grid scale viscosity

Abbreviations

2D	two-dimensional
3D	three-dimensional
DNS	direct numerical simulation
GC	gravity currents
IC	intrusion currents
LES	large eddy simulation
SGS	sub-grid scale

CHAPTER 1

INTRODUCTION

Predicting and understanding the evolution of gravity currents (GCs) is of considerable interest because these flows are often encountered in engineering and geosciences. Of particular interest is the study of their impact on the environment (e.g., see Fannelop, 1994 and Simpson, 1997). Gravity currents are flows driven by density differences within a fluid. These density differences can be the result of temperature differences in the atmosphere (e.g., sea breeze or thunderstorm fronts), temperature differences within large bodies of water (e.g., lakes, reservoirs) due to heating and radiation from the atmosphere, presence of dissolved substances that modify the density (e.g., salt in water or hazardous release of buoyant pollutants in the environment), spilling of a fluid into another (e.g., oil into water) or presence of particulates in the flow (e.g., sediment particles in turbidity currents, or powder snow in avalanches).

1.1 Motivation

Locking operations in an urban estuarine environment create unique location-specific problems to fish passage and the environment. One example of this is the Lake Washington Ship Canal in Washington. The Hiram M. Chittenden lock and dam facility (Chittenden facility) was completed in 1914 as part of the Lake Washington Ship Canal system to facilitate transport of logs and coal. The Chittenden facility is unique in the United States as it separates seawater in Puget Sound and fresh water from Lake Washington. This separation has created ecological and environmental problems including saltwater intrusion; zero dissolved oxygen (DO) levels in the hypolimnion of the lake towards the end of summer; warm surface water temperatures; longer stratification periods of the lake; and last but not least, flushing limited to the northern end of the lake with the exception of spring when the spring runoff is important.

Ecological and environmental problems are due in part to the high traffic volume of the facility. The Chittenden facility is regarded as the busiest lock facility in the United States. These ecological and environmental problems are both a threat to the urban consumer and the salmonids that pass through the system. The canal is the only means of migration for salmonids that spawn in Lake Washington, Lake Sammamish and the Cedar River watersheds. Due to the thermal or saline differential created at the lock, spawning adult salmons congregate near the lock, delaying their acclimatization to fresh water conditions and subsequently, their upstream migration. The anoxic conditions at the hypolimnion and high surface temperatures also create non-conducive environments for salmonids migrating upstream.

Besides the ecological problems linked to the formation and transport of saline and thermal wedges, another problem of great practical interest is the amount of sediment entrained, the distances over which the sediment is carried and the deposition patterns downstream in the channel, each time the lock facility is operated. This is because, each time a saline or thermal GC is propagating over a loose bed, it entrains sediment and it induces the formation of a turbidity current. Over time, the bathymetry of the channel downstream of the lock facility can change significantly due to the scour and erosion induced by the turbidity current.

In the present work, the focus is on a simplified geometry which corresponds to the formation of saline / thermal gravity currents in lock exchange configurations in a straight channel. This simplified geometry retains most of the fundamental flow features associated with the formation and evolution of gravity currents at real lock facilities. Besides studying the details of the formation, evolution and decay of these currents under different flow conditions, the present study focuses on the spatial and temporal distributions of the bed shear stress which is the main variable that determines the capacity of the saline / thermal gravity current to entrain sediment.

1.2 Research Needs And Research Objectives

One of the main parameters that determine the evolution of a lock-exchange flow is the value of the Grashof number. The Grashof number represents the ratio between the buoyancy forces and the viscous forces. One of the main challenges related to the study of gravity currents encountered in practical applications is the quantification of scale effects, as both laboratory experiments and three-dimensional Direct Numerical Simulation (DNS) studies are conducted at Grashof numbers that are substantially lower. In fact, in the case of three-dimensional DNS studies information is available only at low Grashof numbers where the flow inside the head of the gravity current is, at best, mildly turbulent. This is in stark contrast to gravity currents observed in rivers, lakes and oceans where the flow inside the gravity current is strongly turbulent.

At a more fundamental level, gravity current flows are, to a great extent, determined by the evolution of several 3D flow instabilities. The first one is the Kelvin-Helmholtz instability behind the front of the current, at the interface between the current and the ambient fluid, which is responsible for the formation of billows and for much of the mixing. This instability starts as a predominantly 2D instability. The second one is the instability responsible for the formation of the lobes and clefts at the front of the gravity current. The lobes are defined as the large scale structures in the forms of bulges that develop at the front of the current and continually change shape. They are linked by clefts that are observed to grow and merge or, on the contrary, split as the current continues to propagate. For high Grashof number currents, where the flow is expected to be highly turbulent some distance behind the front of the current, the near bed flow is expected to contain the usual turbulent structures and associated instabilities observed in constant-density turbulent boundary layers. The most obvious one is the formation of high and low streamwise velocity streaks. The growth of these instabilities and the formation and evolution of the coherent structures associated with them is still not well understood.

In the range of Grashof numbers ($Gr>>10^8$) of practical interest in most practical applications in river, coastal and ocean engineering, no detailed quantitative information concerning the phenomena present at the head of a bottom-propagating gravity current or of an intrusion gravity current (e.g., the instabilities and mechanisms leading to the lobe-and-cleft structure at the front), the flow structure in the near-bed region, or detailed measurements of the velocity and density fields within the current are available from previous experimental or numerical studies. Additionally, in many applications related to turbidity currents or to compositional currents propagating over loose beds, information on the spatial and temporal distributions of the bed shear stress is essential to determine the amount of sediment entrained and carried by the current. The measurement of the instantaneous bed shear stress distribution is practically impossible to achieve experimentally. This kind of information can be used in simpler models that try to predict the sediment entrained by the current in an integral sense, besides qualitatively understanding the way the sediment is entrained. Finally, information on the global energy balance at different stages of the evolution of the gravity current is quite difficult and very expensive to achieve experimentally.

In this regard, high resolution three-dimensional eddy resolving simulations like Direct Numerical Simulation (DNS) or Large Eddy Simulation (LES) can provide additional valuable insight needed to understand the development of lock-exchange gravity currents. For the Grashof / Reynolds numbers of practical interest ($Gr>>10^8$), where the flow inside part of the GC is highly turbulent, LES using non-dissipative numerical models and sub-grid scale models, that can account in a physical way for the effect of the smallest unresolved scales on the larger ones in a flow in which phenomena such as relaminarization and transition are present, appears to be the best available numerical tool at the present time.

Therefore the major research objectives of this study are:

- Validation of an existing LES model to simulate Boussinesq gravity currents in lock-exchange configuration using experimental data and theory
- Quantifying the capabilities and limits of the much less expensive 2D LES simulations.
- Investigating the flow structure and phenomena present at the head and tail of the gravity current for different lock-exchange configurations (bottom propagating and intrusion currents) over a wide range of Grashof numbers
- Investigating the bed shear stress distribution (bottom propagating currents), global energy balance and the spatial and temporal distributions of the dissipation rate

The chart in Fig. 1.1 provides an overview of the 2D and 3D simulations and parametric studies (e.g., effect of the Grashof number, effect of the ratio of initial aspect ratio of the lock fluid, etc.) performed as part of the present investigation in which lock exchange flows are simulated for three generic configurations:

1) lock exchange bottom-propagating compositional gravity currents with an infinite amount of lock fluid (this configuration corresponds to the case when the lateral wall in the tank or channel is situated at large distances from the lock gate such that the backward propagating current does not interact with the lateral end wall)
2) lock exchange bottom-propagating compositional gravity currents with a finite amount of lock fluid (this is the case that would correspond to gravity currents forming at lock facilities)
3) lock exchange intrusion compositional gravity currents with a finite volume of lock fluid (this is the case when dense water intrudes into a stratified reservoir)

The outline of the thesis is as follows. Chapter 2 provides a review of previous experimental and numerical studies for each of the lock-exchange configurations considered in the present investigation. Chapter 3 presents the numerical model used to perform the simulations. Chapter 4 presents 2D LES simulations of lock-exchange flows. Chapter 5 discusses 3D LES simulations of infinite-volume lock-exchange flows at Grashof numbers in the range of 10^6 to 10^9. Chapter 6 discusses 3D LES simulations of finite-volume lock-exchange flows over the slumping and inviscid self-similar phase at Grashof numbers in the range of 10^9 to 10^{12}. Chapter 7 compares results from two 3D LES simulations of intrusion currents propagating into a two-layer ambient fluid at $Gr \sim 10^9$. In the first case the intrusion propagates symmetrically while in the second case the intrusion propagates non-symmetrically, mostly inside the upper layer of ambient fluid. Chapter 8 summarizes the main findings of the study and provides some recommendations for future work.

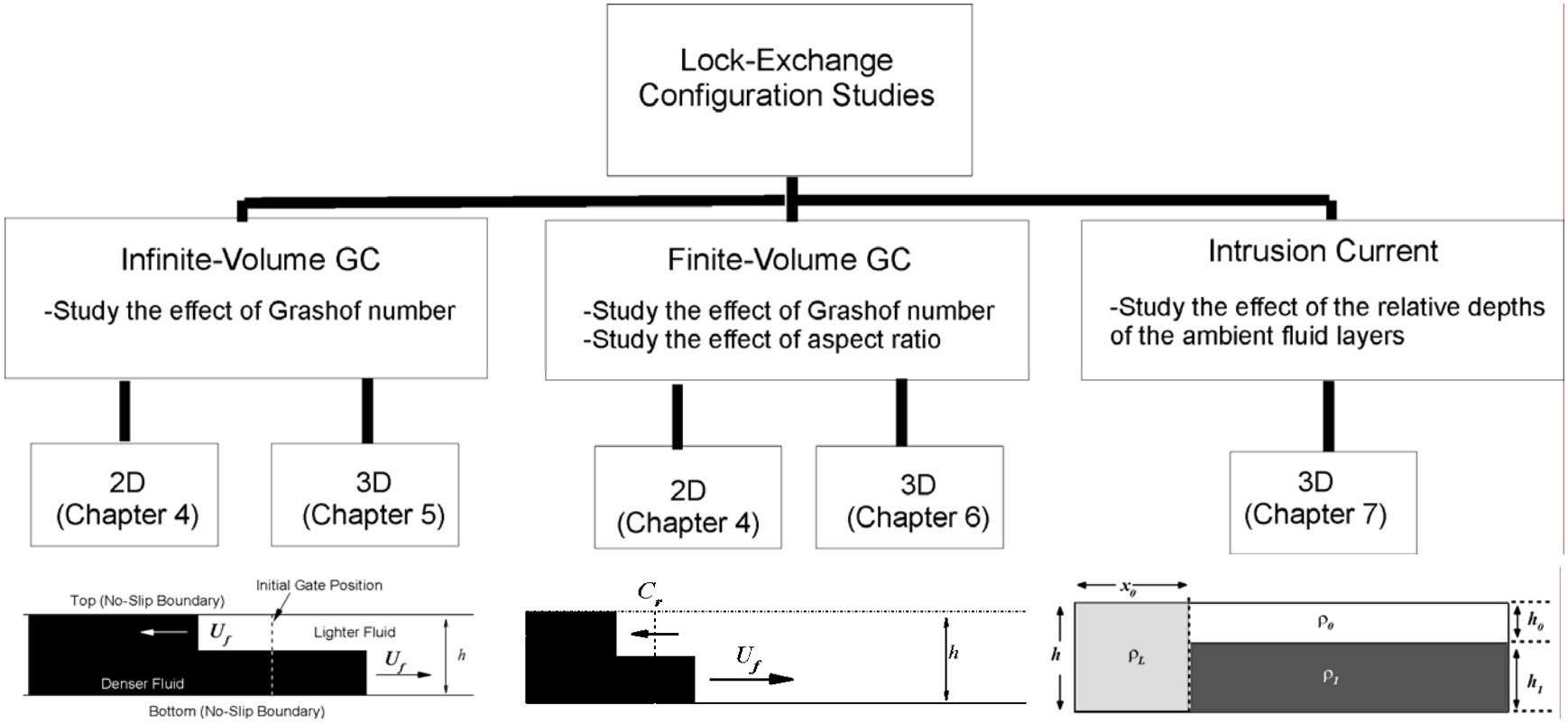

Figure 1.1. Summary of Lock-Exchange Configuration Studies performed in the present work.

CHAPTER 2

GENERAL DESCRIPTION OF LOCK-EXCHANGE FLOWS, EXAMPLES AND LITERATURE REVIEW

2.1 Basic Gravity Current Studies

A large number of experimental and theoretical studies have been conducted to isolate the various mechanisms that drive GCs and predict the temporal evolution of global parameters such as the front velocity, U_f, the height of the head region, etc. Most of these studies considered the case of low-density differences where the Boussinesq approximation is valid (Benjamin, 1968; Simpson, 1972; Britter & Simpson, 1978; Simpson & Britter, 1979; Huppert & Simpson, 1980; Huppert, 1982; Keller & Chyou, 1991; Hallworth et al., 1996; Shin et al., 2004). These studies of GCs developing in horizontal or tilted channels showed that the dynamics of the current can be explained using shallow-water theory if sufficiently accurate front conditions are prescribed for the non-hydrostatic flow at the head of the current (Hartel et al., 2000a). For the Boussinesq case, most of these integral models, which are based on shallow-water equations or other theoretical approaches, assume that the GC generated by the lock release is energy conserving. In many of these studies the model is derived by averaging momentum and mass over the depth and assuming vertically-uniform flow with hydrostatic pressure distribution. Recently, Lowe et al. (2005) conducted experiments on non-Boussinesq lock-exchange flows and proposed several theoretical models. They found that the model that assumes that the light and heavy GCs, propagating in opposite directions near the top and the bottom of the channel, are connected by a simple wave of expansion without an internal bore is the most representative for the non-Boussinesq case. Two of the most important outcomes of these experimental studies were the visualization of the shape of the current and the measurement of its speed of propagation. It was also observed (e.g., Britter & Simpson, 1978) that most of the mixing took place along the interface between

the two fluids behind the head and the Kelvin-Helmholtz (KH) billows that were shed behind the head were responsible in a great measure for the mixing between the two fluids.

Benjamin (1968) proposed one of the first models that allowed calculation of the front velocity of a GC during the slumping phase in the inviscid (infinite Grashof number) limit. In his model the height of the current was assumed to be constant over the length of the current. For the case in which the initial depth of the lock fluid is equal to that of the channel (2h), the non-dimensional front velocity given in the form of a Froude number ($U_f / \sqrt{g'(2h)}$, g' is the reduced gravity) is equal to 1/2. This corresponds to $U_f/u_b=1/\sqrt{2}$, where the buoyancy velocity is defined as $u_b = \sqrt{g'h}$ ($g' = g(\overline{C}_{\max} - \overline{C}_{\min})/\overline{C}_{\min}$, where g' is the reduced gravitational acceleration, $\overline{C}_{\max}, \overline{C}_{\min}$ are the maximum and minimum concentrations / densities in the domain, g is the gravitational acceleration and h is the channel depth). His model did not account for viscosity effects, the no-slip condition at the bottom and/or top boundaries or for the mixing at the interface. Shih et al. (2004) extended Benjamin's model. They proved that, for the case in which the initial height of the lock fluid was equal to that of the channel, the height of the energy conserving head is half the channel depth. For this case their theory gives the same value for the Froude number.

Linden & Simpson (1986) have shown that the mixing behind the head significantly affects the dynamics of the current. For example, in one of their experiments they demonstrated that the current is destroyed once the denser fluid is vertically mixed with the lighter ambient fluid through turbulence; the turbulence within the flow was added by bubbling air. Experimental studies (e.g., see Parsons & Garcia, 1998) also showed that the effects of the Grashof / Reynolds number on the evolution of the GC can be important. Mixing was found to intensify at larger Reynolds numbers.

2.2 Infinite Volume Lock Exchange Gravity Currents

The simplest type of lock-exchange flow, which is the focus of Chapter 5, corresponds to two intrusion gravity currents that develop in an infinite channel. Initially, the heavier and lighter fluids (their initial depth is equal to that of the channel) are separated by a vertical lock gate that is removed instantaneously (see sketch in Fig. 2.1). The fluids do not mix once the lock gate is removed. Rather, the less dense fluid intrudes above the heavier (denser) fluid and creates a gravity current moving to the left (backward propagating) in Fig. 2.1. Meanwhile, the denser fluid slides toward the right, displaces some of the lighter fluid and creates a second (forward propagating) current moving to the right. In the case in which the channel and the amounts of light and heavy fluid are infinite, the maximum and minimum densities in the domain remain constant and the speeds of the two currents, after a short accelerating phase, reach a practically constant value. In the case of small density differences (Boussinesq case) and of identical top and bottom boundaries (e.g., no-slip smooth walls), the two speeds are expected to be equal (Lowe et al., 2005), especially if the gate is released in such a way that induces very small disturbances in the lock region. The flow is dominated by two instabilities: the predominantly two-dimensional (2D) Kelvin Helmholtz (KH) instability at the interface between the heavier and the lighter fluid, and the 3D lobe-and-cleft instability at the two fronts.

A larger number of numerical studies have been attempted to complement the information usually obtained from experimental studies. Many of the earlier computational studies (e.g., Jacobsen & Magnussen, 1987; Klemp et al. 1994) employed coarse computational grids and low-order dissipative numerical schemes, coupled with empirical models to predict the evolution of the GC. A review of numerical models based on integral models is available in Choi & Garcia (2002). Integral models require additional closure relationships for the bed resistance and water entrainment. RANS models were used to model lock-release flows by Chen & Lee (1999) and density

currents on a slope by Choi & Garcia (2002). The challenge related to the use of RANS models is that practically all these models are calibrated for fully developed turbulent flows and are not capable of accurately predicting transition and relaminarization, which is essential for simulating lock-exchange flows. High resolution numerical simulations of gravity currents using eddy-resolving techniques have only recently been attempted. Most of these studies are two-dimensional, employ DNS and use the Boussinesq approximation. For the geometry and flow conditions considered Chapter 5 in which the GCs do not interact with the channel ends, non-Boussinesq lock exchange flows were studied recently using 2-D DNS by Birman et al. (2005) at Reynolds numbers up to 12,000. The simulations successfully captured the head height and propagating velocity of the light and dense currents.

The only numerical simulations that can capture the development of the lobe and cleft instability at the front, the formation and breaking of the KH billows into smaller 3D eddies at the current interface, and the interaction between the near-wall turbulent structures (e.g., hairpin vortices, low and high speed streaks, etc.) that are present in high Grashof number currents with the regions away from the walls are eddy resolving 3D simulations. The first 3D well-resolved numerical simulation of a Boussinesq lock-exchange flow in an infinite channel was reported by Hartel et al. (2000a, 2000b), who used DNS at a relatively low Grashof number ($Gr = (u_b h/\upsilon)^2 \sim 1.5\times10^6$, ν is the molecular viscosity). Their simulation successfully captured the formation of the lobe and cleft instability at the front of the gravity current and allowed, for the first time, a detailed investigation of the flow topology in the head region. The simulation highlighted the important role played by the lighter fluid present below the head, in the unstably stratified region between the foremost point and the stagnation point (in a reference system translating with the front velocity). Previously (e.g., Simpson, 1972), it was thought that the main reason for the development of the lobe and cleft instability was the thin layer of light fluid pulled underneath the front (for the current propagating to the

right in Fig. 2.1). Their 2D DNS simulations at Reynolds numbers up to about 30,000 (Gr~10^9) showed that the topology of the flow in the head region remained similar to that of the spanwise-averaged flow from the 3D DNS conducted at a lower Reynolds number.

2.3 Finite Volume Lock-Exchange Gravity Currents

The case of a finite-volume lock-exchange flow corresponding to the collapse of a finite volume of heavier intrusion fluid into the lighter ambient fluid when the lock is released and its subsequent spreading over a bottom (horizontal) wall in the form of a gravity current (GC) is very often encountered in practical applications. Even in the case in which the density differences are small enough for the current to be simulated using the Boussinesq approximation, compositional GCs in rivers, estuaries, lakes and oceans can travel over large distances and entrain, carry and deposit large quantities of sediment at considerable distances from the entrainment location, in the case in which they propagate over a loose sediment bed. In all these applications, the Grashof / Reynolds numbers are very high and the current is strongly turbulent.

A classical example is related to locking operations in an urban estuarine environment where a salinity driven GC develops each time the facility is operated. Saltwater intrusions can cause serious problems to the environment. Moreover, a turbidity current is induced by the passage of the forcing salinity-driven GC propagating over a loose bed. The bed morphology can change significantly over time with unwanted effects on the environment and channel navigability.

In the case of finite-volume lock-release GCs in straight open channels (see sketch in Fig. 2.2), a lateral wall is present at one of the ends of the channel. The heavier lock fluid initially occupies a finite volume between the lateral wall and the lock gate. The top boundary, corresponding to the channel free surface, is usually assumed to be a slip boundary. When the lock-gate wall is removed instantaneously, a GC will start forming and propagate along the bottom wall. This case is the main focus of Chapter 5.

Also, the present investigations are limited to compositional currents where density differences are produced by a difference in a property of the fluid (e.g., temperature, salinity, etc.) and these differences are small enough for the Boussinesq approximation to be valid. Only the case where the initial height of the heavier lock fluid is equal to the channel height is studied.

In many respects, the case of a finite-volume lock-exchange flow propagating over a no-slip wall is similar to the infinite-volume lock-exchange flow in a channel. Among the important flow similarities between compositional GCs developing in the two cases are the fact that both currents are propagating over a thin layer of dislocated fluid that produces a region of unstable stratification near the bottom wall; the topology of the flow at the head, at least during the common slumping phase, is similar; the mixing is driven by the Kelvin-Helmholtz (KH) billows that are shed behind the front and which promote mixing. In both cases, at sufficiently high Grashof numbers, the KH interfacial billows are subject to intense straining and stretching which forces their break up into three dimensional (3D) flow structures.

However, there are also important differences due to the finite amount of potential energy available in the case of finite-volume GCs which make their evolution more complex. If in the case of an infinite-volume lock exchange flow the current will propagate indefinitely with practically constant speed starting some short time after the gate release, for finite-volume lock-exchange GCs several distinct phases (e.g., see Huppert & Simpson, 1980, Rottman & Simpson, 1983) can be identified in the evolution of the current.

A short acceleration phase (Fig. 2.2a) is present immediately after the release of the lock gate. A bore of lighter fluid is observed to form concomitantly with the main gravity current containing heavier fluid in the lower part of the channel. The bore and front of the current propagate with about the same speed initially. Over this initial acceleration phase the velocity at the front of the bore and at the front of the bottom GC

increases sharply from zero. The front velocity of the bore then starts decreasing as it starts interacting with the lateral wall, while the front velocity of the GC continues to vary before reaching a relatively constant value that characterizes the next (slumping) phase of evolution of the GC.

Once the bore propagating backwards (Fig. 2.2a) has reflected from the end wall (Fig. 2.2b), a flow of lighter fluid than the one inside the GC starts propagating toward the front of the current in the form of a wave of depression with a relatively constant velocity (U_{bore}) that is slightly higher than the front velocity (U_f). At this point the current is in the slumping phase. Hallworth et al. (1996) showed that because the head remains essentially unmixed during the slumping phase, the front propagates at different rates for different initial values of the lock length or, equivalently, of the volume of the initial lock fluid. Rottman & Simpson (1983) have shown that if the initial depth of the lock fluid is equal (the case considered in the present work) to the depth of the channel, the bore advancing toward the front has the form of an internal hydraulic jump. Though the front propagates with practically constant depth and constant velocity (U_f), the flow is not self similar. The ratio between the front velocity and the buoyancy velocity, $u_b = \sqrt{g'h}$, is a parameter that is dependent on the Grashof number, and the ratio between the initial depth of the lock fluid and the total depth of the channel.

The inviscid self-similar phase starts when the forward propagating bore reaches the front of the current (Fig. 2.2c). From this moment the front velocity is not constant anymore and the front velocity decays in time following a power law with a negative coefficient ($U_f \sim t^{-1/3}$). Hoult (1972) obtained a self-similar solution of the shallow water equations that describes this phase. The flow is determined by the balance between the inertial force of the GC and the buoyancy force induced by the horizontal density gradient. The time at which the transition between the slumping and inertial phases occurs is dependent on the initial volume of lock fluid. The time interval to transition increases with the size of the initial volume. In the limiting case of an infinite volume of

lock (heavier) fluid which is studied in Chapter 5, the flow never transitions to the inviscid self-similar phase.

If the channel is long enough such that viscous effects become dominant, the current will transition to the viscous phase. During this phase, the flow at the front decelerates faster ($x_f \sim t^{-1/5}$, $U_f \sim t^{-4/5}$) and the current head further decreases in height (see Huppert, 1982, Rottman & Simpson, 1983). The inviscid self-similar phase may not be present if the Grashof / Reynolds number of the GC is sufficiently low (Rottman & Simpson, 1983), in which case the current can transition directly from the slumping phase into the viscous phase.

The lock-exchange flow corresponding to a bottom compositional GC in a channel with a lateral end wall was studied experimentally and analytically by among others, Huppert & Simpson (1980), Rottman & Simpson (1983), Choi & Garcia (1995), Hacker et al. (1996) and Shin et al. (2004). In these experiments the evolution of the GC over the slumping and inertial phases was studied. Huppert & Simpson (1980) proposed empirical relations for the Froude number defined with the front velocity as a function of the non-dimensional height of the GC during the slumping and inertial phases. They also proposed a box model in which the main assumption is that the current advances as a series of boxes of equal volume. Assuming the mass is conserved, this allows one to relate the position of the front to the height of the current. Using the empirical relations and the conservation of mass, the position of the front and its velocity can be expressed function of time over both the slumping and inertial phases. The resulting expression for the front velocity during the slumping phase, however, predicted a small (power) decay with time instead of a constant value. The expression for the front velocity during the inviscid phase was consistent with the expected power law decay in time with an exponent of -1/3 as predicted by Hoult (1972).

More complicated cases include the propagation of a lock-exchange compositional GC into a linearly stratified fluid. This case was studied experimentally

and numerically by Maxworthy et al. (2002). Their 2D highly resolved DNS simulations employed meshes with around 10^6 grid points for Grashof numbers up to 4×10^8. The case of a particle-driven finite-volume lock-exchange flow at $Gr=5\times10^6$ was studied by Necker et al. (2002). This investigation was the first to use highly resolved 3D DNS simulations for particulate currents. It focused on the investigation of the front structure and sedimentation profiles. Recently, Necker et al. (2005) performed a detailed analysis of the energy budgets, dissipative losses, influence of initial level of turbulence inside the lock fluid and of the mixing between interstitial and ambient fluid for particle-driven GCs over the same range of Grashof numbers. More complex cases, such as particulate currents over slopes of varying angles and resuspending GCs on sloped surfaces were investigated using 2D DNS simulations by Blanchette et al. (2005a) and Blanchette et al. (2005b), respectively. Although the governing equations were solved on a Cartesian mesh in a rectangular domain, the influence of the varying bottom slope was accounted for by introducing a spatially varying gravity vector.

2.4 Finite-Volume Lock-Exchange Intrusive Gravity Currents

For the case where the density of the lock fluid is between the minimum and maximum densities of the ambient fluid, the GC will propagate in the form of an intrusion at a level where the lock-fluid density is comparable to that of the ambient. The dispersion of buoyant pollutants in a stably-stratified atmospheric boundary layer behaves like an intrusion front once the plume of pollutant reaches the level where its mean density is equal to that of the surrounding air. A commonly cited example of a flow that can be modeled as an intrusive GC is the Morning Glory phenomenon (Sutherland et al., 2004) which consists of a fast moving band of clouds intruding along an atmospheric inversion into a stratified system. Another example of great practical importance corresponds to denser water (e.g., cold river water, water containing sediments, sewage

outfalls, buoyant pollutants, etc.) intruding into a stratified reservoir, lake or ocean in which the density of the intrusion is less than the density of the water at the bottom of the reservoir. In this case the denser water initially propagates as a bottom intrusion until it reaches the level when the density of the water in the reservoir is close to its density. Then the bottom intrusion continues to propagate as a subsurface, relatively horizontal, IC. The intrusion can be considered to occur in a two-layer fluid, in a multiple-layer fluid or in a continuously stratified fluid, depending on the reservoir stratification at the time of the intrusion. The propagation of the IC can be accompanied by generation of strong Kelvin-Helmholtz (KH) billows behind the head region and by the formation of trailing and leading internal waves, depending on the flow conditions.

If there is a relatively sharp interface between the two layers and the Reynolds number is large enough, several experimental investigations show that once the intrusion forms, it propagates with a relatively constant velocity, similar to the slumping phase observed in lock-exchange GCs propagating over no-slip surfaces. One of the main purposes of the various theoretical models is to predict the value of the front velocity and the thickness of the intrusion head. Benjamin (1968) was one of the first to propose a model that could be applied to either symmetrical intrusions or GCs propagating over slip surfaces. In his inviscid energy-conserving model, the mixing between the intrusion current and the ambient flow due to the growth and break-up of KH billows was neglected. Kao (1977) proposed a theoretical model for ICs developing into a two-layer fluid for the case in which the interface thickness is negligible and the depths of the two layers are infinite. Holyer & Huppert (1980) considered the case of finite depths of the two layers and based their model on Benjamin's (1968) theory for steady inviscid (non-dissipative) currents propagating over a slip surface. Their model allows for an arbitrary density value (within the range defined by the densities of the two ambient layers) inside the intrusion, for the presence of energy losses and is not limited to Boussinesq ICs. The analytical model of Holyer & Huppert (1980) was extended by de Rooij et al. (1999) who

also included the effects of sedimentation of particles and detrainment of interstitial fluid for the case of a particle-driven interfacial intrusion. For these applications, the model was found to successfully predict the length of the IC and associated sediment distribution. Starting from the general equations derived by Holyer and Huppert (1980), Sutherland et al. (2004) obtained simpler expressions for the propagation speed and height of the intrusion. They also derived approximate analytical solutions using perturbation theory. Their theoretical model agreed very well with experiments for the case in which the density of the lock fluid was equal to the mean density of the ambient fluid, even if the depths of the two layers of ambient fluid were not equal. The model underpredicted the front velocity in the other cases.

Faust & Plate (1984) investigated the effects of the Grashof / Reynolds number ($800<Re_f<30{,}000$) and the shape of the initial density distribution of the ambient fluid on the propagation of a symmetrical IC created by a lock release of saline fluid in a water tank. The case of a sharp density interface between two layers of constant-density ambient fluid and that of a mildly (linearly) stratified interface were considered. Viscous effects where observed to be important only below Re_f~2,000. The case of a relatively sharp interface was also investigated experimentally by Britter and Simpson (1981). Both investigations found that the front speed and the intrusion height increase with the decrease of the interface thickness. If the ratio between the interface thickness and the intrusion height was less than 0.2, they found that the front velocity becomes independent of the interface thickness. De Rooij et al. (1999) performed experiments with saline and particulate intrusions at Reynolds numbers of about, Re_f=4,000. It was observed that the interfacial waves generated by the saline intrusions were weaker for intrusions that were more symmetrical. The propagation of an IC into a two-layer fluid was studied experimentally by Sutherland et al. (2004) for configurations in which the depths of the two layers were not equal and / or the density of the lock fluid was different from the mean density of the ambient mass of fluid in the tank. For non-symmetric cases, they

found that leading waves can be excited in front of the current head at the interface between the two layers.

Lowe et al. (2002) used digital Particle Tracking Velocimetry (PTV) methods to study the structure (e.g., velocity distribution, stability of the interface) of a doubly-symmetric IC ($3{,}700<Re_f<14{,}500$) created by a lock-exchange flow in a tank. They found that the velocity in the head region was almost uniform and equal to the front velocity. Their experiments showed that the fluid velocity was non-uniform inside the dissipative wake region and its maximum speed was around 50% higher than the front velocity. The velocity in the downstream part of the tail region was slightly higher than the front velocity. The presence of an internal flow within the IC was also predicted by Simpson and Britter (1979) based on experiments that produced GCs propagating on no-slip surfaces. Lowe et al. (2002) argued that the role of the faster internal flow is to supply the flux of lock fluid lost, mainly in the wake region, by mixing with the ambient fluid.

Amen and Maxworthy (1980) studied the case of an intrusion propagating into a mildly stratified fluid. More recently, Mehta et al. (2002) studied experimentally the case of a three-layer system in which the middle layer was a stratified layer in between two constant density layers. The experimental conditions ensured that the intrusion propagated along the middle layer. They found that if the thickness of the stratified middle layer exceeds a certain critical depth, the IC decelerates and eventually stops. This is caused by the loss of momentum due to the generation of large-amplitude trailing internal waves and a double-humped solitary wave in front of the head. Gravity currents intruding along the interface between a uniform upper layer and a linearly stratified lower layer were studied experimentally by Flynn & Sutherland (2004).

Hartel et al. (2000) used 2D DNS ($Gr=10^6$-10^9) to study the case of a bottom propagating current over a slip surface in which the lateral boundaries were situated far from the lock gate position. This flow can be considered similar to the one present in a

doubly-symmetric IC before the return flow reflects off the lateral end wall. They found that the foremost point of the current was located on the slip boundary, in contrast to the case of bottom GCs propagating over a no-slip surface. They found that the position of the formation of the first KH billow behind the head in their simulations was in good agreement with the one observed in the intrusion experiments of Lowe et al. (2002) but, because of the 2D constraint, the KH billows remained coherent for a much larger time behind the head region. The front speed in the high Reynolds number simulations was also correctly predicted. The shape of the current in the head region was similar to Benjamin's (1968) prediction. From the review, it appears that no highly resolved, 3D eddy resolving simulations (DNS or LES) are available for intrusion currents.

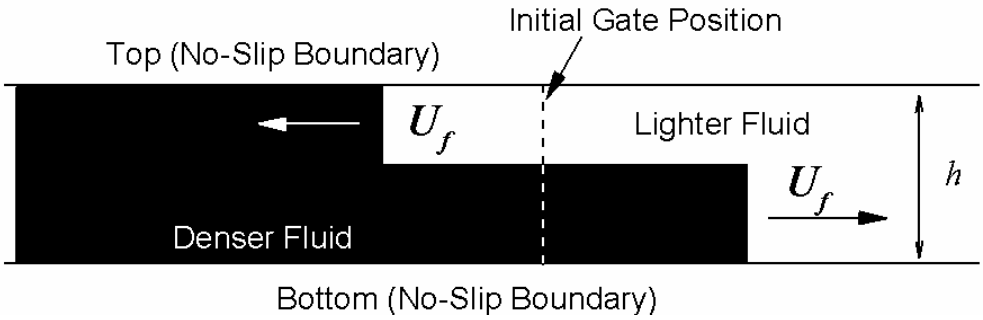

Figure 2.1. Sketch of an infinite-volume lock-exchange flow in a channel.

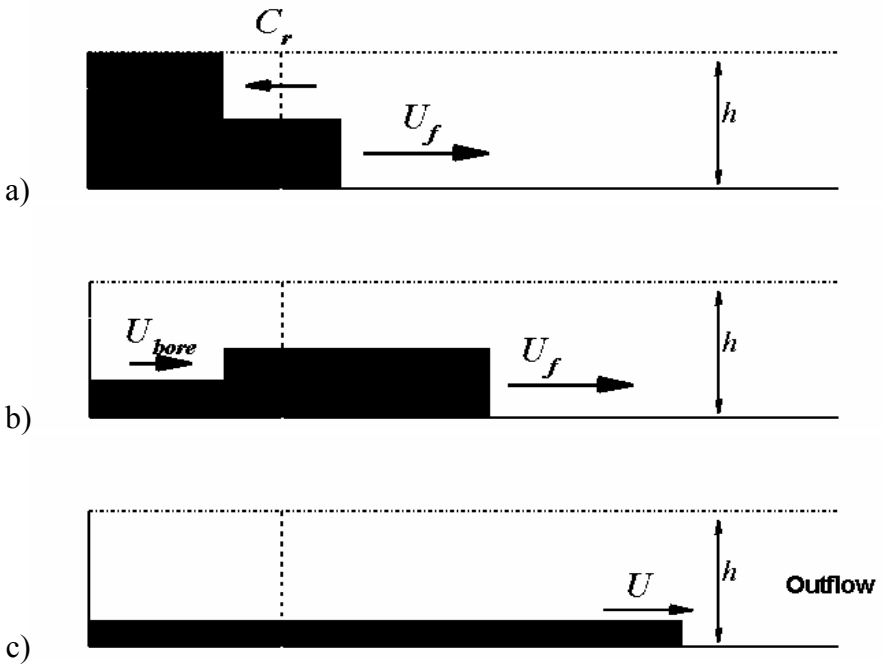

Figure 2.2. Sketch of a finite-volume lock-exchange flow in a channel. a) gravity current immediately after the gate is removed with associated front velocity of denser fluid and bore velocity of lighter fluid; b) gravity current during the slumping phase after the bore has been reflected; c) gravity current during the self-similar inviscid phase after the bore has caught up the front.

CHAPTER 3

NUMERICAL SOLVER

The numerical solver is a finite-volume non-dissipative DNS / LES code. A detailed description of the code and computational technique is available in Pierce & Moin (2001) along with a validation study (see also Pierce & Moin, 2004). Additionally, detailed validation of the code for 3D LES simulations of cavity flows with or without an incoming turbulent flow is described in Chang et al. (2006). The conservative form of the Navier-Stokes equations is integrated on non-uniform Cartesian meshes. A semi-implicit iterative method that employs a staggered conservative space-time discretization is used to advance the equations in time while ensuring second order accuracy in both space and time. A Poisson equation is solved for the pressure using multigrid. The algorithm discretely conserves energy, which ensures robustness at relatively high Reynolds numbers in the LES regime. This is essential for simulations conducted at very high Grashof numbers using a dynamic model that maintains the subgrid-scale (SGS) viscosity and diffusivity at a minimum level, compared to the classical Smagorinsky model. All operators are discretized using central discretizations except the convective terms in the scalar transport equations for which the QUICK scheme is used. The code is parallelized using MPI.

The focus of the present study is only on the case of small density differences between the lock fluid and the ambient fluid such that the Boussinesq approximation is valid. The fluid density is assumed to vary linearly with the non-dimensional concentration C. The Navier-Stokes and transport equations for the fluid scalar property (e.g., salinity, temperature) that determines the local value of the density are made dimensionless using the channel half depth, h, and the buoyancy velocity, $u_b = \sqrt{g'h}$, ($g' = g(\overline{C}_{\max} - \overline{C}_{\min})/\overline{C}_{\min}$, where g' is the reduced gravitational acceleration, $\overline{C}_{\max}, \overline{C}_{\min}$ are the maximum and minimum concentrations / densities in the domain, g is the

gravitational acceleration). The time scale used in the discussion of the results is $t_0=h/u_b$. The non-dimensional concentration is defined as $C = (\overline{C} - \overline{C}_{\min})/(\overline{C}_{\max} - \overline{C}_{\min})$. The governing momentum (i=2, vertical) and concentration transport equations can be rewritten using two dimensionless parameters, the Grashof number, $Gr = (u_b h/\nu)^2$ which is the ratio of the buoyancy and viscous forces and the Schmidt number, $Sc = \nu/\kappa$, which is the ratio of the molecular viscosity, ν, to the molecular diffusivity, κ. The Reynolds number (Re=$\sqrt{Gr}$) which is sometimes used to characterize the gravity current is also defined in lock-exchange flows with the buoyancy velocity. Thus, its physical significance is still that of the ratio between buoyancy and viscous forces, as opposed to the usual definition as the ratio between inertial and viscous forces. Simulations in the present study assumed a unity value for the Schmidt number. As demonstrated by Hartel et al. (2000a), the value of the Schmidt number is not expected to significantly alter the generality of the results. In the case of LES, due to filtering, the governing equations contain the extra SGS terms.

$$\frac{\partial u_i}{\partial x_i} = 0 \tag{3.1}$$

$$\frac{\partial u_i}{\partial t} + \frac{\partial (u_i u_k)}{\partial x_k} = -\frac{\partial p}{\partial x_i} + \frac{\partial}{\partial x_k}\left(\left(\frac{1}{\sqrt{Gr}} + \nu_{SGS}\right)\left(\frac{\partial u_i}{\partial x_k} + \frac{\partial u_k}{\partial x_i}\right)\right) - C\delta_{i=2} \tag{3.2}$$

$$\frac{\partial C}{\partial t} + \frac{\partial (C u_k)}{\partial x_k} = \frac{\partial}{\partial x_k}\left(\left(\frac{1}{\sqrt{Gr}\,Sc} + \alpha_{SGS}\right)\frac{\partial C}{\partial x_k}\right) \tag{3.3}$$

where p is the dimensionless pressure. The equivalent Reynolds numbers in the momentum and concentration equations are equal to $\sqrt{Gr}$ and $\sqrt{Gr}$ Sc, respectively. No assumptions are needed on the value of the turbulent Schmidt number as the dynamic procedure (Pierce & Moin, 2001) directly estimates, based on the resolved velocity and concentration fields, the value of the SGS diffusivity. The dynamic procedure has also the advantage that it does not need extra corrections to account for buoyancy or rotation

effects on the resolved velocity and concentration fields. The need to use empirical near-wall viscosity corrections (e.g., Van Driest damping functions) is avoided when using the dynamic model as the governing equations are integrated up to the wall ($\Delta n_1^+ \sim 1$, where $n^+ = nu_\tau / \nu$, u_τ is the friction velocity) and the model coefficient decays automatically to zero as the solid boundary is approached.

Most of the 3D numerical simulations were run on 40 processors of a Xeon PC cluster with Myrinet. A complete simulation required around 30,000 CPU hours. The 2D simulations were run on 4 or 8 processors. The total CPU time was around 500 CPU hours per run. The code was found to scale practically linearly with the total mesh size over this number of processors.

CHAPTER 4

2D LES SIMULATIONS

4.1 DNS/LES Of Lock-Exchange Flow In An Infinite Channel

The main objective of this chapter is to evaluate the accuracy of 2D LES simulations in predicting the structure (spanwise-averaged) of a gravity current at high Grashof numbers and some integral quantities (e.g., front speed, bore velocity) related to its evolution. The use of 2D simulations for simulation of GC flows is limited by two main flow phenomena that cannot be accounted in these simulations. The first one is vortex stretching and the associated break of the 2D KH billows into small scale turbulence. The second one is the formation of the lobes and clefts at the front. While acknowledging these limitations, evidence will be shown that 2D highly resolved simulations can still predict some important quantities accurately, at least over the initial stages of the evolution of the gravity current.

To validate the code for gravity current flows, 2D LES and DNS simulations that correspond to the conditions considered in Härtel et al. (2000) were performed. Two simulations were conducted corresponding to Gr=1.25×10^6 and 2×10^9 with the top and bottom surfaces simulated as no-slip. The length of the computational domain was 25h (h = 2 is the nondimensional distance between the walls) which is long enough to prevent any interaction of the current with the channel ends for t<20h/u_b. The grid size was 2048×160 in both DNS and LES simulations which contrasts with the grid size of 8192×1200 used by Härtel et al. (2000) for a 2D DNS simulation at the higher Grashof number (Gr = 2.00×10^9). The grid size in the streamwise direction was 0.01h everywhere except near the ends of the domain where it was stretched to 0.03h. The grid size in the vertical direction away from the walls was around 0.02h. Near the walls the grid size was

reduced to $0.00075h$. Assuming conservatively that $u_\tau/U_f \sim 0.04$ the wall normal grid size at the wall in wall units is equivalent to $\Delta n^+ \sim 1$ for the higher Grashof number.

At the lower Grashof number ($Gr = 1.25\times10^6$) both LES and DNS simulations were conducted as the mesh was fine enough to conduct well resolved DNS. The physical Reynolds number was only $Re_f = U_f(h/2)/\nu = 648$. The results from the DNS and LES simulations were practically identical. This was expected as the LES module uses the dynamic model to estimate the sub-grid scale viscosity and diffusivity. This model has the property that it predicts practically zero values (couple of orders of magnitude lower than the molecular viscosity/diffusivity) if the grid is fine enough to resolve the small scales up to the dissipation range.

Fig. 4.1 compares the results of the present simulations to the corresponding 2D DNS of Härtel et al. (2000) at different stages of the evolution of the gravity current ($t=0t_0$ to $t=20t_0$, where the time scale is $t_0=(h/2)/u_b$). The KH billows are generated behind the gravity current front, as the front advances. Very good agreement is observed with regards to the number, shape and position of the KH billows and the position of the front at different stages of the evolution of the gravity current ($t=0t_0$ to $t=20t_0$) between the present simulations and the corresponding 2D DNS of Härtel et al. (2000a). The good agreement observed in Fig. 4.1 for the front position is consistent with the accurate prediction of the Froude number defined with the head velocity ($Fr = U_f / \sqrt{g'(h/2)}$) which is estimated at 0.58 in the present 2D LES simulations, practically identical to the value obtained by Härtel et al. (2000a) and various experimental investigations (see Fig. 4.4).

Instantaneous concentration contours at various time instances in the higher Grashof number ($Gr=2.00\times10^9$) LES simulation (Fig. 4.2) show the presence of much smaller 2D eddies that disturb the large KH billows. As opposed to the lower Grashof number simulation, the contours of these billows is very far from smooth indicating the fact that even in a 2D simulation these large eddies are breaking into smaller ones.

Though this process is observed in reality, the mixing in the interface region behind the front is taking place much slower because the only small scale instabilities allowed in the present simulations are 2D while in reality 3D instabilities are present. These 3D instabilities are very efficient at enhancing local mixing and thus inducing a faster decay of the coherence of the large KH vortices behind the two fronts. As the current advances, due to the initial presence of the small scale disturbances around the lock position, the symmetry of the current is more and more lost (e.g., especially for $t>15t_0$ in Fig. 4.2) and the flow becomes turbulent, though the turbulence is constrained to remain 2D. This is in contrast to the low Grashof number simulation where the current was observed to remain practically symmetrical during the whole simulated period.

In spite of the absence of the transition to three-dimensionality in the LES simulation, the front velocity is accurately predicted. The associated Froude number is 0.65, practically identical to the value obtained in the 2D DNS simulation of Härtel et al. (2000a) on a much finer mesh (see Fig. 4.4). The predicted front Reynolds number is close to 30,000 (see Table 4.1) which indicates that the flow is turbulent at least in the region immediately behind the two fronts. This is also confirmed by the contours of the non-dimensional sub-grid scale viscosity, ν_t/ν at $t=20t_0$ in Fig. 4.3 which show the presence of large regions where ν_t/ν is of order of unity, particularly around the KH billows and the interface. Contour plots of the instantaneous sub-grid scale diffusivity (not shown) are relatively similar because $Sc=1$ but not identical as the dynamic procedure for the sub-grid scale diffusivity is applied on the concentration equation rather than momentum. Though these instantaneous values may not appear large compared to the eddy viscosity values obtained from a RANS model, they are essential in providing the extra local dissipation needed near grid scale level to obtain a converged solution on a mesh sensibly coarser than DNS requirements.

Fig. 4.5 provides more details on the evolution of the front head position (x_f) with time starting at the moment when the lock gate was released. It is observed that for $t>2t_0$

the front position varies linearly with time in log-log scale. The slope of 1 in the plot in Fig. 4.5 confirms the fact that the front velocity is constant for $t>2t_0$ regardless of the value of the Grashof number. The accurate prediction of the front velocity by the 2D simulations is believed to be due to the fact that the real flow in the front regions is quasi 2D (e.g., main structures are the KH billows which are practically 2D in the formation region), and not much affected by the 3D flow structures that are observed to develop behind them.

The streamlines in a moving frame of reference in Fig. 4.6 indicate that, for both the high and low Grashof number simulations, some of the lighter fluid is overrun by the front while the rest travels above the front. This is because the stagnation point is located at a point that is below and behind the foremost part (nose) of the front in a frame of reference moving with the front velocity. Table 4.1 also indicates the height of the nose and that of the stagnation point, $\Delta y_n/h$ and $\Delta y_s/h$ respectively. The corresponding values in the 2D DNS simulations of Härtel et al. (2000a) are shown in parenthesis. The region of unstable stratification in between the interface delimited by the nose and the stagnation point of the current, and the bottom is thought (Härtel et al., 2000a) to be at the origin of the lobe and cleft instability observed experimentally and in the 3D DNS at Re_f~750 of Härtel et al. (2000a). The ratio of the light fluid flux underneath the front, $\dot{V}_u$, to the expected incoming flux of light fluid, $\dot{V}_0 = S_0 U_f$ (in 2D the incoming flow area per unit width is $S_0 = h$) is summarized in Table 4.1 and characterizes the strength of the instability due to the sheet of light fluid overrun by the front. Accurate prediction of this ratio is significant because using stability analysis Härtel et al. (2000a) have shown that the region of unstable stratification between the nose and the stagnation point, and not the buoyancy-induced rise of the sheet of light fluid overrun by the front, is the main cause of the lobe-and-cleft instability at the front. The predicted ratio decreases from 1.18% in the lower Grashof number simulation to about 0.32% in the higher Grashof number simulation. The values predicted by the 2D DNS simulations of Härtel et al. (2000) of

1.25% and 0.34% (Table 4.1) are comparable to present simulation results at both Grashof numbers.

4.2 LES Of Lock-Exchange Flow In A Channel With A Lateral Wall

The lock exchange flow corresponding to the laboratory experiments carried out by Hacker et al. (1996) is simulated using 2D LES. The bottom-propagating denser lock fluid which in all three experimental cases (A, B and C) considered by Hacker et al. (1996) extends up to the free surface is released into a less dense ambient fluid by the rapid extraction of a gate separating the two fluids as shown in Fig. 2.2a. The focus of the analysis of the gravity current evolution is on cases B and C, but present validation results related to the prediction of the main quantities characterizing the development of the current for all three cases. Additionally a simulation (case C-HI) at a much higher Grashof number ($Gr=10^{12}$, $Re_f = U_f(h/2)/\nu \sim 245{,}000$, $h/2$ is used because it characterizes the mean height of the current in a channel of depth h) was performed to test the robustness of the model to simulate currents at Grashof numbers outside the range typically studied using DNS and even outside the usual range at which laboratory experiments are performed and to investigate the effect of Grashof/Reynolds number on the development of the current.

The Reynolds numbers in cases A, B and C are in the range of 7,000 to 20,000 in the slumping phase, so the flow, at least in the front region, is turbulent. In agreement with the experimental setup (Fig. 2.2), no-slip boundaries were specified on the bottom wall and on the end wall while the top was treated as a slip boundary (zero shear). A convective outflow boundary condition was used at the right extremity of the computational domain that allows coherent structures to exit the domain in a time accurate way. The size of the grid was 3072×192 in all three simulations, the length of the computational domain varied between $9h$ and $18h$. The typical size of a cell is

$0.0025h$ in streamwise direction and $0.005h$ in vertical direction. Near the right boundary the streamwise cell size increases to $0.025h$. Near the end and bottom walls the cell size in the wall-normal direction decreases to $\Delta n=0.0005h$. In wall units assuming conservatively $u_\tau/U_f \sim 0.04$ this translates into $\Delta n^+ \sim 1$ for case B. The other two cases should be slightly better resolved. In the case C-HI simulation in which the aspect ratio of the initial lock fluid is the same as in case C, the mesh size away from the solid boundaries was very similar to the one used in case C, however the mesh was refined near the end and bottom walls to $\Delta n=0.00002h$ to insure $\Delta n^+ \sim 1$ at the walls. The mesh size was 3072×240.

Depending on the value of the initial aspect ratio of the denser lock fluid, $R = h/x_o$ (x_o is the initial lock length), the evolution of the gravity current is observed to be very different. Table 4.2 summarizes the parameters of the four simulations including the total length of the computational domain L and the initial aspect ratio R along with the predicted and measured values of the Reynolds and Froude numbers during the slumping phase when the front velocity U_f is constant. Figures 4.7 and 4.8 visualize the evolution and structure of the gravity current using concentration isocontours as predicted by the simulations (cases B, C and C-HI) along with the corresponding experimental results reported in Hacker et al. (1996) for cases B and C. The position of the reflected bore is denoted x_b in these figures. In case C it is possible to follow the evolution of the gravity-current in the experimental setup until it approaches the self-similar phase. In this case, the higher initial aspect ratio R (shorter lock length) causes the lighter fluid to reflect from the end wall much earlier compared to cases A and B (e.g., compare Fig. 4.7 and Fig. 4.8).

It is observed that the flow in the initial moments after the lock release (e.g., compare frame a in Figs. 4.7 and 4.8 corresponding to $t<2t_0$, $t_0=h/u_b$) is similar in all three cases, in the sense that a gravity current of denser fluid moving downstream (right) develops at the bottom of the domain. The head region of the current becomes unstable

due to the amplification of the KH instabilities on the interface between the denser and lighter fluids, and coherent billow structures are forming. These billows are clearly visible in frames a and b of Fig. 4.7. The evolution of the density contours in time show that in all the cases most of the mixing between the lock fluid and ambient fluid takes place in the region behind the front of the current (nose region) where the fluid becomes stratified at the interface.

In the present 2D simulations as the current develops in time, a sharp density gradient is maintained at the front while highly coherent KH billows are observed to shed from the region just behind the front and then propagate downstream with a speed that decays slowly in time (the front velocity is practically constant) while diffusing and enhancing the mixing locally. These structures are not as clearly defined in the corresponding experimental results where 3D instabilities have the effect of quickly destroying the coherence of these billows while enhancing the small scale mixing inside and behind the nose region. Careful inspection of the structure of the nose region as shown by experimental visualizations, particularly the waviness of the top of the nose region, suggests that some of the large billows obtained in the simulations are also present in the experiments. The correlation between the crests observed near the current-ambient fluid interface in simulations and experiments is strong especially for the first few eddies behind the front of the current.

In Case B (Fig. 4.7) the overall shape and structure of the gravity current, including the nose region, appear to be reasonably well predicted by the 2D simulations, at least over part of the slumping phase. This is despite the fact that in the experiment the gate removal has clearly introduced secondary motions that broke the symmetry of the gravity current (see frame a, and also discussion in Hacker et al., 1996). Analysis of the simulation results at the same moment in time (t=1.4t_0) shows that the flow is practically perfectly symmetric around x/h=1.0 (the gate position) except for the regions very close to the bottom wall and free surface, where different boundary conditions (no-slip vs. slip)

were used. In this respect numerical simulations have the advantage of allowing 'ideal' initial conditions to be specified. However, by $t=4.6t_0$ (frame c) the overall shape and length of the nose region are quite similar in experiment and simulation. A large billow is present at the rear of the nose region in frames c to e. If one follows the formation of this billow one can observe that the original KH eddies are energized as the bore reflected by the end wall is catching the rear of the gravity current nose at the location of these eddies. The main effect is the formation of this large structure and local enhancement of mixing. Some of the denser fluid from the rear of the nose is in fact drawn upwards into this structure as the bore is passing. Once the bore has past, this structure practically detaches from the gravity current in the 2D simulation. In frames d and e one can clearly observe that the region of high mixing corresponding to the large eddy at the back of the nose region situated around $x/h=1.0$ is well predicted by the simulation. The other region characterized by high mixing (second large billow from the left in frames d and e) is situated in the experiment at $x/h\sim2.7$ while in the simulation its position is around $x/h\sim2.0$.

For case C (Fig. 4.8), where experimental visualizations are available until the end of the slumping phase, one can see that the structure of the gravity current is fairly well captured at the earlier stages of the slumping phase (frames b to e). In the 2D simulations the KH billows are observable not only on the top of the interface where they form but also at large distances behind the nose where they partially maintain their coherence. During this process they lose part of their kinetic energy and the velocity at which they are convected downstream decreases toward zero. In reality these structures will loose their two-dimensionality fairly rapidly and eventually break into 3D turbulence producing the relatively mildly stratified region behind the nose observable in the experiments (frames g to j). As the reflected lighter fluid begins to catch up with the gravity current head (frame f), the KH billows break off the back of the head in the

simulations. For $t>10.4t_0$ (frames h to j), as the bore of lighter fluid catches the head of the gravity current, significant mixing occurs just behind the front.

Comparison of the corresponding frames in Fig. 4.8 shows that qualitatively the evolution of the gravity current in case C-HI is similar to the one in case C. The structure of the two currents is initially very similar (frame a) but differences in their subsequent evolution become noticeable for $t>2.7t_0$. The front speed is slightly higher, as observed from comparison of the front positions in the two simulations, and the diffusion of the large KH billows that separate behind the nose region as the bore passes by is faster in case C-HI. Interestingly, for $t>10.4t_0$ (frames h to j) the KH billows in case C-HI appear to be larger and to slightly move away from the bottom after the bore has overtaken them.

Results in Figures 4.7 and 4.8 suggest that the front position is accurately predicted at all times in the case B and case C simulations. The corresponding range of Froude numbers ($Fr = U_f / \sqrt{g'h}$) defined with the front velocity varies between 0.44 and 0.45 during the slumping phase for cases A, B and C (see Table 4.2) which compares reasonably well with the experimental values, Fr = 0.45/0.46±0.01. For the Reynolds number, the values from the simulations are Re = 6,820, Re = 19,730, and Re = 10,755 which are reasonably close to the experimental values of Re = 7,000, Re = 19,700, and Re = 11,000 for case A, B, and C respectively. For case C-HI the predicted value of the front velocity during slumping phase is 0.48 (Re~245,000) which corresponds to a 6-7% increase relative to case C.

The propagation of the bore in the slumping phase is difficult to infer directly from the concentration contours of the current because the bore propagates into the mixing layer created by the advancing head region of the gravity current moving away from the end wall. A more accurate way of determining the bore position is to look at the concentration vs. time variation on a line at a certain distance from the bottom. Such a plot is shown in Fig. 4.9 for case C at a relative distance of d/h=0.1 from the bottom. In this figure, one can observe the presence of a dark region in the form of a triangle with a

very sharp angle corresponding to the intersection of the trajectories followed by the front and the bore at that distance from the bottom. As these trajectories are close to straight lines, one deduces that the associated front and bore velocities are constant. The slope of the bottom border (red line) corresponds to the speed of the front while the slope of the top border (yellow line), which sometimes cuts through the billows (observe the dark streaks present above the yellow lines), corresponds to the speed of the reflected bore. One can see that the slope, relative to the time axis, of the red line is slightly higher than the one of the yellow line confirming that the bore velocity is higher than the front velocity. Table 4.3 summarizes the predicted values of the front and bore velocities.

For all simulations the ratio of U_{bore}/U_f is between 1.35 and 1.4, which agrees well with the experimental observed range (Rottman and Simpson, 1983). It should be noted that it appears that the increase in the Grashof number (compare case C and case C-HI results) left unchanged the ratio of U_{bore}/U_f (Table 4.3) though, as expected, the predicted front and bore velocities are larger. Examining case C in detail (Fig. 4.9), it can be observed that the intersection of the two trajectories takes place inside the computational domain at x/h~5.9, t~12.5 (Fig. 4.9) corresponding to a nondimensional streamwise length of l~9.5, ($l = \left(x_f - x_o\right)/x_o$, x_f is the front position). The values of l obtained for cases A (l=7.8) and C (l=9.5) are consistent with experiments and theory (Rottman and Simpson, 1983). The length of the domain in case B was too short to capture the transition to the inviscid self-similar phase. In Fig. 4.9, once the bore overtakes the front, the border between the ambient fluid and the gravity current curves up, meaning the velocity of the front of the gravity current starts decaying in time.

This is made clearer in Fig. 4.10 which shows the front position as a function of time in log-log scale for cases B, C and C-HI. As expected, during the slumping phase all curves have a practically constant slope equal to 1. The slope of 1 in the l-t plot corresponds to a constant front velocity. As the bore overtakes the front, the slope of the trajectory $l=l(t)$ decreases over a relatively short time period corresponding to the

transition between the two phases before regaining a fairly constant value close to 2/3 (this slope corresponds to a velocity decay in time proportional to $t^{-1/3}$) in the case C and case C-HI simulations. For these cases, the simulations were run until approximately $35t_0$, well past the start of the inviscid phase. The measured slope over the inviscid phase was 0.6 for case C and 0.64 for case C-HI. These values are close to the analytical value (2/3) obtained from theory indicating that even a 2D simulation can capture some of the main flow characteristics in the self-similar phase. The slightly higher velocity decay observed for case C is believed to be due to the fact that the flow at the head of the current appears to be more mixed compared to the experiment once the bore overtakes the front. This causes a smaller buoyant force at the interface between the head and the light fluid in front of it and thus eventually into a faster decay of the front velocity.

It is also interesting to look closer at the dynamics of the flow immediately after the gate is removed. Case C is again chosen for discussion. It has already been shown that after a short initial adjustment phase, the front velocity becomes practically constant (start of the slumping phase). The duration of this initial phase can be inferred from Fig. 4.11, where the position and velocity of the front (continuous line) and initial bore (dashed line) propagating toward the end wall are plotted, as being equal to $\Delta t=1.8t_0$. At this time the value of U_f is very close to the asymptotic value of $0.45\sqrt{g'h}$ and the variation of x_f is practically linear. During this time the bore starting at $x=x_0$ moves toward the end wall ($x=0$). At times very close ($t<0.3t_0$) to the initiation of motion, the influence of the end wall is not felt by the forming bore and the flow is practically symmetrical with respect to $x=x_0$ meaning that the front and the bore travel at same speed in opposite directions (the two lines are practically superimposed). Though the symmetry is lost for $t>0.3t_0$ the evolutions of the front and bore are still close until $t\sim0.75t_0$. In the experiments due to the physical removal of the lock and the associated motions induced locally in the lock area, the symmetry of the flow is lost once the gate was removed. While the front continues to develop as in a channel of infinite length, the bore movement

becomes affected more and more by the end wall and the bore velocity decays sharply for $t>0.85t_0$ to become practically zero at $t\sim1.65t_0$ when the bore is reflected by the end wall.

The streamline patterns in a coordinate system advancing with the front velocity (Fig. 4.12) indicate that for gravity currents developing in channels with a lateral wall, the foremost point (nose) is not a stagnation point, similar to the case when the current was developing in an infinite channel (Fig. 4.6). This is found to be true not only over the slumping phase when the physics of the two flows is very similar (Fig. 4.12a), but also over the inviscid phase when the flow beneath the nose but outside the current head becomes more mixed (Fig. 4.12b). The ratio of the light fluid flux underneath the front, $\dot{V}_u$, to the expected incoming flux of light fluid, $\dot{V}_0$, is close to 0.49% during the slumping phase and equal to 0.54% at $t=22.4t_0$ in the self-similar phase. For case C-HI the ratio is even smaller, the corresponding values are 0.10% and 0.11%, respectively. This make us to expect the lobe-and-cleft instability in the case of finite channel lock exchange gravity currents to be driven by the same mechanism (unstable stratification region between the nose and the stagnation point) identified for the case of infinite channel gravity currents.

The contour plots of the non-dimensional sub-grid scale diffusivities, α_t/α at $t=16t_0$ for case C and case C-HI in Fig. 4.13 show that at these high Grashof and Schmidt (Sc=600) numbers the sub-grid scale diffusivity controls the dissipation at the grid scale level in the concentration equation. The instantaneous values of the ratio of α_t/α are as high as 100 in case C and up to 1000 in case C-HI. As expected, the largest values are predicted around the KH billows and the interface. Thus for the parameters considered in these simulations the sub-grid scale model in LES is expected to have a non-negligible impact on the results. In this regard the dynamic model has several advantages over the classical constant coefficient Smagorinsky model as no empirical damping functions have to be used near the wall and the model predicts very small values of the sub-grid scale viscosity and diffusivity in regions where the flow is not turbulent but the mean shear is

non-zero. This is important especially in the relaminarization region behind the current. Also, as the dynamic model is overall much less dissipative than the constant coefficient version, less damping occurs on the large scales present in the flow, thus one expects more accurate predictions especially at high Grashof and/or Schmidt numbers.

4.3 Summary

The present simulations demonstrate that 2D LES with a dynamic sub-grid scale model can capture several important aspects of lock-exchange flows in infinite channels and in channels with a lateral end wall at moderate and large Grashof and Reynolds numbers and at Schmidt numbers as high as 600. For these flow parameters even 2D non-dissipative DNS simulations are very expensive. The largest Grashof number in the simulations was equal to 10^{12}. At this Grashof number it was shown that the flow inside the head part of the current is highly turbulent and the effects of the sub-grid scale model are very important both in the momentum and scalar transport equations.

Over the range of Grashof numbers where both 2D DNS and LES was attempted, it was shown that the present energy conserving non-dissipative (momentum) code can predict the main aspects of the flow at levels comparable to those of 2D DNS simulations on much finer meshes. The main limitation of 2D simulations is related to the prediction of the development of the KH billows in the later stages of decay. If in experiments it is observed that the KH billows do not preserve their structure across the width of the channel and break relatively rapidly into smaller 3D structures, in the 2D simulations in which the 3D instabilities are not allowed to develop these structures maintain their coherence for a much longer time. Still, the overall structure of the nose region was found to be similar to experiment at least over the early stages of the slumping phase (e.g., the size and shape of the main 2-3 large billows shed behind the front is well reproduced in the simulations in finite length channels).

The constant value of the front velocity during the slumping phase and the associated Froude and Reynolds numbers were correctly predicted for both the infinite channel and the finite channel simulations. The ratio between the predicted bore and front velocities for the finite channel simulations was found to be in the range of 1.35-1.4 and the transition toward the self-similar phase was predicted to take place at around 7-10 initial lock lengths, within the experimental observed ranges (e.g., see Rotman and Simpson, 1983). It was shown that an increase by more than one order of magnitude in the Reynolds number left the ratio of the bore to the front velocity unchanged though, as expected the actual velocities were slightly higher for the current with a higher Reynolds number. The simulations correctly predicted the evolution of the front trajectory and velocity during the inviscid self-similar phase, in particular the velocity decay with $t^{-1/3}$. It was found that the structure of the nose region in a frame of reference moving with the front velocity was similar in the infinite channel simulations and in the finite channel simulations not only during the slumping phase but also during the inviscid phase. The ratio between the light fluid flux underneath the front $\dot{V}_u$ to the expected incoming flux of light fluid, $\dot{V}_0$ was found to be around or less than 1% for $Gr>10^8$, which suggests that the unstable stratification region between the nose and the stagnation point is the main cause for the lobe and cleft instability observed in experiments and in 3D DNS simulations at lower Reynolds numbers.

Table 4.1.Details of the gravity current simulations in channels with no lateral walls.

Case	*Gr*	Re_f	*Fr*	$\Delta y_n/h$	$\Delta y_s/h$	V_u/V_0 (%)
Low-Gr	1.25×106	648	0.58	0.26 (0.26)	0.067 (0.065)	1.18 (1.25)
High-Gr	2.00×109	30,000	0.65	0.11 (0.11)	0.021 (0.018)	0.32 (0.34)

Note: Values in brackets are the results of Härtel et al. (2000).

Table 4.2. Details of the lock-exchange simulations in channels with a lateral wall.

Case	*Gr*	*L/h*	Aspect ratio, $R=h/x_0$	Experiment		Simulation	
				Re_f	*Fr*	Re_f	*Fr*
A	9.6×10^8	18	0.67	7,000	0.45±0.01	6,820	0.44
B	7.7×10^9	9	1.00	19,700	0.45±0.01	19,730	0.45
C	2.3×10^9	13.483	1.78	11,000	0.46±0.01	10,755	0.45
C-HI	1.0×10^{12}	13.483	1.78	-	-	245,000	0.48

Table 4.3. Comparison of bore and front velocities during slumping phase for simulations in channels with a lateral wall.

Case	$U_{bore}/\sqrt{g'h}$	$U_f/\sqrt{g'h}$	U_{bore}/U_f
A	0.61	0.44	1.39
B	0.61	0.45	1.35
C	0.62	0.45	1.35
C-Hi	0.65	0.48	1.35

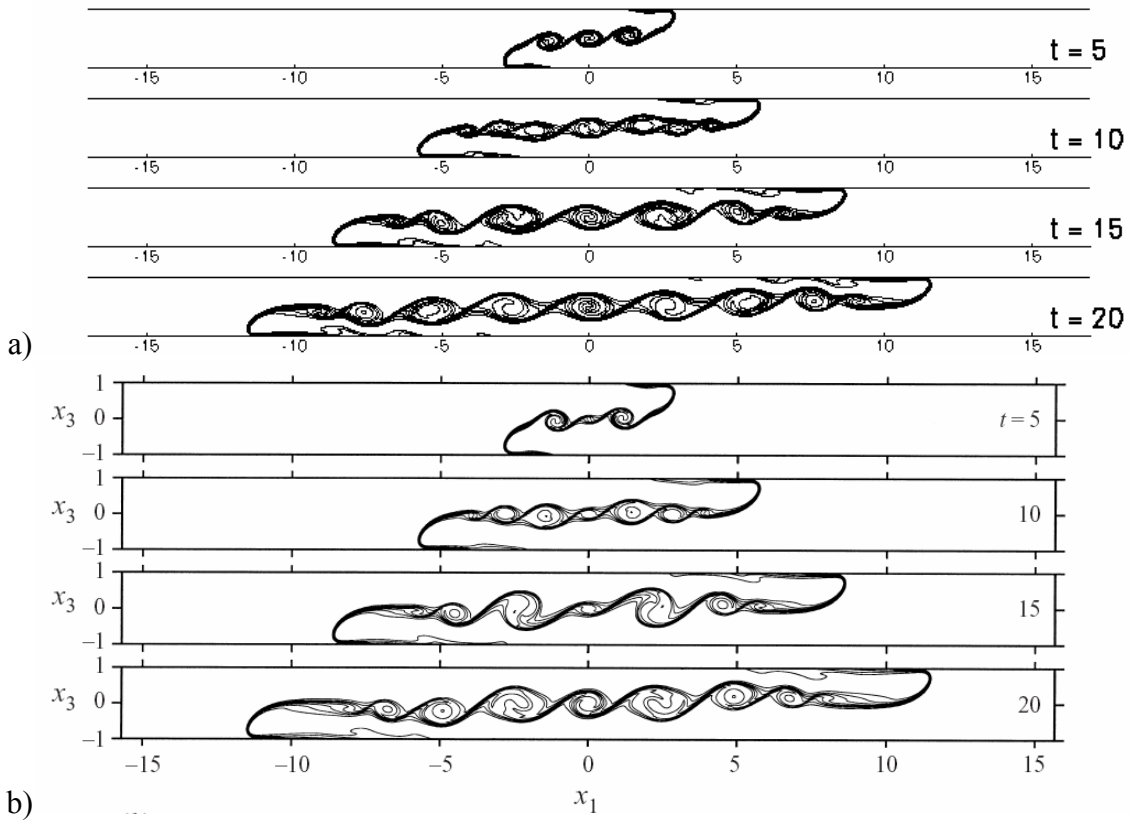

Figure 4.1. Density contours corresponding to 2D lock-exchange flow in an infinite channel with no-slip walls at $Gr = 1.25 \times 10^6$. Nondimensional time from top to bottom is t/t_0=5, 10, 15 and 20. (a) Flow field of present 2D LES. (b) Flow field of 2D DNS of Härtel et al. (2000).

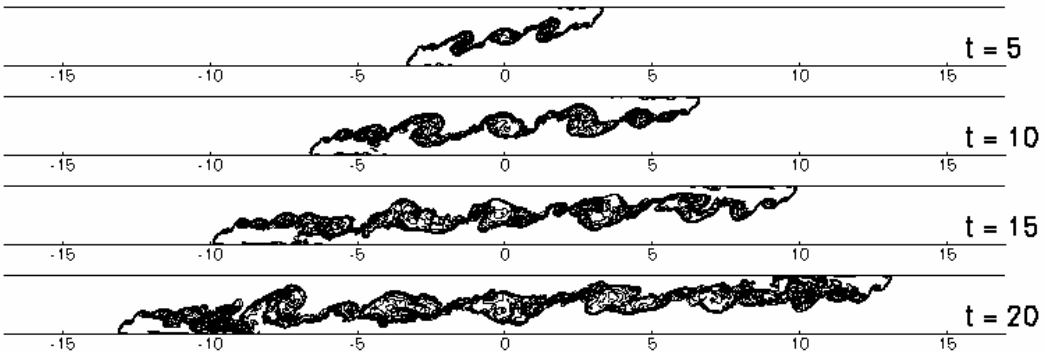

Figure 4.2. Density contours corresponding to 2D lock-exchange flow simulation in an infinite channel with no-slip walls at $Gr = 2.00 \times 10^9$. Nondimensional time from top to bottom is t/t_0=5, 10, 15 and 20.

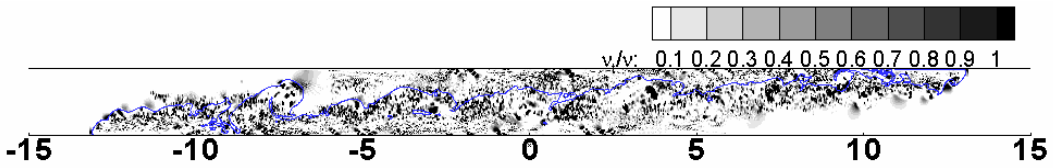

Figure 4.3. Instantaneous non-dimensional sub-grid scale viscosity contours at $t/t_0 = 20$ for 2D LES of lock-exchange flow in an infinite channel. The line corresponds to the current interface.

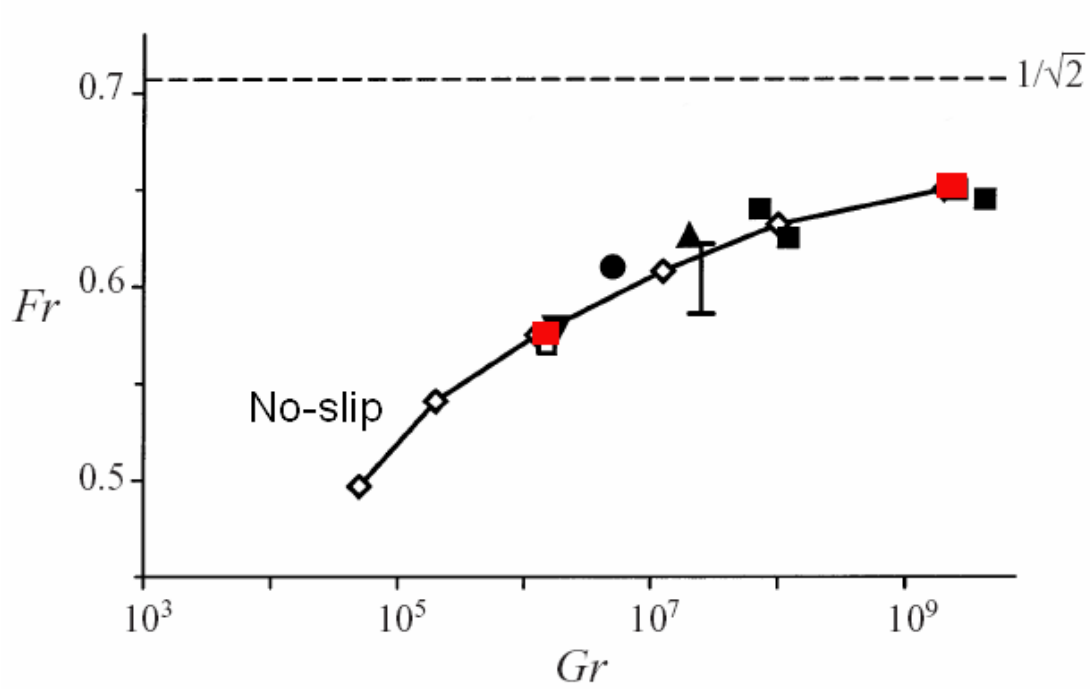

Figure 4.4. Froude number of the front of the gravity current, *Fr*, as a function of the Grashof number, *Gr*. Red squares correspond to present 2D LES. Open symbols correspond to DNS simulations of Härtel et al. (2000). Experimental data: ■, Keulegan (1957); ●,Simpson & Britter (1979);▲ Rottman & Simpson (1983);▼, Keller & Chyou (1991). $1/\sqrt{2}$ is the theoretical result of Benjamin (1968).

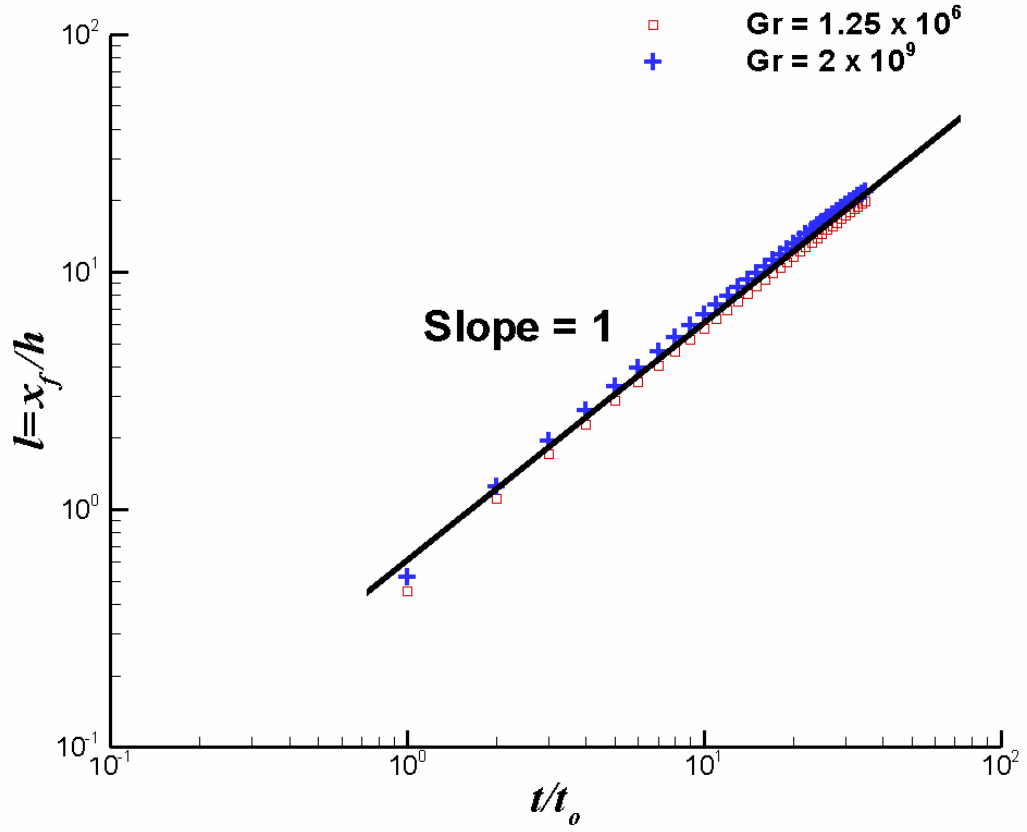

Figure 4.5. Front position vs. time in log-log scale for infinite channel simulations.

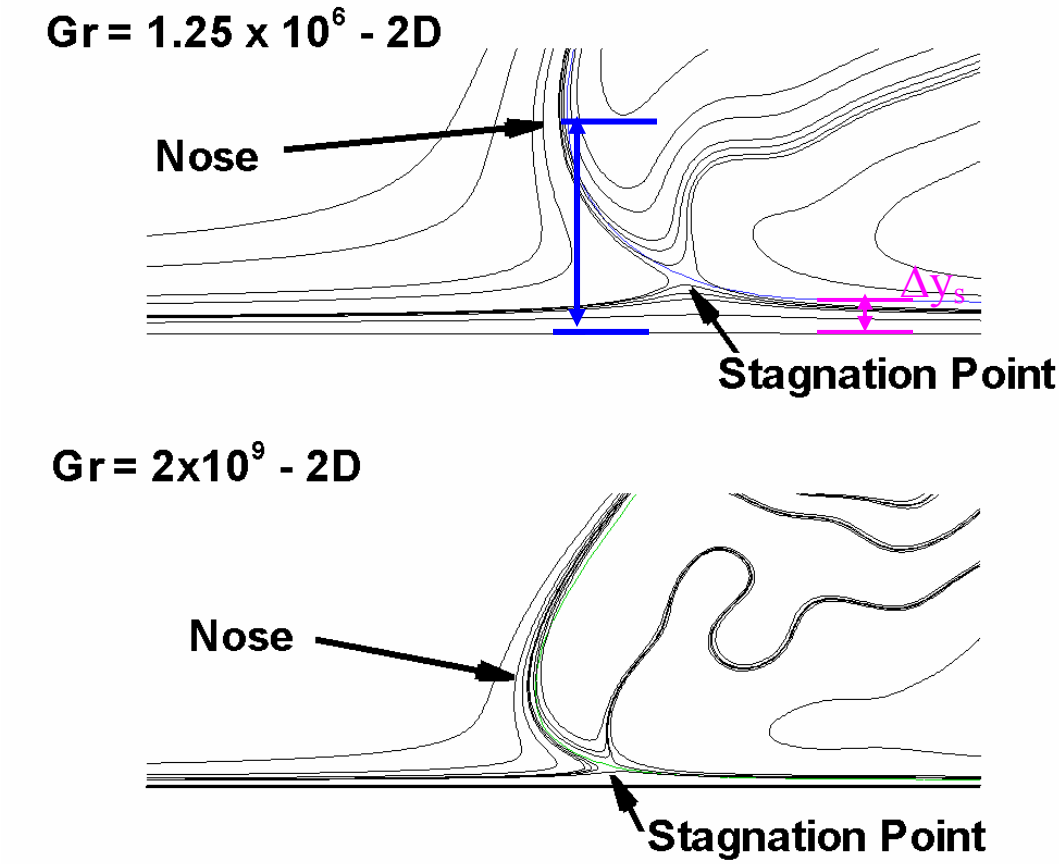

Figure 4.6. Comparisons of the positins of the stagnation point and nose of the current head in a moving frame of reference for infinite channel simulations.

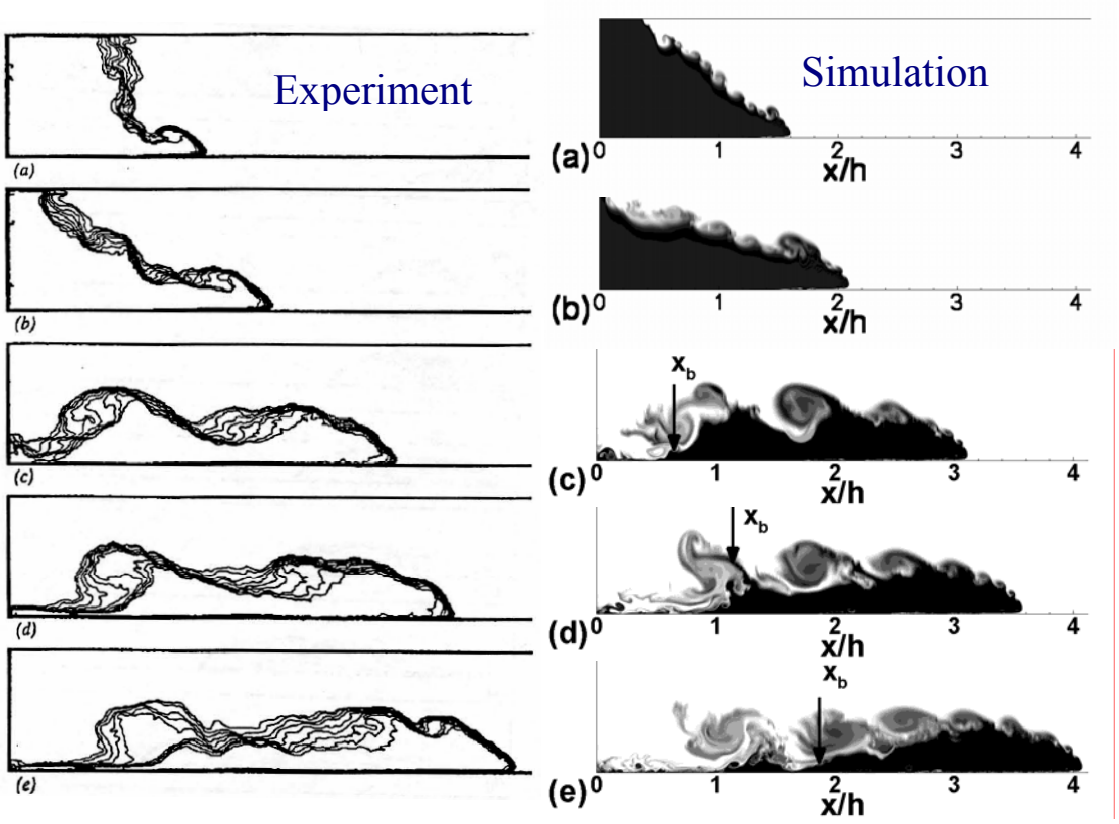

Figure 4.7. Evolution of gravity current for case B. Density contours at subsequent non-dimensional front positions, $l=(x_f-x_0)/x_0$, and simulation times, t; (a) l = 0.60, t=1.4 (b) l = 1.11, t=2.4 (c) l = 2.10, t=4.6 (d) l = 2.56, t=5.6 (e) l = 3.08, t=6.6.

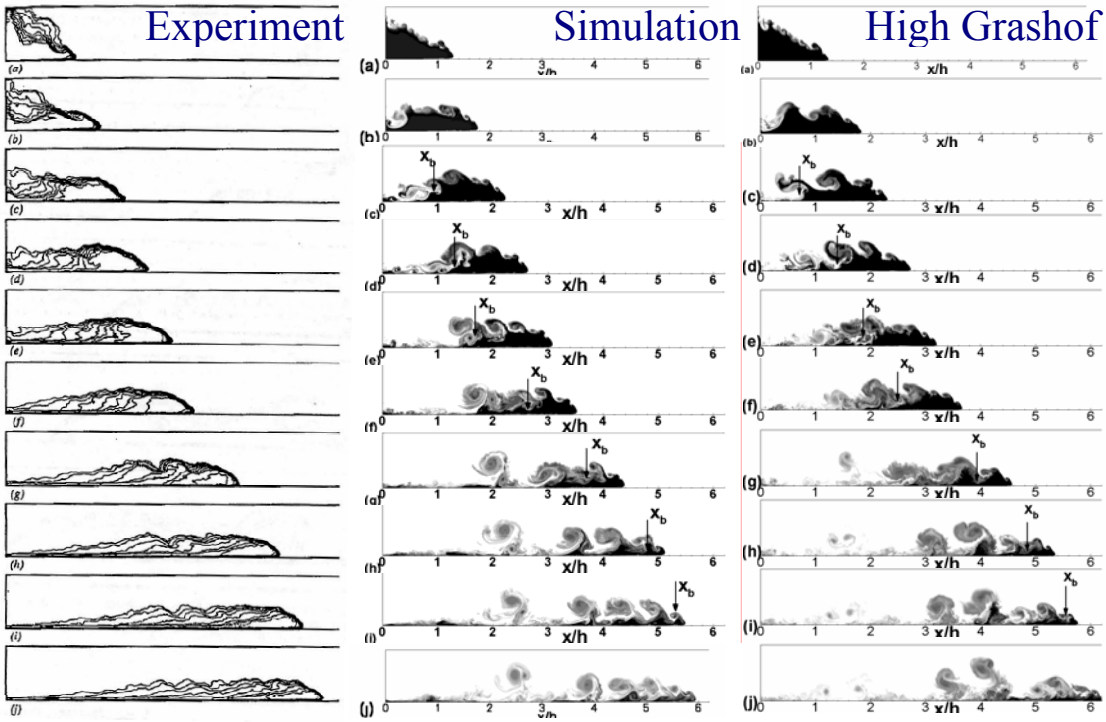

Figure 4.8. Evolution of gravity current for case C experiment (left), case C LES (center) and case C-Hi LES (right). Density contours at subsequent simulation times, t/t_0; (a) t/t_0=1.7 (b) t/t_0=2.7 (c) t/t_0=3.7 (d) t/t_0=4.6 (e) t/t_0=5.6 (f) t/t_0=6.6 (g) t/t_0=8.6 (h) t/t_0=10.4 (i) t/t_0=11.6 (j) t/t_0=12.4.

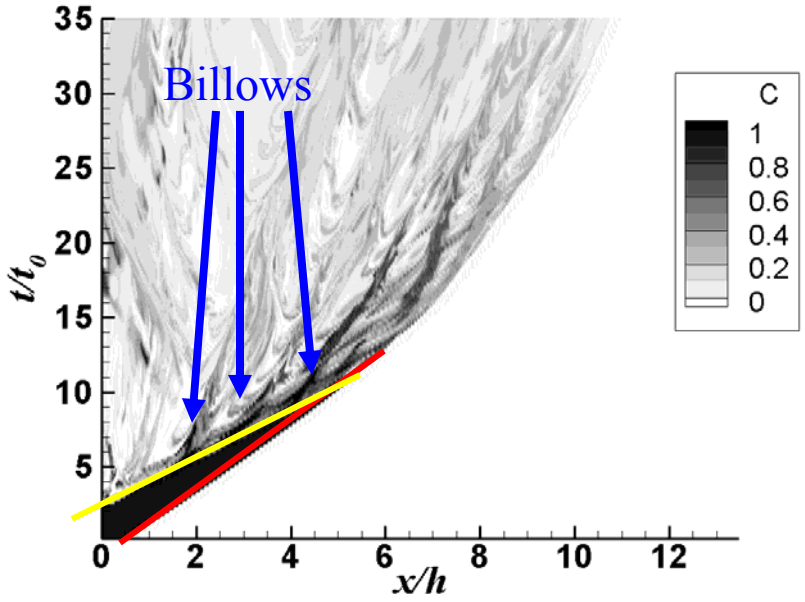

Figure 4.9. Evolution of density with time along the *x* axis for Case C. Distance from the bottom is *d/h* = 0.1.

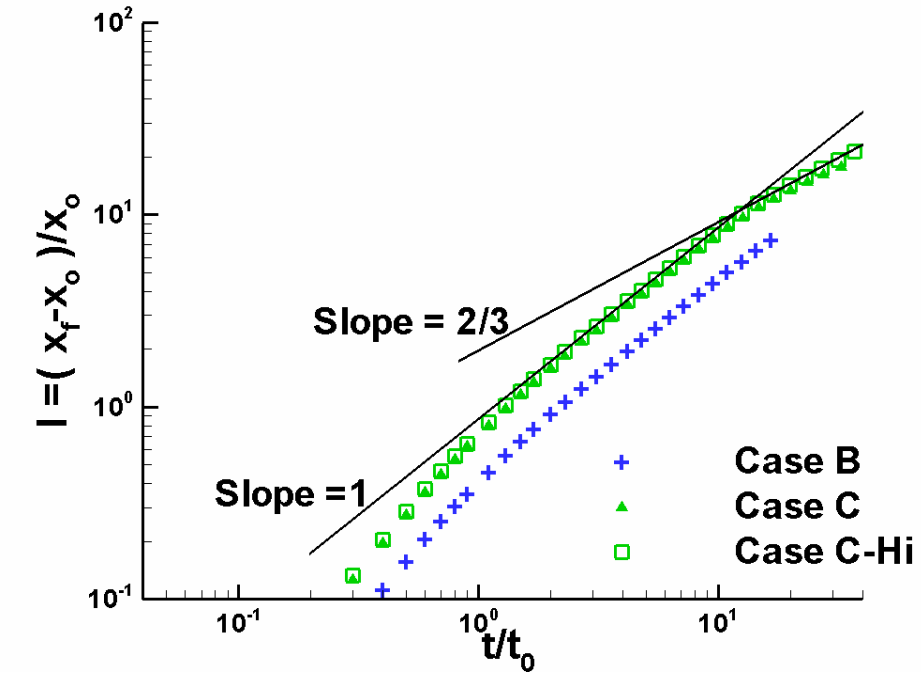

Figure 4.10. Front position vs. time in log-log scale for finite-channel simulations.

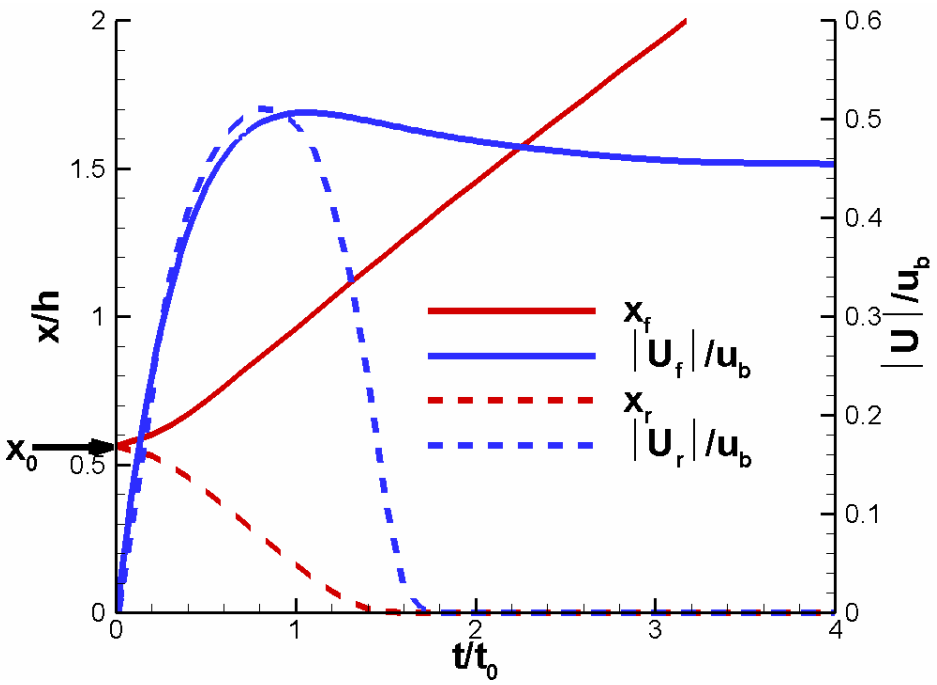

Figure 4.11. Position and velocity of the gravity current front and bore (before reflection at the end wall) for case C.

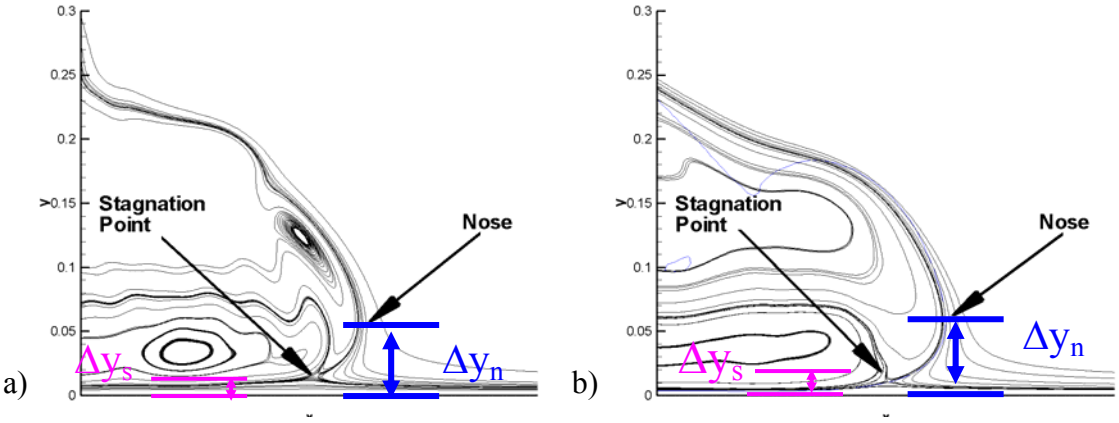

Figure 4.12. Structure of the head of the gravity current and comparisons of the positions of the stagnation point and nose in a moving frame of reference for finite-channel simulation (case C) during a) slumping phase, $t = 4.6t_0$; b) inviscid self-similar phase, $t = 12.4t_0$

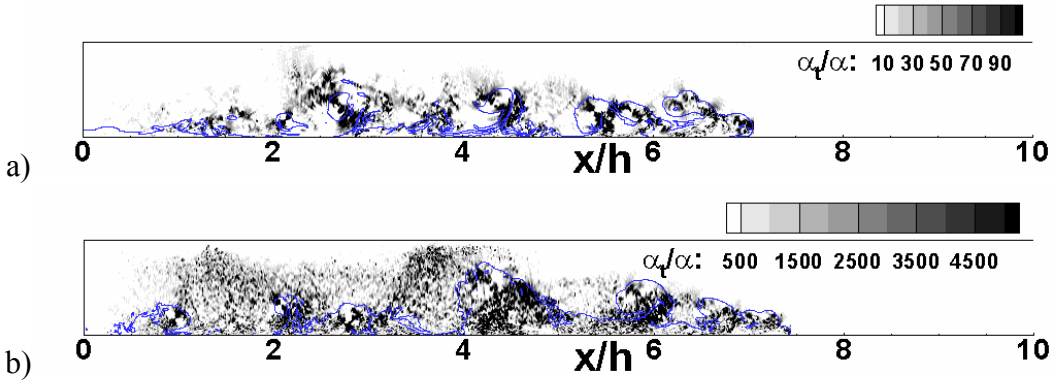

Figure 4.13. Instantaneous non-dimensional sub-grid scale eddy diffusivity contours at $t = 16t_0$ for 2D LES of lock-exchange flow in a finite channel: a) Case C, b) Case C-Hi. The line corresponds to the current interface.

CHAPTER 5

3D LES SIMULATIONS OF INFINITE-VOLUME LOCK-EXCHANGE FLOWS

5.1 Simulation Setup

The 3D LES simulations (see Table 5.1) conducted at $Gr=1.25\times10^6$ ($Re=\sqrt{Gr}=1{,}118$) and $Gr=2\times10^9$ ($Re=44{,}721$) are referred to as LGR and HGR, respectively. Some comparisons with 2D simulations conducted at the same values of the Grashof number are also discussed. The top and bottom surfaces are simulated as no-slip smooth walls similar to the experiments and DNS simulations used for validation. The flow in the spanwise direction is assumed to be periodic.

The length of the computational domain was $L_1=48h$ which is long enough to prevent any interaction of the GCs with the lateral boundaries for $t<35t_0$. The domain sizes in all three directions are close to the ones used by Hartel et al. (2000a) in their 3D computation at $Gr=1.5\times10^6$ and allow the development of several lobes and clefts in the spansise direction at both Grashof numbers. The grid size was $2048\times80\times160$ in the streamwise, spanwise (domain width $L_3=3h$) and vertical directions ($L_2=2h$), respectively. This corresponds to approximately 26.2 million mesh points. The grid size in the streamwise direction was $0.02h$ everywhere except near the ends of the domain where it was stretched to $0.06h$. The grid size in the vertical direction, away from the walls, was around $0.04h$. The grid size near the walls was reduced to $0.001h$. Assuming conservatively that $u_\tau/U_f\sim0.04$, $U_f/u_b=0.65$, the wall normal grid size at the wall is equivalent to $\Delta n^+\sim1$ wall unit for the higher Grashof number. In the spanwise direction, the grid size was $0.038h$. This mesh size, especially at the walls, was sufficiently fine for the code to resolve the turbulent structures without resorting to wall functions in the HGR simulation. In the 2D simulations the size of the computational domain was (L_1,L_2) and the number of grid points was similar to the one used in a z=constant plane in the 3D simulations.

The flow field was initialized with the fluid at rest. The time step in all the simulations was equal to $0.001t_0$, corresponding to a maximum value of the Courant number of 0.25. Most of the solutions were advanced in time until $t=35t_0$. At that moment, the distance between the front of the current and the lateral boundaries was larger than $4h$, sufficient to ignore their interaction (Hartel et al., 2000a). The non-dimensional concentration field was initialized with a constant value of one in one half of the channel and a constant value of zero in the other half. Additionally, a small random disturbance was applied on the concentration interface (lock-gate region) at the start of the simulations to accelerate the growth of 3D instabilities and transition to turbulence. A no-flux boundary condition was assumed for the concentration at the top and bottom boundaries.

5.2 Analysis Of The Evolution Of Gravity Currents And The Dynamics Of Coherent Structures

In the following discussion, the head of the current refers to the part of the GC that contains the region behind the front (generally called the energy conserving head region) and the dissipative wake region where small KH billows are forming at the interface between the two fluids.

The evolution of the two currents in the LGR 3D simulation is shown in Fig. 5.1a at several non-dimensional times ($5<t/t_0<20$) during the slumping phase using spanwise averaged concentration isocontours. Similar results from the HGR 3D simulation are presented in Fig. 5.2a. Instantaneous visualizations of the front and interface regions at the two Grashof numbers are shown in Fig. 5.3 at t/t_0=5, 10 and 20 using a concentration isosurface (C=0.5). Significant differences are observed in the evolution and structure of the lock-exchange flow between the LGR and HGR simulations; this shows that Grashof number effects are important between 10^6 and 10^9.

Over the time period simulated in the LGR simulation, the flow is highly three-dimensional only in the front region where the lobe and clefts start developing once the head has formed at the end of the acceleration phase (see inset pictures in Fig. 5.3). Quasi 2D KH interfacial vortices are generated behind the front, as the current advances. This can be observed in Fig. 5.3 where the shape of the deformations in the concentration isocontour surface clearly shows the presence of KH billows. The KH vortices that populate the interface region between the two currents remain quasi 2D until $t \sim 12t_0$ when large scale oscillations develop in the spanwise direction (e.g., see Fig. 5.3c at $t \sim 20t_0$). This affects the size of their cores and deforms the axes of these vortices. Between the region just behind the front, where the vortex tubes are originating, and the middle of the channel ($x/h=0$), where the current started, the interfacial vortices appear to extend over the whole span of the computational domain.

Three-dimensional instabilities, as expected, are present and their energy becomes larger as the current develops (e.g., compare shape of the interface at $t=10t_0$ and $t=20t_0$ in Figures 5.3b and 5.3c). The spanwise-averaged flow in Fig. 5.1a is practically anti-symmetric with respect to the original position of the lock gate until $t \sim 15t_0$. After this point, the growth of the 3D instabilities induces a clear loss in symmetry of the evolution of the forward and backward propagating currents. For instance, in Fig. 5.1a at $t \sim 20t_0$ the second KH billow behind the backward propagating current is much more coherent and its shape is more circular compared to the corresponding billow behind the forward propagating current. The other observation is that the coherence of the KH billows remains high, and their dissipation in time is very slow. Even in the lock-exchange flow at $t=20t_0$ (Figures 5.1a and 5.3c) all nine KH billows are clearly observable. The predominant 2D character of the flow is also confirmed by the good agreement observed between 2D simulations and the present 3D simulation even in the later stages of the evolution of the current. Figures 5.1b and 5.1c show the density contours corresponding to a 2D simulation performed with the same code and to a 2D simulation by Hartel et al.

(2000a) at $t \sim 20t_0$. Though the mixing inside the KH billows appears to be somewhat larger in the spanwise averaged contours obtained from the 3D simulation, the head shape, front position and the number of interfacial vortices are reproduced correctly by the 2D simulation. The 2D and the 3D spanwise averaged results are in excellent agreement for $t<15t_0$.

In contrast to the LGR simulation, in the HGR case the break in the (anti) symmetry of the evolution of the forward and backward propagating currents is observed very early. It is clearly distinguishable at $t=5t_0$ in Figures 5.2a and 5.3a. Still, at that time instance the KH billows maintain their predominantly 2D character as observed in Fig. 5.3a. However, at $t=10t_0$ (Fig. 5.3b) only the first two to three billows which were just shed from the front region, maintain their coherence and are easily identifiable. The KH billows in the middle of the domain rapidly loose their coherence due to their interaction with small 3D eddies that are caused by the amplification of the 3D instabilities in the interface region and interaction with the turbulent flow in the head region. These 3D structures have enough energy to strongly distort, stretch and eventually break the KH billows into smaller turbulent eddies a relatively short time after their formation. The process continues in time, such that at $t=20t_0$ only the first one or two KH billows can be identified in Figures 5.2a and 5.3c. Even the cores of the KH billows in the formation region are strongly disturbed in the spanwise direction. This is due in part to their interaction with the lobes and the clefts in the front region. These interactions are comparatively much smaller in the LGR simulation (see Fig. 5.3c).

The simulation captures the details of the mixing process in the interface region. The shedding of the KH billows introduces an important amount of energy into the interface region behind the front. This energy is redistributed once the KH billows lose their coherence. Wisps of heavy or light fluid are displaced by the highly energetic 3D structures that resulted from the breaking of the KH billows. These structures can engulf patches of fluid and transport them away from the interface. Then, by the action of the

small scale eddies and dissipation these wisps of heavier / lighter fluid are mixed with the surrounding fluid. Once the current head has passed a certain location there is no source of energy toward the large scales around that location. Eventually the large scales will be depleted of energy, but the small scales can still be quite energetic for a relatively long time before they dissipate and the flow relaminarizes. As a result for $t>25t_0$, the flow in the mixing layer that forms at the interface, away from the fronts of the two currents, does not contain large scale structures. The end effect is the formation of a stably stratified, slightly tilted layer that corresponds to the interface region away from the two fronts. This layer can be observed in the spanwise averaged density contours in Fig. 5.2a. The thickness of the mixing layer in the central part of the channel is relatively constant. The length of the tilted layer of mixed fluid grows from about $14h$ at $t=24t_0$ to about $19h$ at $t=33t_0$. Over this interval the tilting angle relative to the horizontal is about 14º and it is slowly decaying with time.

More details on the concentration distribution within this layer are given in Fig. 5.4 where the spanwise-averaged concentration profiles across the layer are plotted at $x/h=0.0, \pm2$ and ±4. The concentration profiles were plotted taking into account the expected anti-symmetry of the spanwise-averaged fields over the central region of the channel. Indeed for $t>27t_0$ the concentration profiles appear to collapse into a unique curve at $x/h=0$. The time at which the collapse begins increases with the distance from the original position of the lock gate. For example, at $x=2h$ the time is $29t_0$. The concentration profile is still symmetric around the $C=0.5$ value at sections with $x/h>0$ but, due to the tilting, the value of y/h corresponding to $C=0.5$ is not equal to one except at the center of the channel. However, if the profiles at different sections are superimposed on top of each other such that the $C=0.5$ value occurs at the same point (see Fig. 5.4d), the profiles appear to be relatively close to each other and can be approximated using a unique hyperbolic tangent function (see dashed line in Fig. 5.4d).

In contrast to the 3D simulation, the KH billows in the 2D simulation (Fig. 5.2b) maintain their coherence for much longer time intervals as 3D instabilities cannot develop, stretch the cores of the interfacial KH vortices and eventually destroy their spanwise symmetry. For example, the billows are clearly distinguishable in the frame at $t=20t_0$ in the 2D simulation. Their intensity is high and, though small 2D eddies are present, it is the large KH billows that drive the mixing process in the interface region. Related to the differences between the 2D and 3D simulations for the HGR case it is also interesting to consider the effect of the SGS model on the instantaneous solutions in the two cases.

The contour plots (x-y plane) of the non-dimensional SGS viscosity, ν_{SGS}/ν, at $t=20t_0$ are show in Fig. 5.5. As expected, the largest values of the SGS viscosity and SGS diffusivity (not shown) were predicted around the KH billows and the interface. In the 3D simulation the region of large SGS viscosity is much more compact around the interface between the two currents and the values are higher compared to those predicted by the 2D simulation. This is an indication that the energy in both the unresolved and the smallest resolved scales is much larger in the 3D simulation and is consistent with the presence of energetic small scale highly 3D turbulent eddies in the interface region as observed in Figures 5.3b and 5.3c. These eddies are of course absent in the 2D simulation where the position of the KH billows is easily identifiable in the SGS viscosity plot. The other region of relatively high SGS viscosity values is situated at the head of the two currents and spans the whole height of the head suggesting that the flow is turbulent in the head region. The instantaneous values of ν_{SGS}/ν are as high as 10 in the two HGR simulations. Though the ν_{SGS} values are comparable to the molecular viscosity, its inclusion in the model has a very important effect on the numerical stability of the Navier-Stokes solver. Observe also that the dynamic model correctly predicts negligible SGS viscosity levels in regions of high, resolved shear, where the flow is not turbulent. Thus, on the meshes used in the present simulations and for Grashof numbers around 10^9,

the SGS model in LES is expected to have a certain impact on the results as opposed to simulations with $Gr \sim 10^6$ where the sub-grid scale contribution is one to two orders of magnitude smaller than the molecular viscosity / diffusivity.

The lobe and cleft structure at the front of the two currents starts as an instability of the front surface in the near-wall region and is observable in the LGR simulation at $t=10t_0$ (Fig. 5.3b) and in the HGR simulation at $t=5t_0$ (Fig. 5.3a). For $t>15t_0$ the spanwise perturbations induced by the lobes and clefts in the HGR simulation produce a strong three-dimensionality of the flow in the front region and interfere with the flow in the region where the KH billows are forming. The presence of the no slip surfaces (e.g., see Simpson, 1972, Hartel et al., 2000a) is thought to play a major role in the development and growth rate of the lobe and cleft instability. Consistent with the development of the individual lobes and clefts, the local front velocity is not constant in the spanwise direction.

More information about the development in time of the lobe and cleft structures is given in Fig. 5.6, which shows the positions of the front at a time interval of $t/t_0=1$ in a horizontal plane intersecting the current at a distance of $0.016h$ from the bottom wall for the LGR and HGR cases. In both simulations the number of lobes and clefts varies as the current continues to propagate. New lobes are created from disturbances occurring on the surface of an existing large lobe. At other locations two lobes merge together. At both Grashof numbers the size of the penetration of the ambient fluid in the clefts is of the same order as the lobe size, consistent with the experimental observations of Simpson (1972). However, the mean sizes of the lobes and of the clefts observed in the HGR simulation are clearly smaller and their deformations are sharper than the ones observed at the same nondimensional time in the LGR simulation. The estimated average and maximum size of the lobes during the slumping phase in the LGR simulation is $0.5h$ and $0.93h$, respectively. The values inferred from the experiments conducted by Simpson (1972) at the corresponding Reynolds number are $0.55h$ and 1-$1.05h$. In the HGR

simulation ($Re_f=U_f h/\nu=29{,}000$) the mean and maximum size of the lobes are $0.13h$ and $0.35h$, respectively. Though no direct comparison with experiment is possible as the maximum value of the Reynolds number defined with the front velocity and head height in Simpson's (1972) experiments was only 11,000, one can get an estimate from the correlation proposed by Simpson. The inferred values for the average and maximum size of the lobes at $Re_f=29{,}000$ are $0.12h$ and $0.25h$, respectively. The agreement for the mean size between our simulation and the value predicted by Simpson's correlation is excellent.

The streamline patterns (x-y section) shown in Fig. 5.7 in a coordinate system advancing with the front velocity, at a time instance during the slumping phase, confirm the findings of Hartel et al. (2000a) regarding the flow topology in the nose region. Our HGR results show that even at Reynolds numbers that are more than one order of magnitude higher than the ones considered in the 3D DNS of Hartel et al. (2000a) the foremost point (nose) is not a stagnation point in a translating coordinate system. As the Grashof / Reynolds number increases, the vertical distance Δy_n between the nose and the bottom wall decreases from $0.21h$ in the LGR case to $0.06h$ in the HGR case. Meanwhile, the gap between the nose and the bottom wall at the location of the stagnation point decreases from $0.06h$ to $0.01h$. More importantly, the ratio of the flux of light fluid underneath the front, $\dot{V}_u$, to the expected total incoming flux of light fluid, $\dot{V}_0=2hU_f$, is close to 1.21% in the LGR simulation and equal to only 0.05% in the HGR case. This further strengthens the argument made by Hartel et al. (2000a) that the lobe-and-cleft instability in the case of a GC propagating on a solid surface is driven by the unstable stratification region between the nose and the stagnation point. Their observation was based on 3D simulations at $Re_f\sim750$ and 2D simulations at $Re_f<30{,}000$. In both their and our 2D simulation the predicted ratio $\dot{V}_u/\dot{V}_0$ for the HGR case is around 0.34%, sensibly higher compared to the value of 0.05% predicted by the present 3D simulation. For the LGR case the value predicted by the 2D simulation (1.18%) is quite close to the 3D

prediction (1.21%). The values of these quantities are summarized in Table 5.1 where the numbers in parenthesis correspond to the values obtained from the 2D simulations. In the same table, the values of Δy_n inferred from the measurements of Simpson (1972) or, for the HGR case, from the correlation curve are also given (the nose height is about $1.1h$ in our simulations). The agreement, for the 3D simulations, especially at the higher Grashof number, is very good.

5.3 Front Velocity

The evolution of the spanwise-averaged front position function of the dimensionless time is plotted in Fig. 5.8 for the LGR and HGR 3D simulations. During the slumping phase the slope of the curve describing the advancement of the forward propagating front (continuous line) and backward propagating front (circles) in time is practically constant and equal for the two currents (at least until $t=35t_0$) indicating a practically constant front velocity after the initial acceleration phase when the GCs are forming. The value of the front velocity, however, is clearly dependent on the Grashof number, as the slope of the line corresponding to the HGR simulation is higher than the one for LGR simulation. The front velocity is obtained by differentiating the front position from the spanwise-averaged frames with time. The inferred values of the front Reynolds number, Re_f, defined with the asymptotic slumping-phase velocity, U_f, are 648 and 29,050 for the LGR and HGR 3D simulations. It is interesting to note that the strong three-dimensionality of the flow in the interface region did not result in large oscillations of the front velocity in the HGR simulation. In both simulations, the head heights of the two currents are close to $1.1h$ for $t>10t_0$ which corresponds to values of 712 and 31,900 for the Reynolds numbers defined with the front velocity and the head height. The corresponding Froude numbers ($Fr=U_f/u_b$) are 0.58 and 0.65, respectively. These values are plotted in Fig. 5.9 along with results from the 2D and 3D DNS simulations of Hartel et al. (2000a) and values from various experiments. The top straight line in Fig. 5.9 at

$Fr=1/\sqrt{2}$ corresponds to the theoretical results of Benjamin (1968) and Shin et al. (2004) for inviscid currents (infinite Grashof numbers). The front velocity over the slumping phase is accurately predicted by the present simulations.

In the LGR case no noticeable differences are observed in the front position at least until $t=30t_0$ between the 2D and 3D simulations. During the slumping phase the presence of the lobe and cleft structure at the front of the current and of strong spanwise disturbances in the position and strength of the KH billows in the HGR 3D simulation did not result into a front velocity value significantly different than the one predicted by a 2D simulation where these phenomena are absent. However, a slight underprediction of the front velocity by the 2D simulation is observable for $t>15t_0$. For example at $t=20t_0$ (Fig. 5.2) the current in the 3D simulation traveled an additional 0.1h compared to the 2D simulation. The values of the Reynolds numbers defined with the mean front velocity over the slumping phase (Re_f) are compared in Table 5.1 for the 2D and 3D simulations.

More information on the front speed in the initial stages of the flow, when the flow accelerates from rest, are given in Fig. 5.10 where the temporal variations of the position and velocity of the forward propagating front were plotted for the LGR and HGR simulations. The head and nose of the two currents are forming over this period and 2D effects dominate. One can observe that in both cases the velocity variation, before it reaches an approximately constant value that corresponds to the slumping phase, is not monotonic. Rather, the front velocity first reaches a maximum of $0.74u_b$ and of $0.67u_b$ in the HGR and LGR simulations, respectively. The maximum is reached after around $1.9t_0$ from the gate release. Then, the velocity slowly oscillates until it reaches the fairly constant values ($0.65u_b$ and $0.58u_b$, respectively) that characterize the front movement during the slumping phase. The transition between the acceleration phase and the slumping phase appears to take place at $t\sim3.5t_0$ in the LGR simulation and at $t\sim5.5t_0$ in the HGR simulation.

5.4 Analysis Of Near-Wall Flow Structures

As the Reynolds number defined with the height of the head and the front velocity is well above 5,000 after the initial stages of the current development in the HGR simulation, the flow inside the head region is expected to be turbulent and the near-wall flow is anticipated to contain the usual coherent structures associated with a turbulent boundary layer over a wall. The instantaneous vertical vorticity contours (two vorticity levels corresponding to $\omega_y = \pm 2u_b / h$ are represented in Fig. 5.11b and the view is from the exterior of the channel looking laterally toward the bottom of the forward propagating current) at t/t_0=20 clearly show the presence of a streaky structure near the wall between the front (x~13h) and x~5h.

These vertical vorticity streaks are in fact associated with the high and low streamwise velocity streaks that develop in the immediate vicinity of the wall. Evidence of that is given in Fig. 5.12 where the same vertical vorticity streaks are shown on the bottom wall (frame a) along with the streamwise velocity contours in a plane located at y^+~11 from the bottom surface (frame b). The forward propagating current at that time instance is visualized in frame c using concentration contours. The correspondence between the vertical vorticity streaks and the low and high speed streaks is evident (the maximum in the vertical vorticity field occurs in the gap between the low and high velocity streaks). For $|x|<5h$, the velocity and vorticity streaks disappear since the local Reynolds number is decaying below values at which turbulent streaks can form or be maintained. The average width of these streaks is about 0.075h and their mean length is about 1.0h. The presence of these streamwise velocity streaks in turbulent boundary layers and channel flows is associated with the legs of the hairpin like vortices that are present over the near-bed region. It is suspected that a similar phenomenon is present in the turbulent flow region of the current where these counter-rotating vortices can displace fluid from the immediate vicinity of the wall (including from the thin layer of fluid overrun by the head of the current) toward the middle of the channel. The associated

sweep and ejection phenomena are expected to promote mixing. In the region close to the GC front, the action of these longitudinal vortices can induce further perturbations of the front region that can amplify the instabilities responsible for the formation and growth of the lobes.

The distribution of the same vertical vorticity contour levels in the LGR simulation (Fig. 5.11a) is clearly different. Practically, only one row of large (mean width ~0.23h), very long (mean length ~4.5h) streaks can be identified immediately behind the front. This suggests that the nature of the instability is similar in both simulations, but the Reynolds number is not high enough for the streaky structure to develop and be sustained over longer distances behind the front.

5.5 Analysis Of The Spatial Distribution Of The Wall Shear Stress During The Propagation Of The Current

The spatial and temporal distributions of the bed shear stress have to be known to estimate global quantities related to the capacity of the current to entrain bed particles (e.g., the total amount of sediment entrained by the current and the associated bed morphology changes), especially in numerical models in which the entrainment is generally a function of the difference between the actual bed shear stress and the critical bed shear stress value given by the Shields diagram. In this regard, accurate prediction of this quantity is of critical importance for the overall practical use of the model.

The focus of the discussion will be on the HGR simulation where the flow is strongly turbulent over part of the GC and thus is more representative of practical applications. The instantaneous distribution of the nondimensional wall-friction velocity contours, u_τ/u_b, is shown in Fig. 5.13a for t=10t_0 and in Fig. 5.13b for t=20t_0. In Fig. 5.13a, 2D streamlines are also shown in an x-y section in a frame of reference translating with the front velocity. The friction velocity is $u_\tau = \sqrt{\tau_b / \rho}$ and the modulus of the wall shear stress vector is calculated using the definition. This is possible because the mesh in

the wall normal direction is fine enough to resolve the viscous sub-layer (no wall functions are used).

The first obvious feature of the friction velocity distributions is the streaky structure of the zones characterized by high wall shear stress (friction velocity) values in the region beneath the head of the GC. These streaks of high wall-shear stress are obviously related to the high speed streamwise velocity streaks present in the near-wall region over the part of the current body where the flow is turbulent (see discussion of Fig. 5.12). The length of the streaky zone characterized by high bed friction values is about $4h$ at $t=10t_0$ and $8.5h$ at $t=20t_0$. This indicates that a longer part of the current becomes turbulent as the gravity current advances. It is, however, expected that at a certain point in the evolution of the GC in an infinite-volume lock exchange flow, an equilibrium state will be reached such that the length of the region where the flow is turbulent in the wall vicinity will remain approximately constant. The flow is expected to relaminarize behind this region.

The other feature of the friction velocity distribution in Fig. 5.13a is the presence of several spanwise bands of respectively high and low friction velocity values starting behind the front. These bands of high friction velocity values (see dashed lines in Fig. 5.13a) correlate relatively well with the position of the cores of the vortices present inside the GC in the vicinity of the wall when the velocity vector is represented in a frame of reference moving with the front velocity. These vortices in the head region observed in the translating frame of reference can be related to the quasi 2D KH billows (see C=0.5 contour line in Fig. 5.13a) present in the head region at $t=10t_0$. As the friction velocity values inside these spanwise bands are comparable to those observed in the front region, it is clear that the GC will entrain sediment over a relatively large distance behind its front.

The total length of the region characterized by relatively high values of the friction velocity ($u_*/u_b>0.045$) is $6h$ at $t=10t_0$. It is also interesting to consider the

distribution of u_τ at later times of the evolution of the current when the KH billows shed behind the front lose their coherence over a short distance. For example, the distribution at $t=20t_0$ is shown in Fig. 5.13b. The spanwise bands observed at $t=10t_0$ have practically disappeared both over the region where the friction velocity displays a streaky structure and behind it. The length of the region characterized by relatively high values of the friction velocity ($u_\tau/u_b>0.045$) has increased to $8.5h$. As for the velocity streaks, it is expected that as the infinite-volume lock exchange flow further develops in time, a sort of equilibrium configuration of the turbulent region of the current will be reached. This is when the length of the region characterized by large wall-shear-stress values and thus the amount of sediment entrained from the bed will practically be independent of time.

An interesting question is whether the position and intensity of the spanwise-averaged wall-shear-stress distribution can be accurately captured by a much less expensive 2D model at the different stages of the evolution of the current. Fig. 5.14 shows the comparison between the spanwise averaged wall friction velocity predicted by the 3D simulation (red line) and the one predicted by the 2D simulation (blue line) of case LGR in the right side of the channel ($x/h>0$) at $t=10t_0$ and $t=20t_0$. The position of the front corresponds to the first peak from the right at $x\sim6h$ and $x\sim11.3h$, respectively. Besides the front, large values of the friction velocity, comparable to the ones observed in the front region, are present especially in the later stages of the development of the current, during the slumping phase. The predictions given by the 2D models are relatively accurate though the errors increase as the current develops and 3D effects become more and more important. However, at this relatively low Grashof number where 2D effects are predominant (see discussion of Fig. 5.3), the good accuracy of the 2D predictions is not surprising.

In the HGR simulation (Fig. 5.15), some differences are observed especially in the later stages of the evolution of the current, though the range of values of u_τ/u_b remains similar to that observed in the LGR simulation. For example, in Fig. 5.15b corresponding

to $t=20t_0$ the spanwise averaged wall-friction velocity (continuous red line) is relatively constant behind the front region. This is obviously due to the fact that the KH billows lost most of their coherence at that stage of the evolution of the current in the HGR 3D simulation, which was not the case in the LGR simulation. In addition to the spanwise averaged values, the instantaneous values in an *x-y* section (dashed red line) were also plotted in Fig. 5.15 to get a better idea of the influence of 3D effects on the distribution of the wall friction velocity. Observe that the amplitude of the oscillations around the spanwise-averaged values is relatively high especially in the region where the flow is strongly turbulent. Behind that region (e.g., for $x/h<5$ at $t=20t_0$, see also Fig. 5.13b) the amplitude of the oscillations of the instantaneous friction velocity in the spanwise direction decreases substantially. The 2D predictions (blue line) at both $t=10t_0$ and $t=20t_0$ show very large variations in the streamwise direction and, locally, do not correlate well with the 3D predictions. The large-scale oscillations are associated with the presence of the KH billows in the interface region (Fig. 5.2b) that were shown to maintain their strong coherence even at $t=20t_0$ in the 2D simulation.

Thus, 2D simulations appear not to be effective in predicting the spatial and temporal evolution of the bed shear stress for high Grashof numbers. Therefore, they also do not accurately predict the local sediment entrainment in the case of a current propagating over a loose bed. Still, as the mean (streamwise averaged) value over the region characterized by large bed shear stress values is comparable to the one predicted by the 3D simulation, information obtained from a 2D simulation may be used with a certain degree of success when trying to predict, in an integral sense, the total amount of sediment entrained by the current at a certain moment in time.

5.6 Energy Budget Of The Infinite-Volume Lock-Exchange Flow

Gravity currents are flows driven by the conversion of potential energy into kinetic energy, which is then dissipated by viscous friction. The dissipation is solely caused by the gradients in the velocity field for compositional GCs. For LES simulations, in which the model can directly calculate only the gradients in the resolved velocity field, the total dissipation rate, ε, has two components. One is the viscous dissipation and the other in the sub-grid scale (SGS) dissipation due to velocity gradients at the unresolved scales that have to be modeled. To examine the variation of the kinetic energy in time, the momentum equation for the i direction (3.2) is multiplied with u_i and then a summation is performed over the index i to obtain the transport equation for the resolved kinetic energy:

$$\frac{D}{Dt}\left(\tfrac{1}{2}u_i u_i\right) = -\frac{\partial}{\partial x_i}\left(p u_i\right) + u_i \frac{\partial}{\partial x_k}\left(\frac{1}{\sqrt{Gr}} + \nu_{SGS}\right)\left(\frac{\partial u_i}{\partial x_k} + \frac{\partial u_k}{\partial x_i}\right) - u_2 C \tag{5.1}$$

where D/Dt indicates the material derivative. By integrating equation (5.1) over the entire flow domain, Ω, an equation for the temporal evolution of the total kinetic energy, E_k, is obtained.

$$\frac{dE_k}{dt} = \int_\Omega u_i \frac{\partial}{\partial x_k}\left(\frac{1}{\sqrt{Gr}} + \nu_{SGS}\right)\left(\frac{\partial u_i}{\partial x_k} + \frac{\partial u_k}{\partial x_i}\right) dV - \int_\Omega u_2 C dV \tag{5.2}$$

where

$$\frac{dE_k}{dt} = \frac{d}{dt}\int_\Omega \frac{1}{2} u_i u_i dV \tag{5.3}$$

In integrating (5.2) to obtain equation (5.3), the convective term and the pressure term which are in divergence form reduce, using Gauss's theorem, to integrals over the boundaries of the domain. Both terms contain the velocity which is assumed to be equal

or very close to zero on all the boundaries. Thus, the contribution of these terms to the temporal evolution of E_k is neglected. The total potential energy over the flow domain is:

$$E_p(t) = \int_{\Omega} Cx_2 \, dV \tag{5.4}$$

The time derivative of the potential energy E_p can be rewritten as:

$$\frac{dE_p}{dt} = \int_{\Omega} \frac{D(Cx_2)}{Dt} dV = \int_{\Omega} C \frac{D(x_2)}{Dt} dV + \int_{\Omega} x_2 \frac{DC}{Dt} dV \tag{5.5}$$

Ignoring the effects of diffusion in the concentration equation (Eq. 3.3) such that one can write $DC/Dt \sim 0$, the equation for the total potential energy E_p simplifies to:

$$\frac{dE_p}{dt} = \int_{\Omega} Cu_2 dV = \gamma \tag{5.6}$$

The right hand side of equation (5.6) is equal and of opposite sign to the last term in equation (5.2). Summing equations (5.2) and (5.6) and assuming there is no change in the potential energy across the boundaries of the domain one obtains an equation for the temporal evolution of the total mechanical energy:

$$\frac{d}{dt}(E_k + E_p) = \int_{\Omega} u_i \frac{\partial}{\partial x_k} \left(\frac{1}{\sqrt{Gr}} + \nu_{SGS} \right) \left(\frac{\partial u_i}{\partial x_k} + \frac{\partial u_k}{\partial x_i} \right) dV \tag{5.7}$$

The right hand side of equation (5.7) is the total dissipation of energy ε with a negative sign.

$$\frac{d}{dt}(E_k + E_p) = -\varepsilon \tag{5.8}$$

In LES, the total dissipation ε can be split into the viscous dissipation, ε_0, and the SGS dissipation, ε_t. The expressions for the two terms are:

$$\varepsilon_0 = -\int_{\Omega} u_i \frac{\partial}{\partial x_k} \left(\frac{1}{\sqrt{Gr}} \right) \left(\frac{\partial u_i}{\partial x_k} + \frac{\partial u_k}{\partial x_i} \right) dV \tag{5.9}$$

and

$$\varepsilon_t = -\int_{\Omega} u_i \frac{\partial}{\partial x_k}(\nu_{SGS})\left(\frac{\partial u_i}{\partial x_k} + \frac{\partial u_k}{\partial x_i}\right) dV \tag{5.10}$$

Examination of the relative magnitude of ε_t and ε_0 can provide useful information on the effect of the unresolved scales on the numerical solution. It also helps to quantify the effect of the LES model for a simulation run on a mesh with a certain grid density. Integrating (5.8) with respect to time gives an integral energy balance equation:

$$E_k + E_p + E_d = const. = E_{k0} + E_{p0} \tag{5.11}$$

where E_{k0} and E_{p0} are the total initial kinetic energy and initial potential energy in the domain. The term E_d represents the time integral of the total dissipation.

$$E_d(t) = \int_0^t \varepsilon(\tau) \quad d\tau \tag{5.12}$$

The time evolution of the terms in equation (5.11), which are nondimensionalized by the mechanical energy at the start of the lock-exchange flow is plotted in Fig. 5.16. The solid lines refer to the HGR simulation while the dashed lines refer to the LGR simulation. The individual terms were estimated using equations (5.4), (5.9) and (5.10) and by integrating in time equation (5.3). The volume of integration corresponds to that of the computational domain. As expected, the total energy given by the left-hand side of equation (5.11) is conserved in time. The larger values of the kinetic energy observed in the HGR simulation are due, at least partially, to the increase in the front velocity with the Grashof number. The kinematic part of the viscous dissipation term ($\varepsilon_0\sqrt{Gr}$ in equation (5.9)) is larger in the HGR simulation compared to the LGR simulation due to the presence of small scale velocity fluctuations that induce larger velocity gradients, especially in the region where the flow is turbulent. However, the viscous dissipation term scales with the inverse of the square root of the Grashof number. Though the increase in the SGS dissipation partially compensates for the much smaller values of ε_0 in the HGR simulation, the increase in the total dissipation E_d with time is somewhat smaller in the HGR simulation.

More details on the energy balance can be inferred from Fig. 5.17 in which the terms in the differential equation for the resolved kinetic energy (equation 5.2) are plotted. During the initial acceleration phase there is a clear increase in the rate of growth of the kinetic energy within the domain. Then, in both simulations, the rate of growth decays slowly in a non-monotonic fashion. For $t>20t_0$ the growth rate dE_k/dt appears to be relatively constant in the HGR simulation. A monotonic increase in the total dissipation rate, ε, is observed in the HGR simulation until $t\sim15t_0$ after which the dissipation within the domain starts decaying slowly until $t\sim20t_0$ when it becomes almost constant. The change in the slope of the curve describing the variation of the total dissipation is related to the occurrence of a maximum in the variation of the SGS component (ε_t) of the total dissipation. The curves in Fig. 5.17 suggest that the rate of change of the kinetic and potential energy and the total dissipation rate become relatively constant for $t>20t_0$ in the HGR simulation. This is consistent with the linear variation of the potential and kinetic energy observed in Fig. 5.16 for $t>20t_0$. Whether or not this balance will continue indefinitely is not entirely clear as the simulation had to be stopped once the front approached the lateral boundaries of the computational domain.

However, such a scenario may be possible. As two currents get further away from each other, the flow in the middle region (centered around the position of the lock gate) of the channel relaminarizes and the streams of light and heavy fluid propagating in opposite directions in the upper and lower halves of the middle part of the channel are relatively uniform. At that point there is not much interaction between the forward and the backward propagating currents and the flow in the middle region does not significantly contribute to the individual terms in equation (5.2). The length of the region behind the front of each current, where the flow is turbulent, or where large velocity gradients are present, is also going to become practically independent of time. Thus, the total amount of dissipation will be relatively constant.

Fig. 5.18 gives more details on the role of the LES model in the present simulations. The viscous and SGS contributions to the total dissipation are plotted. In the LGR simulation the SGS contribution is practically negligible over the whole simulated period confirming that, at the Grashof number used in the LGR case and given the mesh used to obtain the solution, our simulation is in fact very close to a DNS. The situation changes dramatically in the HGR case in which, after the short acceleration period when the SGS contribution is very small, the SGS component becomes larger than the viscous one. The largest value of the ratio of $\varepsilon_t/\varepsilon$ is recorded at t~$15t_0$ where the maximum value of the total dissipation is observed. This value is around 67.3%. Then, the SGS component starts decaying mildly, while the viscous component continues to increase, such that at t=$25t_0$, $\varepsilon_t/\varepsilon$ ~58%. The enlarged plots of the variation of the total dissipation in Fig. 5.18 suggest that the shape of the curves in the LGR and HGR simulations are similar and a maximum in the value of the total dissipation is reached even the LGR simulation. This maximum appears to occur around t~$29t_0$. One possible explanation for the longer time the dissipation needs to attain its maximum value is the much stronger coherence of the KH billows in simulations at relatively low Grashof numbers where the growth of 3D instabilities, that are very efficient in breaking the coherence of these billows, is very slow (see Fig. 5.3).

5.7 Analysis Of The Spatial And Temporal Distributions Of The Dissipation

Information on the spatial and temporal distribution of the dissipation rate within a GC is important not only for understanding the physics of lock-exchange flows (e.g., what are the main flow structures responsible for most of the dissipative losses) at different stages of the current evolution but also for developing theoretical models of these flows (e.g., see Huppert & Simpson, 1980) which incorporate the effect of the dissipation and for determining the parameters in these models. As the dissipation cannot

be estimated directly in these simplified models, one possible solution is to calibrate these parameters using the distributions of the dissipation rate determined from high resolution simulations. This is also because accurate measurements of the distribution of ε within a current are practically impossible to obtain experimentally. Moreover, the separate contributions of the head and tail regions of the current, or the contribution of the interface region to the total dissipation can be calculated and modeled independently. Necker et al. (2005) were the first to perform such an analysis for a finite-volume particulate current at $Gr=10^6$-10^7. In the present chapter, the analysis is focused on the HGR simulation at $Gr=2\times10^9$.

To study the distribution of the dissipative losses along the channel, the local dissipation rate $\varepsilon_L=\varepsilon_L(x_1,x_2,x_3)$ is first integrated over the spanwise and vertical directions. This leads to a variable ε^{23} which is function only of the streamwise position and which allows us to infer the distribution of the dissipation along the forward or backward propagating currents.

$$\varepsilon^{23}(x_1)=-\int^{L_3}\int^{L_2} u_i \frac{\partial}{\partial x_k}\left(\frac{1}{\sqrt{Gr}}+\nu_{SGS}\right)\left(\frac{\partial u_i}{\partial x_k}+\frac{\partial u_k}{\partial x_i}\right)dx_3dx_2 \tag{5.13}$$

Similarly, the SGS contribution can be calculated as:

$$\varepsilon_t^{23}(x_1)=-\int^{L_3}\int^{L_2} u_i \frac{\partial}{\partial x_k}(\nu_{SGS})\left(\frac{\partial u_i}{\partial x_k}+\frac{\partial u_k}{\partial x_i}\right)dx_3dx_2 \tag{5.14}$$

In Fig. 5.19 the two distributions of ε^{23} and ε_t^{23} are plotted at four nondimensional times t/t_0=5, 10, 15 and 30, which are representative of the evolution of the forward propagating current over the slumping phase. The corresponding spanwise-averaged concentration contours are also shown in the same figure. Similar plots for the backward propagating current show that the total dissipation rate in the two currents, at a certain moment in time, is practically the same. Consistent with the variation of the total dissipation rate $\varepsilon=\int^{L1}\varepsilon^{23}(x_1)dx_1$ in Fig. 5.17, the maximum in the total dissipation (area

beneath the curve defined by the variation of ε^{23}) is observed to occur at $t=15t_0$. At that moment, large dissipative losses are observed practically over the whole length of the current starting at $x/h=0$.

As previously discussed, a relatively constant width mixing layer, in which large scale structures are practically absent, starts developing as the currents advances. At $t=30t_0$, it extends until about $x/h=10$ (see also Fig. 5.2a). This corresponds to the region over which the values of the variable ε^{23} are clearly smaller compared to the ones observed over the head region ($x/h>10$). Inside the head region, the flow is strongly turbulent (the SGS contribution ε_t^{23} is about 60-70% of the total dissipation term ε^{23}) and large scale structures are still present. The SGS dissipation contribution over the region $0<x/h<8$, as a percentage of the total dissipation is relatively small, suggesting that the flow is starting to relaminarize in that region. It is expected that as the current continues to advance, the values of ε^{23} and ε_t^{23} will continue to decay in the middle part of the channel (low x/h values). This makes it reasonable to believe that the length of the region where most of the dissipative losses occur will eventually become independent of time and the total dissipation within that region will relatively constant in time, consistent with the trend suggested by the variation of ε in Fig. 5.17 for the HGR simulation.

The distribution of the dissipation along the vertical direction can be examined by integrating the local dissipation rate ε_r over the length and width of the channel. This quantity is denoted by ε^{13} and its expression is:

$$\varepsilon^{13}(x_2) = -\int^{L1}\int^{L3} u_i \frac{\partial}{\partial x_k}\left(\frac{1}{\sqrt{Gr}} + \nu_{SGS}\right)\left(\frac{\partial u_i}{\partial x_k} + \frac{\partial u_k}{\partial x_i}\right) dx_1 dx_3 \tag{5.15}$$

Similarly, the SGS component is defined as:

$$\varepsilon_t^{13}(x_2) = -\int^{L1}\int^{L3} u_i \frac{\partial}{\partial x_k}\left(\nu_{SGS}\right)\left(\frac{\partial u_i}{\partial x_k} + \frac{\partial u_k}{\partial x_i}\right) dx_1 dx_3 \tag{5.16}$$

Fig. 5.20 shows the variation of these quantities along the vertical axis at four time instances, t/t_0 = 5, 10, 15 and 30. Only the lower part (y/h<1) is shown as the distributions are practically symmetrical with respect to the mid-plane $y=h$ between the two walls. Two areas of high dissipation are observed along the vertical axis in the four frames.

The first area is located very close to the bed (y/h<0.2) and is produced by the large streamwise velocity gradients in the thin boundary layer on the bottom wall and by the turbulent structures present in the near wall region at streamwise locations corresponding to the front region and some distance behind it, where the flow is turbulent. In this layer, the overall contribution of the SGS term to the total dissipation is relatively small, in part due to the fact that the mesh is refined in the wall normal direction near the walls (this reduces the SGS contribution), and also because the integration is made over the whole length of the channel. As in the mid-channel region (small |x/h| values) the flow is, at best, only mildly turbulent in the near-wall region in the later stages of the evolution of the current; the dominant contribution to the total dissipation comes from the viscous component.

The second area is located around the horizontal mid-plane (0.4<y/h<1 in the lower part) and corresponds to the interface between the two currents, where most of the mixing occurs, and to the head region where the flow is turbulent. The SGS contribution to the total dissipation in these regions is around 80%, consistent with the fact that a broad range of resolved turbulent scales is observed in the interface region (Fig. 5.3, case HGR) at wavelengths comparable to the grid size.

Consistent with the variation of ε in Fig. 5.17, the total dissipation in the two regions characterized by high ε^{13} values in Fig. 5.20 is increasing monotonically from t=5t_0 to t=15t_0, where the maximum value of ε is recorded. The contribution of the near wall region to the total dissipation is around 7% to 9% over this time interval. After t=15t_0, the dissipation in the near wall region continues to increase but the dissipation in

the regions away from the bed starts decreasing. For example, at $t=30t_0$ the contribution of the near-wall region to the total dissipation has increased to 13%. Still, most of the energy is dissipated over the interface and head regions.

The high dissipation near the bed is expected to be largely caused by the streamwise velocity gradients in the wall normal direction. To investigate this, the component ε_{12}^{13} which contains these gradients in the expression for ε was plotted in Fig. 5.20. Its expression is:

$$\varepsilon_{12}^{13}(x_2) = -\int_0^{L1}\int_0^{L2}\left(\begin{array}{l} u_1 \dfrac{\partial}{\partial x_2}\left(\dfrac{1}{\sqrt{Gr}}+\nu_{SGS}\right)\left(\dfrac{\partial u_1}{\partial x_2}+\dfrac{\partial u_2}{\partial x_1}\right) \\ +u_2 \dfrac{\partial}{\partial x_1}\left(\dfrac{1}{\sqrt{Gr}}+\nu_{SGS}\right)\left(\dfrac{\partial u_2}{\partial x_1}+\dfrac{\partial u_1}{\partial x_2}\right) \end{array}\right) dx_1 dx_3 \qquad (5.17)$$

One can see that this component accounts for more than 95% of the total dissipation in the region between the wall and $y/h<0.2$. This confirms our supposition if one takes into account that, for flows propagating over a flat surface in the streamwise direction, the streamwise gradient of the vertical velocity is much smaller than the vertical gradient of the streamwise velocity in the wall region. As expected, farther from the wall ($0.2<y/h<1$) the contribution of this component is small (less than 20% of the total dissipation). This is consistent with the strong three-dimensionality of the flow in this region.

5.8 Summary

Results from two high resolution LES simulations of compositional gravity currents developing into an infinite channel in which the two fluids were separated initially by a lock gate were discussed with the goal of highlighting the changes in the evolution of lock exchange flows between Grashof numbers of the order of 10^6 where DNS results (e.g., see Hartel et al., 2000a) were already available and Grashof numbers of the order of 10^9 where highly-resolved DNS using non-dissipative algorithms is

computationally too expensive. Whenever possible, qualitative and quantitative comparisons with experimental data and/or results from previous numerical investigations were presented. Overall, the agreement between the results was found to be satisfactory. The use of a non-dissipative discrete energy conserving finite-volume Navier-Stokes solver with a dynamic Smagorinsky model insured that a minimum amount of dissipation was added to the regions where unresolved small scale turbulence was present.

The forward and backward propagating currents were found to exhibit the classic characteristics of a GC propagating over a no-slip wall. This includes the lobe-and-cleft structure at the leading edge of the head and the shedding of KH billows from the front region. However, the development of these flow structures was found to be strongly dependent on the Grashof / Reynolds number. In a statistical sense, though the two currents propagating in opposite directions were not exactly anti-symmetric, the values of the global parameters describing the evolution of the GCs, including the variation of the front velocity in time, the mean sizes of the lobes and clefts, etc. were found to be very close. The values of these quantities were also found to be consistent with results from experiments and/or simulations conducted at similar Grashof numbers. The front velocity was observed to peak during the short initial acceleration phase in both simulations before reaching a relatively constant value during the slumping phase.

The topology of the current in the nose region was found to be unaffected by the Grashof number. Results from the present 3D simulations confirmed that there is a strong decrease in the amount of low density fluid trapped beneath the current as it propagates over the bottom wall. In fact, the amount of low density fluid predicted by our 3D HGR simulation was significantly lower than previous predictions based on 2D simulations by Hartel et al. (2000a). This finding strengthens the argument proposed by Hartel et al. (2000a, 2000b) that the unstable stratified region between the nose and the stagnation point plays the determinant role in the growth of the lobe and cleft instability.

The LGR simulation was conducted at a Grashof number of 1.25×10^6, very close to the one (Gr=1.5×10^6) simulated using 3D DNS by Hartel et al. (2000a, 2000b), for which the Reynolds number defined with the front velocity was about 700. At this Reynolds number, the turbulence effects, even if present, are not expected to play a major role in determining the evolution of the lock-exchange flow. Though the development of the forward and backward propagating currents was originally anti-symmetric, the growth of the three-dimensional instabilities eventually destroyed the symmetry of the large-scale KH billows. However, over the simulated period of time, the coherence of the KH billows in between the two fronts, including in the middle of the channel (around the initial position of the lock gate), remained strong.

The HGR simulation was conducted at a Grashof number of 2.00×10^9. As the associated front Reynolds number was close to 30,000, this simulation allowed the study of the evolution of the gravity current and associated instabilities for the case in which the flow, at least in the head region was strongly turbulent. In this simulation, the KH billows were found to lose their spanwise coherence very quickly. As the current continued to propagate well into the slumping phase, only the first one or two billows were recognizable. Their cores were strongly deformed in the spanwise direction due to the lobes and clefts that started influencing the growth rates of the KH instabilities in the formation region. The interface region became populated with small scale energetic eddies that broke the KH billows into smaller structures. The small scale eddies in the mixing layer were also found to be very effective in locally enhancing the mixing. As a result, the relatively constant thickness interface region farther from the two fronts did not appear to contain any large-scale structures in the later stages of the simulation. Additionally, vertical vorticity streaks were observed to form in the near-wall region at streamwise positions corresponding to the head region and some distance behind it. These streamwise vorticity streaks are induced by the low and high speed streaks present a short distance from the walls and are similar to the ones observed in turbulent wall

boundary layers and turbulent channel flows. As the turbulence in the tail region behind the head started decaying, the streaky structure was found to disappear confirming that these streamwise streaks are associated with the local presence of a strong turbulent flow propagating along the walls.

The analysis of the terms in the transport equation for the total kinetic energy showed that in the later stages of the current evolution, the rate of change of the kinetic and potential energy and the total dissipation rate become relatively constant suggesting that the two currents reach some sort of equilibrium state. The SGS dissipation was shown to contribute significantly to the total dissipation in the HGR simulation. Both the SGS dissipation and the total dissipation were observed to reach a maximum at some point during the slumping phase. Prior to this, the dissipation in the near-wall and interface regions were observed to increase monotonically with time. After peaking, the total dissipation in the interface region starts decaying while the dissipation in the near-wall region continues to grow such that the total dissipation in the channel decays slowly. Eventually, the total dissipation appears to reach an almost constant value.

The spatial and temporal distributions of the friction velocity were investigated because the amount of sediment entrained by a GC propagating over a loose bed is determined to a great extent by the local values of the bed-shear stress and sediment size. In the LGR simulation, significant oscillations were found to be present in the spanwise-averaged distribution of the wall-friction velocity behind the head due to the persistence of the quasi 2D KH billows at the interface. In contrast to that, the distribution of the friction velocity in the HGR simulation was found to be more uniform behind the front region. Though 2D simulations were relatively successful in predicting the spatial distribution of the friction velocity in the LGR simulation, they were not able to accurately predict the distribution of the friction velocity behind the front of the GC in the HGR simulation. This is because in the 2D simulation the 3D instabilities cannot grow and thus strong KH billows are present in the interface region for longer periods of

time compared to the 3D simulation. These KH billows induce very large oscillations in the distribution of the friction velocity over the head and tail of the current. These limitations should be considered when 2D simulations are used to predict sediment entrainment patterns for high Grashof numbers gravity currents.

Table 5.1 Details of the lock-exchange LGR and HGR 3D simulations during the slumping phase.

Case	Gr	$Re=\sqrt{Gr}$	Re_f	Fr	$\Delta y_n/h$	$\Delta y_s/h$	V_u/V_o (%)
LGR	1.25×10^6	1,118	648 (648)	0.58 (0.58)	0.21 (0.26){0.18}	0.06 (0.065)	1.21 (1.18)
HGR	2.00×10^9	44,721	29,000 (28,900)	0.65 (0.65)	0.06 (0.11){0.062}	0.01 (0.018)	0.05 (0.34)

Note: Values in () are 2D results. Values in {} are from Simpson (1972).

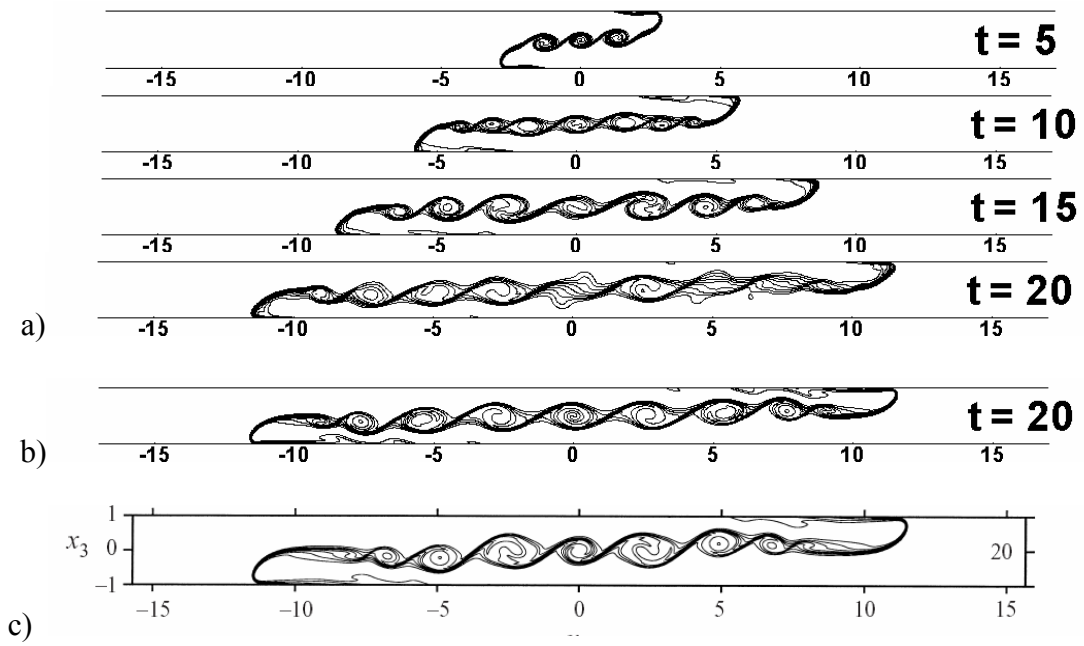

Figure 5.1. Visualization of the lock-exchange flow at Gr=1.25×10^6 using concentration contours. a) LGR 3D simulation showing spanwise averaged contours at non-dimensional times t/t_0 = 5, 10, 15 and 20; b) LGR 2D simulation at t/t_0 = 20; c) DNS of Härtel et al. (2000a) at same Grashof number and t/t_0 = 20.

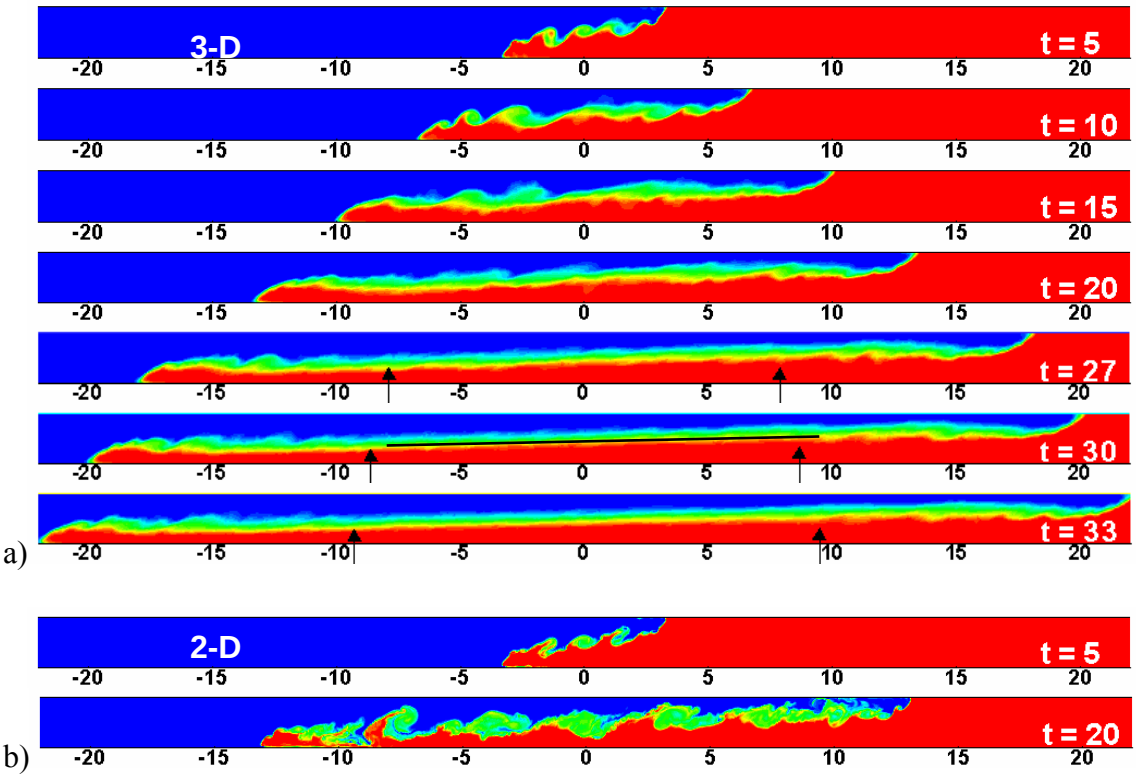

Figure 5.2. Visualization of the lock-exchange flow at Gr=2.0×10^9 using concentration contours. a) HGR 3D simulation showing spanwise averaged contours at non-dimensional times t/t_0 = 5, 10, 15, 20, 27, 30 and 33; b) HGR 2D simulation at t/t_0 =5 and 20.

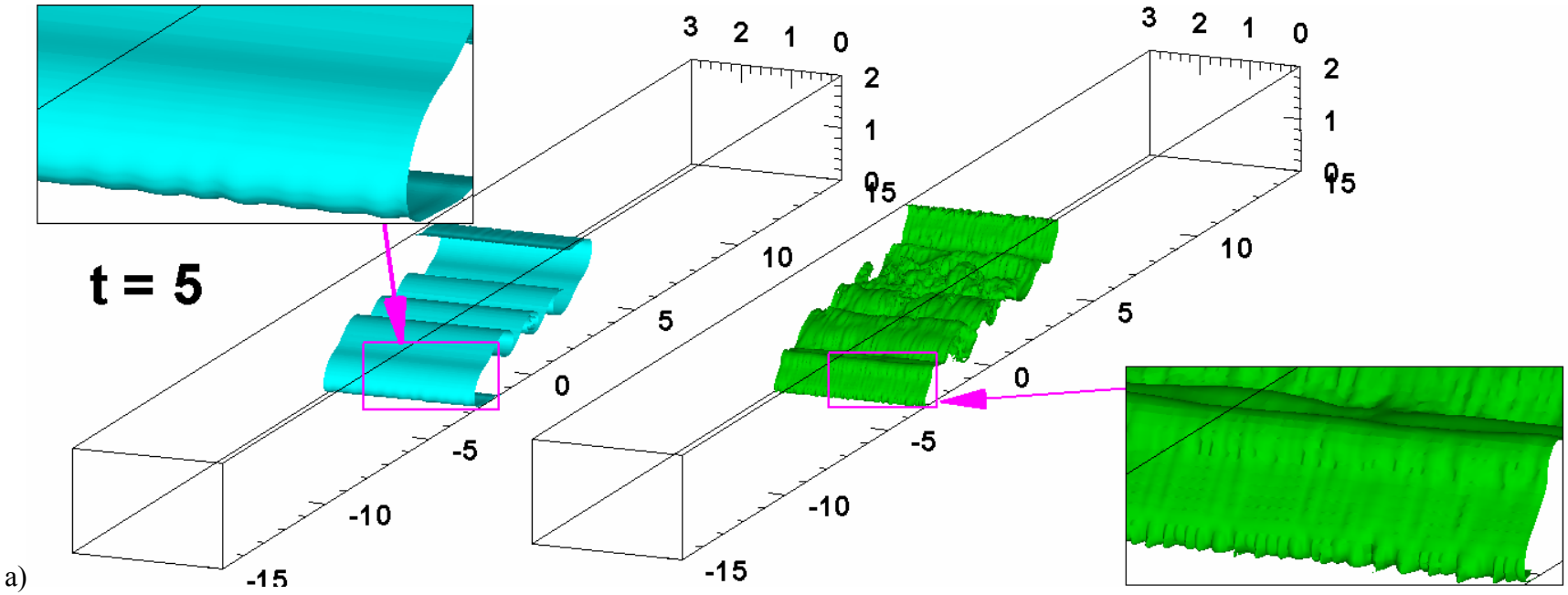

a)

Figure 5.3. Visualization of gravity current interface using a concentration isosurface ($C = 0.5$) for LGR and HGR 3D simulations with insets showing development of the lobe and cleft structures at the front. a) t/t_0=5; a) t/t_0=10; b) t/t_0=15; d) t/t_0=20.

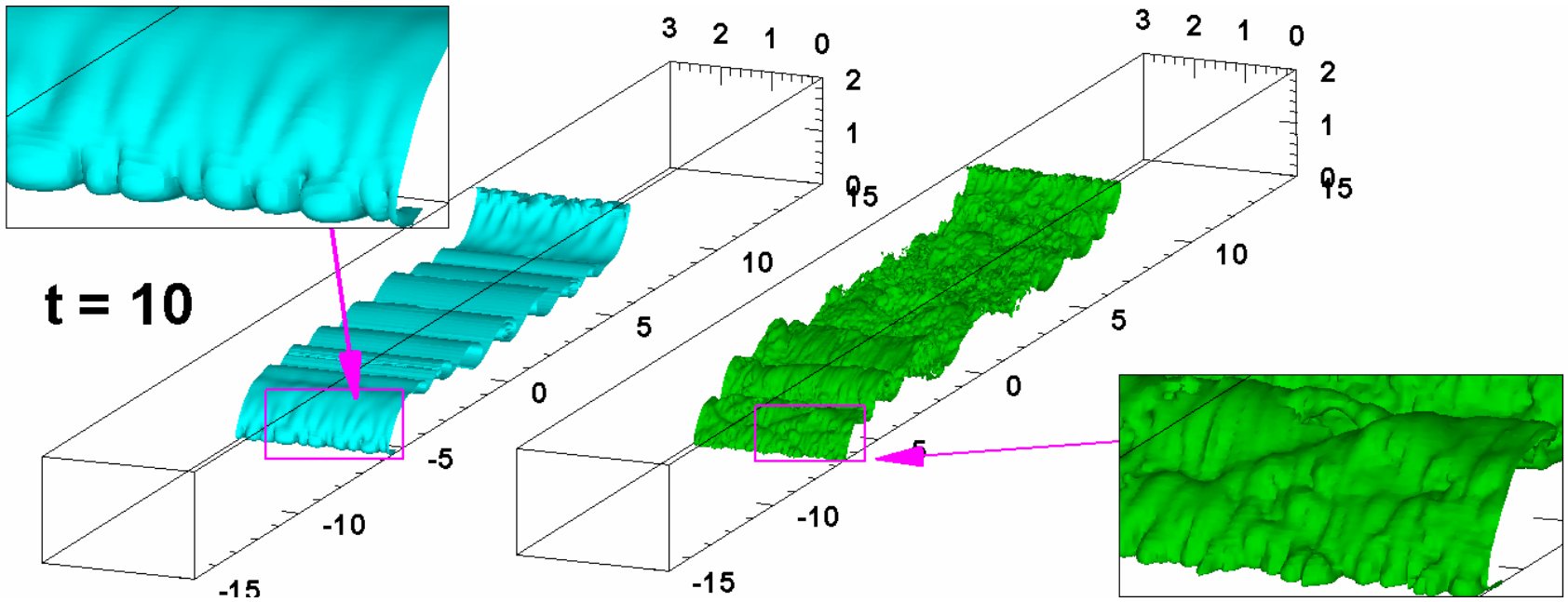

b)

Figure 5.3 continued

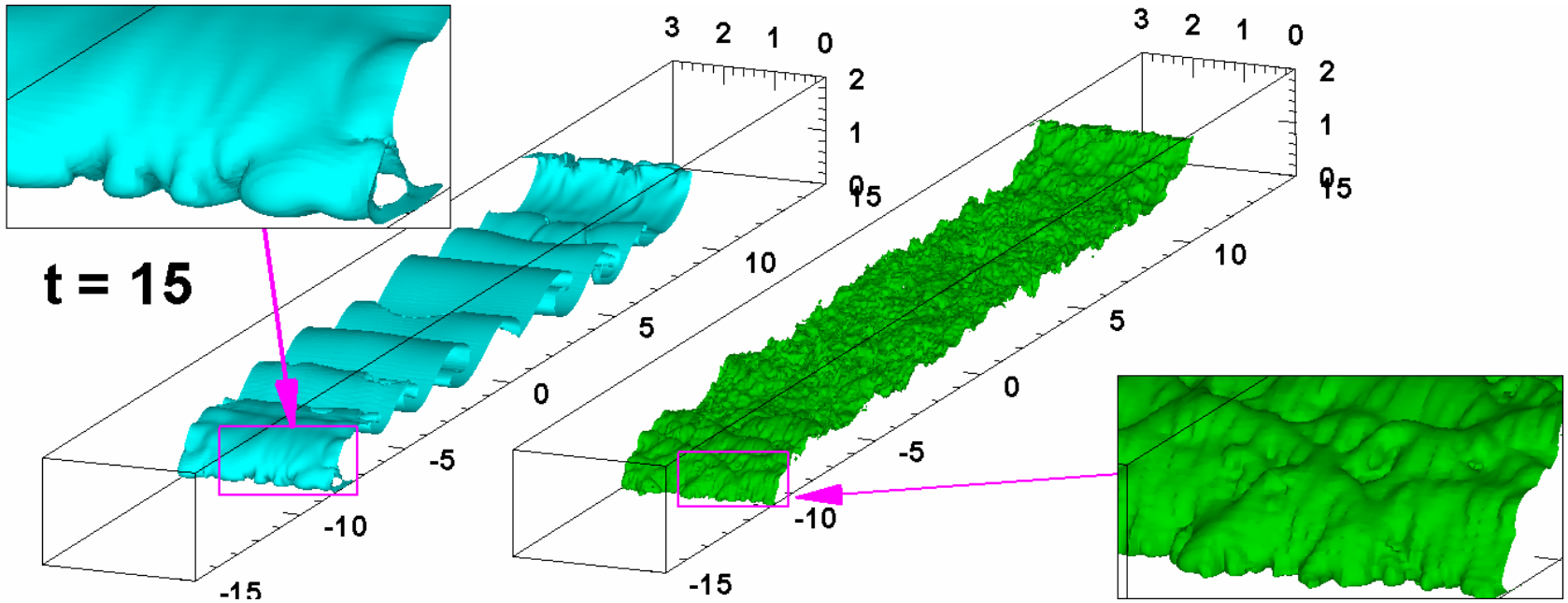

c)

Figure 5.3 continued

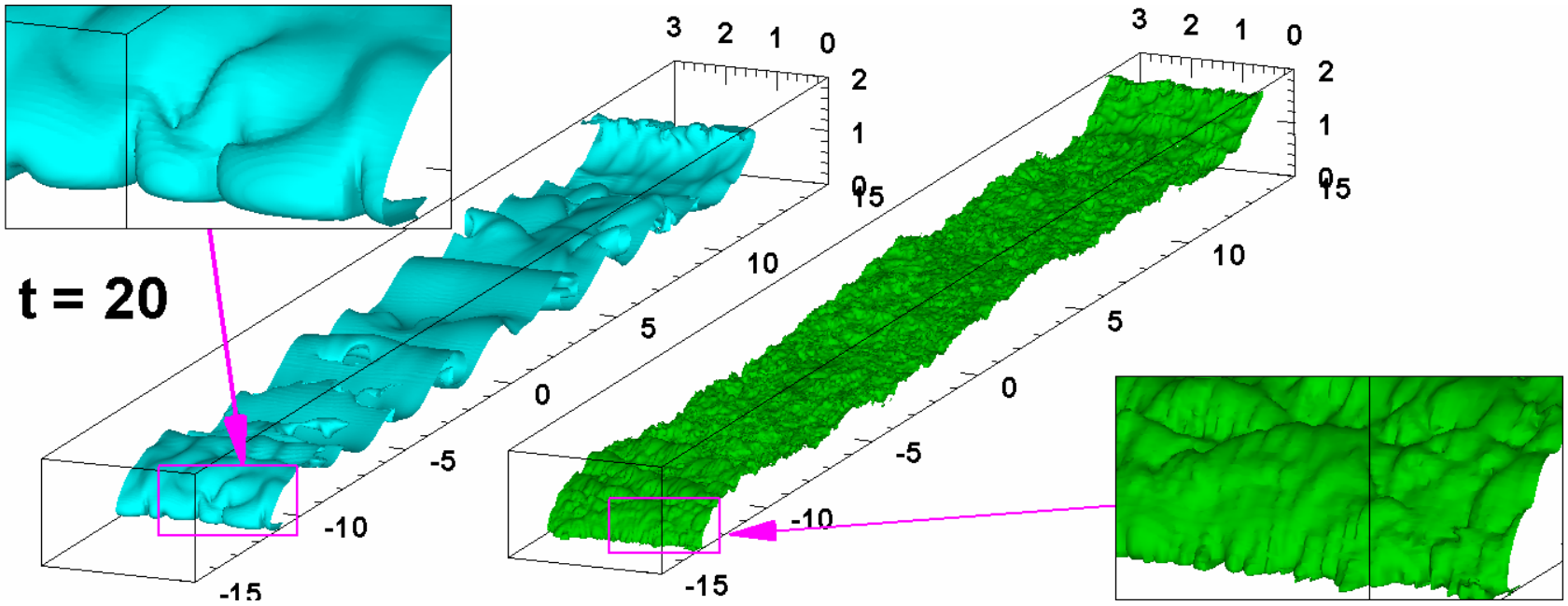

d)

Figure 5.3 continued

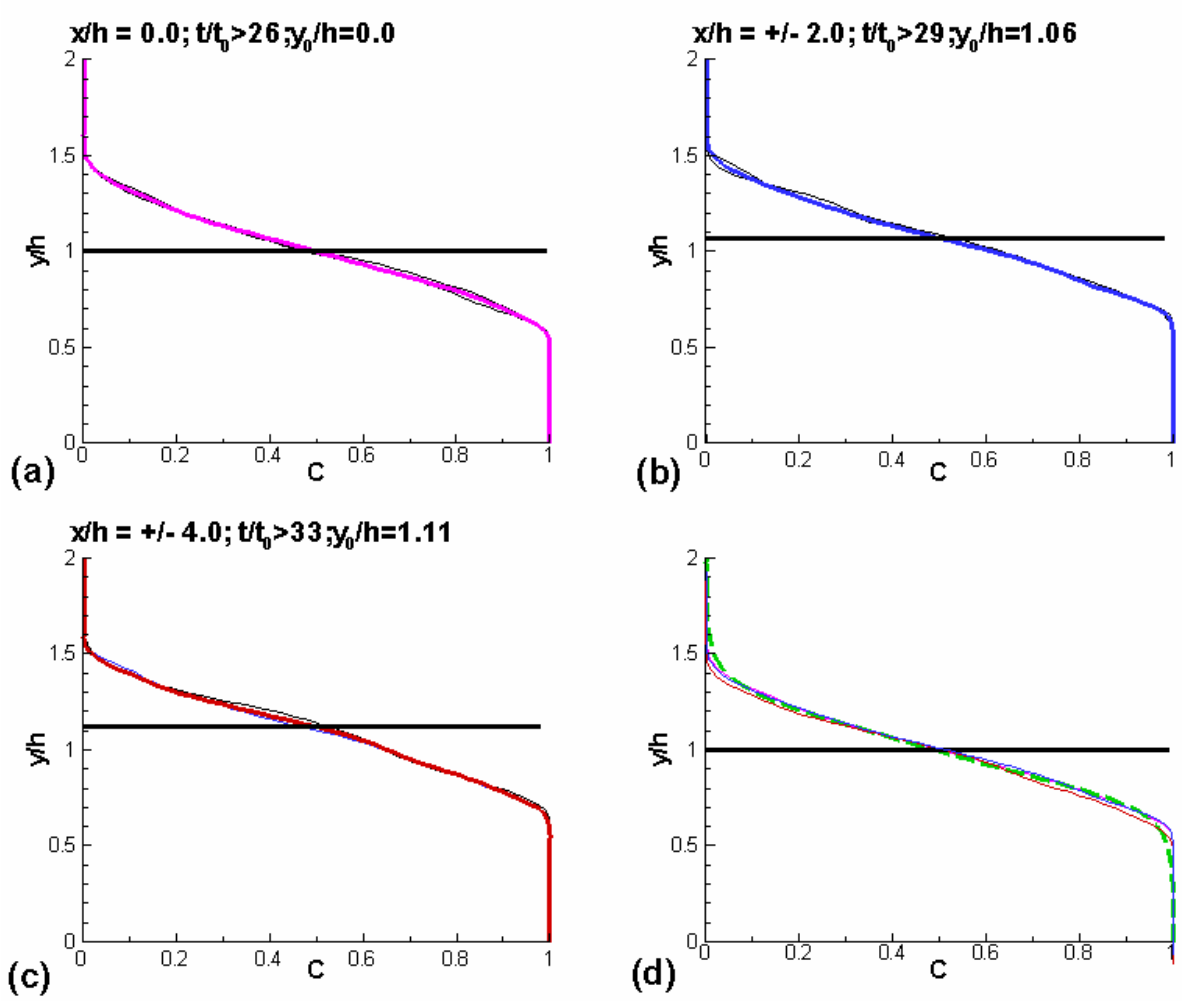

Figure 5.4. Vertical spanwise-averaged concentration profiles in the central region of the channel where a mixing layer of relatively constant width is present in the later stages of the HGR simulation. The thick lines correspond to the mean profile. The thin lines correspond to instantaneous profiles in the section x/h=constant. a) x/h=0.0; b) x/h=2.0; c) x/h=4.0; d) mean profiles at the various streamwise sections with a best-fit hyperbolic tangent profile.

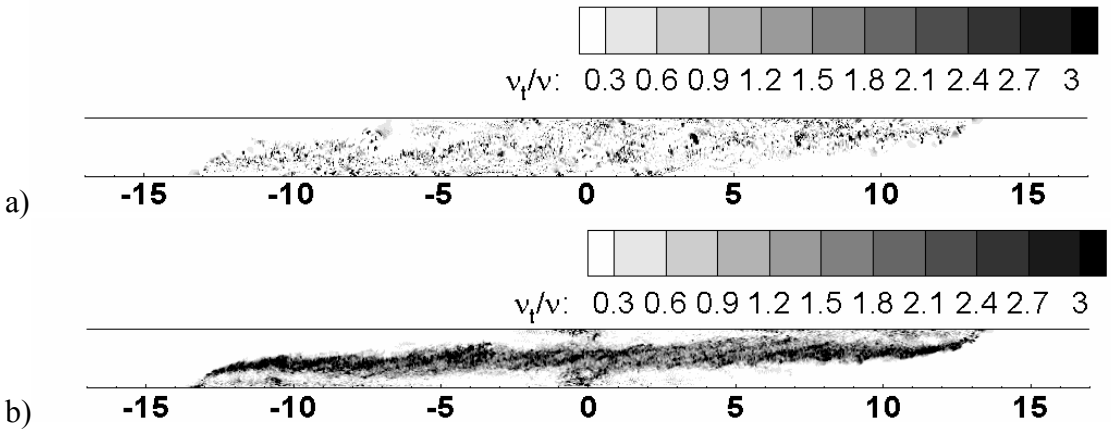

Figure 5.5. Visualization of the instantaneous ratio of SGS viscosity to kinematic viscosity at $t/t_0 = 20$ in the HGR case. a) 2D simulation; b) 3D simulation (spanwise-averaged profiles).

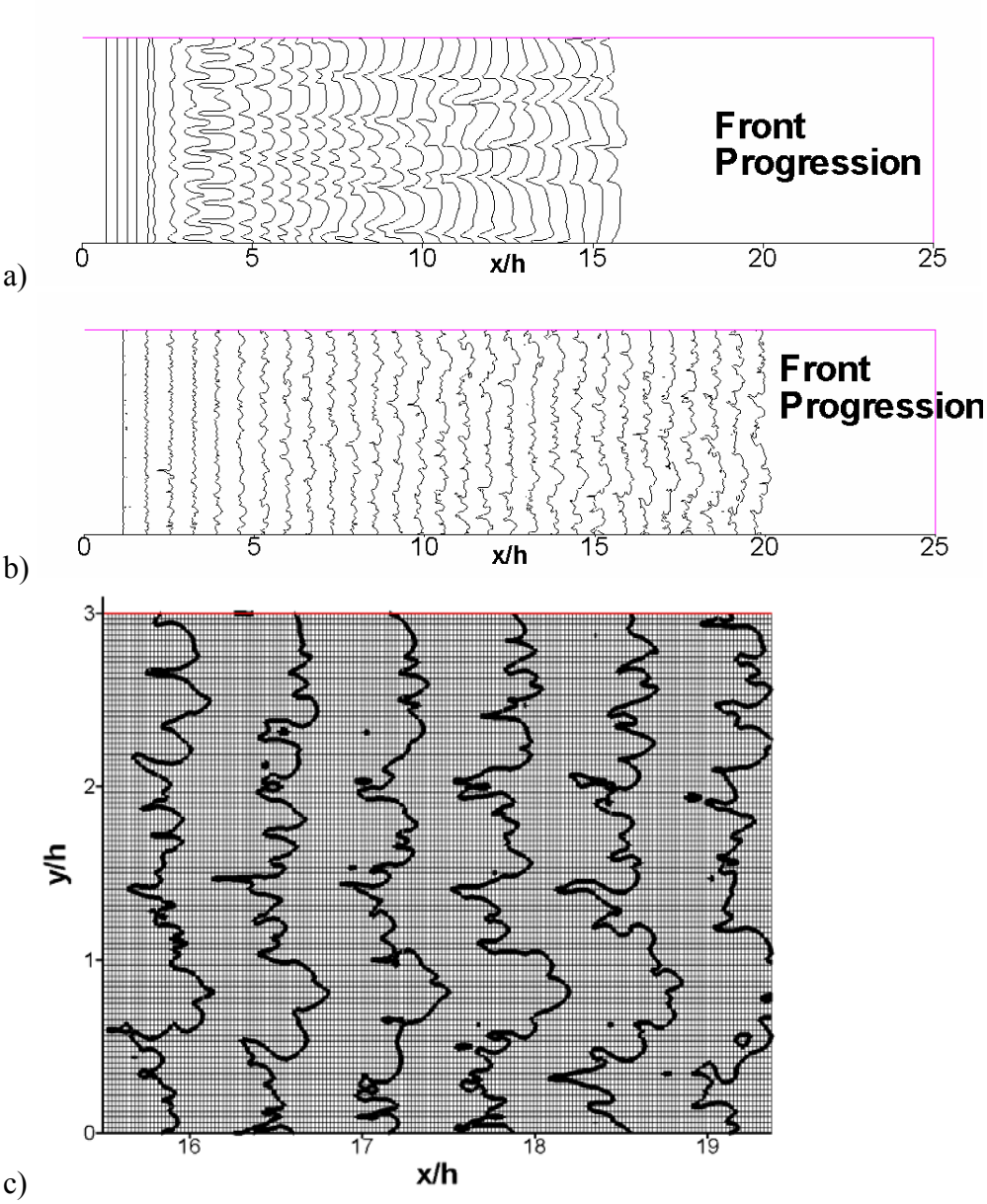

Figure 5.6. Visualization of the development of the lobe and cleft instability in the x-z plane situated at a distance of y/h=0.016 from the bottom wall. Consecutive lines indicate front position at a time intervals of $\Delta t/t_0$ = 1. a) LGR simulation; b) HGR simulation; c) Close-up view showing front position superimposed on the mesh in the HGR simulation.

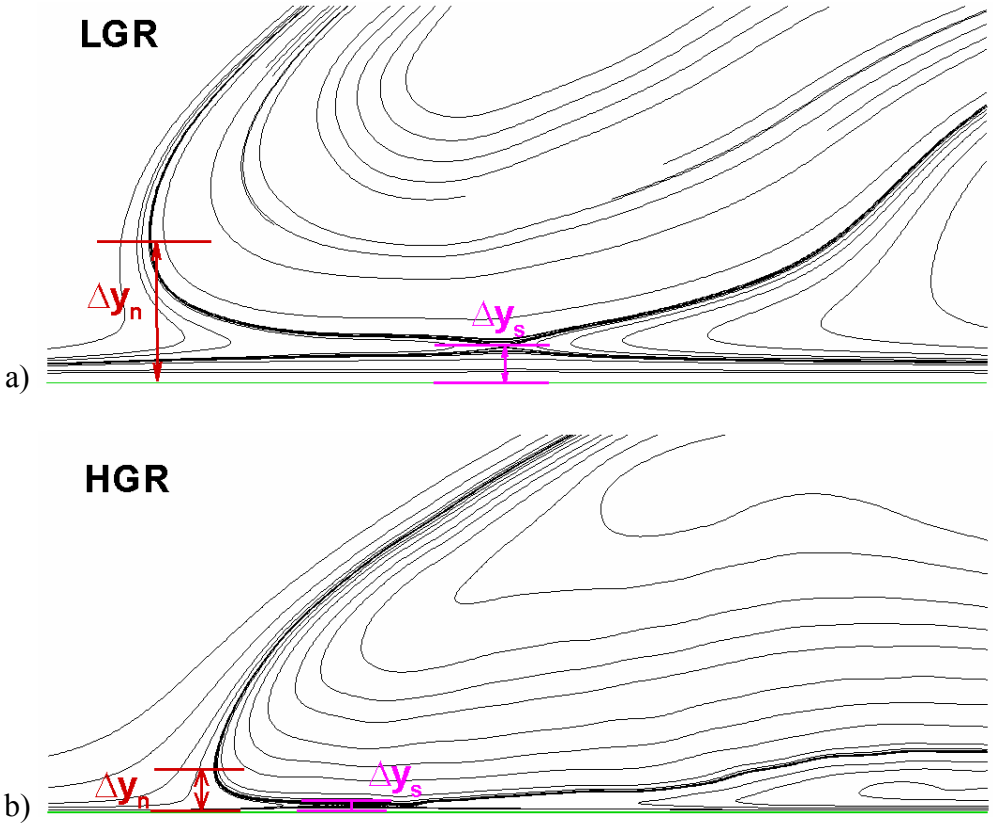

Figure 5.7. Visualization of the spanwise-averaged flow topology in the nose region using streamlines in a frame of reference translating with the front velocity. a) LGR simulation; b) HGR simulation.

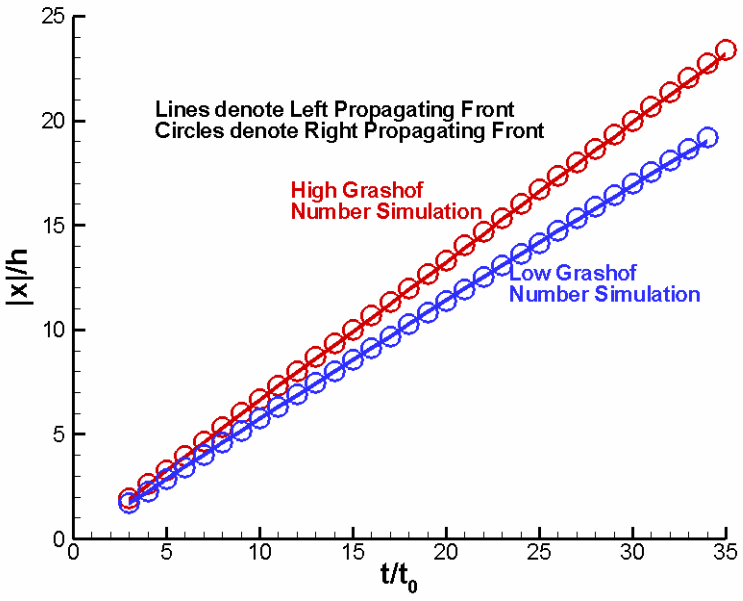

Figure 5.8. Evolution of the front position for the forward and backward propagating currents in the LGR and HGR simulations.

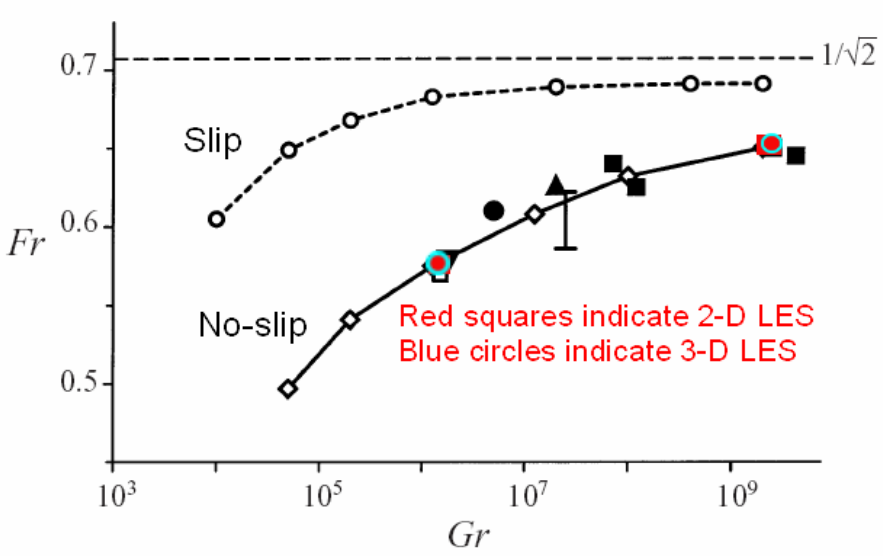

Figure 5.9. Froude number, *Fr*, as a function of Grashof number, Gr for lock-exchange flow in a channel with no slip walls. Simulation data: Open squares correspond to present 2D LES; Open circles correspond to present 3D LES. Open diamonds correspond to DNS simulations of Härtel et al. (2000a). Experimental data: ■, Keulegan (1957); ●,Simpson & Britter (1979);▲ Rottman & Simpson (1983);▼, Keller & Chyou.$1/\sqrt{2}$ is the theoretical result of Benjamin (1968).

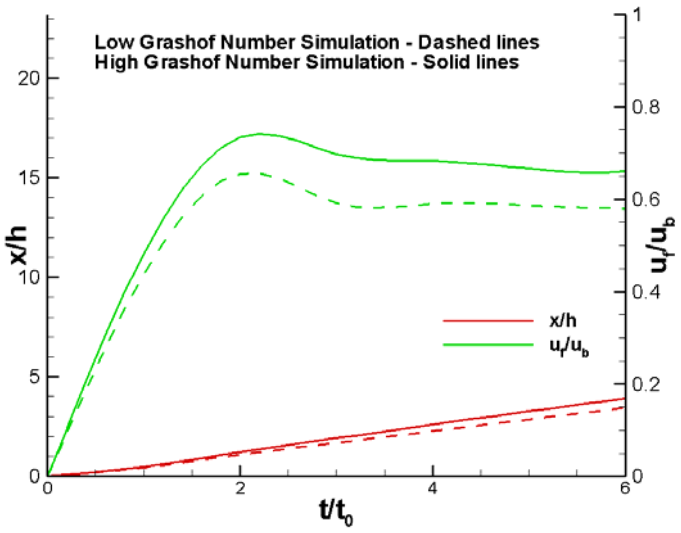

Figure 5.10. Evolution of front position and front velocity for the forward propagating current in the LGR and HGR simulations.

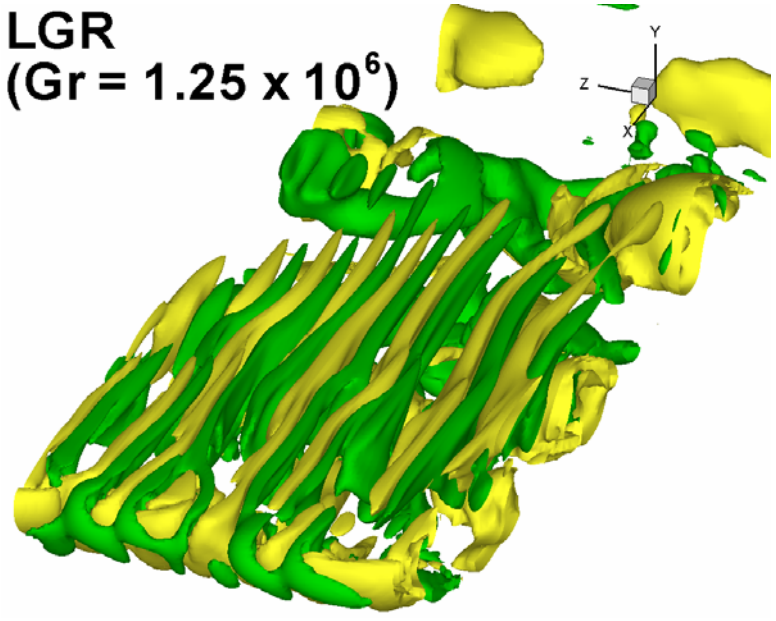

a)

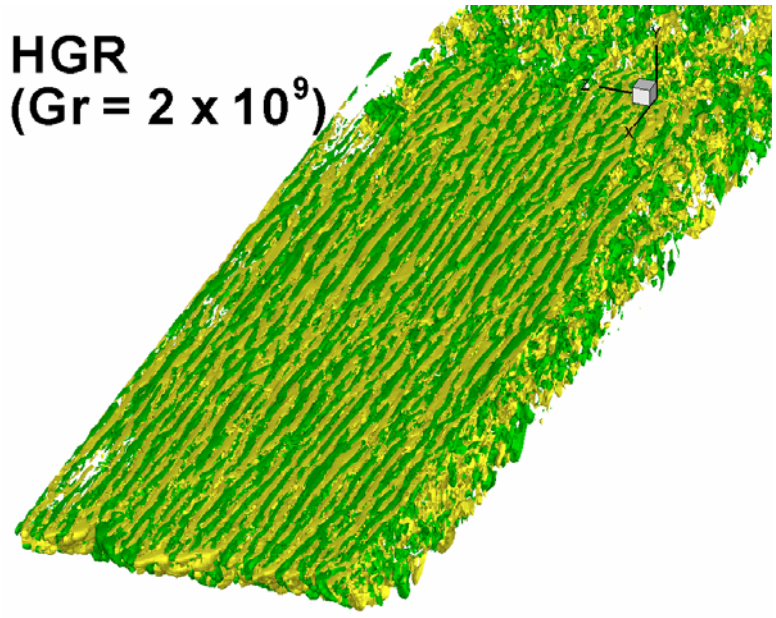

b)

Figure 5.11. Visualization of the instantaneous vortical structure of the forward propagating current in the near bottom-wall region (lateral view from below) at $t/t_0 = 20$ using vertical vorticity isosurfaces ($\omega_y = \pm 2u_b / h$) a) LGR simulation; b) HGR simulation.

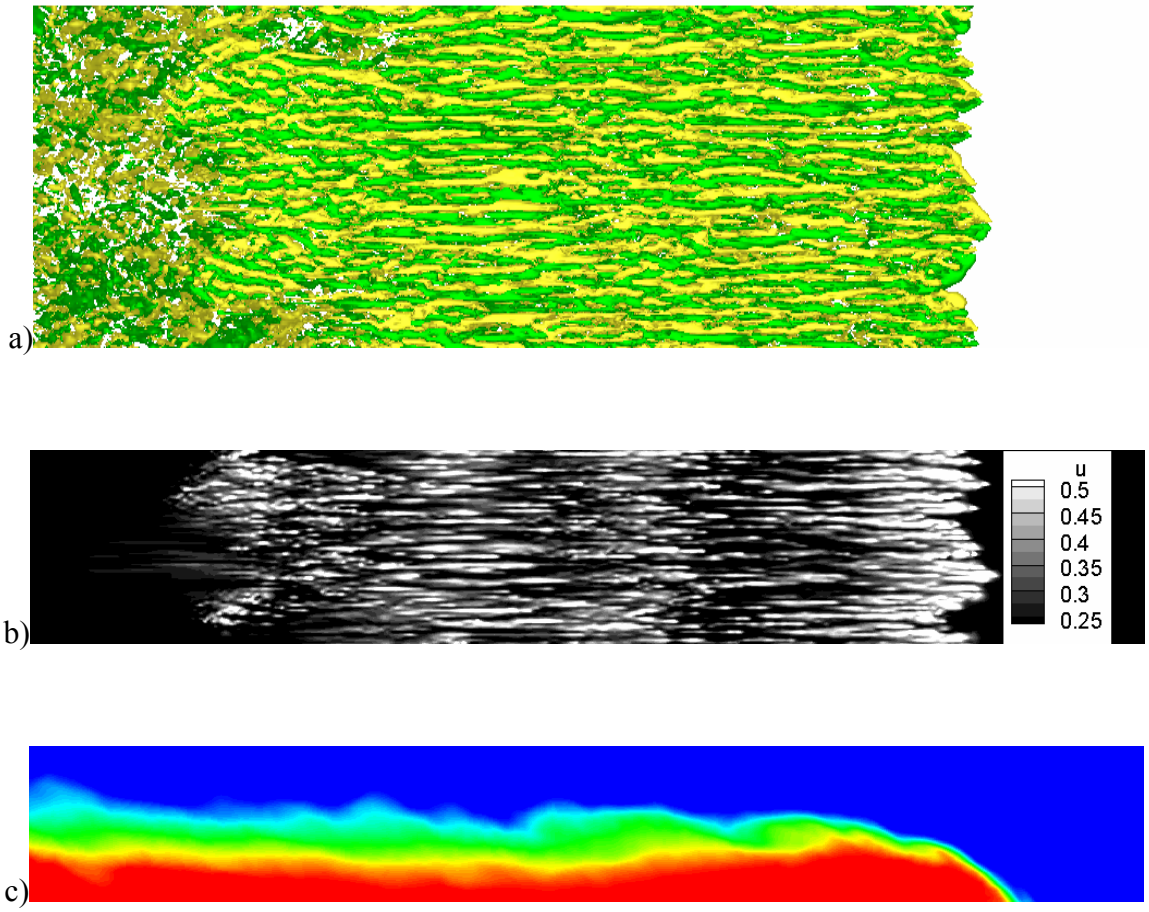

Figure 5.12. Visualization of the flow structure in the near wall region at t/t_0=20 for the HGR simulation. a) Vertical vorticity contours (vertical view from below); b) Streamwise velocity contours showing the high and low speed streaks in a plane located at y^+~11 from the bottom wall; c) Spanwise-averaged concentration distribution showing the forward propagating current.

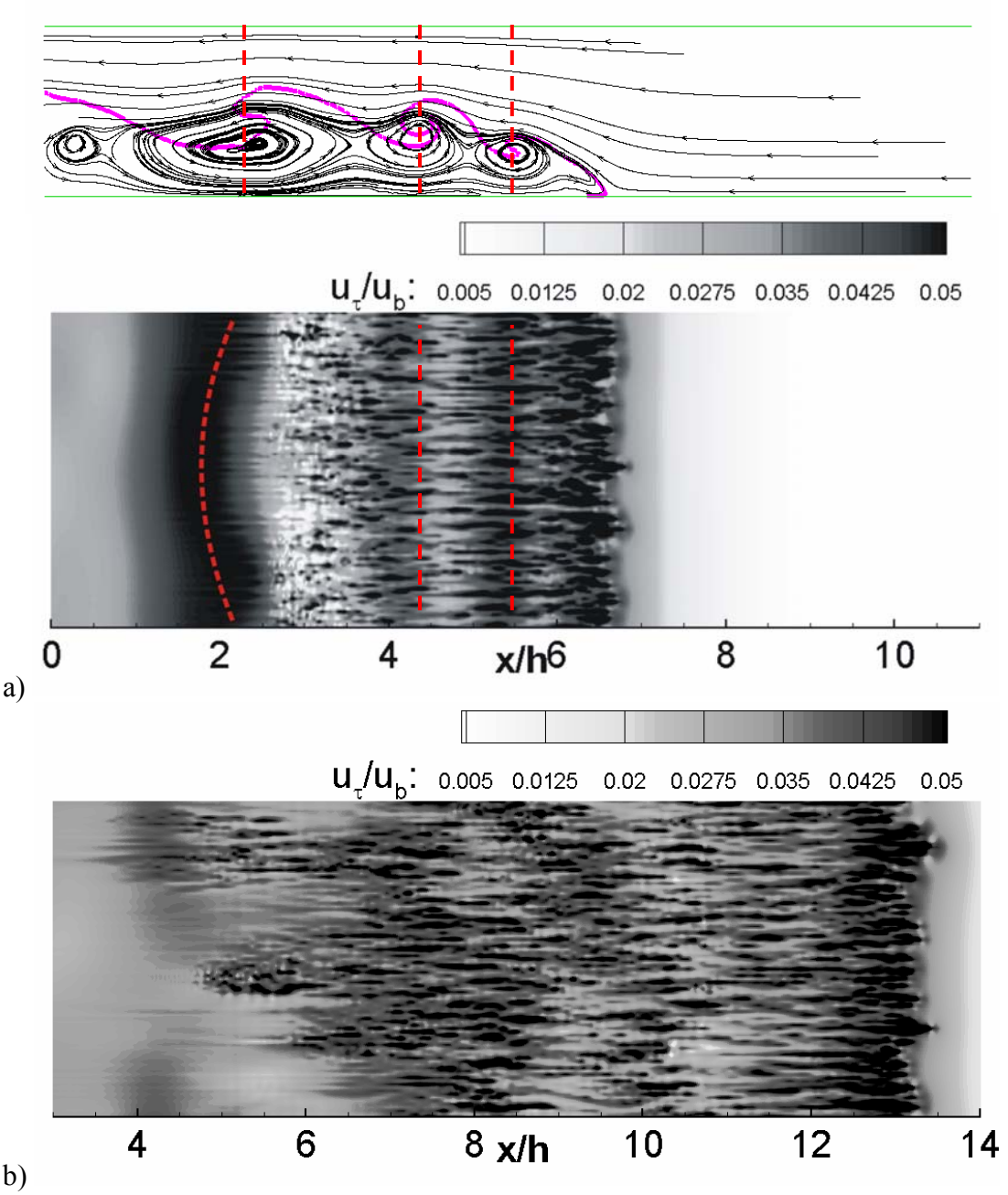

Figure 5.13. Spatial distribution of the friction velocity u_τ/u_b on the bottom wall in the HGR simulation. a) t/t_0=10. Streamlines in a moving frame of reference translating with the front velocity are also shown; b) t/t_0=20.

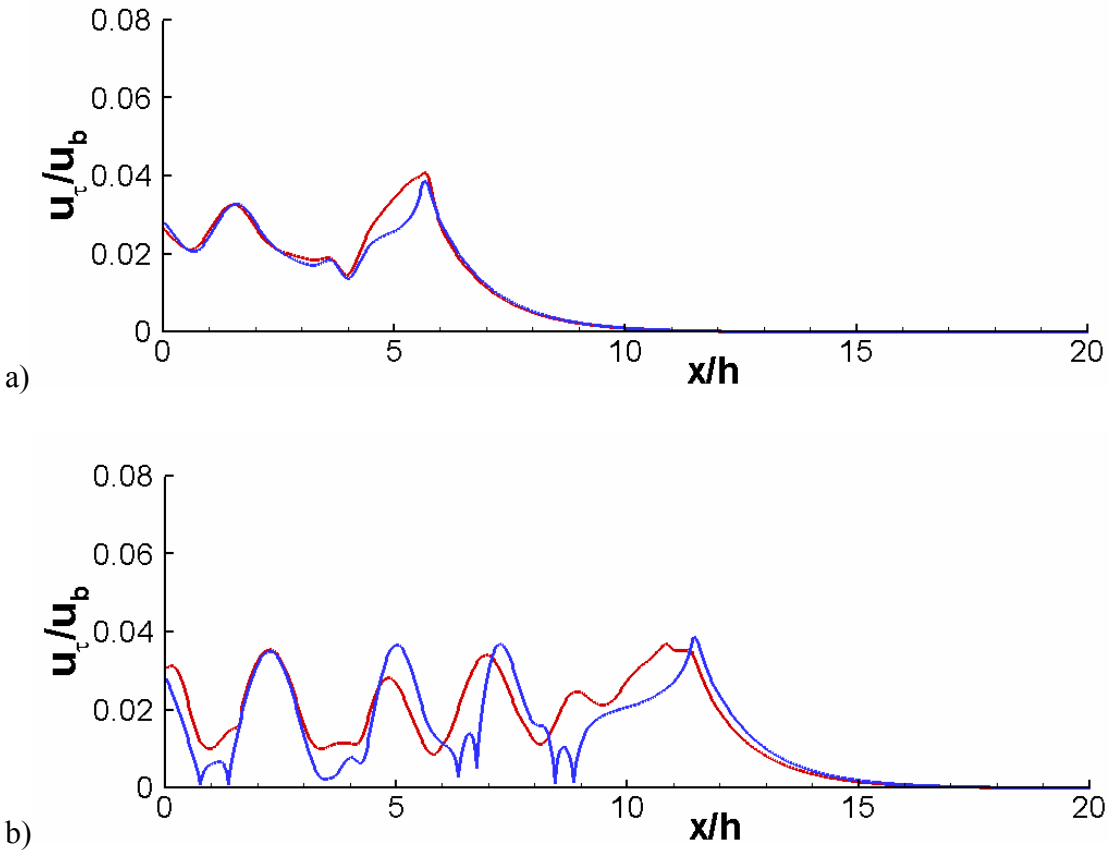

Figure 5.14. Streamwise variation of the spanwise-averaged friction velocity on bottom wall in the LGR simulation. Results from the 2D and 3D simulations are shown. a) t/t_0=10; b) t/t_0=20.

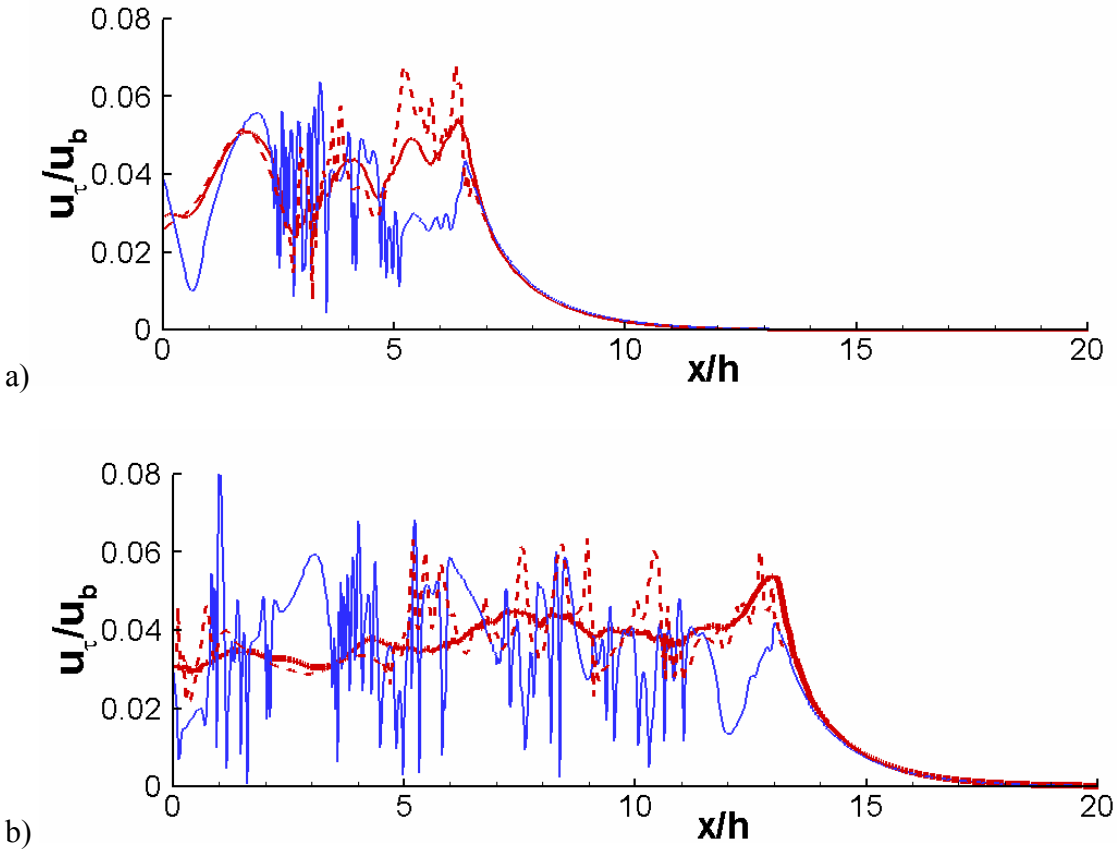

Figure 5.15. Streamwise variation of the spanwise-averaged friction velocity on bottom wall in the HGR simulation. Results from the 2D and 3D simulations are shown. a) t/t_0=10; b) t/t_0=20.

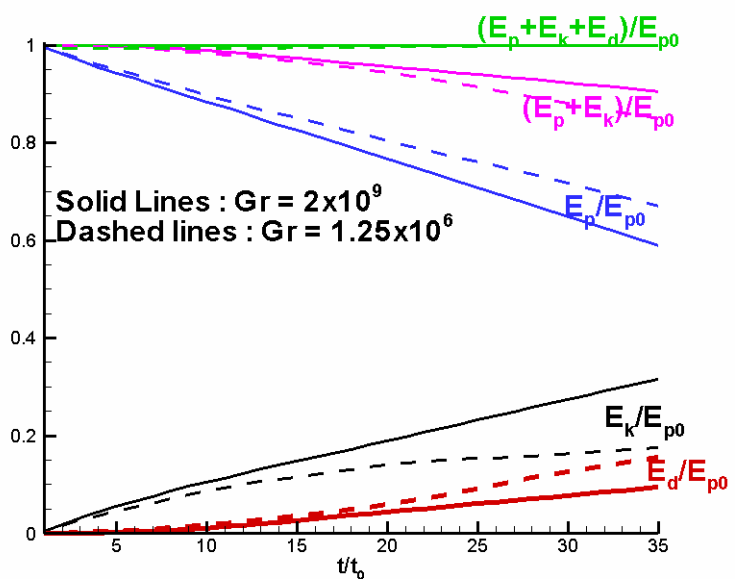

Figure 5.16. Time history of the potential energy, E_p, kinetic energy, E_k, and integral of the total dissipation, E_d, in the LGR and HGR 3D simulations.

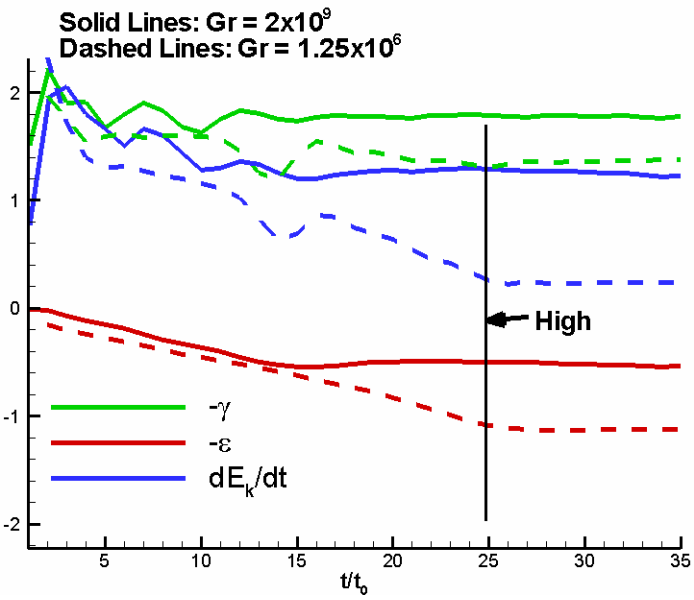

Figure 5.17. Temporal evolution of the terms in the transport equation for the total kinetic energy (equation 11) in the LGR and HGR 3D simulations.

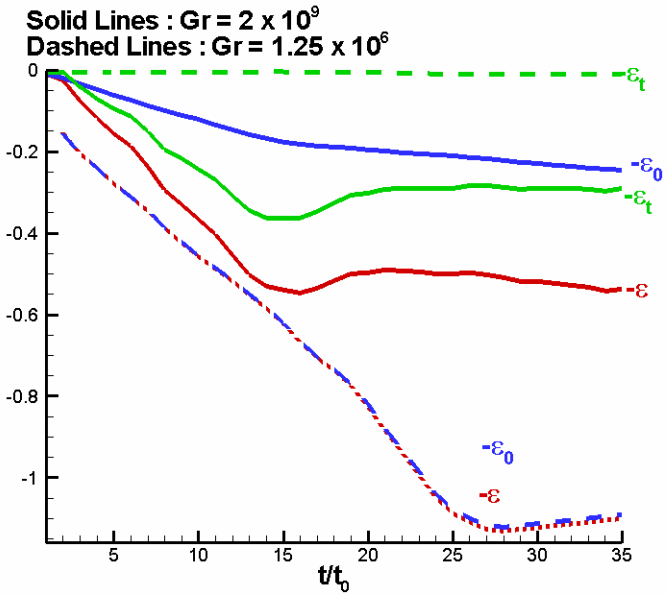

Figure 5.18. Temporal evolution of the total dissipation, ε, SGS dissipation, ε_t and viscous dissipation, ε_0 in the LGR and HGR 3D simulations.

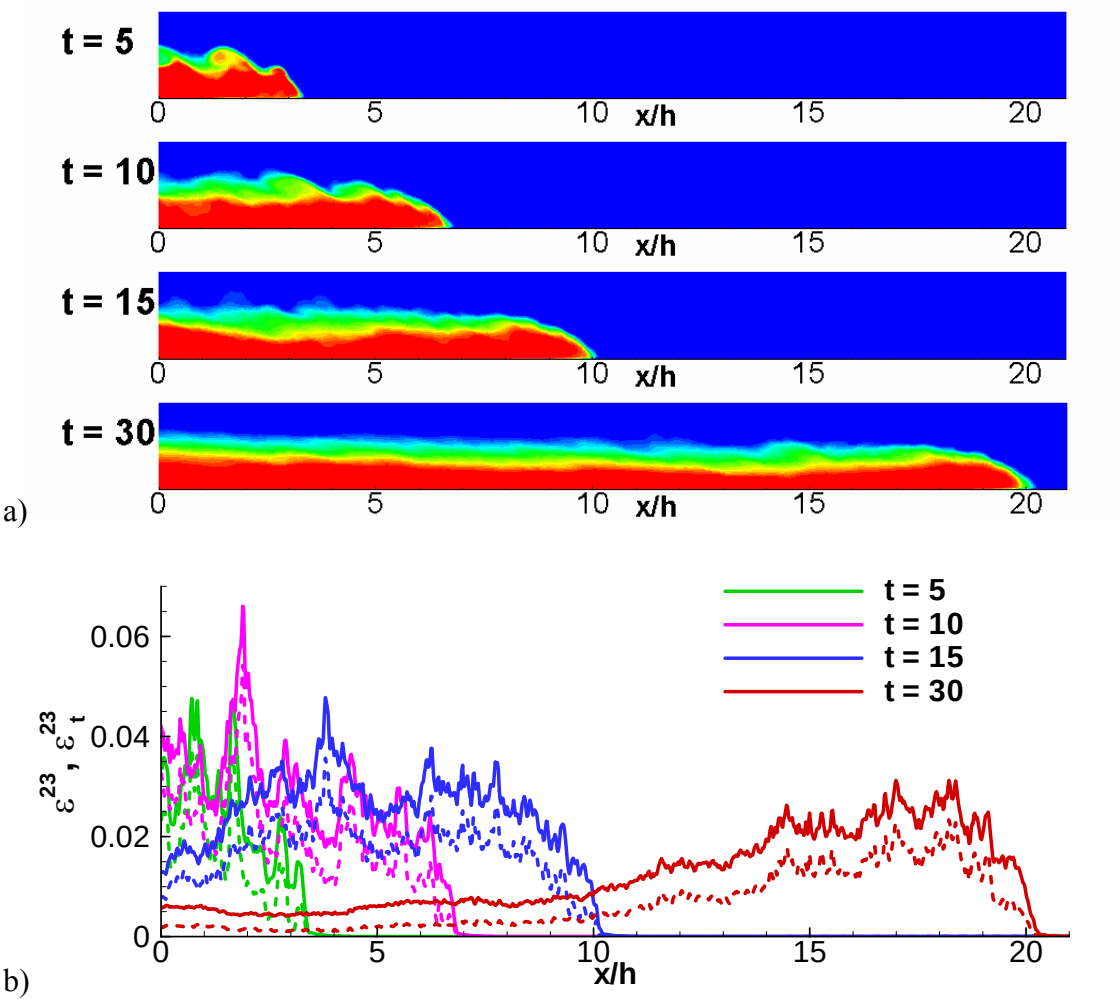

Figure 5.19. Streamwise distribution of the dissipation at t/t_0=5, 10, 15 and 30 in the HGR simulation. a) visualization of the forward propagating current using spanwise-averaged concentration contours; b) distribution of the total dissipation term $\varepsilon^{23}(x_1)$ and SGS term $\varepsilon_t^{23}(x_1)$ calculated using equations (16) and (17), respectively.

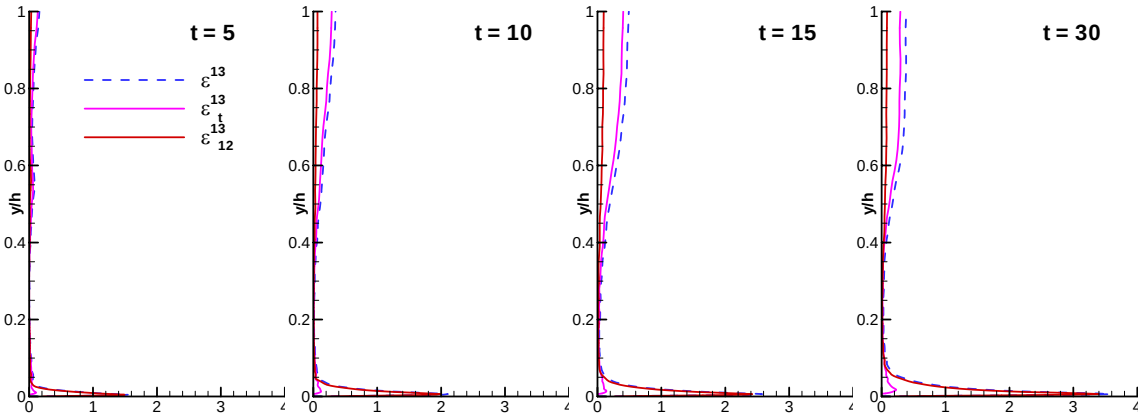

Figure 5.20. Vertical distribution of the dissipation in the lower half of the channel at t/t_0=5, 10, 15 and 30 in the HGR simulation. The distributions of the total dissipation term $\varepsilon^{13}(x_2)$, SGS term $\varepsilon_t^{13}(x_2)$ and dissipation term containing the vertical gradient of the streamwise velocity $\varepsilon_{12}^{13}(x_2)$ are calculated using equations (5.15), (5.16) and (5.17), respectively.

CHAPTER 6

3D LES SIMULATIONS OF FINITE-VOLUME LOCK-EXCHANGE FLOWS

6.1 Simulation Setup

The length scale in the finite-volume lock fluid simulations is set equal to the channel depth h (domain height L_2=h). The present simulations are somewhat different from previous 2D and 3D DNS simulations of finite-volume lock exchange flows. In the present simulations the boundary layers on all the walls are resolved by clustering the grid points in the streamwise and vertical directions such that the first point off the wall is situated at less than one wall unit (assuming turbulent flow) from the surface. This includes the end wall, which is treated as a no-slip boundary, instead of using a more approximate symmetry boundary condition and uniform meshes in the streamwise direction, that are typically employed in spectral or semi-spectral codes. This setup allows a more accurate study of the interaction between the bore and the end wall. There is also interest in the flow dynamics in the transition region between the slumping phase and the self-similar inviscid region, both of which were not discussed in previous DNS studies of compositional currents.

In all the present simulations the initial lock fluid extends up to the free surface. All simulations were performed with a value of the molecular Schmidt number equal to 600 which corresponds to saline diffusion in water. In agreement with the experimental setup of Hacker et al. (1996), the top surface of the open channel was treated as a slip boundary (zero shear). A convective outflow boundary condition was used at the right extremity of the computational domain. This allows coherent structures to exit the domain in a time accurate way. In the spanwise direction the flow was assumed periodic. The flow field in all simulations was initialized with the fluid at rest, i.e., $u_i = 0$. The non-dimensional concentration field was initialized with a constant value of one in the lock region and a constant value of zero inside the channel. A random disturbance was

applied on the concentration field in the lock-gate region to accelerate the growth of 3D instabilities. The time step in the simulations was $0.001t_0$. The maximum Courant number was around 0.35.

The lock exchange cases that are denoted as A, B and CL (see Table 6.1) correspond to the laboratory experiments carried out by Hacker et al. (1996). The main difference among these cases is the initial volume of lock fluid. As in all simulations the depth of the lock fluid is equal to the channel depth, the difference in the initial volume can be characterized by the initial aspect ratio of the lock fluid, $R=h/x_0$ (x_o is the initial lock length) which is equal to 0.67, 1.00 and 1.78, respectively. The Reynolds numbers defined with the front velocity and the channel half depth ($Re_f = U_f(h/2)/\nu$) are in the range of 7,000 to 20,000 during the slumping phase (see Table 6.1). Thus, the flow inside the current is expected to be turbulent is cases A, B and CL, at least in the region behind the front. A fourth 3D simulation (case CH) was performed at $Gr=10^{12}$ (Re_f~248,000). The other parameters in case CH are identical to those in case CL. Additionally, a 2D simulation (case D) with $R=1$ at a very low Grashof number ($Gr=2.8\times10^5$, Re_f~98) was performed. For the conditions in case D, the GC is expected to transition directly from the slumping phase into the viscous phase (see Rottman & Simpson, 1983). At this low Grashof number the flow in the head region and over part of the tail is expected to remain two dimensional.

The size of the grid was 3072×160×72 in all the 3D simulations. The dimensions of the computational domain in cases A, B and CL were the similar to the ones in the physical experiments. In some cases (e.g., case CL) the length of the domain, L_1, was longer (see Table 6.1). The domain size in the spanwise direction (L_3) varied between $0.768h$ and $1.025h$, over which the computational points were distributed uniformly. The typical size of a cell was $0.0045h$ in the streamwise direction, $0.018h$ in the vertical direction and $0.012h$ in the spanwise direction. As the right boundary was approached, the streamwise cell size was progressively increased to $0.03h$. Near the end

and bottom walls, the cell size in the wall-normal direction was decreased to $\Delta n=0.001h$. Assuming conservatively $u_\tau/U_f\sim0.04$ and $U_f/u_b\sim0.5$ this translates into $\Delta n^+<1$ wall unit for case B which had the highest Grashof number among cases A, B and CL. For case CH the stretching in the wall normal direction was somewhat larger, to insure $\Delta n^+\sim2$ for the first row of points off the walls. The mesh size in cases A, B and CL, including near the walls, was fine enough for the code to be able to resolve the dynamically important turbulent structures. The use of wall functions in case CH was avoided by insuring that the governing equations are integrated through the viscous sub-layer. However, in the other two directions the grid density expressed in wall units is much coarser compared to case CL. Some results from previous 2D simulations of cases A, B and CL are also included. The number of grid points in the streamwise (x) and vertical (y) directions was comparable to the one used in a z=constant plane in the 3D simulations.

6.2 Role Of The Initial Aspect Ratio Of The Lock Fluid And Grashof Number In The Development Of The Gravity Current

Most of our analysis regarding the effect of the initial aspect ratio of the lock fluid is focused on cases B and CL, but some validation results and values of parameters characterizing the evolution of the current for case A are included. Comparison between cases CL and CH allow the study of the Grashof / Reynolds number effects on the development of a GC from its formation until well into the self-similar inviscid phase. As in Chapter 5, in the present discussion the head region of the GC contains the region behind the front and the dissipative wake region.

As expected, the general evolution of the GC and location of transition from the slumping to the inviscid phase are affected by the initial aspect ratio of the lock fluid. This is evident from comparison of the spanwise-averaged concentration contour plots in Figures 6.1 and 6.2 which visualize the evolution of the current in cases B (R=1) and CL

(R=1.78) in the 3D simulations and experiments (Hacker et al., 1996). The arrow indicates the position of the reflected bore. In both cases, simulation results are presented at time instances past the time for which experimental data is available. This is important especially for case CL, where experimental data was reported only until the end of the slumping phase (Figure 6.2j, t/t_0=12.4). In the 3D simulation the evolution of the current was studied until t/t_0~40, thus covering a significant amount of time for which the current was in the inviscid phase. In case B, to avoid interaction with the downstream boundary, the simulation was stopped around the time the bore was about to catch the front. In the same figures, several frames show both the 2D and 3D solutions.

Comparison of Figures 6.1a and 6.2a show that the flow is relatively symmetric with respect to the initial position of the gate before the bore hits the end wall (t<1.8t_0). In both cases KH billows start forming on the interface between the current and the lighter ambient fluid. The mixing is strongest in the interface region. As the current develops (subsequent frames in Figures 6.1 and 6.2 corresponding to cases B and CL), the interfacial vortices grow in size, are stretched and deformed by 3D flow instabilities and eventually break into smaller, highly 3D turbulent eddies before diffusing in the ambient flow (see also discussion of Figure 6.4). As the coherence and energy of the large-scale KH billows diminish, small-scale mixing phenomena become dominant. As a consequence, the flow in the interface region and over most of the body of the GC becomes mildly stratified.

Despite these similarities, there are some differences between the evolution of the GC in cases B and CL. For instance, at t/t_0=5.6 (Figures 6.1d and 6.2e) the tail region is much more developed in case CL while in case B the main KH billows are more compact and their number is higher. In case B, the length of the region of practically unmixed lock fluid in the upstream part of the current is twice as long as that in case CL. The streamwise position of the front and non-dimensional time when the bore catches the front are substantially different in cases B and CL. However, at that stage the overall

shape of the two currents and the degree of mixing in the tail are relatively similar (compare Fig. 6.1g at $t=16.0t_0$ and Fig. 6.2h at $t=10.4t_0$).

Direct comparison with the experimental data in Fig. 6.1 allows estimation of the accuracy of the numerical predictions for case B, at least over a substantial part of the slumping phase. The overall shape of the current and the regions where mixing is present appear to be reasonably well predicted by the simulation. Comparison of the position and number of the crests at the top of the unmixed region of the GC suggests that most of the large billows predicted in the simulations are also present in the experiment. For example, the position of the large billow present at the rear of the head of the current (x/h~1) and the associated region of high mixing are correctly captured in Figures 6.1c to 6.1e. The billow is still identifiable in Fig. 6.1f at x/h~2. Also observe that as the bore overtakes the large billows, heavier lock fluid is drawn into the billow from the unmixed lower region. The shape of the large region of mixed fluid present in the experiment behind the head is somewhat different in the simulation where its shape is more circular. A probable reason for this difference is the fact that while in the simulations the gate was removed instantaneously and without inducing any velocities in the flow, in the experiment that was not the case (see also discussion in Hacker et al., 1996). Evidence of that is given by comparing the simulation and experimental results in Fig. 6.1a. While the concentration contours in the simulation appear to be anti-symmetric with respect to x/D=1 (a small break in the anti-symmetry is present near the free surface and the bottom wall where slip and no-slip conditions were imposed, respectively), this is obviously not the case in the experiment where the GC has already formed on the bottom while the rest of the interface is relatively vertical and much thicker near the free surface. Observe also the gradual loss in the coherence of the KH billows especially in the tail (e.g., see Figures 6.1f and 6.1g) as the GC approaches the end of the slumping phase. Though the position and relative size of the main billows are captured relatively accurately over most of the slumping phase in the 2D simulation (e.g., compare the 2D and 3D results in Fig. 6.1e),

the coherence of these billows is larger and the mixing inside them is weaker in the 2D simulation. This is due to the absence of the 3D instabilities in the 2D simulations.

The spanwise-averaged concentration contour plots in Fig. 6.2 visualize the evolution of the current in case CL (R=1.78) in the 3D simulation and experiments (Hacker et al., 1996). The arrow indicates the position of the reflected bore. The simulation results are presented at time instances past the time for which experimental data is available. This is important as experimental visualizations were reported only until the end of the slumping phase (Fig. 6.2j, t/t_0=12.4). In the 3D simulation the evolution of the current was studied until t/t_0~40, thus covering a significant amount of time for which the GC was in the inviscid phase. In the same figure, several frames show both the 2D and 3D solutions.

Fig. 6.2a shows that the flow is relatively symmetric with respect to the initial position of the gate (x_0=0.56h) before the bore hits the end wall (t<1.8t_0). Interfacial billows start forming on the interface between the lock fluid and the lighter ambient fluid. The mixing is strongest in the interface region. As the current develops (subsequent frames in Fig. 6.2), the interfacial vortices grow in size, are stretched and deformed by 3D flow instabilities and eventually break into smaller, highly 3D turbulent eddies before diffusing in the ambient flow (see also discussion of Fig. 6.4). As the coherence and energy of the large-scale KH billows diminish, small-scale mixing phenomena become dominant. As a consequence, the flow in the interface region and over most of the body of the GC becomes mildly stratified.

Comparison of the distributions of the concentration contours in Figures 6.2a to 6.2j show that the 3D simulation of case CL successfully captures the overall shape of the GC during the slumping phase, the dimensions of the region of unmixed fluid at the head and the formation of the stratified tail region in which the action of the small 3D turbulent eddies is very efficient in enhancing the mixing. For example, the length and shape of the unmixed region at the head are very well reproduced in the 3D simulation at t/t_0=5.6

(Fig. 6.2e). In the later stages of the slumping phase (Fig. 6.2j), the concentration distribution in the mildly stratified region behind the head is well predicted. In the D simulation, the growth of the 3D instabilities and their interaction with the KH vortices shed in the formation region behind the front was captured well. This is in stark contrast to results obtained from a 2D simulation (Fig. 6.2j). In general, in the 2D simulations, though the front position is correctly predicted, the KH billows maintain their coherence over the whole body of the GC such that the mildly stratified tail region is practically absent. However, over the initial stages of the slumping phase (e.g., see 2D and 3D results in Fig. 6.2d), when 3D effects are not very important, the 2D predictions are in much better agreement with experiment and 3D simulations. The gate removal in the experiment introduced additional secondary motions (Fig. 6.2a). This explains some of the differences observed in the tail region between simulation and experiment at earlier times (Figures 6.2b and 6.2c). The KH billows in the tail region appear to be slightly more coherent in the simulation until the end of the slumping phase. As the current transitions to the inviscid phase (Figures 6.2k to 6.2m), the flow at the front starts mixing. As a consequence, the highest concentrations are observed to occur in a small elongated near-bed region starting some distance behind the front (see concentration contours in Fig. 6.15b). Results from a 2D simulation (Fig. 6.2m) show that large-scale energetic KH billows are still clearly observable at large distances behind the nose. Their convective velocity is decaying in time but, because of the absence of 3D instabilities, they are less affected by viscous effects and maintain their coherence for much longer times. This is the reason why a tail region, similar to the one observed in the experiment, cannot develop and the relatively compact region of higher concentration fluid inside the head is not present. In comparison, the GC in the 3D simulation at the same moment in time (t/t_0=25) maintains the classical shape observed in experimental visualizations conducted during the slumping phase (Simpson, 1997). Additionally, the front position in the 2D simulation is situated behind the one predicted by the 3D simulation. At t/t_0=25

the difference is equal to 0.77h. This is due to a steeper decay of the front velocity during the inviscid phase in the 2D simulation.

Qualitatively, the evolution of the GC at the higher Grashof number in case CH is similar to the one observed in case CL. The shapes of the two GCs are very similar during the acceleration phase (Fig. 6.2a), when 3D effects are negligible. The front travels slightly longer distances in the CH simulation during the slumping phase. For example, at the end of the slumping phase (Fig. 6.2j) the difference is close to 0.4h. The differences between the positions of the front in the two simulations grow significantly as the current transitions into the inviscid phase. At t/t_0=25 the difference is about 1h. This difference can be related to the fact that in the CH simulation the streamwise gradient of the concentration across the front in the near-bed region is larger compared to the CL simulation at the same non-dimensional time (e.g., compare concentration contours at t/t_0=16 in Fig. 6.15). In both simulations the energy contained in the large scale structures appears to decay significantly in the inviscid phase, such that at t/t_0=25 (Fig. 6.2m) no large-scale coherent structures can be observed over the body of the current at distances greater than 1.5h from the front.

The non-dimensional spanwise-averaged SGS viscosity contours for case CL (see Fig. 6.3) clearly show that the turbulence intensity in the range of the smallest resolved scales (around grid size level) has increased substantially between the initial stages of its evolution (t/t_0=4) and a time instance after the end of the slumping phase (t/t_0=16). The dynamical model correctly predicts large values of the SGS viscosity around the KH billows that are shed from the formation region and around the interface between the GC and the ambient fluid. It shall be shown in the discussion of Fig. 6.4 that the interface at t=16t_0 is populated by small scale energetic 3D eddies between x/h=4 and the front region. Additionally, the cores of the KH billows in the head region and over the upstream part of the tail are strongly distorted and stretched. This explains the larger values and increased thickness of the band of high SGS viscosity values observed around

the interface at t/t_0=16 compared to t/t_0=4. Relatively large values of the SGS viscosity are present inside the region close to the end wall at t/t_0=4. As the mesh, close to the end-wall, is fine enough to resolve the attached boundary layers and the other flow structures, it appears that, as a result of the interaction of the backward propagating bore with the end wall, a large amount of small scale eddies are generated for x/h<0.7. These 3D eddies are thought to be one of the main source of 3D instabilities in the initial stages of the development of the current during the slumping phase. The SGS model also correctly predicts very small SGS viscosity values in the downstream part of the tail (x/h<2.5 in Fig. 6.3b) where the flow relaminarizes.

The influence of the SGS model is even more important in determining the evolution of the current in the CH simulation. As the dynamic model is overall much less dissipative than the constant coefficient version, this means that the damping of the resolved scales will be lower. Thus, one expects that the use of the dynamic model will make a significant difference in the accuracy of the predictions at Grashof numbers of the order of 10^{12}, where the values of the SGS vorticity in the regions where the flow is strongly turbulent are one to two orders of magnitude higher than the molecular viscosity.

Fig. 6.4 visualizes the interface between the GC and the ambient fluid for cases CL and CH using a concentration isosurface (C=0.5) at t=16t_0 during the inviscid phase. Shifting lobes divided by deep clefts can be observed in the front part of the advancing head. Billows that are formed due to the amplification of the KH instabilities are present in the shear zone (mixing layer) at the upper part of the head region between the front (x~7.2h) and x~6.0h. Though these structures are deformed in the spanwise direction, the billows appear to extend over most of the entire width of the computational domain (~1h), suggesting that the formation of these structures is a predominantly 2D process. The lobes and clefts at the front induce noticeable 3D perturbations of the cores of the KH billows in the formation region in both CL and CH simulations at this stage of the evolution of the current, as observed in the insets showing the front region. This differs

from the flow evolution during the slumping phase when the interaction between the KH billows in the formation region and the lobes is reduced. The amplitude of the interface oscillations associated with the presence of these billows is growing between the region where they form and x~4.0h. The flow inside the head region is strongly turbulent even in the CL simulation. The 3D turbulent eddies from the near bottom-wall region (see also discussion of Fig. 6.11) are swept into the upper parts of the head where they disturb the interfacial vortices and force the transition to turbulence in the mixing layer. Behind the head region the flow remains strongly turbulent for a relatively long distance, but the energy balance between the small scales and the large scales changes as one gets away from the head region. The energy associated with the small scales is growing substantially while the coherence of the large-scale coherent structures is practically lost. The region with x<6h is populated with small scale energetic eddies that are very effective in enhancing the local mixing. These eddies produce the relatively mildly stratified region behind the head of the GC that is observed in the spanwise averaged concentration contours in Figures 6.2 and 6.16. Eventually, these small-scale eddies, that lose their energy by mixing the lock and ambient fluid (see second inset in Fig. 6.4), dissipate and the flow starts to relaminarize. For example, at t~16t_0, this happens in the region where x<2.5h over which the interface deformations in the CL simulation are hardly observable.

Comparing the coherent structures in the front region in Fig. 6.4 it is clear that the average dimension of the lobes is smaller in case CH compared to case CL. This is confirmed by comparing the lines tracking the front position at a distance of 0.015h from the bed, shown at equal time intervals of $\Delta t/t_0$=1 in Fig. 6.5. The comparison is shown both during the slumping phase, starting at t=3t_0, and during the inviscid phase, starting at t=26t_0, when the front velocity and the associated Reynolds number (Re_f) are decaying in time. At the same non-dimensional times, the average and maximum sizes of the lobes are smaller in the CH simulation. These observations are consistent and compare well

with the experimental data obtained by Simpson (1972) which show that the mean size of the lobes decreases with an increase in the Reynolds number defined with the front velocity and the head height. For case CL, the average and maximum size of the lobes are 0.065h and 0.14h, respectively, during the constant velocity slumping phase (Re_f~10,900). These values are within 10% of the experimental observations of Simpson (1972). The average and maximum lobe sizes are 0.09h and 0.19h during the self-similar phase at t/t_0=29 when Re_f~4,600. The mean size of the lobes measured by Simpson (1972) is around 0.095h, in excellent agreement with the simulation. For case CH the mean size of the lobes is 0.03h during the slumping phase and 0.06h at t/t_0=29 during the self-similar inviscid phase.

The topology of the flow in the nose region in a coordinate system translating with the front velocity is shown in Fig. 6.6 at two time instances: one when the GC is in the slumping phase (case CL) and the other when GC is in the self-similar phase (cases CL and CH) at t~16t_0. In all three frames the flow topology is similar in the sense that the foremost point (nose) is not collocated with the stagnation point. This is also consistent with the flow topology observed during the slumping phase for infinite-volume lock-exchange flows (see discussion in Chapter 5). Comparison of Figures 6.6a to 6.6c shows that the nose is situated closer to the bed, and the unstable stratified region between the nose and the stagnation point is getting smaller as Re_f increases. This is true in two situations: the first is when the comparison is made between the slumping (Fig. 6.6a) and inviscid phases (Fig. 6.6b) for the same GC and the other is when the comparison is made between two currents at similar stages of their evolution (compare Figures 6.6b and 6.6c) but for which the initial Grashof numbers are different. The vertical distance Δy_n between the nose and the bottom wall is Δy_n=0.039h at t=4t_0 and Δy_n=0.065h at t=16t_0 for case CL. For case CH, in which the Reynolds number, Re_f, is about 24 times higher compared to case CL, Δy_n=0.014h at t=16t_0 which corresponds to a decrease of more than 4 times. The distance between the stagnation point and the bed is

also strongly dependent on the instantaneous value of Re_f. The ratio of the flux of light fluid underneath the front, $\dot{V}_u$, to the total expected incoming flux of light fluid, $\dot{V}_o = hU_f$, is close to 0.08% at $t=4t_0$ during the slumping phase and to 0.16% at $t=16t_0$ in the CL simulation. The corresponding values for the CH simulation are 0.005% and 0.01%, respectively.

The final simulation (case D) was included in this study because it allows for the analysis of the evolution of a GC during the viscous phase when viscous forces dominate. If the initial Grashof number of the GC is very low, the flow is expected to remain 2D, at least over some distance behind the front. A 2D simulation with $R=1$ was performed at $Gr=2.8\times10^5$. Fig. 6.7 shows the evolution of the GC at three different time instances. At the first two time instances shown in Figures 6.7a and 6.7b, the current is in the slumping phase and the Reynolds number defined with the front velocity is $Re_f \sim 100$. Observe that as the current propagates, the size of the bulk-shaped head reduces. However, very little mixing is taking place between the lock fluid and the ambient fluid. No KH billows were observed to be shed because the viscosity is too high to allow the growth of the KH instabilities. The current advances over a layer of light fluid that is comparatively much thicker than that observed in the simulations at $Gr \sim 10^9$. The ratio $\dot{V}_u / \dot{V}_o$ is close to 2% at $t=4t_0$, more than one order of magnitude higher when compared to case CL. Eventually, the size of the head diminishes to the point where the bulk-shaped head disappears. This corresponds to the transition to the viscous phase (as will be shown in Fig. 6.9, for the given conditions the current transitions directly to the viscous phase). The front of the current continues to propagate downstream with a velocity that decays with time. The shapes of the head region, observed during the slumping and viscous phases, are similar to the ones visualized experimentally for low-Reynolds-number GCs by Schmidt (1911) and reproduced by Simpson (1997). The small, jet-like 2D ejections of light fluid in Figures 6.7b and 6.7c are due to the unstable stratification between the layer of heavier fluid inside the GC and the bottom layer of lighter fluid that is overrun

by the current as it tries to rise. The instability is expected to be three-dimensional in reality.

6.3 Front Velocity

As in Chapter 5, the front velocity is calculated from the position of the front in the spanwise-averaged concentration contour plots. The bore position and associated bore velocity are difficult to directly estimate from the concentration contours (e.g., from Fig. 6.2) because the bore propagates into the stratified layer of fluid that corresponds to the body of the current. A more accurate way to determine the bore position is to plot the temporal evolution of the concentration on a line situated at a small distance (y/h=0.1) from the bottom. The C(x,t) plots are shown in Fig. 6.8 for cases CL and CH. In both plots a dark region in the form of a triangle is observed. The boundaries between the dark region and the remaining domain are marked with thick lines. The two lines that intersect at a small angle correspond to the front and bore trajectories. As these trajectories x=x(t) are close to straight lines, the front and bore velocities should be approximately constant until the position and time at which the intersection takes place (see arrow in Fig. 6.8). The slope of the lower line, which makes a smaller angle with the time axis, corresponds to the speed of the front while the slope of the top line corresponds to the speed of the reflected bore. Observe also that the top line cuts through an array of relatively dark streaks. These streaks correspond to the passage of KH billows over the y/h=0.1 line. The intersection of the two lines corresponds to the start of transition to the inviscid phase. In case CL, the coordinates of the intersection point are x_f/h~5.5, t~11.5t_0, while in case CH the coordinates are x_f/h~5.5, t~10t_0. The non-dimensional streamwise length, $l = \left(x_f - x_0\right)/x_0$, where x_f is the front position, is close to 8.8 in both cases. These values are consistent with experiments and theory (Rottman & Simpson, 1983).

Careful inspection of the slopes of the front and bore trajectories shows that both the front and bore velocities are slightly higher in the CH simulation. The increase of the

front velocity with the Grashof number during the slumping phase is consistent with the results obtained in Chapter 5 for infinite-volume lock exchange flows, where the GC remains indefinitely in the slumping phase. In the cases analyzed in this chapter, the front trajectory starts curving up and its slope with the time axis starts decaying once the bore catches the front (see Fig. 6.8 for $t>11t_0$). This corresponds to the expected decay in time of the front velocity during the inviscid phase.

The non-dimensional front, $Fr=U_f/u_b$, and bore, U_{bore}/u_b, velocities during the slumping phase that are inferred from Fig. 6.8 are 0.45 and 0.62 for case CL and 0.485 and 0.65 for case CH. The results for the other simulations (cases A, B, and D) are summarized in Table 6.3. It is interesting to notice that though the increase of the Grashof number between cases CL and CH produced a 6 to 7% increase in the front and bore velocities, their ratio remained practically unchanged at 1.35. In fact, the ratio changed only from 1.33 in case D to 1.36 in case A over a very wide range of Grashof numbers (10^5-10^{12}).

The values of Re_f are known from experiments for cases A, B and CL. As one can see in Table 6.2, the agreement with the values inferred from the simulations is excellent. The value of the aspect ratio, R, does not appear to have a large influence on the value of Fr. The smallest non-dimensional front velocity (Fr=0.37) is observed for case D when Re_f~98. The value of 0.485 obtained in case CH (Re_f~248,000) approaches the theoretical value (Fr=0.5) obtained by Benjamin (1968) and Shin et al. (2004) for full-depth lock-release inviscid currents during the slumping phase in which the dissipative losses at the bottom wall and mixing due to presence of interfacial billows are neglected. Keulegan (1958) measured a front speed Fr=0.48 at Reynolds numbers around 150,000.

Fig. 6.9 shows the temporal evolution of the front position in a log-log scale for cases CL, CH and D. For $t/t_0>2.5$, a region in which the slope is approximately constant and equal to one is present in all the cases. This is mainly due to the fact that the

buoyancy force at the front remains practically constant as long as the flow at the head of the GC, just behind the front, remains unmixed (C~1). This region in Fig. 6.9 corresponds to the slumping phase. Once the fluid just behind the front starts mixing, the density difference between this fluid and the ambient fluid on the other side of the front starts decaying. As a consequence the driving force decreases and the front starts decelerating. For cases CL and CH there is a change in the slope of the front trajectory between t=10-12t_0 (end of the slumping phase) and t~20t_0 (end of the transition to the inviscid phase). For t>20t_0 the slope in the log-log plot again becomes practically constant and equal to approximately 0.64 very close to the theoretical value of 2/3. This slope corresponds to a decay of the front velocity in time proportional to $t^{-1/3}$. The change in the slope, in case D, takes place faster. Similar to cases CL and CH, the front trajectory reaches again a constant slope after the end of the slumping phase. This slope, however, is equal to 1/5. It is equal to the expected theoretical value for the variation of the front position with time during the viscous phase (Rottman and Simpson, 1983) and corresponds to a velocity decay in time proportional to $t^{-4/5}$. The current transition in case D directly from the slumping phase into the viscous phase was expected, as the flow and geometrical parameters were set according to one of the experiments performed by Rottman and Simpson (1983) in which such a transition was observed to take place.

The front position at the end of the slumping phase is very close in the 2D and 3D simulations in cases A, B and CL, though always slightly behind in the 2D simulations (e.g., see Fig. 6.2j). This is consistent with the results observed for the infinite-volume lock-exchange flow at Gr=2.0×10^9 discussed in Chapter 5. Correspondingly, the values of Re_f in Table 6.2 are very close in the 2D and 3D simulations. Values from the 2D simulations are given in parenthesis in Table 6.2. During the inertial phase, however, the differences between the front positions in the 2D and 3D simulation increases as the coefficient in the power law decay is somewhat underpredicted in the 2D simulation. This results into a too-fast decay of the front velocity. For example, in case CL the

power law coefficient is close to 0.6 in the 2D simulation and close to 0.64 in 3D simulation. This produces greater differences between the front positions as the GC continues to propagate over the inertial phase. For example, at $t=25t_0$ (see Fig. 6.2m for case CL) the front is situated at $x/h=9.1$ in the 2D simulation and at $x/h=9.8$ in the 3D simulation. The underprediction of the front velocity by the 2D simulations is clearly a consequence of the fact that three-dimensional effects cannot be accounted for in these simulations. In fact, it is well known that the drag coefficient is overestimated in 2D simulations of the flow past a bluff body, including past a surface-mounted body, compared to both experiments and 3D simulations in which secondary instabilities in the spanwise direction can develop and lower the coherence of the eddies behind the body. One can idealize the present flow as corresponding to a bluff (nose shaped) body moving in a still fluid at a certain speed along the bottom boundary. The overestimation of the drag in the 2D simulations results in slower front velocities.

The simulation results are used to obtain more information on the GC evolution during the acceleration phase and the transition to the slumping phase. The position and velocity of the forward propagating front and backward propagating bore (before reflection at the end wall takes place) are plotted in Fig. 6.10 for cases CL and CH. The evolution is qualitatively very similar in both cases, except for the fact that the front moves slightly faster in case CH. For $t>3.5t_0$ the front velocity start oscillating around the mean value corresponding to the slumping phase. Up until $0.9t_0$, the bore and the front develop practically symmetrically with respect to the initial position of the lock gate ($x=x_0$). Then, the bore starts being influenced by the presence of the end wall and its velocity decays in a very similar way to the one it had accelerated for $t<0.9t_0$. Its velocity becomes equal to zero when the bore hits the end wall and is reflected. This happens around $t=1.85t_0$ in case CL and at $t\sim1.75t_0$ in case CH. At $t\sim0.9t_0$ the front velocity is slightly higher than the constant slumping phase value for both simulations. In fact, in case CH the front velocity continues to increase until $t\sim2t_0$, when it becomes equal to

$0.55u_b$, before decaying in a non-monotonic fashion toward the asymptotic value. This variation of the front velocity is similar to the one observed in the case of an infinite-volume lock-exchange flow discussed in Chapter 5 (the definition of the length scale h and thus of t_0 is different).

6.4 Analysis Of Near-Wall Flow Structures And Spatial Distribution Of The Wall-Shear Stress

High and low speed velocity streaks are expected to form very close to the bed, as the Reynolds number defined with the height of the current in the head region and the front velocity is above 5,000 in cases A, B, CL and CH both over the slumping phase and over the initial part of the self-similar phase. To investigate this, the streamwise velocity contours in a horizontal plane situated at y^+~11 from the bottom wall are plotted in Fig. 6.11b along with the out-of-plane vorticity contours on the bottom wall (two vertical vorticity levels of equal magnitude but of opposite sign are shown in Fig. 6.11a) for case B at t/t_0=5 during the slumping phase. To make the analysis of the structure of the near-wall flow relative to the position of the head of the current easier to follow, the concentration contours in an x-y plane at the same time instant are shown in Fig. 6.11c. A streaky structure is present in the vorticity contours over the entire length of the head region ($0.5<x/h<2.8$). These vorticity streaks are clearly associated with the high and low streamwise velocity streaks that develop in the immediate vicinity of the bottom wall, as observed by comparing the corresponding velocity and vorticity streaks in Figures 6.11a and 6.11b. The velocity streaks at that position (y^+~11) appear to extend only from the front position (x=2.8h) to x~1.3h. Between x=1.9h and x=0.5h, the variations in the streamwise velocity appear mostly to be associated with the presence of KH billows at the interface. These billows induce relatively large spanwise bands of low and high streamwise velocity and bed shear stress (see also discussion of Fig. 6.14). Observe, for example, the spanwise band of low streamwise velocity present at x~1.7h and the band of

high streamwise velocity at x~0.75h. As shown in Fig. 6.11a, streaks are present up to the rear of the head region but the additional velocity induced by the billows present in the interface region sometimes masks their presence in the streamwise velocity plot in Fig. 6.11b. Behind the head region, the streaks disappear because the local Reynolds number is decaying below values at which turbulent streaks can form or be maintained. The average width of these streaks is about 0.025h and their average length decays from about 0.8h near the front to about 0.5h toward the end of the streaky region. The streaks appear to be well resolved in the simulation of case B, given the grid density used in the spanwise direction. As discussed in Chapter 5, the presence of these streamwise velocity streaks is associated in channel flows with the legs of the hairpin like vortices that form over the near-bed region. These vortices can convect some of the near-bed fluid away from the bottom wall. Their presence also explains the streaky structure of the concentration field that is observed underneath the head of the GC (not shown).

As discussed in the introduction, prediction of the amount of sediment that compositional currents entrain during their propagation (e.g., each time a lock structure at a dam facility is operated) is extremely important in practical applications of GC flows in rivers and estuaries. This sediment is carried some distance in the form of a turbidity current before the sediment deposits again. To be able to estimate the scour produced by each passage of the current, information on the bed shear stress distribution at the different stages of its evolution is necessary. As in these applications the Grashof numbers of the compositional GCs are very high, information about the bed shear stress distributions obtained from numerical simulations at Grashof numbers as high as possible is of great interest. Additionally, information on the variation of these distributions over a range of Grashof numbers over which the GC is turbulent can serve to estimate scale effects.

Figures 6.12 to 6.15 compare the friction velocity distributions (u_τ/u_b) obtained in the CH and CL simulations at t/t_0=2, 4, 8 and 16, respectively. The position and shape of

the GC is also shown using spanwise-averaged concentration contours. The number of mesh points in the spanwise direction in the CL simulation is sufficient to accurately capture the streamwise velocity streaks. This is not the case in the CH simulation in which one expects that the real streaks will be thinner than the spanwise grid size used in the simulation. Still, while acknowledging this limitation, it is expected that valuable qualitative and even quantitative information on Grashof number effects will be obtained. The variation of the spanwise-averaged friction velocity in the streamwise direction (solid line) is shown in Figures 6.16 and 6.17 for cases CL and CH, respectively. In both figures, the variation of the friction velocity in a plane z=constant is also shown (dashed line) to get a better idea on the spanwise variability of the distribution of u_τ. Additionally, for case CL (Fig. 6.15) the u_τ/u_b distribution obtained from a 2D simulation is plotted to quantify the limitations of 2D simulations related to the prediction of this quantity. Observe that the values u_τ/u_b are smaller in the CH simulation by about 50% compared to case CL. This is due to the fact that u_τ is proportional to $Gr^{-1/4}$. In fact, the values of the velocity gradients at the bed are much higher in the CH simulation.

At $t=2t_0$, toward the end of the acceleration phase, the overall shape of the GC in both simulations is similar and the flow is close to 2D. The same is true for the distribution of u_τ/u_b which shows no variation in the spanwise direction, except inside the relatively narrow band starting at the front, where streamwise streaks of large u_τ values are observed. In the CL simulation, they are clearly delimited and followed by a short region of low u_τ values over the whole span, while, in the CH simulation, the streaks are thinner, more closely spaced and there is no region of relatively low friction velocity behind them. Overall, u_τ is more uniform inside the streaky region that extends between x/h=0.9 and x/h=1.5 in the CH simulation.

By $t=4t_0$, at the start of the slumping phase, the region of high values of u_τ has grown in both simulations. In the CL simulation (Fig. 6.13b), the streaks near the front became more irregular, their length and width has grown, and their number has decreased

from 22 to about 11. The positions of these patches of high u_τ values appear to correlate with that of the primary and secondary lobes forming at the front. Thin streaks of relatively high friction velocity, that correspond to the high speed streaks above the bed are observed between x/h=1.1 and x/h=1.7. Additionally, a spanwise band, inside which the values of u_τ are comparable to those observed at the front of the current, is present around x/h=0.4. The large values are induced by the quasi 2D KH billows present around x/h~0.4. The other narrow band around x/h=1.1 where the values of u_τ are relatively high, is also due to the presence of a large billow in the interface region.

In the CH simulation (Fig. 6.13a), the spatial distribution of u_τ beneath the head of the GC is somewhat different. The main differences are observed between x/h=1.25 and x/h=2.5 (front) where the individual streaks of high u_τ values are hardly recognizable. Consequently, the average value of the spanwise averaged friction velocity does not vary much over this region, as observed in Fig. 6.17b. Supposing that the mean values in this region are above the threshold value for sediment entrainment, the amount of sediment entrained by a GC that has the structure observed in the CH simulation will be larger than that of a GC that develops similarly to the current in the CL simulation. The two spanwise bands of large u_τ values at x/h~1.1 and x/h~0.5 are also associated with the presence of large billows some distance away from the bed.

Fig. 6.14 compares the distributions of u_τ at t=8t_0, near the end of the slumping phase. In the CL simulation (Fig. 6.14b), the region containing the streaks of high u_τ values behind the front has enlarged to 1.4h from 0.9h at t=4t_0. The only other region where relatively high u_τ values are observed is around x/h=1.7, behind the KH billows centered at x/h=2.2. The fact that the position of the spanwise band of high u_τ values does not correspond exactly to the one of the billows can be surprising, at first. In fact, inspection of several frames has shown that in most cases a band of large u_τ values is present between two KH billows in the interface region. The same phenomenon is observed in Fig. 6.14a for case CH. Indeed, if one looks at the streamline patterns in a

system of reference translating with the front velocity (second frame in Fig. 6.14a), one observes that the regions of high u_τ values at x/h~1.75 and x/h~3.0 are situated beneath a vortex whose center is close to the bottom surface, while the billows educed using concentration contours are centered around x/h=2.2 and x/h=2.8.

In the CH simulation, large values of u_τ, comparable to the ones observed in the same simulation at earlier times, are observed between x/h=1.7 and x/h=4.4 (front). The spanwise bands of high u_τ values are still present but, in many cases, they no longer extend over the whole width of the domain (e.g., x/h~2.2). Their axis is deformed in the z direction (x/h~2.9), consistent with the structure of the large-scale vortices in the interface region. The relatively uniform region of high u_τ values behind the front is still present and its length is approximately the same as at t/t_0=4. The total surface over which large values of the friction velocity are observed is much larger than the corresponding one in the CL simulation and somewhat larger than the one observed in the same CH simulation at the start of the slumping phase.

Fig. 6.15 shows the distributions of u_τ/u_b during the inertial phase at t=16t_0 when the front velocity and the local Reynolds number have decayed to less than 50% of their values during the slumping phase. This should have a larger influence on the CL simulation where the local Reynolds number behind the front region comes close to, or is lower than, the one at which turbulence can be sustained in the near wall region. Indeed, the only region where the values of u_τ are comparable to the largest levels observed during the slumping phase are situated behind the front and over a part of the spanwise band centered at x/h=4.9 that forms between two KH billows situated at 4.4h and 5.7h (Fig. 6.15b). In case CH, though the levels of u_τ have dropped over most of the GC, they remain relatively high especially between x/h=5 and x/h=7.8 (front). Spanwise bands of high u_τ values are normally situated in between the KH billows (e.g., compare the bands centered around x/h=4, x/h=5.4 and x/h=6.2 in the u_τ/u_b plot with the position of the billows observed in the concentration plot in Fig. 6.15a). The flow over the head and

over most of the tail region remains turbulent, consistent with the low wavelength oscillations observed in the friction velocity distribution.

The spanwise averaged plots of u_τ/u_b in Figures 6.16 and 6.17 serve to quantify the differences in the spatial and temporal evolution of the bed-friction velocity between the CL and CH simulations. In the CL simulation the largest values of u_τ/u_b are close to 0.04. If one arbitrarily defines a threshold value for sediment entrainment to occur at values larger than half of this value, then one can see that the length of the region which cannot entrain sediment behind the front of the current increases from about $0.2h$ at $t=4t_0$ to $1.3h$ at $t=8t_0$ and to $4.5h$ at $t=16t_0$. In case CH the largest values of u_τ/u_b are close to 0.02. Assuming the threshold value is 0.01 then, compared to case CL, the length of the region that cannot entrain sediment is smaller during the inviscid phase ($3.2h$ at $t=16t_0$) and the total length of the regions that can entrain sediment is higher beginning with the slumping phase (e.g., $3h$ in case CH compared to $2.5h$ in case CL at $t=8t_0$ and $4.3h$ in case CH compared to $2.5h$ in case CL at $t=16t_0$).

The instantaneous values of u_τ/u_b in a z=constant plane show that the amplitude of the fluctuations around the spanwise-averaged values are generally smaller in the CH simulation compared to the CL simulation. This is especially so in the head region, which is consistent with the greater homogeneity of the u_τ distribution in the spanwise direction. Finally, the distribution of u_τ/u_b obtained from a 2D simulation of case CL appears to correlate poorly with the spanwise-averaged distribution obtained from the 3D solution. The main reason for this is the presence of strongly coherent billows at the top of the head region and over the tail (e.g., see Fig. 6.2m) that strongly modify the bed-shear stress distribution in the streamwise direction.

6.5 Energy Budget

The variation in time of the total kinetic energy, E_k, total potential energy, E_p, and the time integral of the total dissipation, E_d, are shown in Fig. 6.18 in linear-linear, log-

log and linear-log scales. The exact definition of these quantities is given in Chapter 5. The main difference between the present simulations and the ones discussed in Chapter 5 is that in the present simulations the total potential energy is finite due to the finite volume of the initial lock fluid (assuming C=0 for the ambient fluid). The three terms are integrated over the volume of the computational domain and non-dimensionalized with the initial value of the total (potential) energy.

As observed from Figures 6.18a and 6.18b, during the initial phases of the formation of the current, before the backward propagating bore starts interacting with the end wall, the flow associated with the formation of the bore and of the bottom propagating GC is essentially inviscid and characterized by a fast decay of the potential energy which is converted into kinetic energy (see also Fig. 6.19a for $t<1.8t_0$). The motion starts from rest and the velocity increase in time is close to linear (constant acceleration). This translates into an increase of the total kinetic energy with time proportional to t^2 for $t<1.8t_0$ independent of the value of the Grashof number, as shown in Fig. 6.18b where the slope of the straight line approximating the variation of E_k in both simulations is equal to two. The maximum value of E_k is reached around t/t_0=2. By that time about 61% of the initial potential energy was essentially converted into kinetic energy (59%). The difference is due to the dissipative losses. The increase of E_d in the CL simulation appears to be proportional to $t^{2.36}$ as shown in Fig. 6.18b. In the CH simulation, the initial increase is similar but then, starting at $t\sim0.6t_0$, the slope increases sharply, such that by $t=1.2t_0$ the values of E_d in the two simulations are practically identical. The temporal decrease of the potential energy and the associated increase of the kinetic energy between $0.7t_0$ and $3t_0$ are logarithmic as clearly observed from Fig. 6.18c, where these variables are plotted in the linear-log coordinates.

Most of the differences between the energy balance in the CL and CH simulations occur during the slumping phase, as observed in Fig. 6.18a. The increase in E_d is larger in case CL and, conversely, the decay of E_k is smaller such that, by the end of the

slumping phase (t~10-11t_0), the difference between the corresponding values of these two components of the energy budget is about 6-8% of the total initial energy. Meanwhile, the variation of the potential energy appears to be very similar in both simulations. Finally, the decay rates of the kinetic energy, potential energy and total dissipation are just slightly dependent of the Grashof number once the current starts transitioning toward the inviscid phase, as observed from comparing the CL and CH curves in Fig. 6.18 for t>11t_0. The difference in the energy balance over the slumping phase translates into values of E_d and E_k in the CL simulation (Fig. 6.18a) which are consistently 6-8% higher and, respectively, smaller compared to those observed in the CH simulation. However, the shape of the curves showing the variation of E_k and E_d are very similar. The levels of E_p in the two simulations are very similar over the inviscid phase, though they are slightly higher (by about 1%) at most time instances in the CH simulation.

By t=7t_0 during the final stages of the slumping phase, after the kinetic energy reached its peak and started decaying because of the strong increase in the dissipative losses, the variation of all the three components of the integral energy budget becomes logarithmic (see Fig. 6.18c). The temporal variation of the three components is very well approximated by lines of constant slope in the highly resolved CL simulation. The functions that approximate the variation of the three components for t>7t_0 are:

$$E_p/E_{p0} = 0.53\text{-}0.10ln(t/t_0) \quad (6.1)$$

$$E_k/E_{p0} = 0.85\text{-}0.19ln(t/t_0) \quad (6.2)$$

$$E_d/E_{p0} = -0.38+0.29ln(t/t_0) \quad (6.3)$$

The temporal evolution of the viscous (ε_0) and SGS (ε_t) components of the total dissipation rate (ε) in Fig. 6.20 show, as expected, that in the CH simulation, where (over the simulated time period) the flow remains strongly turbulent inside the head and tail of the gravity current, the $\varepsilon_t/\varepsilon$ ratio is around 85% to 90% for t>7t_0. In the CL simulation, however, the maximum in the $\varepsilon_t/\varepsilon$ ratio is 35% at t~6t_0 when both the viscous and SGS components peak. The ratio in the CL simulation then decays, as the current continues to

propagate in the slumping and inviscid phases (e.g., $\varepsilon_t/\varepsilon$=25% at t=16t_0). Interestingly though, the relative contributions of the viscous and SGS components in the two simulations are very different. The temporal variation of the total dissipation rate after the current finishes its transition to the slumping phase (t~20t_0) are very similar for both simulations.

6.6 Spatial Distribution Of The Dissipation

Figures 6.21 and 6.22 show the horizontal and vertical distributions of the local dissipation rate integrated over x=constant and y=constant planes, respectively. The mathematical definitions of $\varepsilon^{23}, \varepsilon^{13}$ and their SGS components ε_t^{23} , ε_t^{13} are given in Chapter 5. The distributions are shown at t/t_0=2, 4, 8 and 16. The horizontal distribution of ε^{23} in Fig. 6.21 helps to understand over which region of the GC most of the dissipative losses occur at the different stages of its evolution. For example, having information on the split between the dissipative losses in the head and tail regions is important for validating or calibrating simpler integral or theoretical models.

At t=4t_0 (start of the slumping phase), the dissipation in the tail region (x/h<1.2) is larger in the CL simulation. The same observation applies when comparing the two distributions at t=8t_0 toward the end of the slumping phase when the tail starts at x/h~2.9 in both simulations. The overall difference is much smaller over the head region, though the total dissipation is slightly larger in the CL case. Thus, the difference in the integral of the total dissipation E_d that builds over the slumping phase between the two simulations (Fig. 6.18a) is due primarily to the larger dissipation over the tail region in the CL simulation. As the GC transitions toward the inviscid phase (e.g., compare streamwise distributions at t/t_0=16), the variations of E_d over the head and tail regions in the two simulations are similar both qualitatively and quantitatively. This is consistent with the fact that, as shown in Fig. 6.19, the total dissipation rate ($\varepsilon = \int^{L_1} \varepsilon^{23}(x_1)dx_1$) in the two simulations are very close for t>10t_0. Though the streamwise distributions of ε^{23}

are very close, the contribution of the SGS component (dashed line in Fig. 6.21) is quite different in the two simulations. In the CH simulation, the SGS component accounts for more than 80% of the total dissipation over practically the entire length of the GC. This is true even at $t=16t_0$ during the inviscid phase. The total and SGS dissipation rate become very small in the two simulations for $x/h<3$ at $t/t_0=16$ suggesting that the flow relaminarizes in that region. Observe also that especially in the CL simulation the values of ε^{23} during the slumping phase are large starting immediately behind the front. This is due mostly to the dissipation inside the thin shear layers that define the front and to the near-bed dissipation. The values of the local dissipation rate inside the region just behind the front (energy-conserving head) are relatively low.

The vertical distribution of ε^{13} (Fig. 6.22) during the acceleration phase ($t/t_0=2$) is similar in the two simulations, with most of the dissipation occurring between $y/h=0.25$ and 0.65. The only difference is the amount of dissipation in the near bed region ($y/h<0.05$), which is close to 23% of the total dissipation ε in the CL simulation and only 5% in the CH simulation. Though the maximum values over the near-bed region are comparable, the thickness of the near bed region where ε^{13} is high is larger in the CL simulation due to the increased thickness of the boundary layer on the bottom wall. The relative amount dissipated in the near bed region increases as the current transitions into the slumping phase. The values at $t/t_0=4$ are 31% and 8% for cases CL and CH, respectively. By $t/t_0=4$, large billows are already present behind the head. This explains why the vertical coordinate where the maximum of ε^{13} outside the bed region occurs is lower in both simulations at $t/t_0=4$. During the end of the slumping phase ($t/t_0=8$) the tail becomes more homogeneous and, as observed in the discussion of Fig. 6.21, contributes the largest amount to the total dissipation. Most of the large-scale structures in the tail region are situated at distances of 0.3-0.35h from the bed which also corresponds to the position of the maximum of ε^{13} in Fig. 6.22 at $t/t_0=8$.

As the energetic structures that populate the tail get closer to the bed for t/t_0>8, a clear distinction between the near bed region and the region where most of the dissipation is due to the large-scale interfacial structures and their interaction with 3D flow instabilities cannot be made, especially for the CH simulation. In the CL simulation the contribution of the near-bed region decreases from 15% at t/t_0=8 to 11% at t/t_0=16. The total dissipation rate starts decaying as the current transitions to the inviscid phase. This is also observed by comparing the values of $\varepsilon^{13}(y)$ at practically all levels between t/t_0=8 and t/t_0=16. The position of the maximum is situated closer to the bed as the height of the head starts decaying and as the region where most of the dissipation occurs in the tail moves closer to the bed. In the CL simulation, the SGS component, ε_t^{13}, makes a significant contribution to ε^{13} (~30-40%) in the regions where the KH billows and the other large-scale structures are deformed and stretched by the small scale turbulent eddies.

As also shown for the simulations discussed in Chapter 5, most of the dissipation in the near bed region is due to the streamwise velocity gradients in the vertical direction. The contribution of the dissipation term ε_{12}^{13} containing these velocity gradients is shown with the dashed-dotted line in Fig. 6.22. Indeed, in the near-bed region ε_{12}^{13} is found to be very close to ε^{13} in both simulations.

6.7 Spectral Content Of The Flow

The time histories of the instantaneous, spanwise velocity component and scalar concentration are plotted in Fig. 6.23 at several stations situated at 0.2h from the bed in a z=constant plane and at x/h=0.7, 2.0, 5.0 and 9.0 for the CL simulation. The intensity of the turbulent fluctuations (e.g., spanwise fluctuations are shown in Fig. 6.23), as the current reaches a certain section, remains low over the time period when the "energy conserving" head region that contains unmixed lock fluid (C=1) propagates over that streamwise location. The intensity of the fluctuations increases sharply afterwards in the

dissipative wake and tail regions containing mixed fluid (C <1). This can be observed by comparing the spanwise velocity and concentration time series for case CL at x/h=0.7 and x/h=2.0 which are close enough to the gate release position (x_0/h=0.57) such that C =1 behind the front at y/h=0.2. By the time the current reaches the section at x/h=5, no unmixed lock fluid (C =1) is present at a distance of y/h=0.2 from the bed and the level of the spanwise fluctuations is high from the moment the front of the GC reaches the section.

Fig. 6.24 shows the spanwise velocity power spectra in the CL simulation for the four stations (y/h=0.2). No inertial range is present in the velocity spectrum at x/h=0.7 in the range of energetic frequencies (St=0.5 to 10) observed in the corresponding time series. However, at the third station (x/h=5.0) an inertial range appears to develop for $0.5<St<6$ over which the energy decay is close to two decades. The same is true for the spectrum at the last station (x/h=9).

6.8 Summary

Evolution of Boussinesq gravity currents formed in a finite-volume lock-release flow was studied using 3D LES simulations at Grashof / Reynolds numbers sensibly higher than those previously attempted using 3D DNS (Gr=10^6-10^7) and for longer simulation times. This allowed the study of the flow physics during part of the inviscid phase. Highly resolved 3D simulations were carried out for Grashof numbers in the range of 10^9-10^{10}. An additional simulation was carried out at Gr=10^{12} on a mesh comparable to the one used in the simulations at Gr~10^9-10^{10}. The main reason to perform the simulation at Gr=10^{12} was to understand the evolution and structure of finite-volume lock-exchange flows at flow conditions closer to the ones encountered in most of the applications of practical interest. In the simulation conducted at Gr=10^{12}, the GC is expected to be closer to the inviscid state that is often assumed in theoretical models that are used to describe different characteristics of high Grashof number GCs.

Previous 3D highly resolved simulations considered only the case of an infinite channel (no lateral wall) compositional current (Hartel et al., 2000) where the self-similar inviscid phase is not present and the case of a particulate current developing in a finite channel (Necker et al., 2002, 2005) where the physics in the latter stages of evolution of the current is very different from that of a compositional current due to the deposition of the particles. In these previous simulations the values of the Grashof numbers were around 10^6-10^7, corresponding to Reynolds numbers defined with the front velocity of less than 1,000, about an order of magnitude lower than the ones considered in the present study.

The model was found to successfully capture most of the global parameters characterizing the evolution of the finite-volume lock-exchange currents. Their structure was found to be similar to the one observed in the experiments of Hacker et al. (1996) and Rottman & Simpson (1983). The dynamics and evolution of the GC in the simulation with Gr=10^{12} were found to be realistic and consistent with the expected behavior predicted by experiments and theory (e.g., the non-dimensional front velocity was found to be very close to the theoretical value for inviscid currents predicted by Benjamin, 1968 and Shin et al., 2004). This is due in great part to the use of a dynamic SGS model, which is much less dissipative than the constant coefficient version. Thus, its use should result in more accurate predictions, especially at very high Grashof and/or Schmidt numbers where the LES model plays an important role. The other reasons are the use of a discrete energy-conserving Navier-Stokes non-dissipative solver that enabled obtaining robust and accurate solutions on meshes that are much coarser than DNS requirements, and the use of a mesh in the wall normal direction that was fine enough to avoid the use of wall functions.

Several configurations, with different depth over length ratios of the initial lock fluid, were considered, corresponding to the cases studied experimentally by Hacker et al. (1996). The 3D simulations successfully captured the development of the lobe-and-cleft

structure at the leading edge of the current head, the shedding of the KH billows from the front region and their subsequent deformation, stretching and breaking into small scale 3D structures that strongly enhanced the mixing at the interface between the GC and the surrounding fluid. The simulation results were able to accurately replicate the observed evolution of the nose region and stratification within the tail, the ratio between the bore and front velocities over the slumping phase, the variation of the front speed over the slumping ($U_f \sim t_0$) and self-similar ($U_f \sim t^{-1/3}$) phases, the position of the transition between these two phases and the dependence of the lobe size on the front Reynolds number. The topology of the flow in the front region did not change significantly as the current transitioned between the slumping phase and the self-similar phase and was found to be similar to the one observed in 3D DNS simulations at lower Reynolds numbers (Hartel et al., 2000). Additionally, a 2D simulation of a low Grashof number current ($Gr=2.8\times10^5$) was found to directly transition from the slumping into the viscous phase where the front speed decayed at a rate proportional to $t^{-1/5}$, consistent with experiment and theory (Rottman & Simpson, 1983).

High and low speed velocity streaks associated with the presence of hairpin vortices, similar to the ones observed in turbulent flow over no-slip surfaces, were identified in the near-bed region beneath the head of the GC. As the turbulence started decaying in the tail and the flow transitioned back to a laminar regime behind the current, the streaky structure was found to disappear. Details of the distribution of the friction velocity on the bottom wall were investigated at different stages of the evolution of the GC. This is important especially for applications of lock exchange flows in rivers and estuaries with loose beds, where the bed-shear stress distribution controls sediment entrainment. Scale effects were considered by comparing the friction velocity distributions between the simulations at $Gr=2.3\times10^9$ and $Gr=10^{12}$. In both simulations, a streaky distribution of u_τ was observed to occur over the upstream part of the head region. The streaks were observed to diminish and to produce a more uniform overall

distribution of u_τ behind the front in the simulation at Gr=10^{12}. Several spanwise bands of high and low u_τ values were observed to form behind the front region. Their position is related to the large-scale billows present in the interface region. The size of the regions where u_τ remained high was found to be comparatively larger in the simulation at Gr=10^{12}, especially in the later stages of the evolution of the current. This means that the higher Grashof number GC will be more effective in entraining sediment from the bed.

It was also shown that 2D simulations slightly underpredict the coefficient in the power-decay law of the front velocity over the inviscid phase. This is because 3D instabilities cannot develop, which results in a too high coherence of the KH billows. This results in substantial differences of the front positions between 2D and 3D simulations during the later stages of the inviscid phase. The large coherence of the KH billows was also the main reason why the bed-shear-stress distribution predicted by the 2D simulation at Gr=2.3×10^9 was found to be very different than the one observed in the corresponding 3D simulation.

Comparison of the energy balance between the simulations at Gr=2.3×10^9 and Gr=10^{12} showed that the main difference occurred over the slumping phase, when the total dissipation rate was larger in the lower Grashof number simulation. It was also observed that starting toward the end of the slumping phase, the temporal variations of the total kinetic energy, total potential energy and the integral of the total dissipation rate are logarithmic. Investigation of the streamwise distribution of the local dissipation rate integrated over x=constant planes showed that the main difference between the two simulations occurred over the slumping phase when the dissipation rate in the tail region was larger in the Gr=2.3×10^9 simulation. The vertical distribution of the local dissipation rate integrated over y=constant planes showed that in the Gr=10^{12} simulation the contribution of the near bed region is very small compared to the dissipation occurring in the tail and head regions over both the slumping and inviscid phases. Finally, an inertial range was observed to develop in the velocity spectra in the Gr=2.3×10^9 simulation at

stations situated far enough from the initial lock gate position. This confirms that the turbulence characteristics of the flow inside GCs at high enough Reynolds numbers are similar to the ones present in classical constant-density turbulent boundary layers and channel flows.

Table 6.1. Details of the finite-volume lock-exchange simulations during the slumping phase.

Case	Gr	$\mathrm{Re}=\sqrt{Gr}$	L/h	Aspect ratio, $R=h/x_0$
A	9.6×10^{8}	30,980	18	0.67
B	7.7×10^{9}	87,750	9	1.00
CL	2.3×10^{9}	47,750	13.483	1.78
CH	1.0×10^{12}	1.0×10^{6}	13.483	1.78
D	2.8×10^{5}	530	18	1.00

Table 6.2. Summary of simulation results.

Case	Experiment		Simulation (2D in brackets)		Transition (2D in brackets)		
	$\mathrm{Re_f}$	Fr	$\mathrm{Re_f}$	Fr	Location, x/h	Time, t/t_0	$l=(x_f-x_0)/x_0$
A	7,000	0.45±0.01	6,890 (6,820)	0.44	9.9 (10.4)	9.7 (10.2)	5.6 (5.9)
B	19,700	0.45±0.01	19,750 (19,730)	0.45	-	-	
CL	11,000	0.46±0.01	10,875 (10,755)	0.45	5.5 (5.9)	11.5 (12.5)	8.8 (9.5)
CH			248,000	0.49	5.5	10.0	8.8
D			98	0.37	(10.1)	(27.4)	(10.1)

Table 6.3. Comparison of bore and front velocities during slumping phase for simulations in channels with a lateral wall.

Case	$U_{bore}/\sqrt{g'h}$	$U_f/\sqrt{g'h}$	U_{bore}/U_f
A	0.60	0.44	1.36
B	0.61	0.45	1.35
CL	0.62	0.45	1.35
CH	0.65	0.48	1.35
D	0.49	0.37	1.33

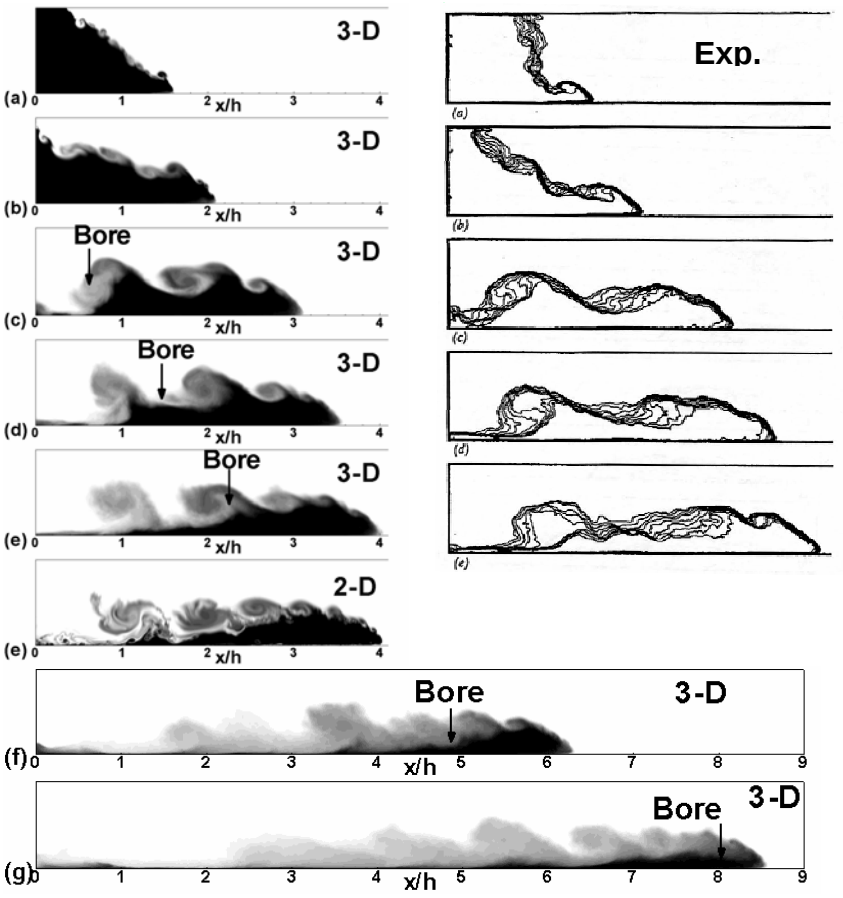

Figure 6.1. Concentration contours showing temporal evolution of gravity current for case B: 3D spanwise averaged (left); experimental results of Hacker et al. (right). a) t/t_0=1.4; b) t/t_0=2.4; c) t/t_0=4.6; d) t/t_0=5.6; e) t/t_0=6.6; f) t/t_0=11.6; g) t/t_0=16.6.

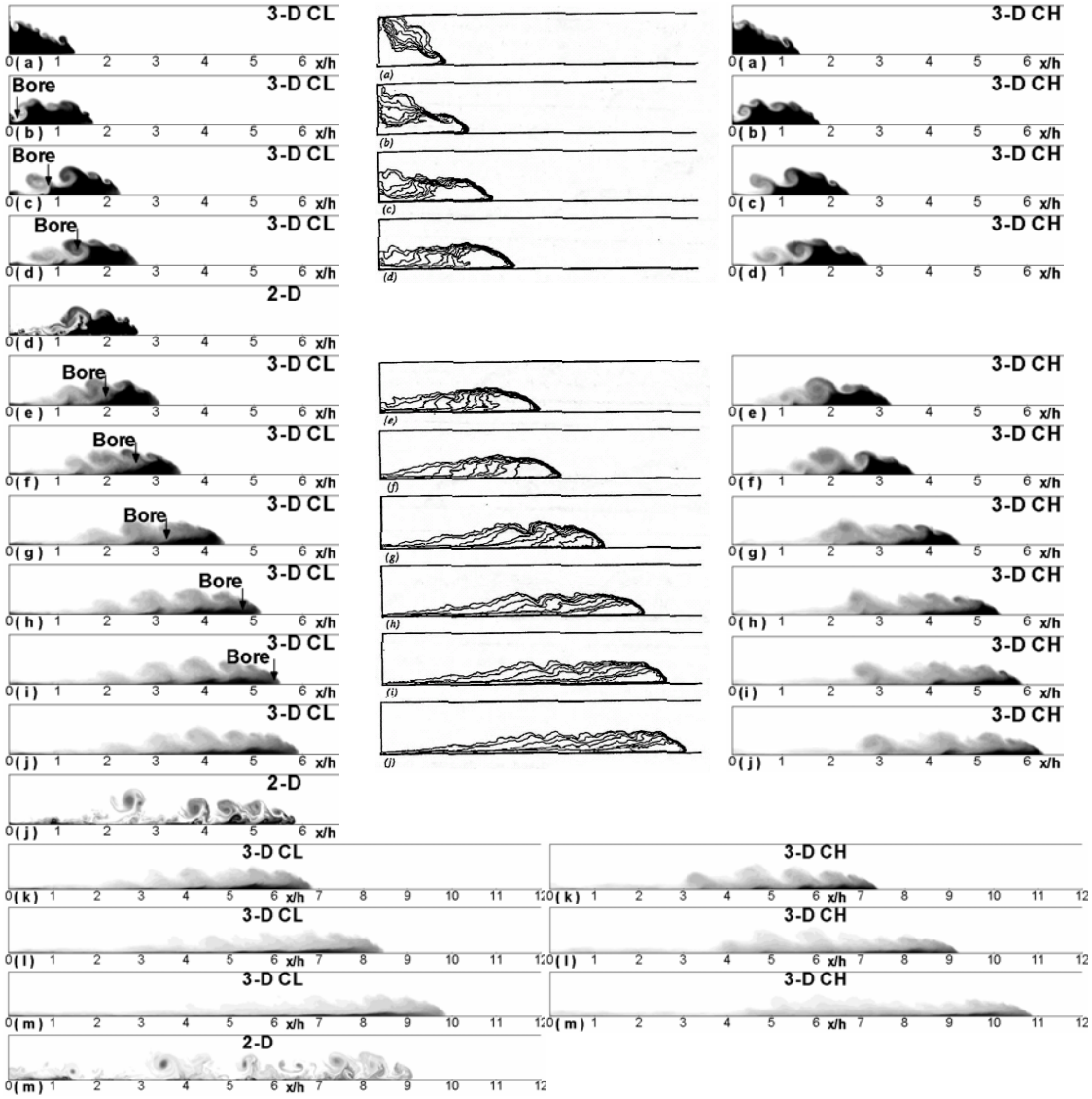

Figure 6.2. Concentration contours showing temporal evolution of gravity current for cases CL and CH: 3D spanwise averaged for case CL (left); experimental results of Hacker et al. for case CL (middle); 3D spanwise averaged for case CH (right). a) t/t_0=1.7; b) t/t_0=2.7; c) t/t_0=3.7; d) t/t_0=4.6; e) t/t_0=5.6; f) t/t_0=6.6; g) t/t_0=8.6; h) t/t_0=10.4; i) t/t_0=11.6; j) t/t_0=12.4; k) t/t_0=15.0; l) t/t_0=20.0; m) t/t_0=25.0.

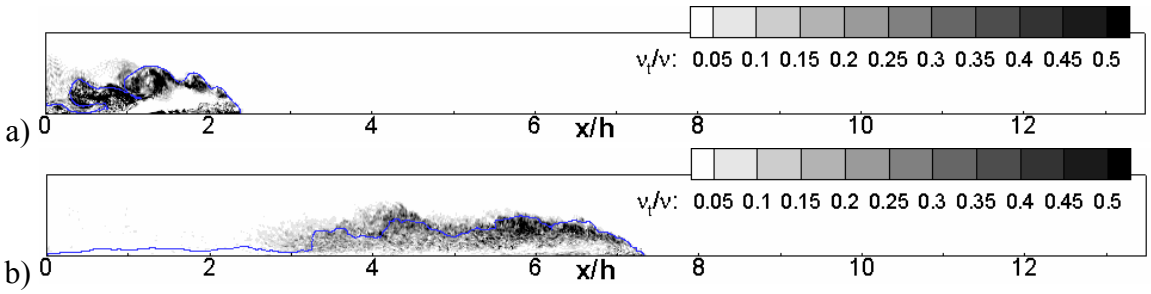

Figure 6.3. Visualization of the spanwise-averaged instantaneous ratio of SGS viscosity to kinematic viscosity in case CL. a) t/t_0=4.0; b) t/t_0=16.0.

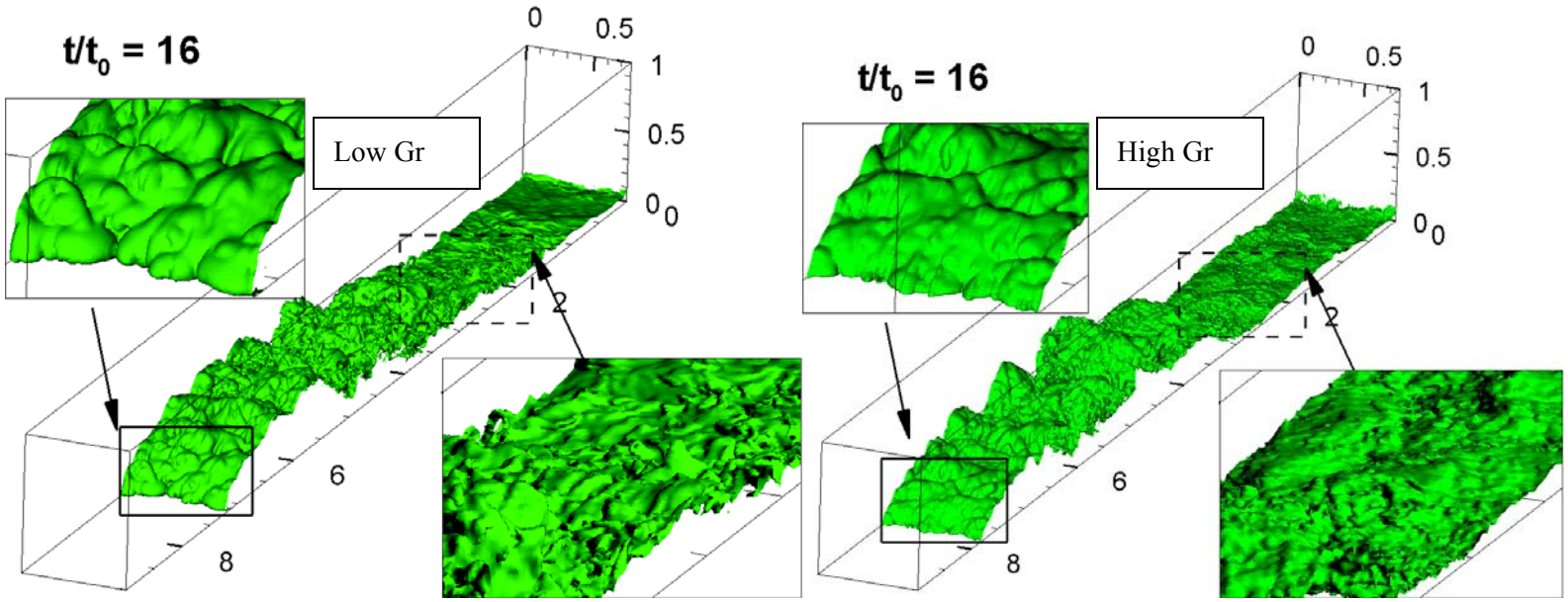

Figure 6.4. Visualization of gravity current interface using a concentration isosurface (C = 0.5) for 3D simulations of cases CL (left) and CH (right) with insets showing development of the lobe and cleft structures at the front and decay of turbulence behind the current at t/t_0=15.0.

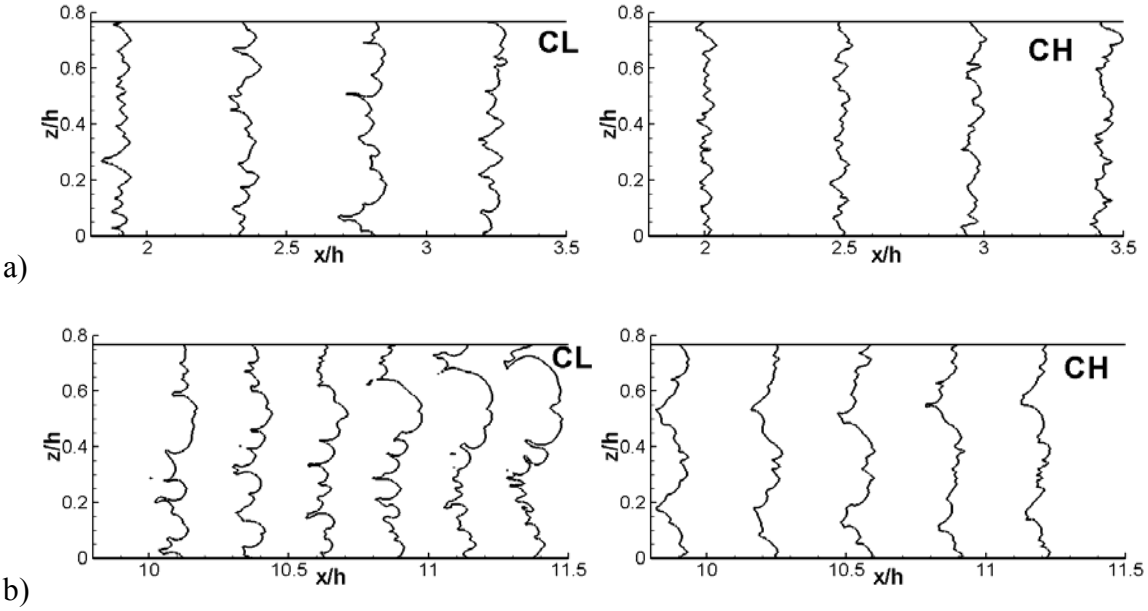

Figure 6.5. Visualization of the development of the lobe and cleft instability for cases CL (left) and CH (right) in the x-z plane situated at a distance of y/h=0.016 from the bottom wall. Consecutive lines indicate front position at a time interval of $\Delta t/t_0$= 1. a) during slumping phase starting at t/t_0=3; b) during inviscid phase starting at t/t_0=26.

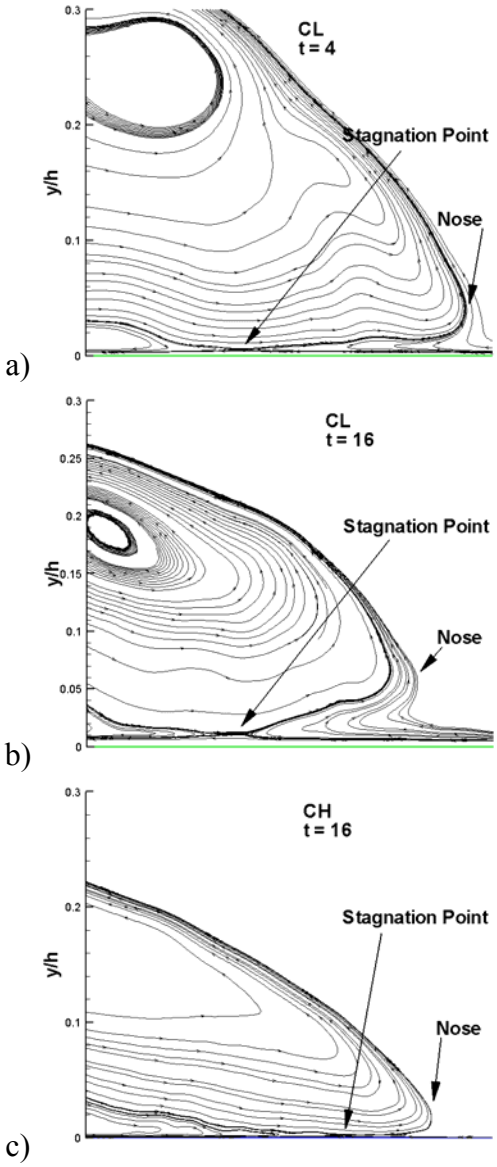

Figure 6.6. Visualization of the spanwise-averaged flow topology in the nose region using streamlines in a frame of reference translating with the front velocity. a) CL simulation during slumping phase; b) CL simulation during inviscid phase (t/t_0=16); c) CH simulation during inviscid phase (t/t_0=16).

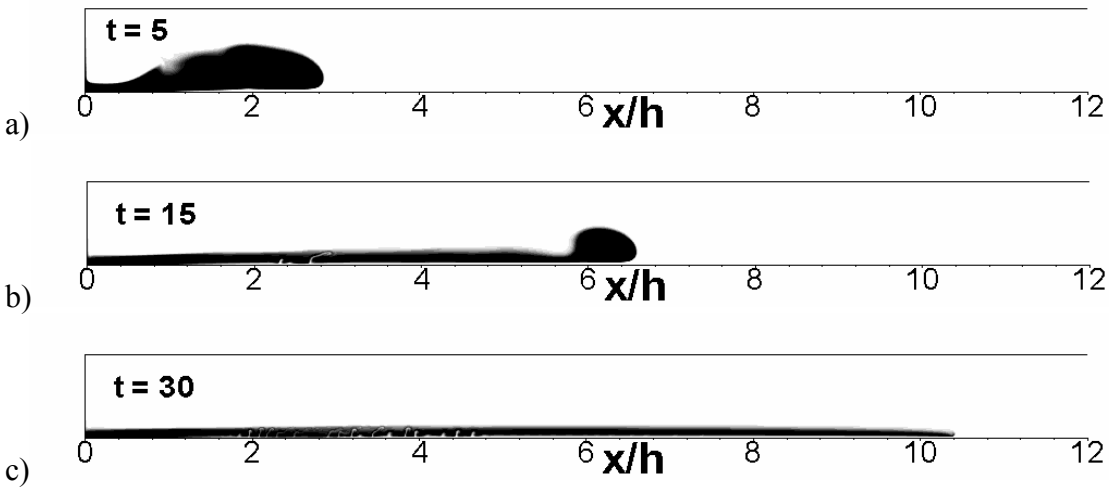

Figure 6.7. Concentration contours showing temporal evolution of gravity current for case D. a) t/t_0=5.0; b) t/t_0=15.0; c) t/t_0=30.0.

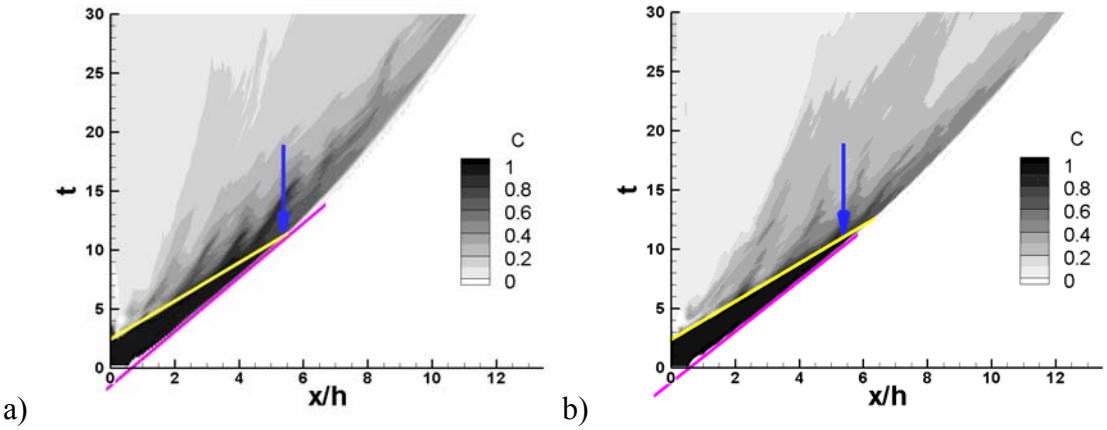

Figure 6.8. Evolution of concentration with time along the *x* axis. Distance from the bottom wall is *y/h* = 0.1. a) case CL b) case CH.

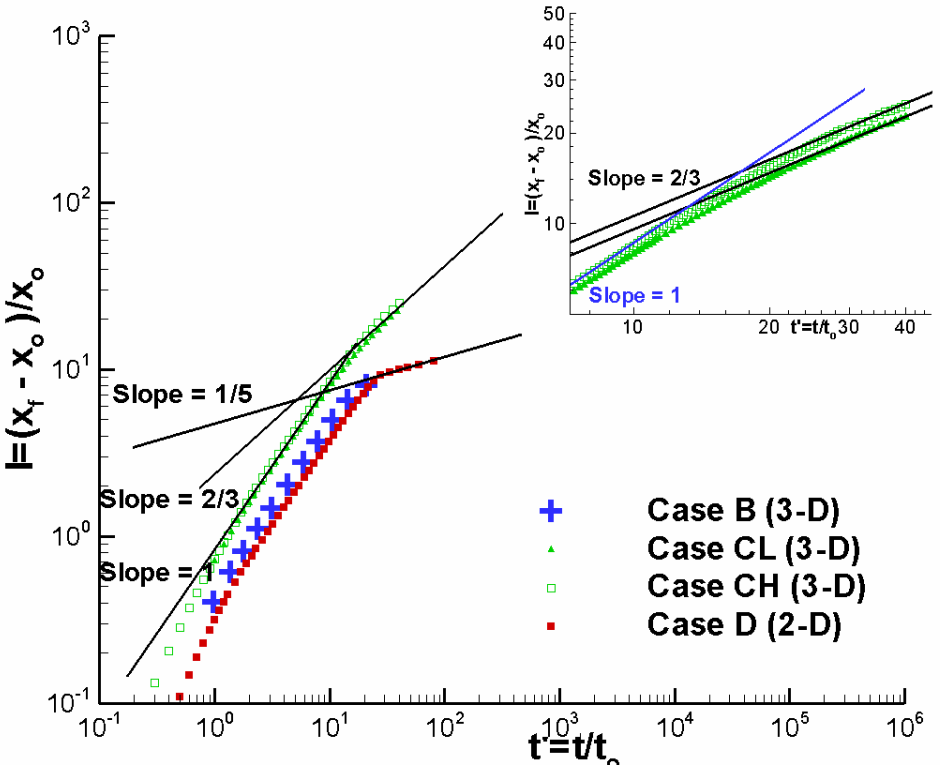

Figure 6.9. Evolution of the non-dimensional front position with time in log-log scale.

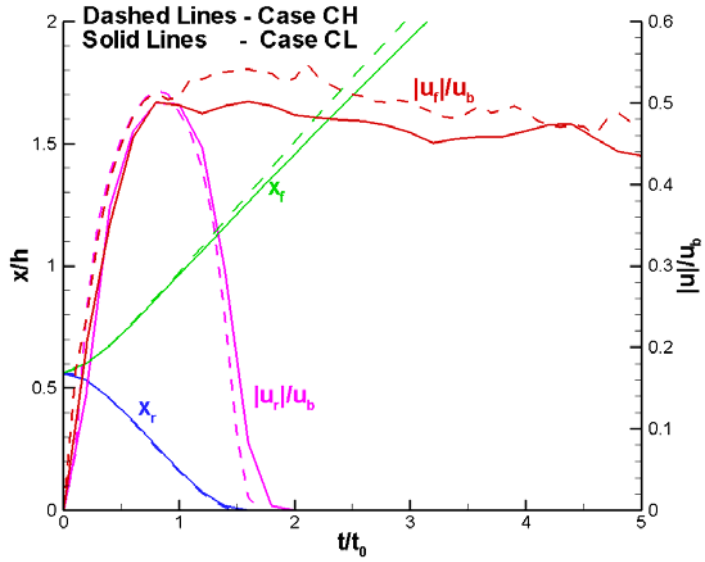

Figure 6.10. Evolution of the front and bore positions and velocities for cases CL and CH during the initial phases of motion.

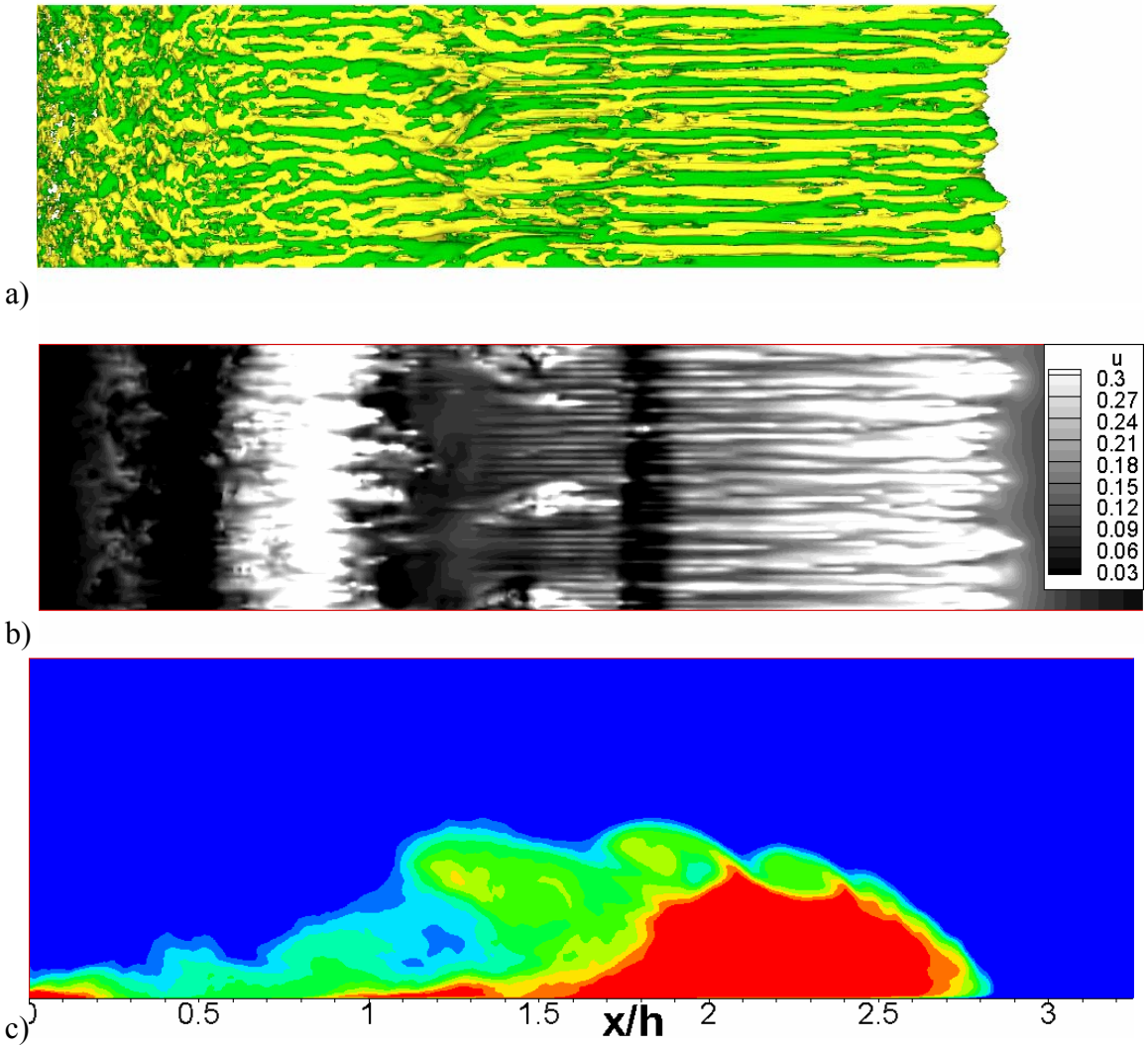

Figure 6.11. Visualization of the flow structure in the near wall region at t/t_0=5 for case B simulation. a) vertical vorticity contours (vertical view from below); b) streamwise velocity contours showing the high and low speed streaks in a plane located at y^+~11 from the bottom wall; c) spanwise-averaged concentration distribution showing the gravity current.

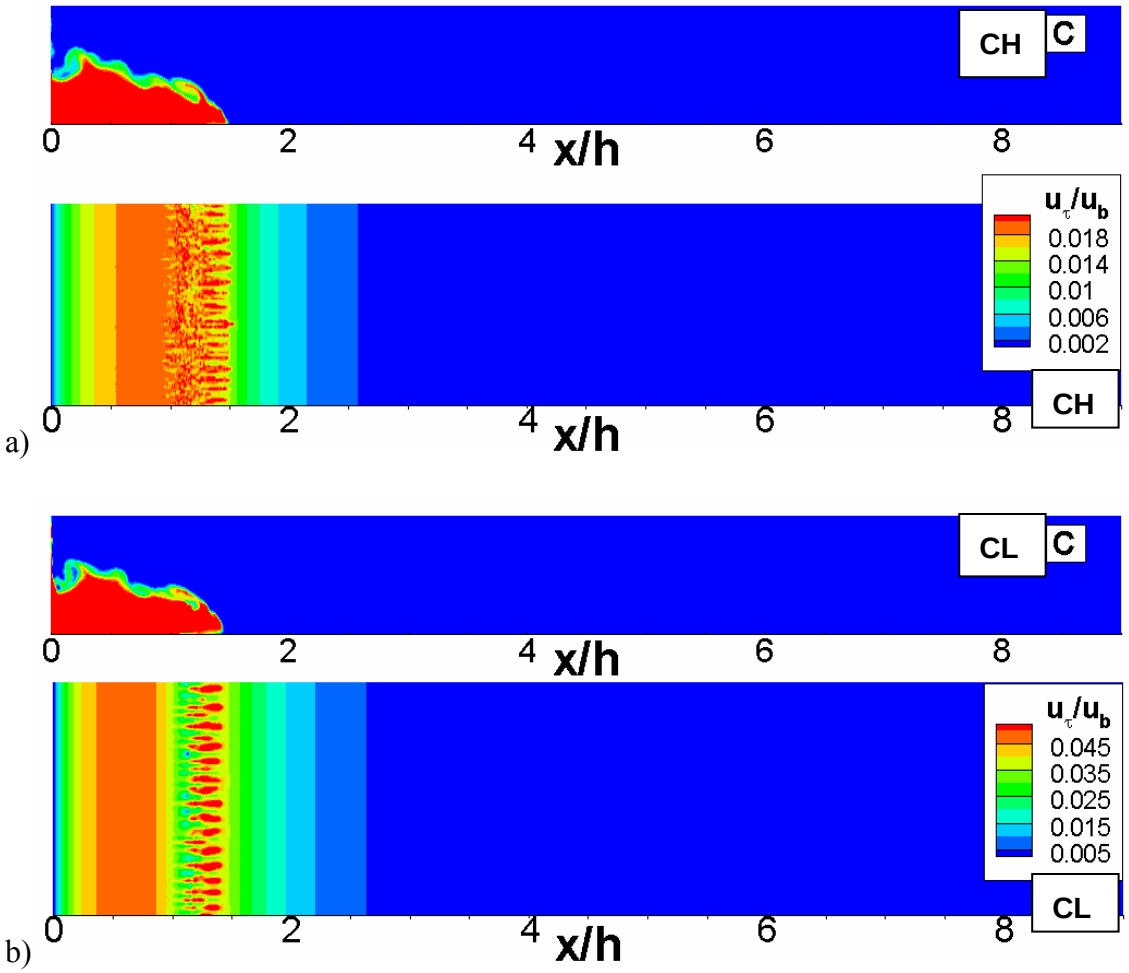

Figure 6.12. Distribution of the friction velocity u_τ/u_b on the bottom wall and spanwise averaged concentration contours at t/t_0=2. a) case CH; b) case CL.

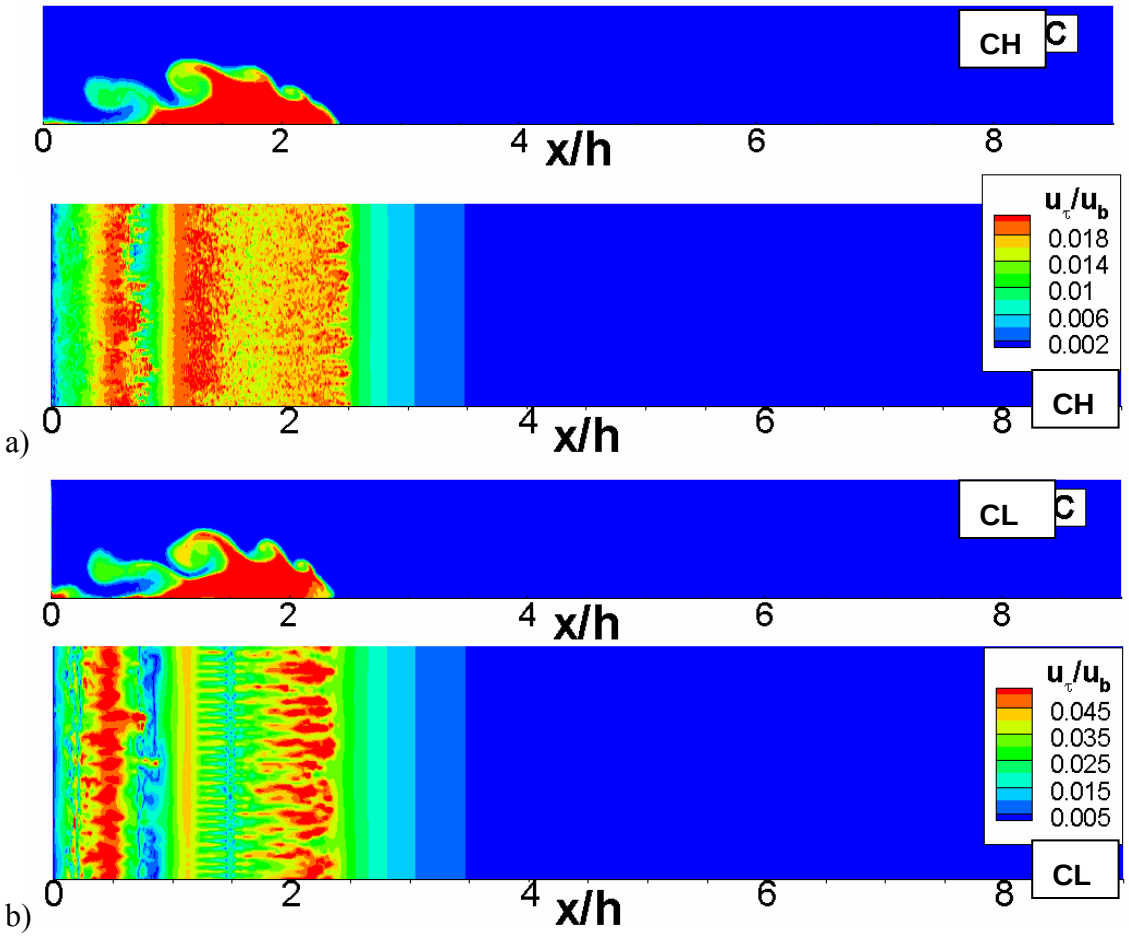

Figure 6.13. Distribution of the friction velocity u_τ/u_b on the bottom wall and spanwise averaged concentration contours at t/t_0=4. a) case CH; b) case CL.

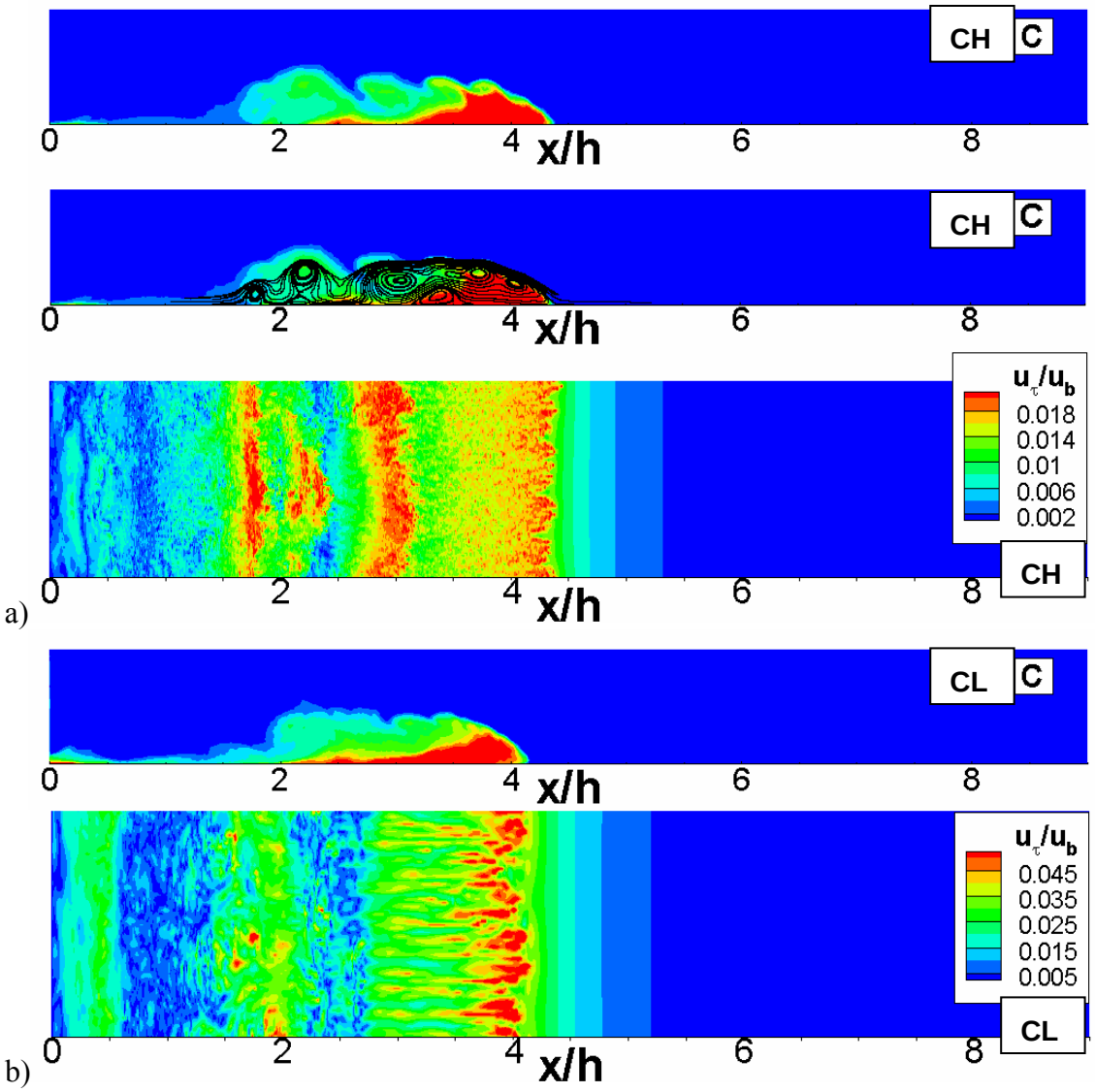

Figure 6.14. Distribution of the friction velocity u_τ/u_b on the bottom wall and spanwise averaged concentration contours at t/t_0=8. a) case CH in which instantaneous streamlines in a translating frame of reference moving with the front velocity are shown; b) case CL.

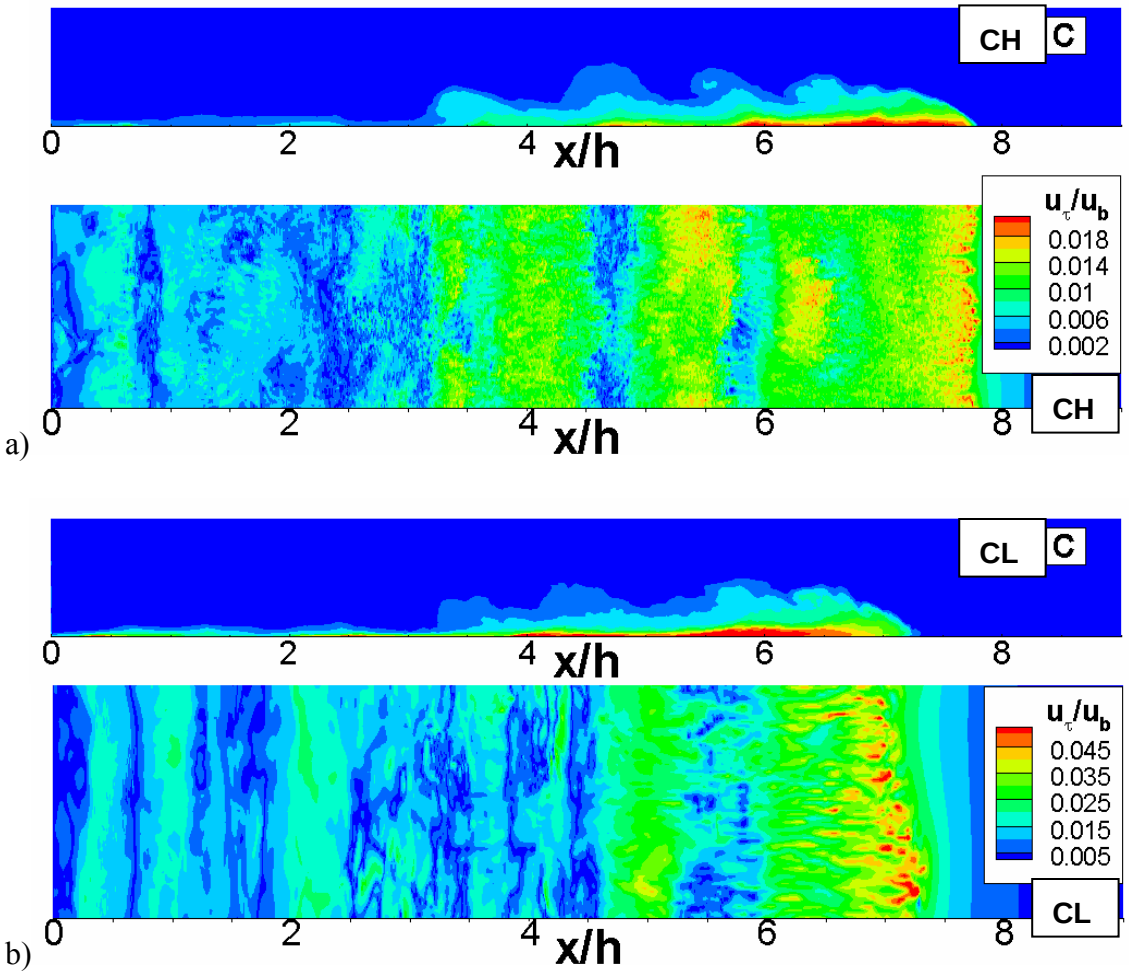

Figure 6.15. Distribution of the friction velocity u_τ/u_b on the bottom wall and spanwise averaged concentration contours at t/t_0=16. a) case CH; b) case CL.

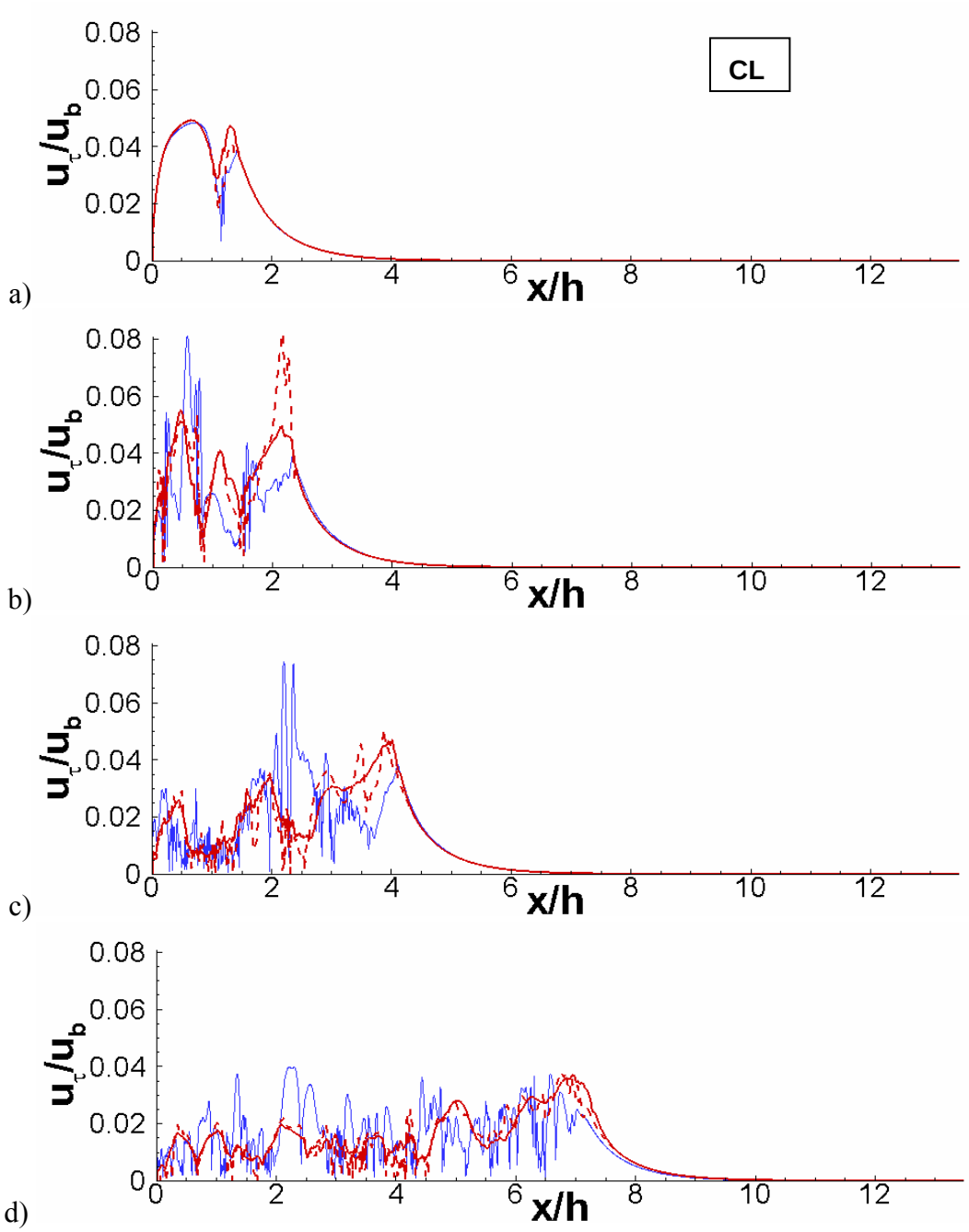

Figure 6.16. Streamwise variation of the 3D spanwise-averaged (solid red line), 3D instantaneous (dashed red line) and 2D (solid blue line) friction velocity on the bottom wall for case CL. a) t/t_0=2; b) t/t_0=4; c) t/t_0=8; d) t/t_0=16.

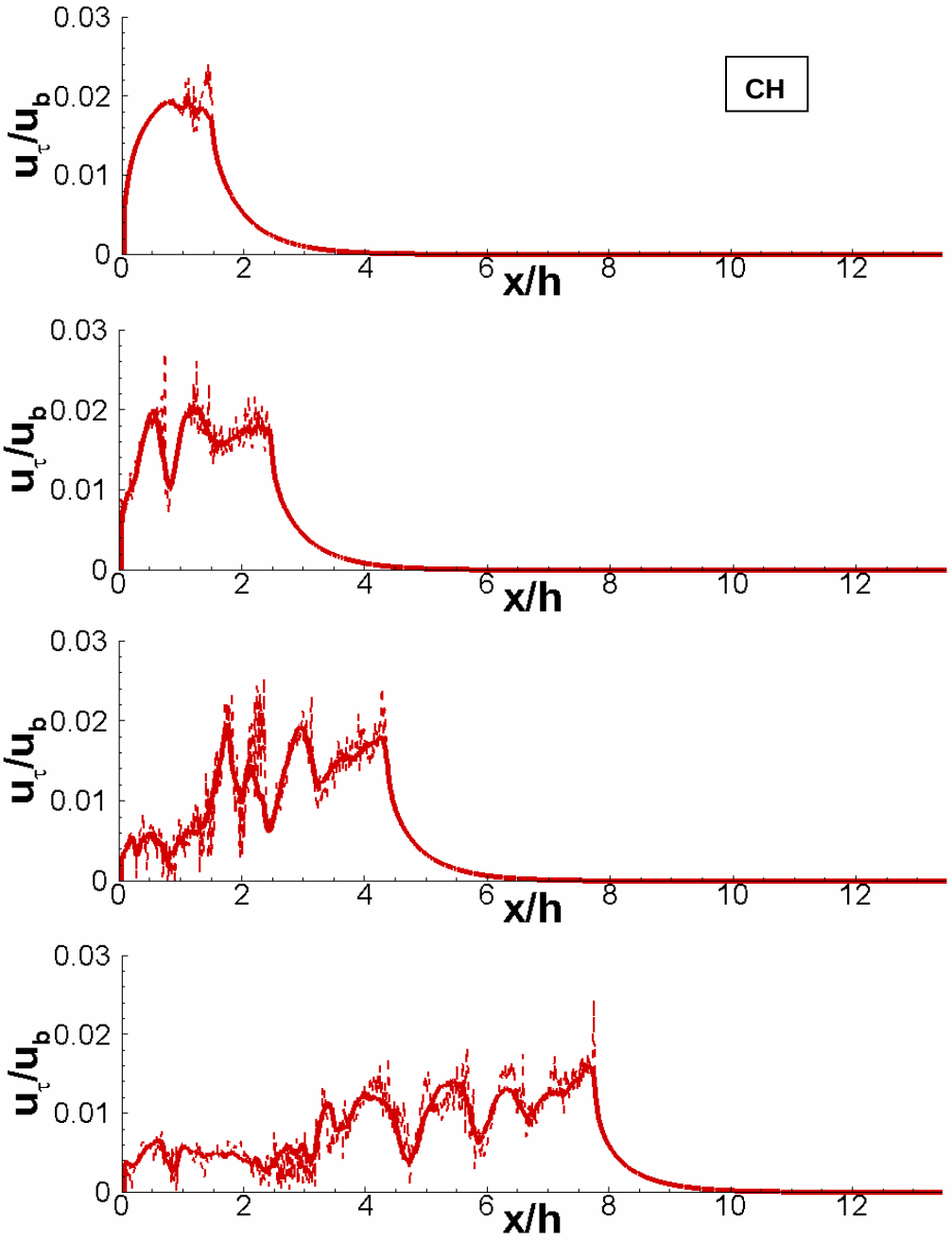

Figure 6.17. Streamwise variation of the 3D spanwise-averaged (solid red line) and 3D instantaneous (dashed red line) friction velocity on the bottom wall for case CH. a) t/t_0=2; b) t/t_0=4; c) t/t_0=8; d) t/t_0=16.

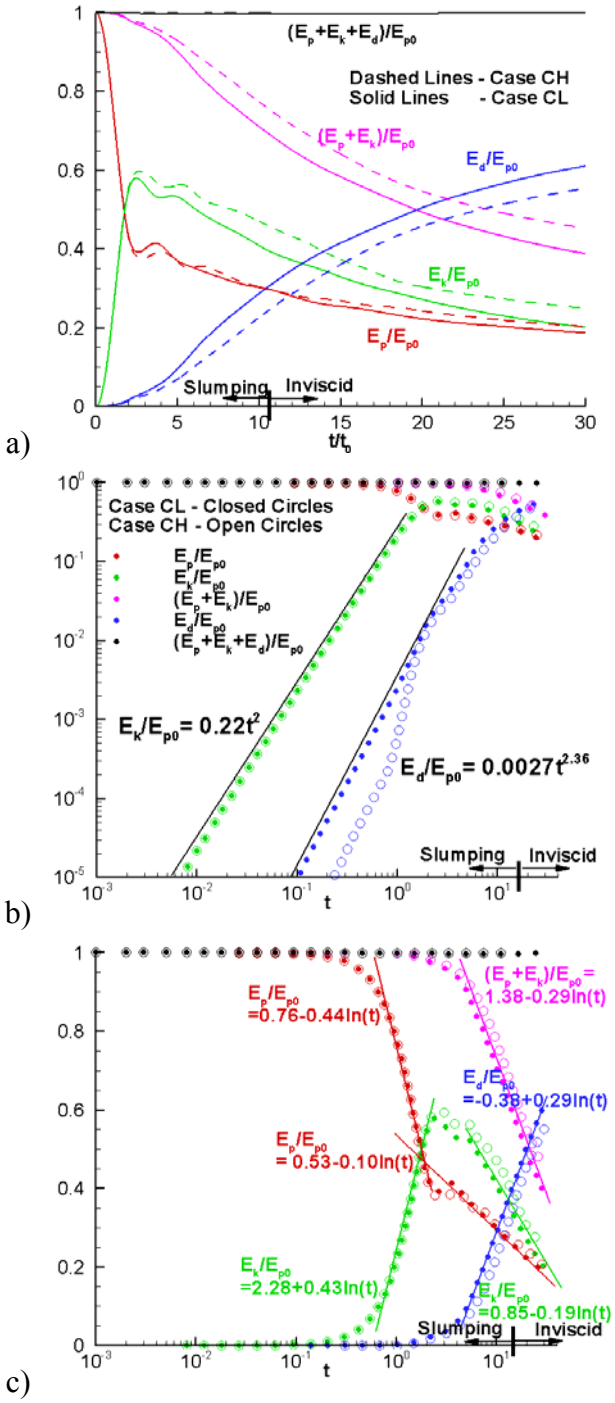

Figure 6.18. Time history of the potential energy, E_p, kinetic energy, E_k, and integral of the total dissipation, E_d, in the CL (solid line) and CH (dashed line) simulations. a) linear-linear scale; b) log-log scale; c) linear-log scale.

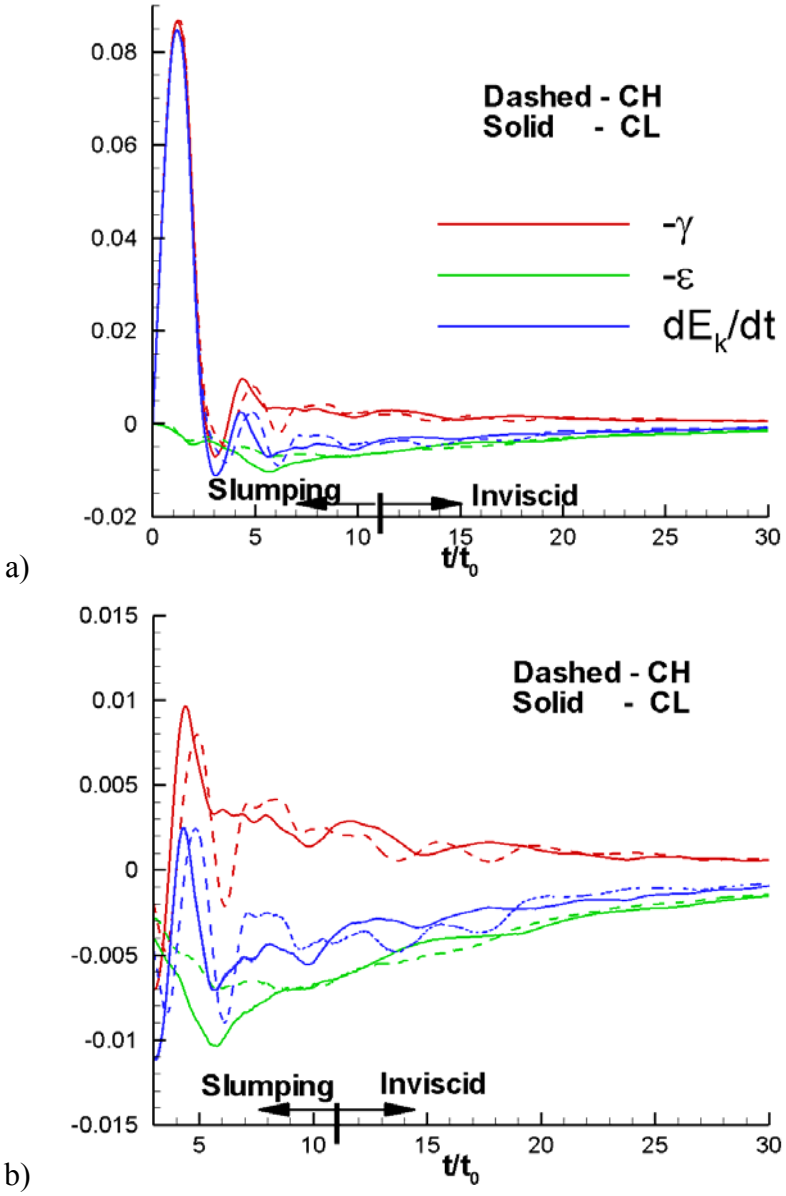

Figure 6.19. Temporal evolution of the terms in the transport equation for the total kinetic energy in the CL (solid line) and CH (dashed line) simulations.

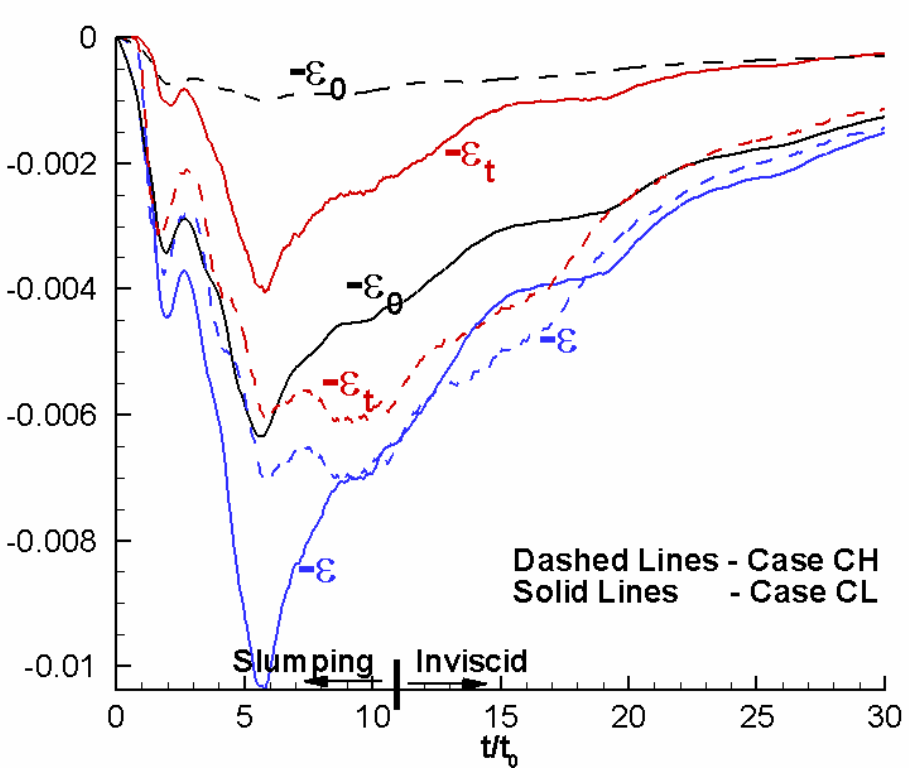

Figure 6.20. Temporal evolution of the total dissipation, ε, SGS dissipation, ε_t, and viscous (resolved) dissipation, ε_0, in the CL (solid line) and CH (dashed line) simulations.

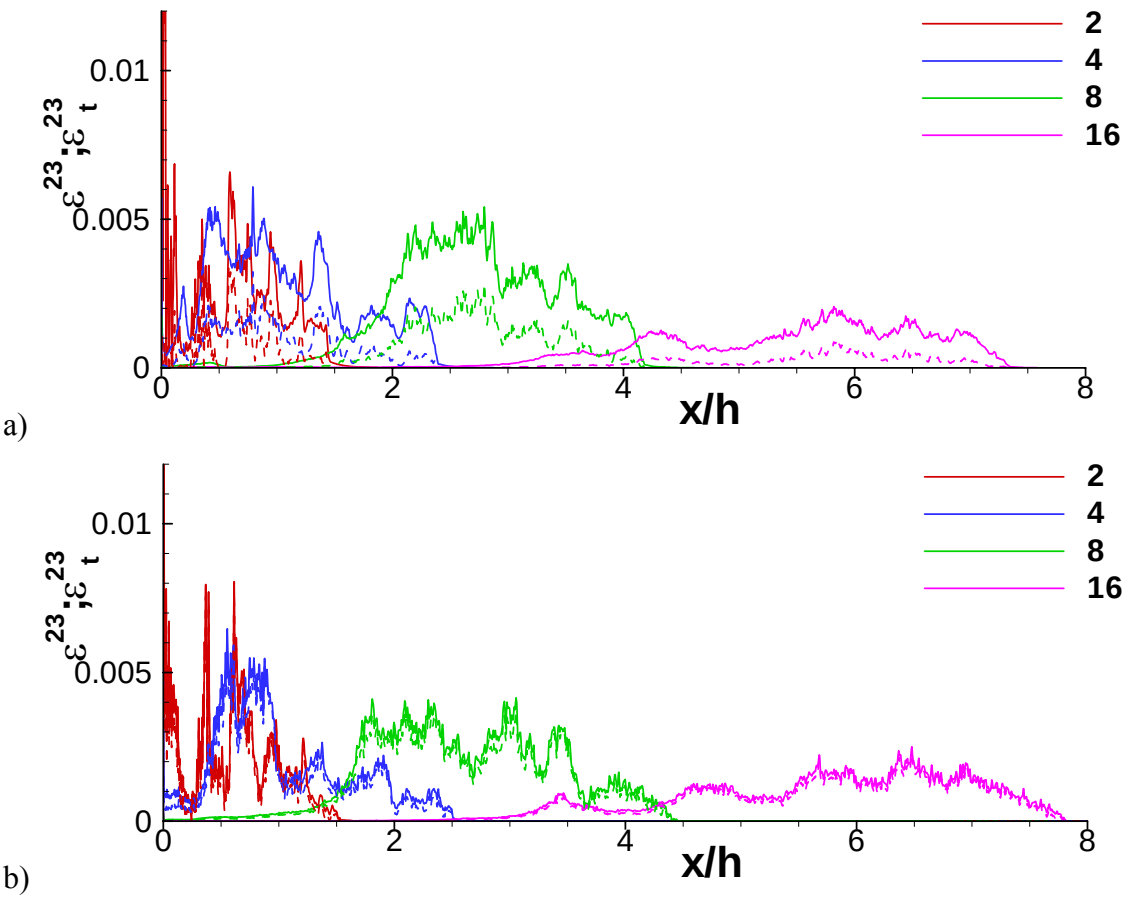

Figure 6.21. Streamwise distribution of the total dissipation term $\varepsilon^{23}(x_1)$ (solid line) and SGS term $\varepsilon_t^{23}(x_1)$ (dashed line) at t/t_0=2, 4, 8 and 16. a) CL simulation b) CH simulation.

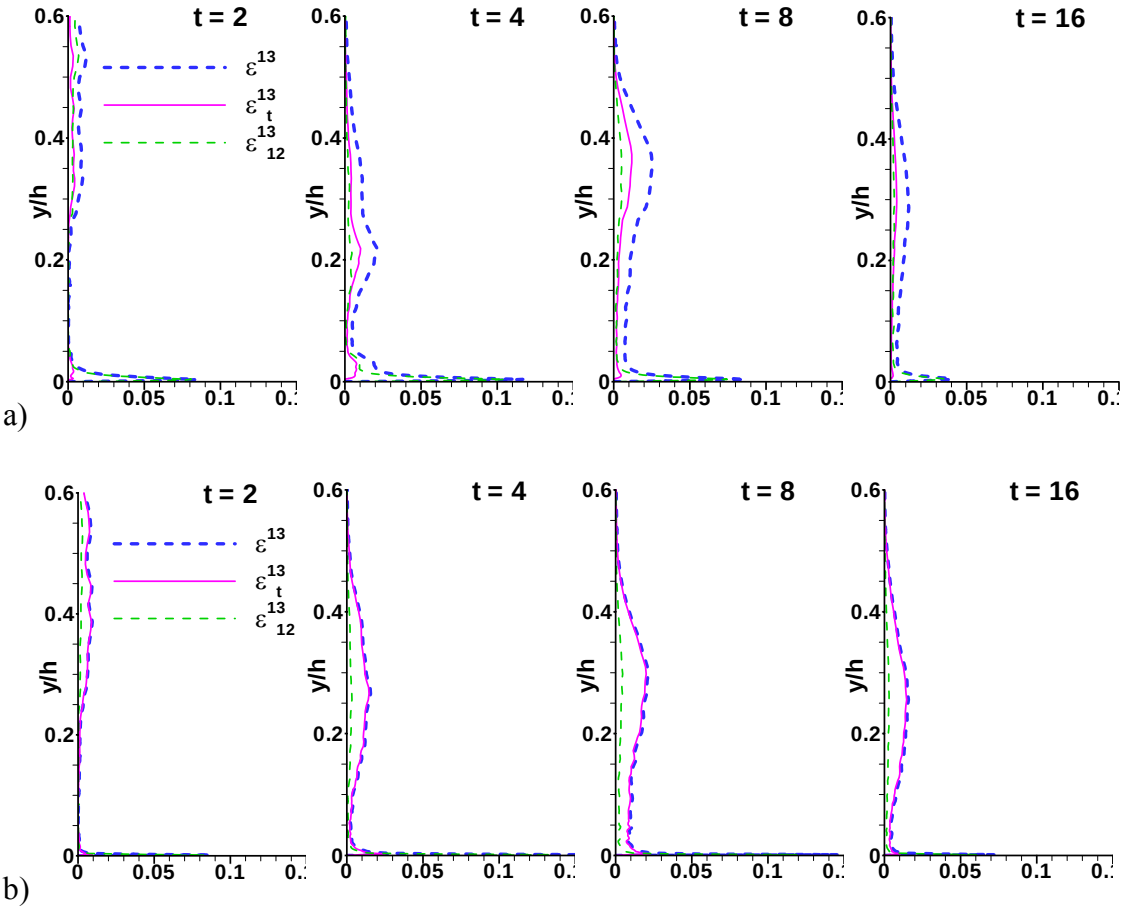

Figure 6.22. Vertical distribution of the total dissipation term $\varepsilon^{13}(x_2)$ (solid line), SGS term $\varepsilon_t^{13}(x_2)$ (dashed line) and dissipation term containing the vertical gradient of the streamwise velocity $\varepsilon_{12}^{13}(x_2)$ (dashed-dot line) at t/t0=2, 4, 8 and 16. a) CL simulation b) CH simulation.

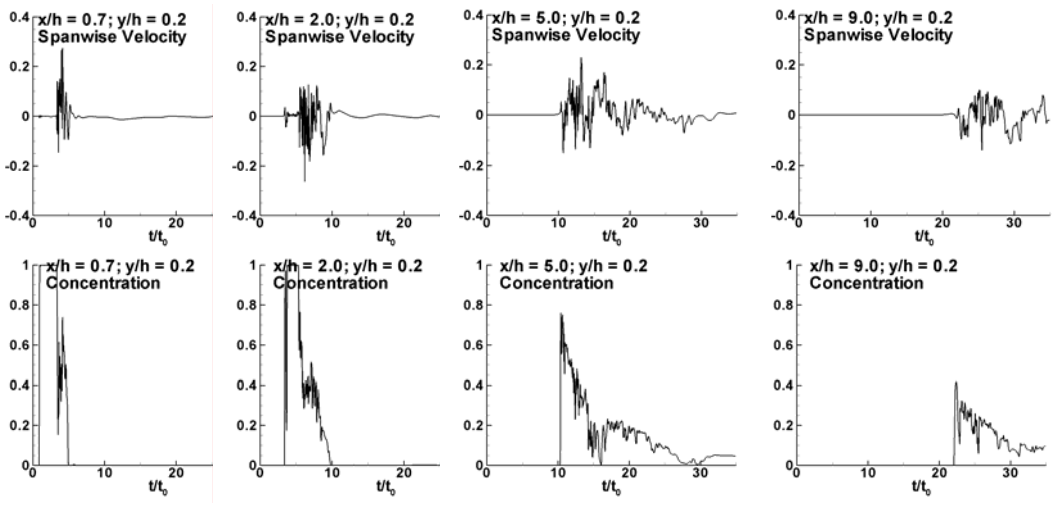

Figure 6.23. Time history of spanwise velocity and scalar concentration for case CL at four stations situated at x/h = 0.7, 2.0, 5.0 and 9.0 and at y/h=0.2.

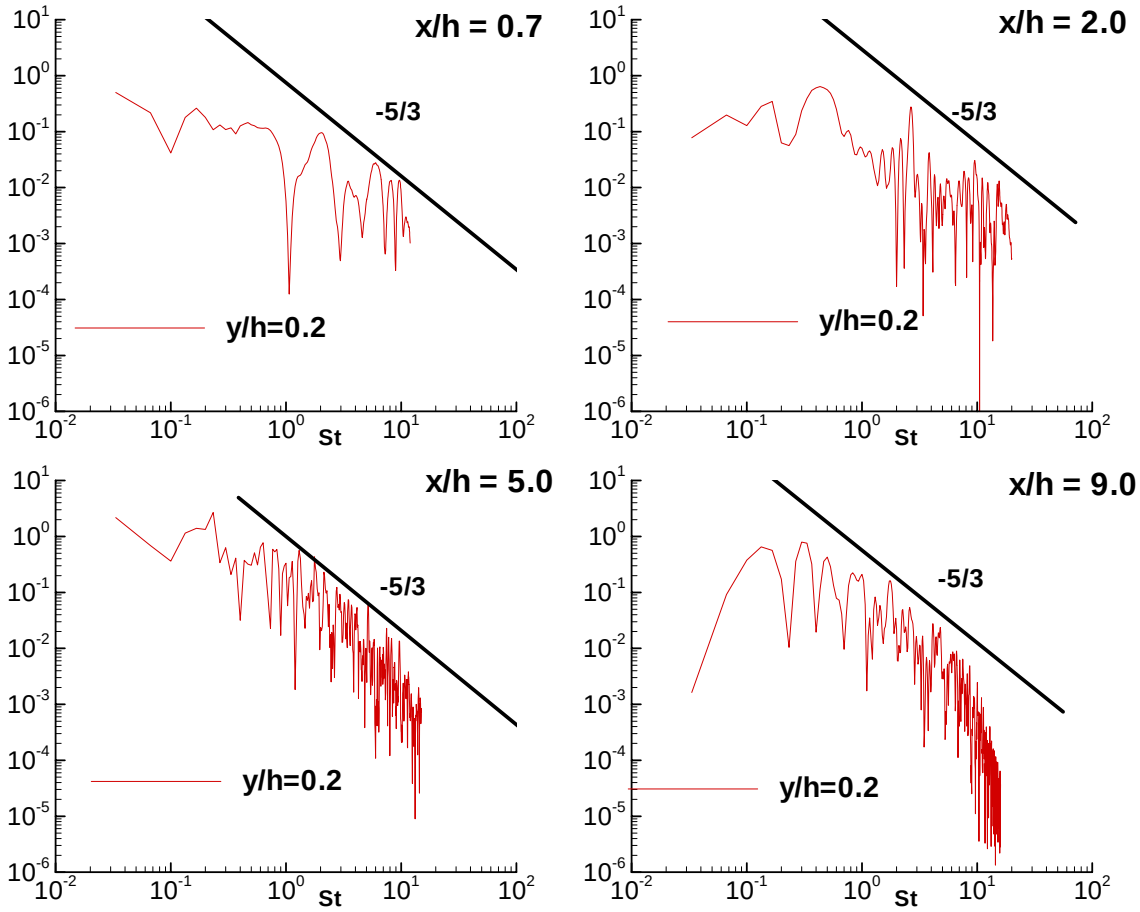

Figure 6.24. Spanwise velocity power spectra (case CL) at four stations situated at x/h = 0.7, 2.0, 5.0 and 9.0 and at y/h = 0.2.

CHAPTER 7

3D LES SIMULATIONS OF INTRUSION CURRENTS

7.1 Description Of Intrusion Currents

The case of an IC that is propagating into a two layer ambient fluid (Fig. 7.1a), in which the densities of the two layers ($\rho_0<\rho_1$) are constant, is studied using highly resolved LES. Only the case in which the constant density of the lock fluid, ρ_L, is between that of the two layers ($\rho_0<\rho_L<\rho_1$) and the initial depth of the lock fluid is equal to that of the channel or tank (h) in where the lock fluid is released (full-release case) is studied here. In the present simulations, the interface between the two fluids is assumed to have zero thickness. In experiments, this corresponds to the limiting case when the density gradient between the two layers occurs over a very short distance compared to the height of the intrusion. The depths of the two layers are denoted h_0 and h_1. The length of the initial volume of lock fluid is denoted as x_0. The mean density of the ambient fluid outside the lock is $\overline{\rho} = (h_0\rho_0 + h_1\rho_1)/h$. The degree of symmetry of the intrusion (e.g., see de Rooij et al, 1999, Sutherland et al., 2004) can be characterized using two parameters Δ and ε. The first one is defined as the difference in the depth of the two layers relative to the total depth $\Delta=(h_0-h_1)/h$, while the second one characterizes the difference between the density of the lock fluid and the mean density of the ambient fluid $\varepsilon_R = (\rho_L - \overline{\rho})/(\rho_1 - \rho_0)$. Only cases where $\varepsilon_R=0$ are considered in the present work. The doubly symmetric case corresponds to $\varepsilon_R=0$ and $\Delta=0$.

As the gate is removed instantaneously, there is a short acceleration phase in which the IC forms and starts propagating forward. Meanwhile, similarly with the case of a finite-volume lock release bottom propagating current, two return flows are forming in the lower and upper layers and start propagating toward the end wall, as shown in Fig. 7.1b. Once they encounter the end wall, they reflect and start propagating forward, below and above the tail of the intrusion (Fig. 7.1c), in the form of bores with relatively constant

speeds (U_{bore0}, U_{bore1}) that are somewhat larger than the constant velocity of the intrusion front (U_f). The IC is in the slumping phase. Leading interfacial waves can form depending on the values of the main flow parameters (e.g. ε_R, Δ, Gr). It is expected that mixing in the head region will become a factor after the bore overtakes the front and the front velocity will start decaying.

Two 3D LES simulations (see Table 7.1) were conducted at a Grashof number of 1.57×10^9 (Re=$\sqrt{Gr}$ ~38,000). The first simulation corresponds to the doubly-symmetric case (h_0=h_1, ε_R=0, Δ=0), while the second one (h_0=7h_1, ε_R=0, Δ=3/4) corresponds to Case 3 in the experimental study of Sutherland et al. (2004). They are referred to as case SC and case NSC within the chapter, respectively. In the experiments and simulations, the value of $\sigma = (\rho_1 - \rho_0)/\rho_1$ was 0.02. Some comparisons with 2D simulations are also provided. The bottom and end-wall surfaces were simulated as no-slip smooth walls. The free surface was treated as a slip (zero shear stress) boundary. This explains the non-symmetry of the flow near the top and bottom boundaries in the SC simulation. The flow in the spanwise direction is assumed to be periodic.

The boundary layers on all the no-slip walls were resolved by clustering the grid points in the streamwise and vertical directions such that first point off the wall is situated at less than one wall unit (assuming turbulent flow) from the surface. For simulations of ICs, this allows a more accurate study of the interactions between the return flow and the left end wall. The flow field in all simulations was initialized with the fluid at rest, i.e., u_i = 0. The non-dimensional concentration field was initialized with a constant value of one in the upper layer and a constant value of zero in the lower layer. The nondimensional concentration of the lock fluid was equal to 0.5 and 0.125 in cases SC and NSC, respectively. A random disturbance was applied on the concentration field in the lock-gate region to accelerate the growth of 3D instabilities. The time step in the simulations was 0.001t_0. The maximum Courant number was around 0.2.

The size of the grid was 2048×160×80 in the streamwise, vertical and spanwise directions, respectively, which corresponds to about 26 million control volumes. The relative dimensions of the computational domain (L_1=9.855h, L_2=1.0h, L_3=0.88h) were identical to the ones in the physical experiment in which h=0.2m. The length of the initial lock fluid volume was x_0=0.903h. The typical size of a cell was 0.005h in the streamwise direction, 0.017h in the vertical direction and 0.011h in the spanwise direction. Near the lateral end walls the mesh size was reduced to 0.*002h*. Near the bottom, the mesh size in the wall normal direction was 0.001h. As the physical Reynolds number associated with the intrusion was below 5,000 in both cases, the mesh is expected to be fine enough to resolve the dynamically important coherent structures.

7.2 Evolution Of Intrusion Current And Coherent Structures

Snapshots of the spanwise-averaged and instantaneous concentration fields are used in Figures 7.2a and 7.2c to visualize the temporal evolution of the intrusion in the SC case and to compare with experimental visualizations (Fig. 7.2b) of Sutherland et al. (2004). In the experiment the dimensional value of t_0 is close to 1s. The lock gate is removed instantaneously, causing the lock fluid to accelerate from rest, collapse practically symmetrically, and start moving along the interface. The front of the intrusion is already visible at t=2t_0 during the acceleration phase. As the return flows above and below the intrusion encounter the end wall, two forward propagating symmetrical bores are formed. At t=13.8t_0, the wedge shaped intrusion is practically developed and contains a main elongated region (head and dissipative wake) followed by a tail. The position of the forward propagating bore is shown using an arrow. As the IC propagates, the bore moves closer to the front, the tail elongates and contains more of the initial lock fluid (see also discussion of Fig. 7.20). At t=25.8t_0, the bore stops its advancement relative to the front in both simulation and experiment. The last frame, just before the

front of the intrusion reaches the end wall, corresponds to $t=37.6t_0$. Observe that the length of the downstream bulb-shaped part of the intrusion is practically the same in the last two frames (see also discussion of Fig. 7.11) but the thickness of the intrusion region is smaller at $t=37.6t_0$. At all stages, the IC appears to intrude relatively symmetrically into the upper and lower layers of ambient fluid. No significant deflections of the interface were observed in front of the intrusion, consistent with previous experimental investigations of the doubly-symmetric case. This is despite the fact that different boundary conditions were imposed on the top (slip) and bottom boundaries (no slip) in the simulations. Only small deformations, corresponding to the presence of weak interfacial internal waves are observed for $t>20t_0$ in the tail region that separates the advancing bores in the upper and lower layers.

In the simulation, the head thickness becomes constant at t~$8t_0$ (start of slumping phase) and is equal to $0.43h$, in good agreement with the experiments of Faust & Plate (1984) in which the interface thickness between the layers of ambient fluid, δ, was small, $\delta/h<0.1$, and $Re_f>2{,}000$. Lowe et al. (2002) estimated the head thickness to be around $0.46h$ based on shadowgraph measurement techniques and about $0.43h$ based on PTV visualizations for Re_f~5,000-7,000. The value is slightly below the value of $0.5h$ predicted by Benjamin (1968) for energy-conserving GCs. As previously mentioned, the head thickness starts to slowly decrease for $t>22t_0$ after the end of the slumping phase.

The foremost point of the intrusion (or nose) remains located in the symmetry plane ($y=0.5h$) at all stages of the evolution of the flow in the SC case. This is inferred from the instantaneous streamline patterns in Fig. 7.3b which are shown in a translating system of coordinates moving with the front velocity at $t/t_0=5$ and $t/t_0=10$. This is in contrast to observations of GCs propagating over no-slip surfaces where the nose is raised above the wall. Still, relatively large-scale structures are observed to form at the front of the intrusion interface, as shown in Fig. 7.4c using a concentration isosurface ($C=0.5$). This demonstrates that the flow at the front is not exactly two-dimensional and

that relatively large-scale structures can develop at the front of an IC, similar to the lobes and clefts observed in the case of GCs propagating over no slip surfaces.

To investigate the shapes and size of these structures, the curved lines corresponding to the intersection between the intrusion front and the horizontal plane y=0.51h are shown in Fig. 7.5 at t=20t_0 and t=30t_0. Also shown in Figures 7.5a and 7.5b are a cut through the front interface of a bottom propagating GCs in the self-similar inviscid phase at two time instances when Re_f~6,900 and 4,600, respectively. The results are taken from the LES study of Ooi et al. (2006b). Additionally, Fig. 7.5c contains a cut through the front interface of a bottom-propagating GC during the slumping phase when Re_f~29,900 (Ooi et al., 2006a). The scale in all the plots is the same. For the bottom-propagating current, the mean size of the lobes clearly scales with the Reynolds number defined with the front velocity. In the intrusion case, the largest structures are much smaller than the largest lobes observed at similar Reynolds numbers for GC over no-slip surfaces. However, the shape and size of the interface deformations corresponding to the secondary lobes observed in the case of a bottom propagating GC are very similar to the ones observed for the IC in case SC (e.g., compare the interface deformations for the bottom propagating current at z/h<0.4 to the ones observed for the IC at t=30t_0 in Fig. 7.4b). Though the mean lateral size of the lobes developing at the front of a bottom propagating GC at Re_f=29,900 is similar to the intrusion at Re_f~4,800, the streamwise length of the intrusions associated with the lobes in the Re_f=29,900 simulation is a few times larger then the one observed in the present IC simulation. This leads to the conclusion that some of the sources of instabilities present in the front region of lock exchange flows are common to both ICs and GCs propagating over no slip surfaces.

The overall growth rate of the 3D instability is clearly lower in the case in which the no-slip surface is absent. One of the main differences between the two types of currents, which may be related to the observed differences in the growth rates of the instabilities in the front region, is that there is much less turbulence production at similar

Reynolds numbers for ICs. This is mainly due to the absence of the near-wall region. These findings are consistent with the conclusions of a recent paper by McElwaine and Patterson (2004) which are based on on-going experimental investigations. They observed that any interface that propagates with relatively constant velocity normal to the front will eventually develop clefts. Then, as the lobes between the clefts increase in size while decreasing in curvature, they become dynamically unstable and can create new clefts. This mechanism is independent of the presence of a no-slip surface below the current.

More details of the overall differences between IC and bottom-propagating GCs during the slumping phase can be inferred from Fig. 7.10, which compares the instantaneous vertical vorticity fields from two 3D LES simulations with similar Grashof numbers. The view in Fig. 7.10a is from below the interface, between the intrusion current and the lower layer of ambient fluid. The structure is very similar for the upper interface. As observed in Fig. 7.10a, no streamwise streaks are present at the interface between the intrusion and the ambient fluid. This includes the dissipative wake region where the flow is strongly turbulent. This contrasts with the vortical structure of the flow in the near-bed region observed beneath high Reynolds number gravity currents (Fig. 7.10b) where a streaky structure is observed to be present over a certain distance behind the front. The length of the streaky structure is determined by the condition that the local Reynolds number remains high enough for the flow to sustain turbulence.

Toward the end of the acceleration phase (e.g., see vorticity fields at t/t_0=5 in Fig. 7.3) the formation and shedding of high vorticity KH billows from the wake region introduces an important amount of energy and momentum around the interface on both sides of the IC. This energy is redistributed once the interfacial vortices roll up and start loosing their coherence while simultaneously mixing lock fluid with the ambient fluid. The stretching of the large KH billows in the SC simulation is very rapid such that by t=13.8t_0 (Fig. 7.4a) only the first one or two billows behind the front extend over the

whole span of the computational domain. These billows eventually break into small scale turbulence. As this happens, wisps of fluid with density close to that of the lock fluid are displaced by the highly energetic 3D structures that resulted from the breaking of the KH billows. Some of these wisps of fluid are then transported away from the interface. Then, by the action of small scale eddies, these wisps of fluid from inside the intrusion mix with the ambient fluid. The amplitude of the deformations and the associated range of wavelengths observable on the interface in Figures 7.4a and 7.4b diminish considerably behind the bore indicating that very little mixing occurs inside the tail. Eventually, even the smaller eddies left behind the wake region will loose their energy and dissipate. As a result, the flow will relaminarize some distance behind the head.

The intrusion interface in Fig. 7.4a corresponds to a moment in the evolution of the intrusion when the overall dissipation rate is close to its maximum value (see also Fig. 7.15). After the end of the slumping phase (t~$22t_0$), the length of the wake region has reduced and the amount of energy in the KH billows has diminished. As a result, there is less energy available for mixing, and the interface in the tail region becomes relatively smooth over a shorter distance behind the wake region. Comparison of the shape of the interface at t=$13.8t_0$ and at t=$37.6t_0$ in Fig. 7.4 offers a good illustration of this evolution.

Several instantaneous spanwise-averaged vorticity magnitude plots are shown in Fig. 7.3a to further clarify the spatial and temporal evolution of the vortical structures and the associated mixing in the SC simulation. Toward the end of the acceleration phase (t=$5t_0$) most of the vorticity is contained in the strongly coherent quasi-2D interfacial vortices present over the whole length of the dissipative wake region. By t=$10t_0$ most of the KH billows no longer span the whole width of the intrusion. Though the circulation associated with these billows is still very high in the formation region, the vorticity distribution becomes irregular indicating the presence of strong turbulent eddies near the interface between the dissipative wake and the ambient fluid. At t=$20t_0$, the length of the wake region has diminished considerably. For t>$20t_0$, the vorticity magnitude inside the

horizontal layers centered at y=0.75h and y=0.25h decays relatively monotonically with the distance from the bore, and appear to contain very little large scale structures, indicating that the billows lose their coherence rapidly. For t>20t_0, the vorticity levels are very low inside the tail region of the intrusion situated in between the two shear layers.

At the start of the slumping phase some interactions are observed between interfacial vortices originating at the lower interface and vorticity patches from the boundary layer on the bottom wall that forms because of the return flow (e.g., for $x/(h/2)$<5). However, to a large extent the vorticity distribution above and below y/h=0.5 remains similar during the evolution of the IC. At all time instances, a very thin but strong shear layer is observed around the head. However, inside the head the vorticity remains low. As will be discussed later, the dissipation occurring inside this shear layer is non-negligible.

The 2D streamline patterns that are shown in Fig. 7.3b in a system of coordinates translating with the front velocity serve to visualize the motions inside the head and wake regions of the intrusion. These motions are ignored in energy-conserving theoretical models of the head region. At t=5t_0, because the lock gate removal did not introduce any disturbances in the simulation, the main vortices in the upper and lower half of the intrusion are practically symmetrical and their positions correlate very well with that of the KH billows educed using vorticity contours in Fig. 7.3a. The main role of these vortices is to advect intrusion fluid and momentum into the KH billows that will detach and mix with the ambient fluid while the main intrusion moves downstream. By t=10t_0, the growth of the 3D flow instabilities was large enough to break the symmetry of the flow inside the head and wake regions, but the position of the main vortices in the streamline plot still correlate with the positions of the main interfacial vortices (see corresponding arrows in the vorticity and streamline plots in Fig. 7.3).

Comparison of Figures 7.2a and 7.2d highlights differences in the evolution of a high Reynolds number lock-exchange symmetrical IC predicted by 2D and 3D simulations. Although the front position and velocity predicted by the 2D and 3D simulations are found to be practically identical, the overall shape of the intrusion current, past the acceleration phase (t/t_0>7), is observed to be quite different. For instance, at t=13.8t_0, the coherence of the KH billows in the wake region is clearly higher in the 2D simulation, while the flow disturbances observed over the tail are larger and do not appear to correspond to an interfacial wave. Rather, they are due to the presence of relatively small but energetic KH billows containing fluid whose density close to that of the lock fluid. Their convective velocity decays with time but, because of the absence of 3D instabilities, they are less affected by viscous effects and maintain their coherence for much longer times. Thus, the flow in the tail region in the 2D simulation is quite different from the one observed in the experiment and 3D simulation. Moreover, past the end of the slumping phase (t~22t_0), strong KH billows start mixing the lock and ambient fluid very close to the intrusion front in the 2D simulation. As a result, the shape of the region behind the front is quite different from the one observed in experiments. In contrast to that, the shape and main features of the intrusion in case SC is correctly predicted by the 3D simulation. As the 3D instabilities grow, they stretch the cores of the interfacial vortices, rapidly alter their spanwise symmetry and break them into small turbulent eddies immediately behind the wake region.

By comparing Figures 7.2 and 7.6, it is observed that the overall shape of the IC is very different in case NSC compared to the doubly-symmetric case. Though the Grashof numbers are identical, the intrusion in case NSC propagates at a slower rate compared to case SC. The details of the evolution of the intrusion current in case NSC are discussed below.

Once the gate is removed, 2D KH vortices form at the interface between the lock fluid and the upper layer (e.g., see Fig. 7.6a at t/t_0=5). The amount of vorticity created, as

a result of the collapse of the return flow in the much deeper upper layer and its interaction with the end wall, is much larger than the one associated with the return flow in the lower layer of ambient fluid. Beginning at the end of the acceleration phase, the intrusion propagates mostly in the upper lighter layer of ambient fluid. At $t=10t_0$, the nose of the current appears to be situated inside the upper layer (see also Fig. 7.8). For $t>20t_0$, the nose of the IC is collocated with the local interface between the two layers which is situated slightly below the level ($y/h=0.125$) corresponding to the two undisturbed layers. In contrast to that, only slight disturbances are observed at the interface between the intrusion and the bottom layer of ambient fluid. This causes the overall shape of the IC to resemble that of a bottom-propagating GC, where the role of the bottom surface is played by the slightly deformed interface between the two layers.

Looking at the flow structures inside the upper layer in Fig. 7.6, one can see that the large billows appear to be more coherent in the simulation, in particular, the ones in the rear part of the tail region. This is due to the fact that in the experiment, as also mentioned by Sutherland et al. (2004), the mixing between the lock fluid and the upper layer fluid was initially dominated by the vorticity produced by the gate removal. This is why the initial mixing was stronger in the experiment. The additional disturbances induced by the secondary flow motions associated with the gate removal reduced the coherence of the KH billows. However, in later stages of the lock-exchange flow, the shape of the intrusion, in both experiment and simulation, becomes similar to each other as observed from the close-up view of the head and wake regions in Fig. 7.7. Observe the elongated shape of the intrusion in the region behind the front and the fact that KH billows are still clearly distinguishable in the wake region.

Both sides of the intrusion interface are visualized in Fig. 7.8 at $t=13.8t_0$ and $t=37.6t_0$. In the NSC simulation the growth of the 3D instabilities is slower and the flow and interface at $t=13.8t_0$ remain largely two-dimensional with the exception of the front where 3D structures are already present. This contrasts with the SC simulation when by

t=13.8t_0 the KH billows were strongly stretched in the wake region (Fig. 7.4a). It also suggests that the 3D structures at the front of the interface form due to a local 3D instability instead of having been triggered by instabilities associated with the deformation, stretching and break up of the KH billows. By t=37.6t_0 (Fig. 7.9d), similar to the SC case, a strong three-dimensionality of the flow is observed around the intrusion front, on the side that intrudes into the upper layer of ambient fluid. Even at t=37.6t_0, the main interfacial billows maintain most of their coherence and extend over the whole width of the computational domain. However, the flow in the interface region is turbulent and a wide range of energetic 3D eddies is observed around the dissipative wake and some distance behind it.

In contrast to the upper interface, the deformations of the lower interface are much smaller at all stages of the evolution of the IC. Though no interfacial leading waves appear to have been generated because of the intrusion, for t>20t_0, waves of relatively small wavelength are observed to travel behind the nose, at the interface between the IC and the lower layer. These waves are visible in Fig. 7.9c and appear to extend over the whole span. At t=37.6t_0, for example, the wavelength is around 0.33h and the amplitude is close to 0.022h. Sutherland et al. (2004) observed that the phase speed of these waves is close to the front velocity. Undulations of the bottom interface were observed at positions that correlate to the ones where quasi-2D vortical structures detach from the vorticity sheet associated with the lower interface (see Fig. 7.8a).

The KH billows that form at the interface between the intrusion and the upper layer of ambient fluid a short time after the instantaneous gate removal (e.g., at t/t_0=5), are visualized in Fig. 7.8a which shows snapshots of the spanwise-averaged vorticity magnitude distribution. The head of the IC is already formed and is practically contained into the upper layer of ambient fluid toward the end of the acceleration phase. As the intrusion evolves into the slumping phase (e.g., see frame at t=10t_0 and Fig. 7.9b), large coherent quasi-2D billows are shed from the dissipative wake region into the upper layer

of ambient fluid. As the intrusion continues to propagate these vortices initially containing mostly lock fluid are stretched and patches of vorticity separate from the main billows. Similar to the SC case, as the quasi-2D billows lose energy, they strongly enhance the mixing around them (e.g., observe the vorticity structure in the region between $x/(h/2)$=2 and $x/(h/2)$=4 in Fig. 7.8a at $t=20t_0$).

Most of the vorticity entrainment into the body of the IC takes place at the bottom interface (e.g., observe the evolution of the eddy situated at $x/(h/2)$=4.2 at t/t_0=10 and at $x/(h/2)$=7.3 at t/t_0=20), somewhat similar to the case of a GC propagating over a no-slip surface where the bottom surface is the main source of vorticity and turbulence production for the fluid inside the head and wake regions. Similar to the SC case, the large KH billows at the interface between the intrusion and the upper layer do not appear to penetrate into the main body of the intrusion. The patches of vorticity left behind the dissipative wake disturb the rear part of the vorticity sheet between the intrusion and the lower layer of ambient fluid. As a result, the vorticity sheet is broken into small scale turbulent eddies (e.g., $x/(h/2)<3$ at $t=20t_0$).

The streamline patterns in a system translating with the front velocity at $t=10t_0$ and $t=20t_0$ (Fig. 7.8b) show that relatively large-scale recirculation motions are present inside the head and wake regions. The positions of these eddies correspond to the positions of the interfacial vortices at the upper side of the interface. Additionally, some smaller but stronger vortices are observed near the bottom side of the interface. They correspond to the vortical structures ejected from the vorticity sheet between the intrusion and the bottom layer of ambient fluid. In later stages of the propagation ($t>30t_0$), these strong ejections become less and less frequent.

7.3 Front And Bore Velocities

The bore position is difficult to directly infer from the shape of the current. Rather, it is deduced from the spanwise-averaged concentration plot $C=C(x,t)$ at a

vertical location situated slightly above or below the interface between the two undisturbed layers of ambient fluid (e.g., at y/h=0.47 in Fig. 7.11 for the bore in the lower layer in case SC). In case SC, the bore in the upper layer propagates with practically the same speed.

The straight line observed between the white region containing lower layer ambient fluid (C=0) and the intrusion head containing unmixed lock fluid (black region with C~0.5) corresponds to the front trajectory $x_f(t)$. The presence of this line is proof that the speed of propagation of the front is constant until the head starts interacting with the right end wall. The non-dimensional front velocity over the slumping phase is $Fr=U_f/u_b$=0.244 in the simulation. This value is practically identical to the one measured experimentally (Fr=0.245). The corresponding values of the Reynolds numbers defined with the front velocity are Re_f=4,833 in the simulation and 4,851 in the experiment (see also Table 7.1). In the experiment a relatively thin mixing layer is always present between the upper and lower layers of ambient fluid due to the diffusion and mixing during the stratification process. The excellent agreement between simulation, in which the mixing layer has zero thickness, and experiment demonstrates that the presence of the thin (~1cm) layer of mixed ambient fluid in the experiment is not the main cause why the front velocity is slightly lower than the theoretical value for inviscid intrusions (Fr=0.25). A detailed analysis of the dissipative losses along the IC which may explain some of the reasons for the differences between theory and simulation is discussed in section 7.5. The front velocity measured by Faust & Plate (1984) ranged from 0.234 to 0.241 for Re_f between 1,500 and 13,700; the interface thickness was about 0.1h. Lowe et al. (2002) measured front velocities close to 0.247 for Re_f=5,000-7,000.

In Fig. 7.11, the first thin, gray region behind the uniform black region corresponds to the bore. This thin region on top of which a solid red line was superimposed makes a constant slope with the time axis until t~24t_0. Its slope is larger than the slope of the line corresponding to the front trajectory. This indicates that the

bore velocity, U_{bore}, is larger than the front velocity. The relative velocity difference $(U_{bore}-U_f)/U_f$ inferred from Fig. 7.11 is equal to 0.29, whereas, the value obtained from experiment (Sutherland et al., 2004) is close to 0.23. Rottman and Simpson (1983) measured values between 0.2 and 0.3 for GCs propagating over no-slip surfaces.

Around $t\sim24t_0$ there is a clear change in the bore trajectory that becomes almost parallel to the front trajectory until the end of the simulation. This signifies that though the bore catches the intrusion head, the bore does not pass the head, and the length of the bulk-shaped region at the front part of the intrusion remains relatively constant (see Fig. 7.2). The fact that the front continues to propagate with the same velocity past the end of the slumping phase in case SC is somewhat surprising. However, this phenomenon was also observed in the corresponding experiment of Sutherland et al. (2004). It is postulated that for the flow conditions of case SC the transition toward the self-similar phase is very slow because the density of the intrusion fluid just behind the front remains practically constant and approximately equal to the lock fluid density. This implies that the driving buoyancy force remains practically the same. However, as already pointed out, the dimensions of the bulb-shaped intrusion region start decaying in time after the end of the slumping phase. So, once mixing and dissipation will start occurring behind the front, one expects the front velocity will start decaying. In this regard, the behavior of a symmetrical IC is different from that of a bottom-propagating GC, when, once the bore overtakes the front, the density of the current behind the front becomes lower than the initial lock fluid density and the front velocity starts decaying immediately.

In the experiment, the end of the slumping phase occurs earlier, around t=18-20t_0. The discrepancy could be due to the secondary motions introduced in the experiment by the removal of the lock gate and also to the fact that the gray scale variations associated with bore trajectory in the $C(x,t)$ plots in both experiment and simulations are not very sharp. At $t\sim24t_0$, the intrusion has reached x_f=6.2h, corresponding to a non-dimensional length of $(x_f-x_0)/x_0\sim5.9$ (see also Fig. 7.12). Several other parallel lines, at an angle close

to that of the bore trajectory, can be observed. They correspond to the tail oscillations behind the main intrusion region. Their propagation speed is close to the bore velocity during the slumping phase and, thus, is larger than the front velocity, consistent with the observations of Mehta et al. (2002) and Sutherland et al. (2004).

Despite the asymmetry of the intrusion in the NSC simulation, its propagation speed after the end of the acceleration phase (t~$8t_0$) is practically constant, at least until t=$40t_0$. The non-dimensional front velocity is 0.160 (Re_f=3,169). The Froude number value obtained from experiment is 0.161, and the one given by theory (Holyer & Huppert, 1980, Sutherland et al., 2004), in which the head is considered to be energy conserving, is 0.165 (A=3/4). The front speed is lower compared to the one observed in the doubly-symmetric case. This is also evident from Fig. 7.12 where the temporal evolution of the non-dimensional front position is plotted in log-log scale. The slope of one (solid lines in Fig. 7.12) corresponds to a constant front velocity. The lower value of the front velocity in case NSC is due to the lower density of the fluid in the head region (C=0.125) as compared to that of case SC (C=0.5). The fluid density in the head is equal to that of the lock fluid which is equal to the mean density of the ambient fluid. In the NSC case, this density is much closer to the upper layer density due to the high ratio between the depths of the upper and lower layers of ambient fluid. As most of the IC propagates into the upper layer, the effective buoyancy force will be smaller compared to case SC. Consequently, the return flow in the upper layer will travel a longer time until it reaches the end wall. As also observed in the experiment, the bore in the upper layer does not catch the head region before the intrusion approaches the right end wall.

Details of the evolution of the IC in cases SC and NSC in the initial stages of the lock-exchange flow can be inferred from Fig. 7.13 where the speeds and trajectories of the intrusion front and return flow in the upper layer of ambient flow are plotted. The velocities of the return flow and intrusion front are practically identical in case SC until t=$3.5t_0$. Then, the return flow decelerates rapidly as it starts interacting with the end

wall. This is not observed in case NSC where the return flow in the upper layer appears to accelerate faster than the intrusion front. The return flow reflects from the end wall at $4.2t_0$ in case SC and at $6.8t_0$ in case NSC. The initial length of the lock fluid, x_0, is not large enough for a region of constant return flow velocity to form for the flow conditions in case SC. Such a region, however, appears to be present between t/t_0=1.5 and t/t_0=4.5 in case NSC for the return flow in the upper layer due to the smaller value of the buoyancy force in case NSC compared to case SC. The front velocity of the return flow is about 10% lower than the intrusion front velocity over this time interval. The variation of the front velocity in the initial stages of the motion is not exactly monotonic. It first reaches a maximum value of $0.29u_b$ in case SC and of $0.2u_b$ in case NSC before slowly adjusting toward the slumping phase values, at the end of the acceleration phase. The maximum value is reached at t=$1.0t_0$ and $1.5t_0$ in cases SC and NSC, respectively, after the release of the lock gate.

7.4 Energy Budget

The temporal variation of E_p is shown in Fig. 7.14a while E_k and E_d are shown in Fig. 7.14b. The individual terms in equation (5.8) are shown in Fig 7.15 for both simulations. All the variables in Fig. 7.14 are nondimensionalized by the value of E_{p0} in case SC, to facilitate the comparison of the SC and NSC simulations for which the Grashof number is the same. The value of E_{p0} in case NSC is only about 0.095 of that in case SC. In both simulations, the variation of E_p can be divided into two regions. The first region, in which E_p decays fast, roughly corresponds to the duration of the acceleration phase (t~$5t_0$ for SC and t~$8.5t_0$ for NSC) which is characterized by the conversion of potential energy into kinetic energy (see also variation of γ and dE_k/dt in Fig. 7.15). The process is practically inviscid as not much dissipation takes place during the acceleration phase. At the end of the acceleration phase, E_k attains its maximum (case SC) or is very close to it (case NSC). In the second region, once the IC enters the

slumping phase, the decay of E_p becomes much slower. This is because the intrusion mainly travels in the horizontal direction.

In the SC simulation the increase in the total dissipation is due mostly to the decay in the potential energy (see Fig. 7.15) from the end of the acceleration phase until t~$15t_0$. Over this interval ε attains its maximum value. The large values of ε are mainly due to the interfacial billows that rapidly break into 3D smaller eddies. Over this time interval, the SGS dissipation rate is close to 22% of the total dissipation. For t>$15t_0$, the increase in ε comes at the expense of both E_p and E_k which are observed (see Fig. 7.14) to decay by similar amounts during the time the intrusion front propagates with practically constant speed. Consistent with that, the values of γ and dE_k/dt are relatively close. The ratio between ε_t and ε decays to about 15% for t~$30t_0$ showing that most of the dynamically important eddies were resolved in the SC simulation. The main difference compared to the SC simulation in the variation of ε is the fact that, though a local maximum is observed at t~$9t_0$, the total dissipation rate continues to increase from t=$20t_0$ until, at least, t=$35t_0$ in the NSC simulation. Eventually, the total dissipation rate is expected to peak and start decaying because the lock-release flow contains a finite volume of lock fluid. The ratio $\varepsilon_t/\varepsilon$ in case NSC is less then 5% until t=$25t_0$. The simulation is very close to DNS regime over this time interval. After that, as more small turbulent eddies are created around the main 2D billows, the ratio $\varepsilon_t/\varepsilon$ increases to 12% at t=$35t_0$.

7.5 Spatial And Temporal Distributions Of The Dissipation Rate And Streamwise Velocity

The changes in the spatial distribution of the spanwise-averaged local dissipation rate, ε_L, are analyzed in Fig. 7.16 at several stages of the evolution of the IC (t/t_0=5, 10, 20 and 30) in the SC simulation. Knowledge of the distribution of ε_L, which is difficult to obtain experimentally, is useful because it helps to better understand the flow physics

and for modeling purposes in theoretical models that incorporate the effect of dissipation. High-resolution simulations can provide this kind of information not only globally but also as an integral over a certain direction or region (e.g., streamwise variation of the dissipation integrated over vertical planes, integral of the dissipation over the dissipative wake region) to make the analysis easier.

Most of the dissipation takes place in the interfacial billow vortices that form at the lower and upper interfaces between the intrusion and the two layers of ambient fluid in the dissipative wake region. This is true at practically all stages of the evolution of the IC as observed in Fig. 7.16. The other region where ε_L is very high is inside the thin shear layers that correspond to the front. The shape of these shear layers is close to the one predicted by Benjamin (1968) for an energy-conserving head (dashed white line in Figures 7.16b and 7.16c). As expected, the shape predicted by Benjamin's (1968) theory gives poorer agreement in the dissipative wake region due to the presence of KH billows at the interface, high dissipation, and the fact that the flow behind the intrusion front is not stagnant (e.g., see discussion of Figures 7.3b and 7.19). The streamwise distance between the nose and the position of the first billows is approximately $0.7(h/2)$ in all the frames of Fig. 7.16. This distance defines the approximate length of the head region.

Another interesting observation is that ε_L is very low not only inside the head region, behind the shear layers at the front, but also in the interior of the dissipative wake region, away from the interface. The dissipation rate in the interior of the head region remains very low even after the end of the slumping phase ($t \sim 22t_0$). Another region where ε_L is high is behind the wake region, at the level of the upper and lower interfaces. In these two layers, the billows shed from the main body of the IC are left behind, stretched and dissipate while mixing the lock fluid from the dissipative wake region with the ambient fluid. The tail region around the centerline $y/h=0.5$ is practically non-dissipative. This explains why, in the experiments and simulation, the tail defined by the lock fluid left behind the main intrusion forms a relatively thin, stably-stratified layer.

Figures 7.17 and 7.18 show the horizontal and vertical distributions of the local dissipation rate integrated over y=constant (ε^{23}) and x=constant (ε^{13}) sections at t/t_0=5, 10, 20 and 30. Their SGS components are denoted ε_t^{23} and ε_t^{13}, respectively. They are shown with dashed lines in Figures 7.17 and 7.18. An important aspect of the streamwise variation of ε^{23} in the SC simulation is the fact that the values at locations intersecting the thin shear layer that defines the interface between the head region ($0<x/(h/2)<0.7$, where x=0 corresponds to the instantaneous nose location and x is measured backwards) and the ambient fluid are comparable to the values observed at locations inside the dissipative wake. This is the case in spite of the interior of the head region being practically dissipation free, as shown in Fig. 7.16. After the end of the acceleration phase the largest values of ε^{23} generally are observed at the back of the dissipative wake region. However, ε^{23} remains relatively high some distance behind the dissipative wake because of the presence of the billows which have already detached from the interface between the wake and the ambient fluid (around y/h~0.25 and 0.75). While these vortices are decelerating, they are being stretched and lose their energy via the energy cascade down to dissipative scales. As a consequence, two layers of relatively high vorticity are observed in Fig. 7.3 around y/h~0.25 and 0.75. The length of this dissipative region is close to 8($h/2$) at t=20t_0 and 4.5($h/2$) at t=30t_0. Notice that the contribution of the head region as a percentage of the total dissipation in the head and dissipative wake regions increases in time. At t=30t_0, the contribution of the head is close to 50%. However, relative to the dissipation occurring over the whole length of the intrusion the percentage is close to 20% at the same time instant.

In the NSC simulation, the distributions of ε^{23} are similar to the ones observed in the SC simulation over the slumping phase. The main difference is that most of the dissipation in case NSC occurs at the interface between the intrusion and the upper layer of ambient fluid, and behind the dissipative wake region in the upper layer (see also the vertical distribution of ε^{13} in Fig. 7.18b). At t=10t_0, ε^{23} is almost uniformly distributed

over the whole length of the intrusion (the larger values at the left end wall are due to the interaction between the lock fluid and the attached boundary layers). The distribution, however, becomes more non-uniform at later times. The largest values at $t=20t_0$ are observed in the head region and over the downstream part of the wake region. Even behind the bore the values of ε^{23} can be relatively high if the billows left behind (see vorticity contours in Fig. 7.8) are still maintaining their coherence (e.g., for $4<x/(h/2)<6$ at $t=20t_0$ and for $6<x/(h/2)<8$ at $t=30t_0$). By $t=30t_0$, the largest values of ε^{23} are observed at the end of the wake region where the last billow interacts with the shear layer separating the intrusion from the lower layer of ambient fluid.

The vertical distributions of ε^{13} in the SC simulation show that most of the dissipation takes place in two horizontal layers centered at $y=0.65h$ and $y=0.35h$. These locations correspond to the two layers of high vorticity magnitude in Fig. 7.3a. The overall decrease of the total dissipation rate starting at $t\sim9t_0$ (Fig. 7.15) is consistent with the variation of the ε^{13} profiles in Fig. 7.18a. The degree of asymmetry, observed in the initial stages of the simulation in the distribution of ε^{13}, in the two high dissipative layers reduces as the flow continues to develop. The asymmetry is due to the presence of a no-slip boundary at the bottom surface and of a slip boundary at the top surface. In fact, the relative contribution of the wall layer present near the bottom boundary ($y/h<0.1$) to the total dissipation in the domain decreases continuously, starting at the end of the acceleration phase. The dissipation near the bottom boundary is expected to be largely caused by the streamwise velocity gradients in the wall normal direction. To investigate this, the ε_{12}^{13} component that contains these gradients in the expression for the total dissipation was plotted in Fig. 7.18. Indeed, one can see that $\varepsilon_{12}^{13} \sim \varepsilon^{13}$ near the bed, in the frames in Fig. 7.18a. The component ε_{12}^{13} becomes much smaller than ε^{13} away from the bed, as the flow three-dimensionality increases.

The profiles of ε^{13} in the NSC simulation show that as the intrusion flow evolves in time, the layer centered around $y=0.65h$, in which the large vortical billows are

forming at the interface between the intrusion and the upper layer of ambient fluid, increases its contribution to the total dissipation within the flow domain. The relative contribution of the layer centered around y/h~0.08 is larger (~32%) at $t=10t_0$ compared to other time instances because of the presence of relatively strong patches of vorticity ejected from the interface between the wake region and the lower layer of ambient fluid (Fig. 7.8a). However, the contribution of this middle layer of high values of ε^{13} decreases monotonically in time, such that by $t=30t_0$ its contribution to the total dissipation is only 16%. In fact, most of the overall increase of the total dissipation within the flow domain between $t=20t_0$ and $t=30t_0$ is due to the increase of the dissipation rate in the top layer. This layer accounts for 61% of ε at $t=20t_0$ and for 79% at $t=30t_0$. Over the same time interval, the dissipation in the middle layer remains practically constant. At all time instances, the contribution of the bottom layer ($y/h<0.05$) to the total dissipation rate ε is less than half that of the middle layer. The fact that the values of ε_{12}^{13} are very close to ε^{13} in the bottom and middle layers of relatively high dissipation confirms that the flow remains relatively two-dimensional in those layers, at least until $t=30t_0$. In the case of the upper layer, for $t>10t_0$ a clear decrease of the contribution of ε_{12}^{13} is observed. This means that the flow becomes strongly three-dimensional in the later stages of the slumping phase.

The instantaneous spanwise-averaged streamwise velocity contours from the SC simulation are shown in Fig. 7.19 along with the streamline patterns and the region containing intrusion fluid which has a density that is very close to the lock fluid density (C~0.5) at t/t_0=10, 20 and 30. The thick line in the pictures showing the streamline patterns and the streamline velocity contours corresponds to the contour line where the streamwise velocity is equal to the front velocity. Fig. 7.19d shows the streamise velocity profiles at the center plane (y/h=0.5). The origin of the streamwise axis is situated at the location of the intrusion nose in Fig. 7.19.

By $t=10t_0$, practically all the lock fluid was convected out of its original location into the horizontal intrusion wedge. At this early stage of the slumping phase, the streamwise velocity in the center of the intrusion is larger than the front velocity. This region of high streamwise momentum was created during the acceleration phase when a considerable amount of the initial potential energy was convected into kinetic energy. This momentum will gradually be lost as the intrusion advances, due to the mixing that takes place at the interface between the dissipative wake region and the ambient fluid, and to the fact that the intrusion fluid at the back of the dissipative wake decelerates slowly. As the mean streamwise velocity decays below the front velocity, some of the fluid will be left behind to form the tail that contains mostly lock fluid. This phenomenon is visible in simulations and experiment (e.g., see Fig. 7.2). One should point out that in the case of a lock exchange flow with an infinite-volume of lock fluid, the scenario is different, as the tail serves to feed lock fluid toward the wake and head regions. Thus, the streamwise velocity in the tail is expected to be higher than the front velocity for such a case.

Comparison of the region containing fluid moving faster than the front speed ($u>U_f$) in Figures 7.19a-c shows that there is an overall loss in streamwise momentum over the main body of the intrusion. If at $t=10t_0$ the maximum streamwise velocities in the wake were as high as $1.45U_f$, around the end of the slumping phase at $t=20t_0$, the maximum velocity is only $1.25U_f$ and the size of the region where $u>U_f$ has reduced by half. The presence of unmixed lock fluid moving relatively uniformly behind the nose during the slumping phase is consistent with the observations of Hacker et al. (1996) for bottom propagating GCs and Lowe et al. (2004) for doubly-symmetric intrusion experiments. By $t=30t_0$, the maximum velocity is only $1.05U_f$. The region where $u>U_f$ continues to shrink. The fact that the head region behind the nose continues to propagate at practically the same speed some time after the end of the slumping phase (e.g., at $t=30t_0$) is due to the fact that the non-dissipative region behind the nose still contains

unmixed lock fluid. However, it is expected that as the thickness of the head gets smaller and the wake moves closer to the nose, dissipative effects will become important behind the nose and the speed of the head will start decaying, similar to the observed evolution of a GC propagating over a no slip wall during the self-similar phase.

As observed from Fig. 7.19d, the velocity in the head region (up to 0.7($h/2$) behind the nose) remains relatively uniform (u~U_f) after the end of the acceleration phase (t>7t_0). Behind the dissipative wake, the streamwise velocity was observed to decay relatively monotonically especially for t>15t_0. The fact that the streamwise velocity near the middle plane is higher than the front velocity is due to the presence of the interfacial vortices at the edge of the wake region. These billows advect some of the unmixed intrusion fluid toward the interface region where the intrusion fluid starts mixing with the ambient fluid. As these billows stretch and break down, they form the two layers observed in Fig. 7.3a. The mixed fluid, however, is not re-entrained into the intrusion. As seen in Figures 7.3 and 7.19, these vortices generally form in pairs at the two sides of the intrusion and their sense of rotation is such that they increase the streamwise velocity of the flow moving in between them toward the nose of the intrusion. The increase in velocity is particularly high at streamwise locations that correspond to the locations of these pairs of vortices and is proportional to their strength. Fig. 7.20 shows similar information for the NSC case.

7.6. Summary

The temporal evolution of lock-exchange intrusion currents developing into a two-layer ambient fluid was analyzed based on high resolution 3D simulations and compared to the experiments of Sutherland et al. (2004) for two test cases. The first one corresponded to the doubly-symmetric case (SC) in which the depths of the two layers of ambient fluid were equal. In the second non-symmetric case (NSC) the upper layer was seven times deeper than the bottom layer. In both simulations, the density of the lock

fluid was equal to the mean density of the ambient fluid and the Reynolds number defined with the front velocity and channel half depth was larger than 2,000 which ensured that viscous effects did not play an important role. The length of the computational domain was not enough to study the evolution of the IC well past the end of the slumping phase, when significant mixing is expected to occur behind the nose and the front velocity starts to decay. The agreement with the experimental data of Sutherland et al. (2004) was found to be satisfactory both qualitatively (structure of the IC) and quantitatively (e.g., front velocity). Some differences in the flow structure were observed in the initial stages of the flow development in case NSC. The disturbances introduced by the removal of the lock gate in the experiment, which introduced relatively strong secondary motions around the gate position, was the main reason for these differences.

In case SC, in which the Reynolds number was higher than in case NSC, the billows that formed at the interface between the dissipative wake region and the two layers of ambient fluid were found to break rapidly after their formation. This created two layers, above and billow the tail, where the vorticity magnitude was high and mixing was very strong. The mixing in the tail was weak and the vorticity magnitude was almost zero. This allowed the tail in the 3D simulation to maintain the linear shape observed in the experiment. Some small amplitude trailing waves were observed to form in the region behind the dissipative wake.

In case NSC, consistent with experimental observations, most of the intrusion advanced into the upper layer of ambient fluid. Thus, most of the mixing took place at the interface between the intrusion and the upper layer. Meanwhile, at the interface with the lower layer waves were observed to form starting behind the nose of the current. Due to the lower Reynolds number, the billows in the upper layer maintained their 2D character for longer times compared to the SC simulation.

Visualizations of the interface surface in the front region showed that, eventually, the 3D instabilities were strong enough to form large-scale deformations, similar to the lobe-and-cleft structures observed for GCs propagating over a no-slip boundary. Our simulation results appear to confirm the conclusions in the work of McElwaine & Patterson (2004), who provide evidence that the instability mechanism responsible for the development of lobes and clefts is not necessarily related to the presence of a no-slip surface, if the Reynolds numbers are high enough. The length scales of the structures in the front region were found to be smaller than the lobe dimensions observed in GCs propagating over a no-slip boundary at similar Reynolds numbers.

The intrusion was found to propagate at a constant velocity after the end of the acceleration phase and no significant leading interfacial waves were observed. In both simulations, the front speed peaked during the acceleration phase before reaching an asymptotically constant value. The front speed during the slumping phase was sensibly higher in the doubly-symmetric case. The agreement with experiment was excellent. The values were slightly lower than the theoretical predictions of Holyer and Huppert (1980) even though the thickness of the interface between the two layers of ambient fluid was equal to zero. In case SC, the bore was observed to catch the back of the head before the intrusion approached the end wall. In both experiment and simulation, however, the front continued to propagate at the same speed for some time, in contrast to bottom propagating GCs (e.g., see experiments of Rottman and Simpson and numerical simulations of Ooi et al., 2006b). For bottom-propagating currents, once the bore overtakes the front, the density of the fluid behind the nose becomes lower than the lock fluid density, the buoyancy force decreases and the front velocity starts decaying immediately. In case SC, the density of the intrusion fluid in the head region remained equal to that of the lock fluid, negligible dissipation and mixing occurred in the interior of the head region and the head front maintained its shape. However, the thickness of the

head and wake regions were found to decay indicating that, a certain point, the flow behind the nose will become affected by mixing and eventually slow down.

Two-dimensional simulations were found to correctly predict the evolution and structure of the intrusion during the acceleration phase and the initial stages of the slumping phase when the flow in the wake region and behind the head remained largely two-dimensional. Though the front velocity was correctly predicted over the whole simulated period, once 3D effects became important, the structure of the IC predicted by the 2D simulations was found to be different from that observed in 3D simulations and experiment. The main difference was that the KH billows left behind the wake region maintained their coherence for much longer times in the 2D simulation because of the absence of 3D instabilities. The structure of the head region was significantly different once the bore cached the head region.

In the SC simulation, the instantaneous distributions of the local dissipation rate showed that the interior of the head and the center of the dissipative wake region containing lock fluid remained practically non-dissipative even after the end of the slumping phase. However, the streamwise distribution of the local dissipation rate integrated over vertical planes showed that the dissipation levels at locations cutting through the very thin shear layers at the intrusion front were close to the ones observed in sections cutting through the dissipative wake. Most of the dissipation taking place behind the dissipative wake originated in the high vorticity layers that were formed by the breaking of the KH billows. In the NSC simulation, as the intrusion continued to propagate in the slumping phase, the amount of dissipation taking place in the high-vorticity layer formed inside the upper layer of ambient fluid was found to increase significantly in time, as 3D effects became more and more important. In contrast to that, the contributions of the bottom layer and of the layer corresponding to the interface between the intrusion and the lower layer of ambient fluid were found to slightly decay with time.

In case SC, the streamwise velocity distributions inside the head and wake regions were found to be qualitatively similar to the ones observed by Lowe et al. (2004). In particular, it is confirmed that the head region contains unmixed lock fluid and the flow is close to uniform ($u \sim U_f$). In the wake region, the flow becomes non-uniform because of the large interfacial billows that locally induced an increase in the streamwise velocity of the intrusion flow. The size of the region containing velocities higher than the front velocity was observed to decay monotonically with time. Even after the end of the slumping phase, some unmixed lock fluid was present behind the nose and a region with $u > U_f$ was still present. However, the size of this region diminished considerably as the thickness of the head started to decay. Starting at the end of the acceleration phase, the forward propagating bore reduced the size of the wake region. As this happened, some of the originally unmixed lock fluid situated in the center of the channel ($y/h \sim 0.5$), toward the back of the dissipative wake region, started to decelerate. This left behind a relatively thin layer of unmixed lock fluid (downstream part of the tail), also observed in the experiment. At a given moment, the streamwise velocity inside the tail is decaying with the distance from the end of the wake region. Very little dissipation is taking place inside the tail region.

Table 7.1. Details of the intrusion front simulations.

Case	L/h	$Gr = (u_b h/\nu)^2$	$Fr = U_f/u_b$	$Re_f = U_f(h/2)/\nu$	$\Delta=(h_0-h_1)/h$	$\varepsilon_R = \frac{\rho_L-\rho}{\rho_1-\rho_0}$
SC	9.855	1.57×10^9	0.243 (0.245)	4813 (4851)	0	0
NSC	9.855	1.57×10^9	0.160 (0.161)	3169 (3267)	¾	0

Note: Values in () are from Sutherland et al. (2004)

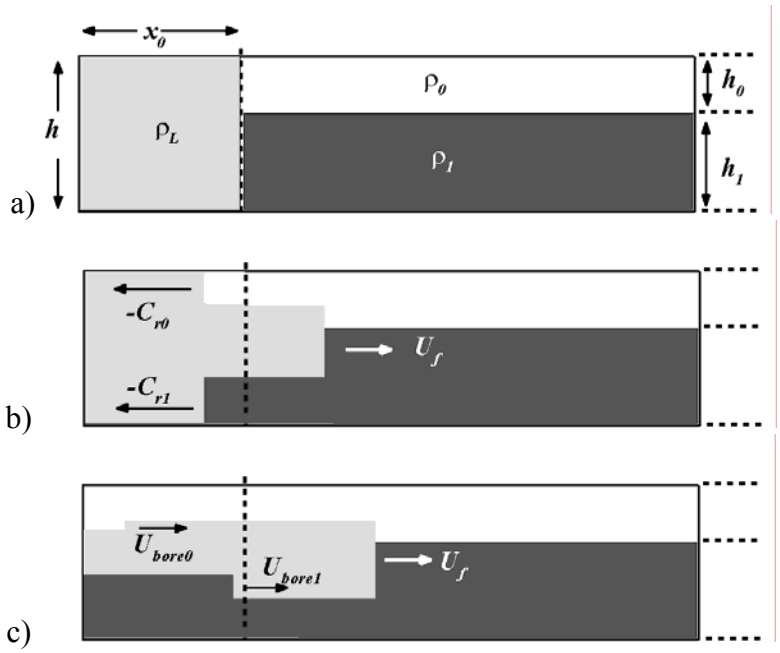

Figure 7.1. Sketch of a lock-exchange intrusion flow into a two-layer fluid in a channel with lateral walls. a) initial conditions; b) intrusion current immediately after the gate was removed; b) intrusion current during the slumping phase after the return flows have reflected and forward propagating bores have formed.

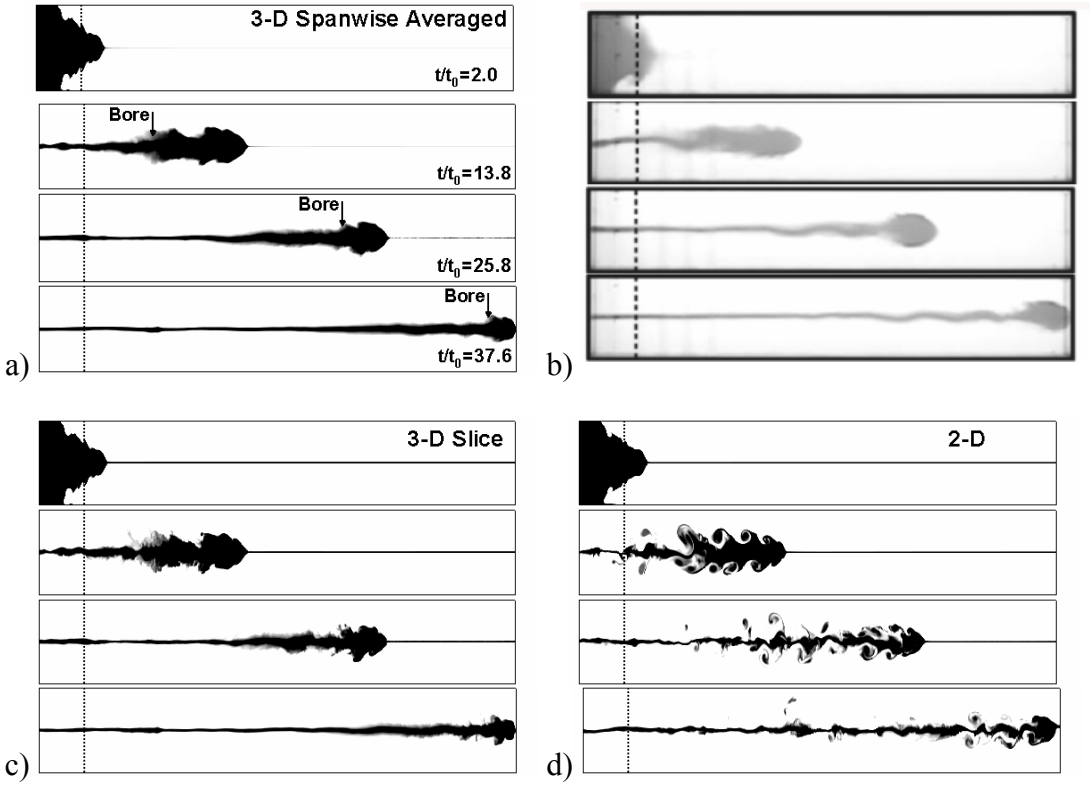

Figure 7.2. Concentration contours showing temporal evolution of intrusion current for case SC at t/t_0=2.0, 13.8, 25.8 and 37.6. a) spanwise-averaged contours from 3D simulation; b) experimental results of Sutherland et al. (2004); c) z=constant plane from 3D simulation; d) 2D simulation.

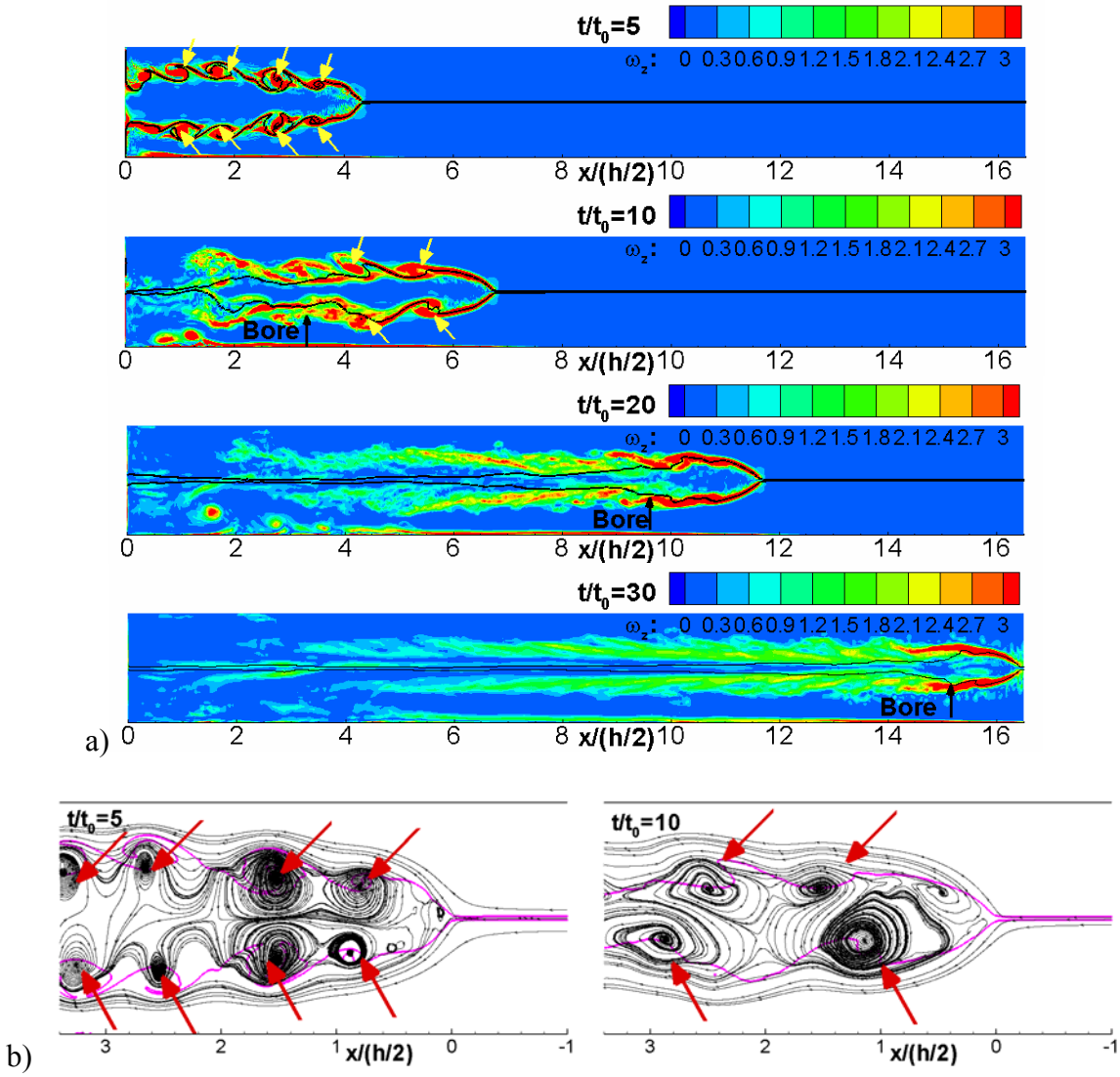

Figure 7.3. Visualization of vortical structure of intrusion current for case SC. a) spanwise averaged vorticity magnitude contours at t/t_0=5, 10, 20 and 30; b) streamline patterns showing vortical structure behind the intrusion front in a system translating with the front velocity at t/t_0=5 and 10.

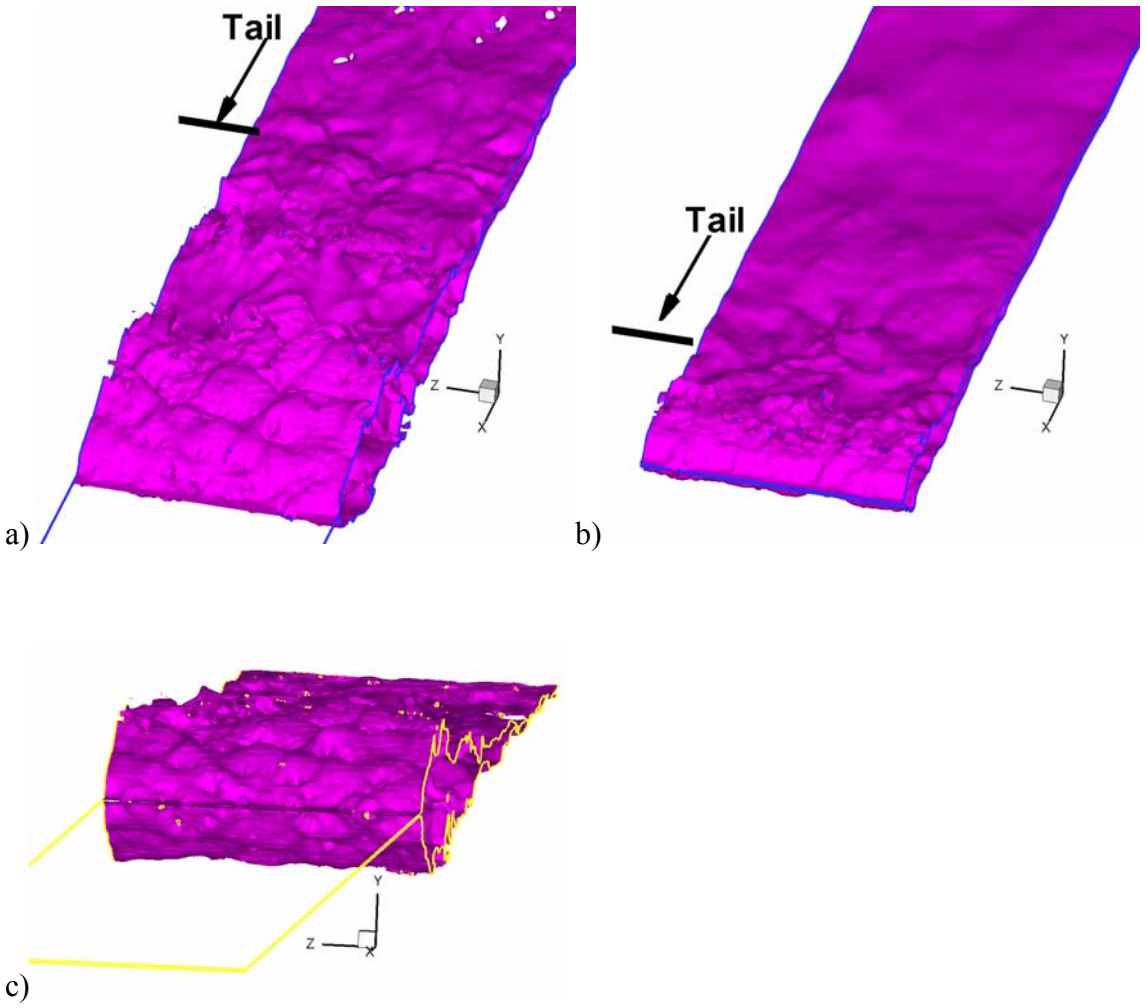

Figure 7.4. Visualization of intrusion current interface using a concentration isosurface (C = 0.5) for case SC a) t/t_0=13.8; b) t/t_0=37.6; c) close-up view showing development of large-scale structures at the front.

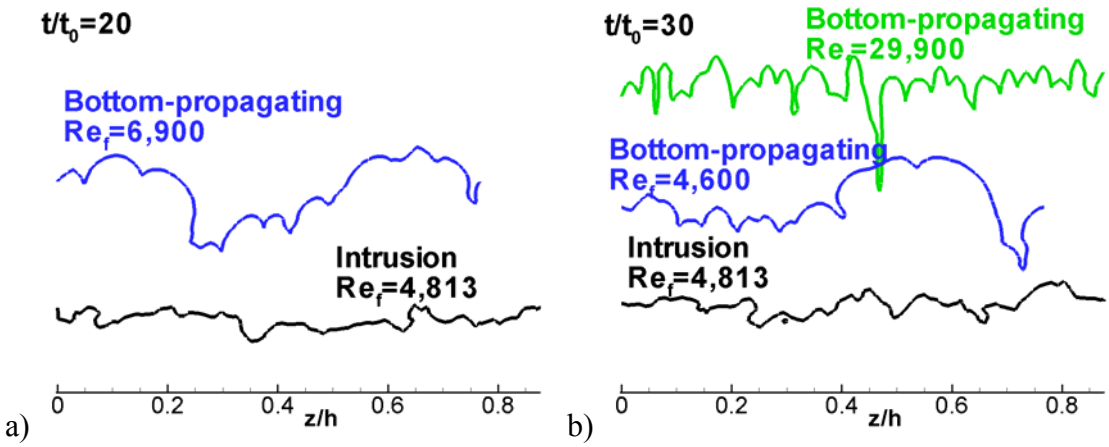

Figure 7.5. Visualization of the development of large-scale structures at the intrusion front for case SC. The front shapes of gravity currents propagating over no-slip surfaces are shown for comparison. a) t/t_0=20; b) t/t_0=30.

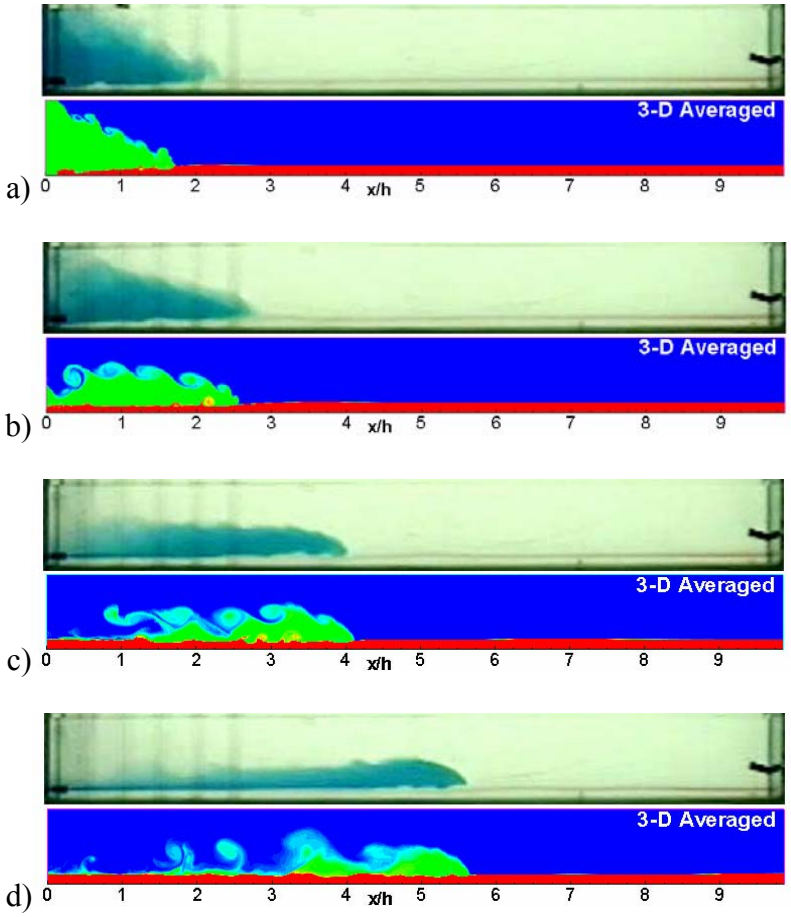

Figure 7.6. Concentration contours showing temporal evolution of intrusion current for case NSC. a) t/t_0=5.0; t/t_0=10; c) t/t_0=20; t/t_0=30. Top picture in each frame shows experimental results of Sutherland et al. (2004). Bottom picture shows spanwise-averaged concentration contours from 3D simulation.

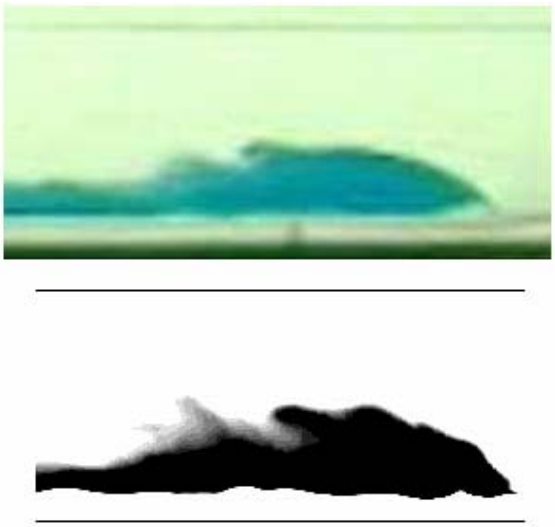

Figure 7.7. Visualization of the head and dissipative wake regions in the later stages of the slumping phase for case NSC. a) experimental results of Sutherland et al. (2004; b) spanwise-averaged concentration contours from 3D simulation.

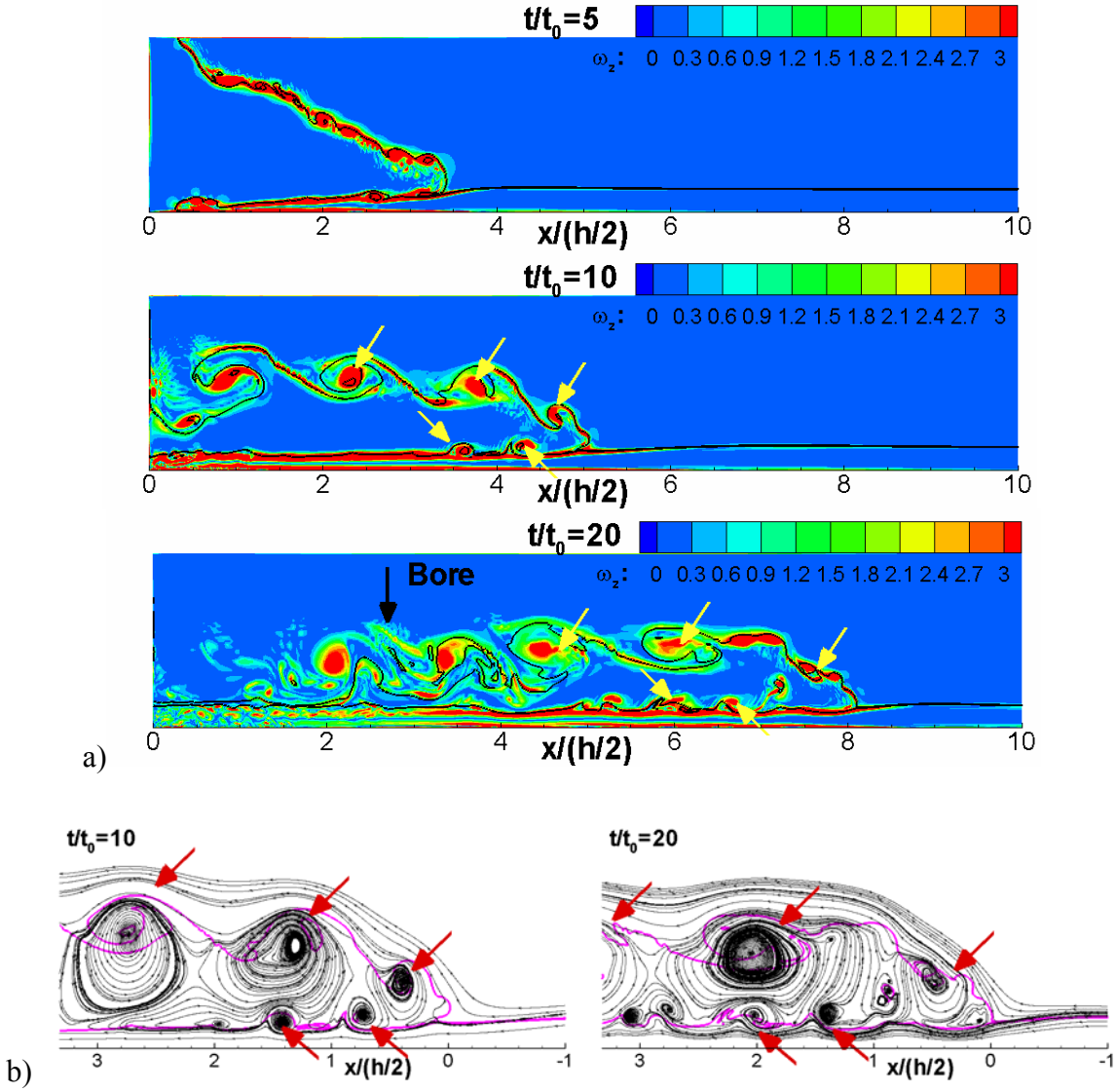

Figure 7.8. Visualization of vortical structure of intrusion current for case NSC. a) spanwise averaged vorticity magnitude contours at t/t_0=5, 10 and 20; b) streamline patterns showing vortical structure behind the intrusion front in a system translating with the front velocity at t/t_0=10 and 20.

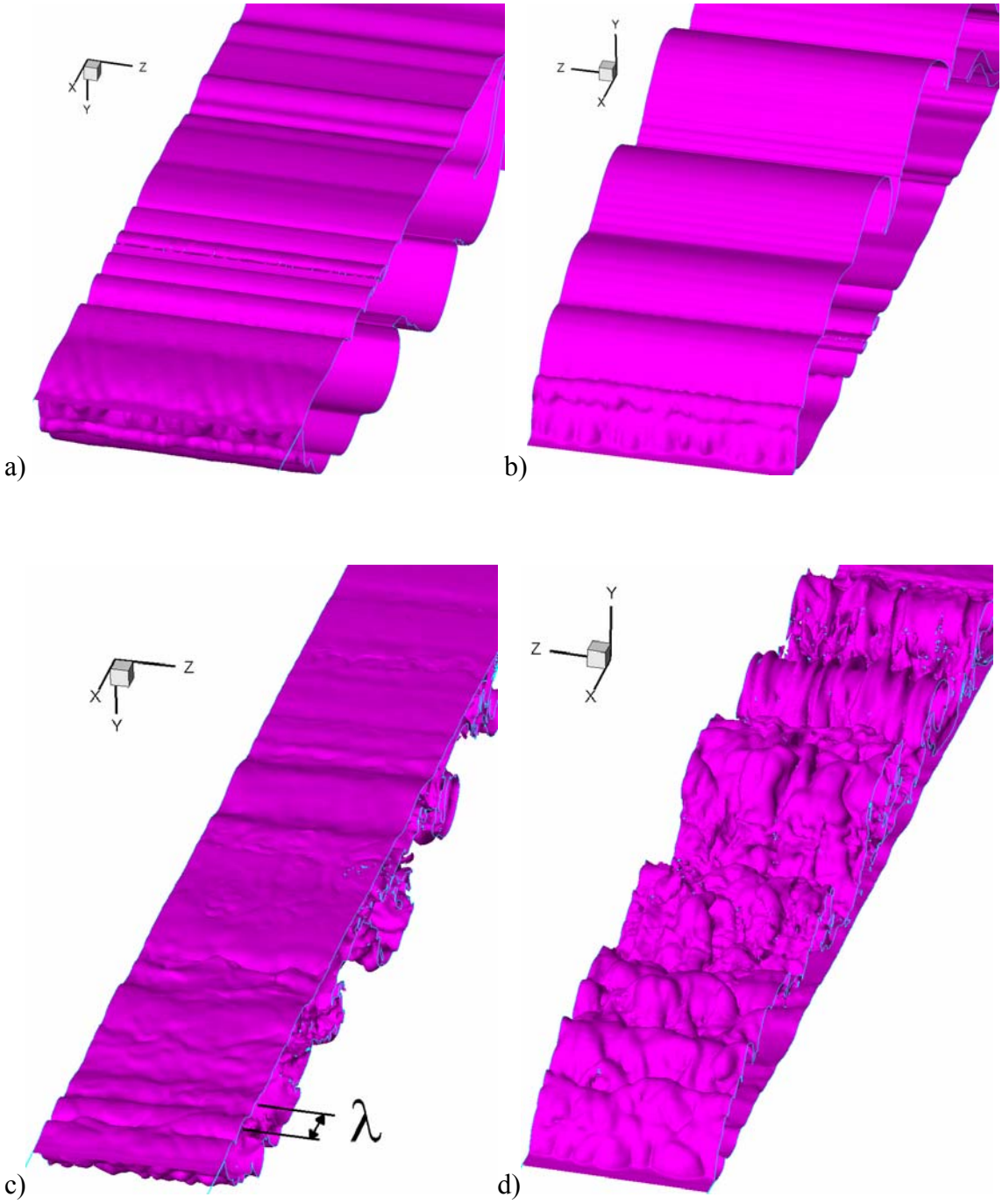

Figure 7.9. Visualization of intrusion current interface using a concentration isosurface (C = 0.12) for case NSC a) t/t_0=13.8 lower interface; b) t/t_0=13.8 upper interface; c) t/t_0=37.6 lower interface; d) t/t_0=37.6 upper interface.

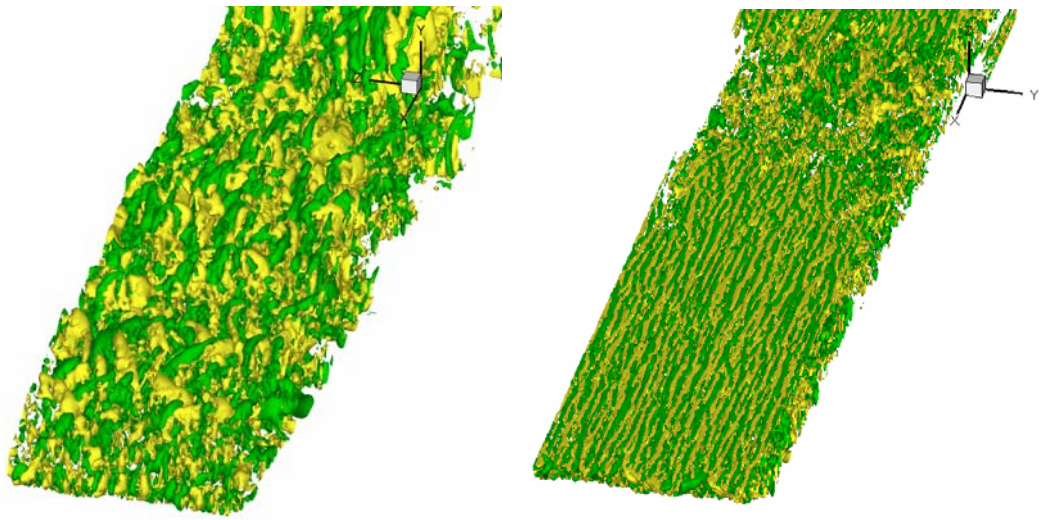

a) b)

Figure 7.10. Visualization of the instantaneous structure of gravity currents using vertical vorticity contours. a) lower interface of intrusion current in case SC; b) view from below of a finite-volume lock exchange gravity current propagating over a no-slip surface.

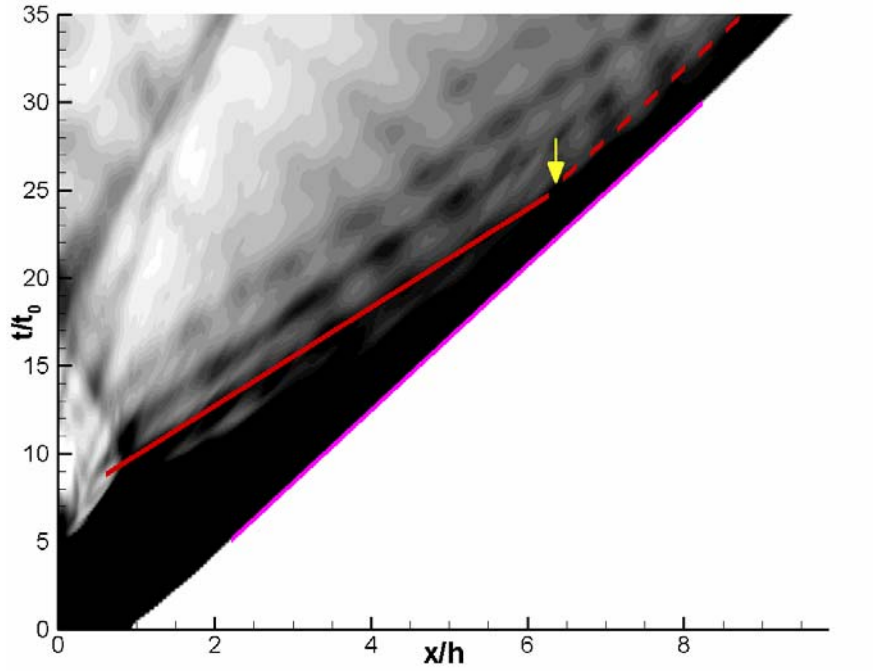

Figure 7.11. Evolution of density with time along the *x* axis for case SC. Distance from the bottom is *y/h* = 0.47.

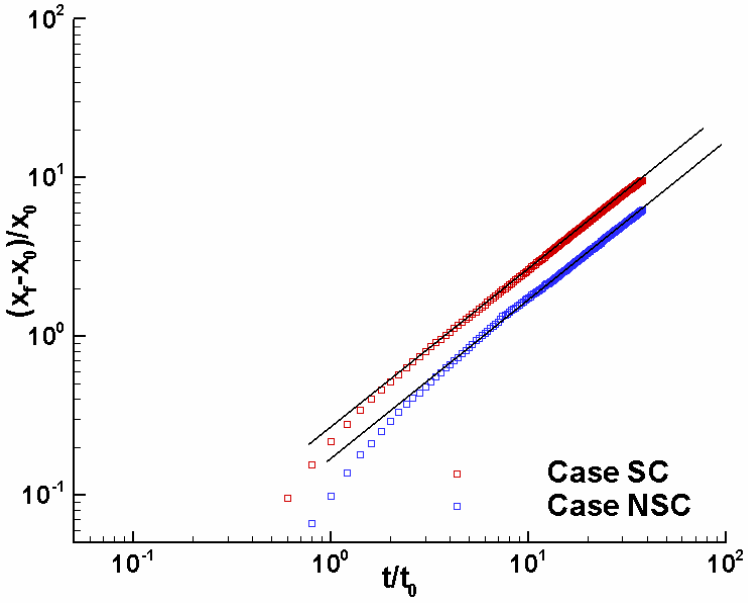

Figure 7.12. Evolution of the non-dimensional front position with time in log-log scale.

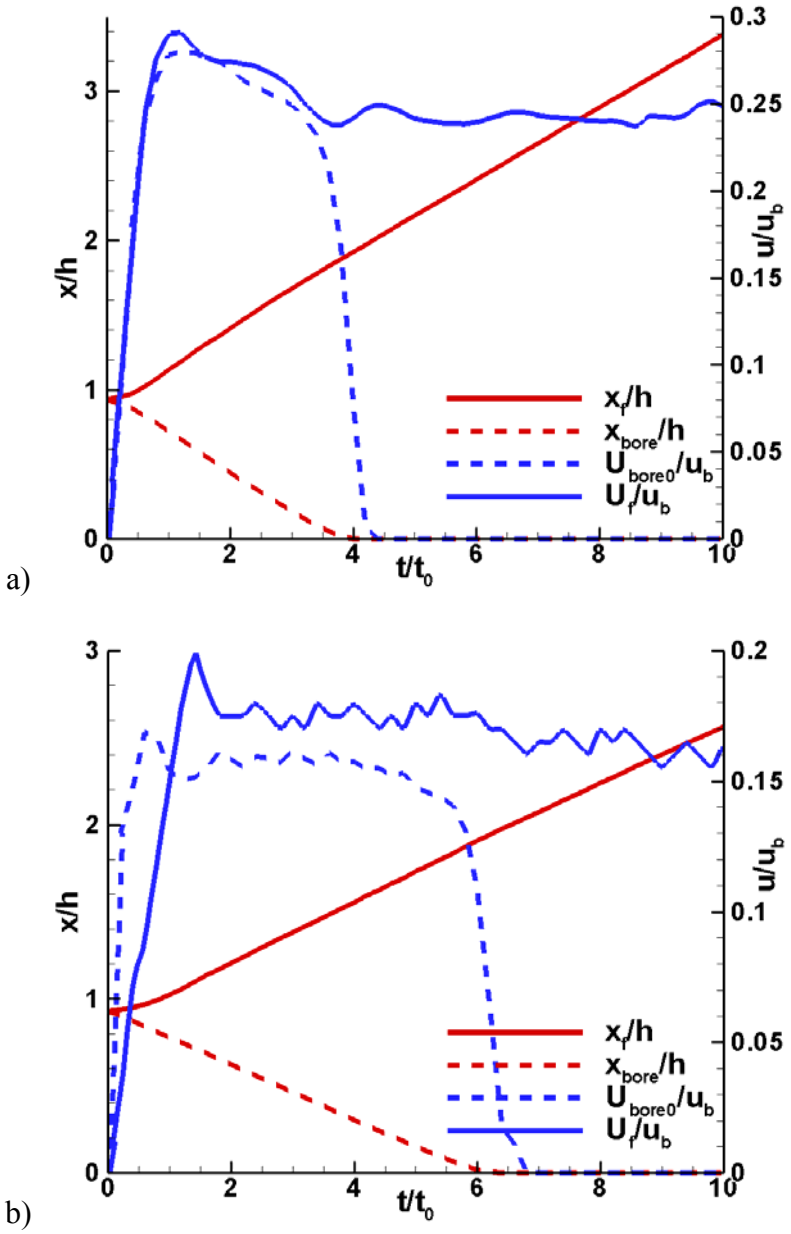

Figure 7.13. Evolution of the front and bore positions and velocities for cases SC and NSC during the initial phases of motion.

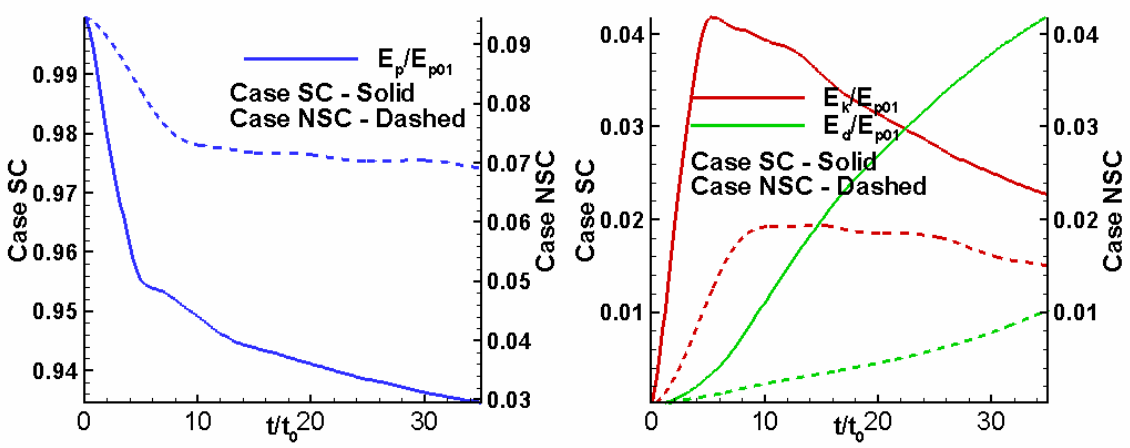

Figure 7.14. Time history of the components of the global energy budget in the SC (solid line) and NSC (dashed line) simulations. a) potential energy, E_p, b) kinetic energy, E_k, and time integral of the total dissipation rate, E_d.

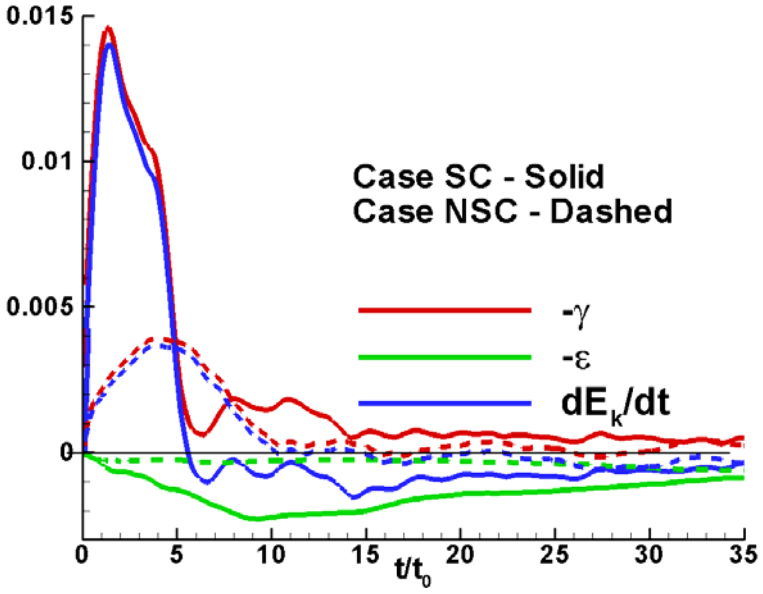

Figure 7.15. Temporal evolution of the terms in the transport equation for the total kinetic energy in the SC (solid line) and NSC (dashed line) simulations.

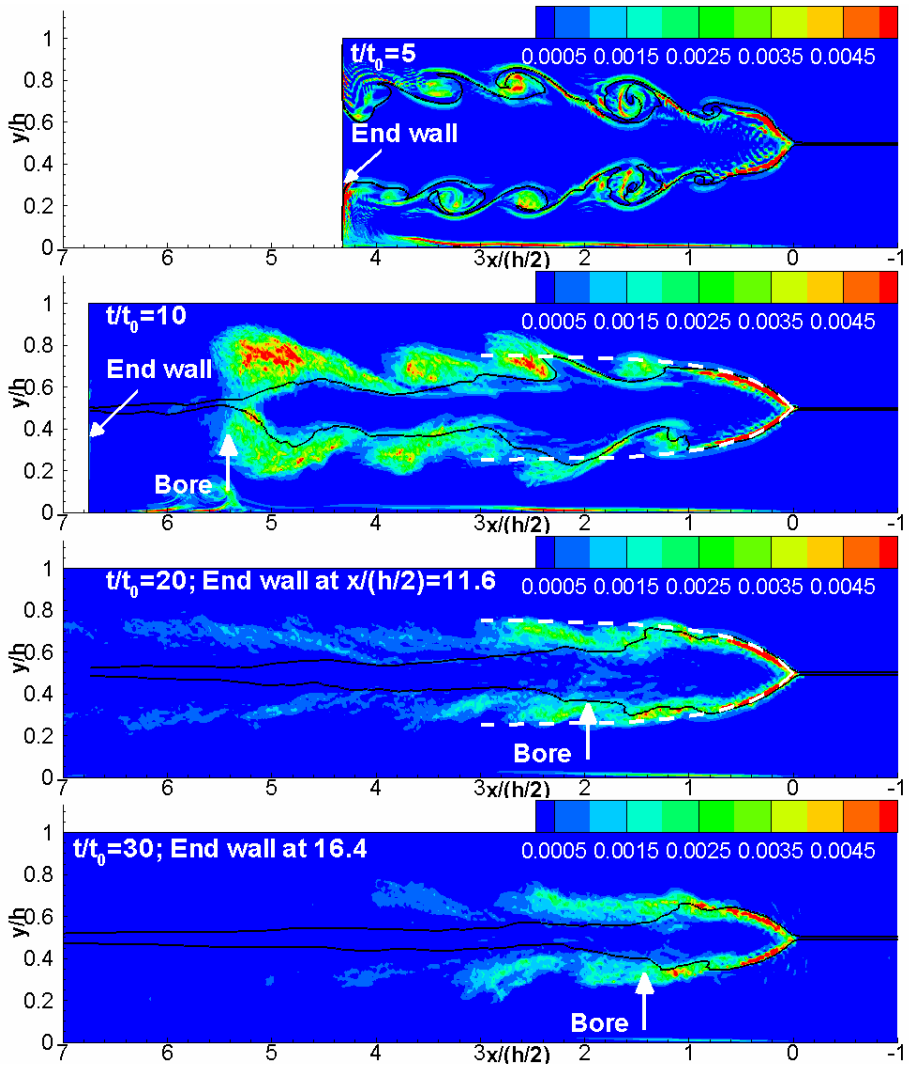

Figure 7.16. Distribution of the spanwise-averaged local dissipation rate ε_L in the SC simulation at t/t_0=5, 10, 20, 30.

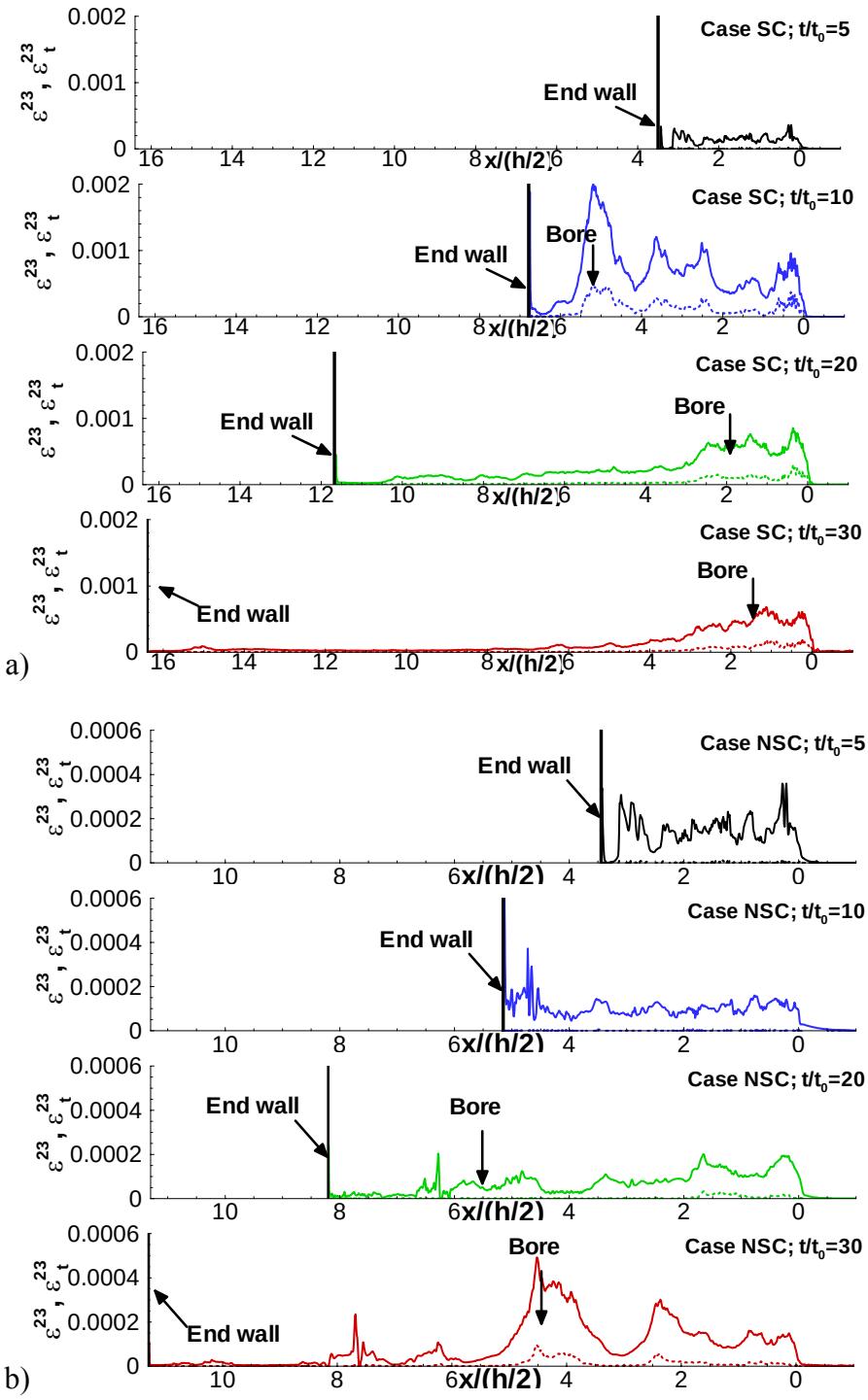

Figure 7.17. Streamwise distribution of the total dissipation term $\varepsilon^{23}(x_1)$ (solid line) and SGS term $\varepsilon_t^{23}(x_1)$ (dashed line) at t/t_0=5, 10, 20 and 30. a) SC simulation; b) NSC simulation.

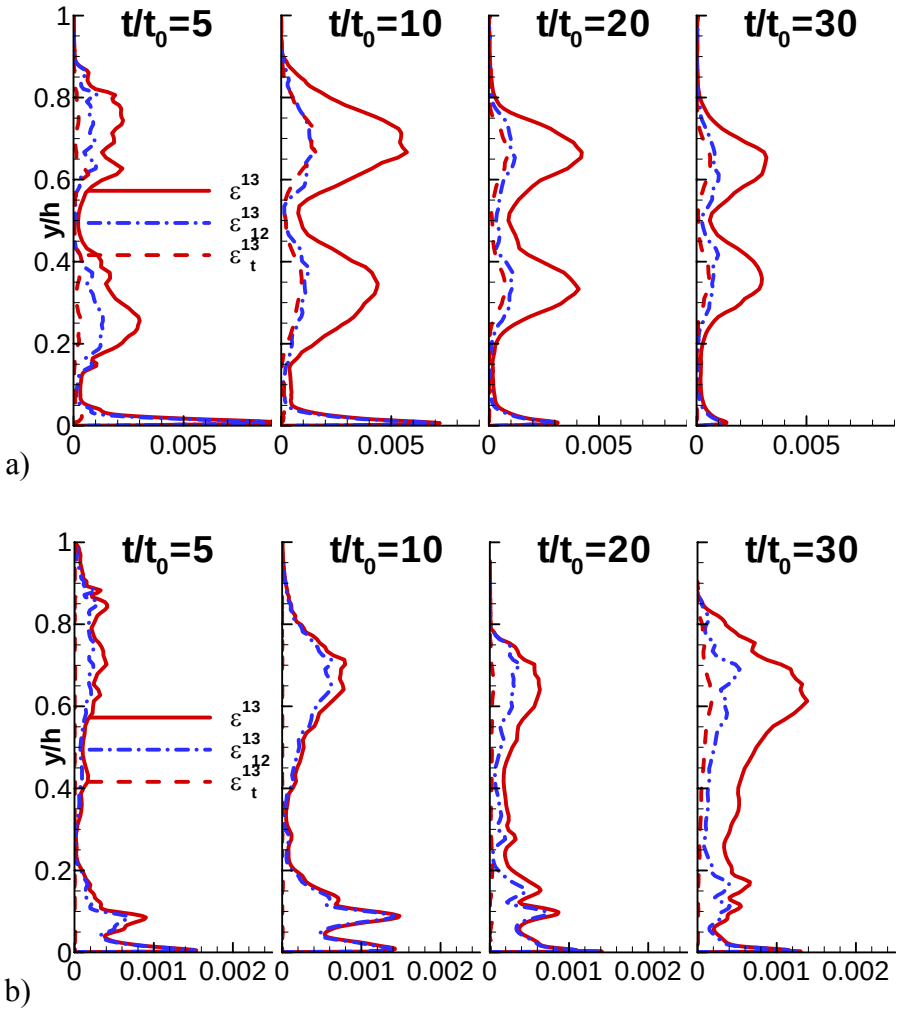

Figure 7.18. Vertical distribution of the total dissipation term $\varepsilon^{13}(x_2)$ (solid line), SGS term $\varepsilon_t^{13}(x_2)$ (dashed line) and dissipation term containing the vertical gradient of the streamwise velocity $\varepsilon_{12}^{13}(x_2)$ (dashed-dot line) at t/t_0=5, 10, 20 and 30. a) SC simulation; b) NSC simulation.

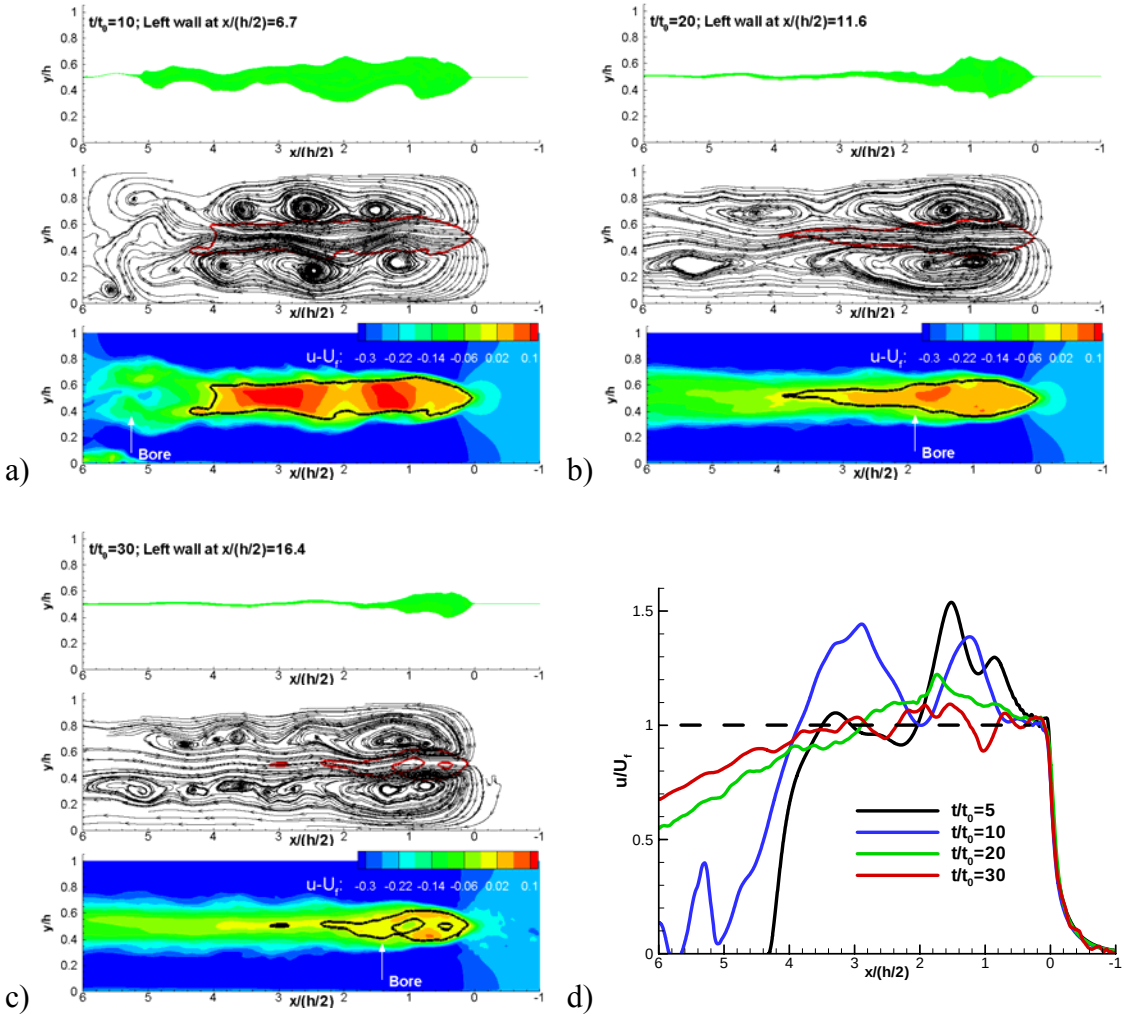

Figure 7.19. Unmixed lock fluid distribution, streamline patterns and streamwise velocity contours at different stages of the evolution of the intrusion current in case SC. a) t/t_0=10; b) t/t_0=20; c) t/t_0=30; d) streamwise velocity variation along the mid-plane y/h=0.5.

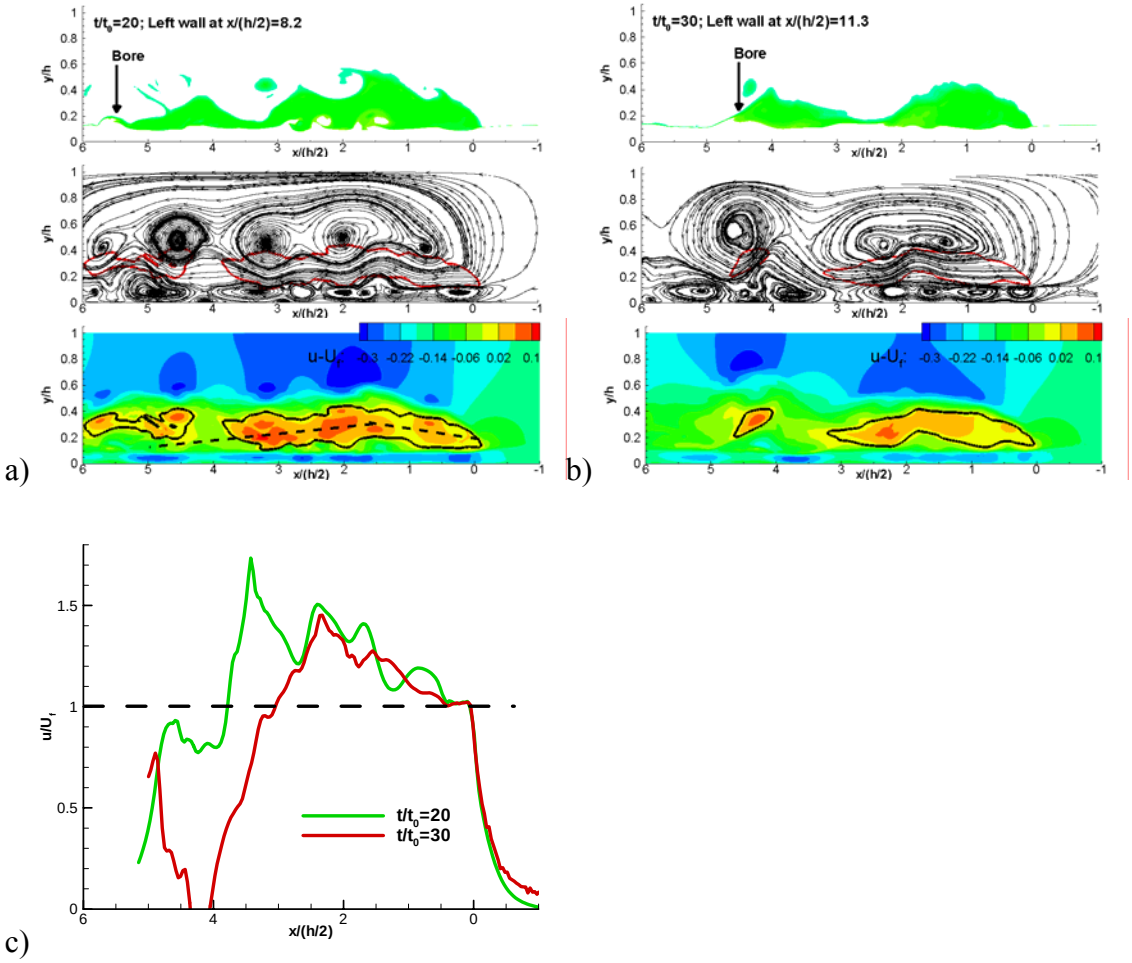

Figure 7.20. Unmixed lock fluid distribution, streamline patterns and streamwise velocity contours at different stages of the evolution of the intrusion current in case NSC. a) t/t_0=20; b) t/t_0=30; c) streamwise velocity variation along a curved line starting at the nose of the intrusion and following the centerline of the intrusion current.

CHAPTER 8

CONCLUSIONS AND RECOMMENDATIONS

8.1 Conclusions

The numerical simulations performed as part of the present study demonstrate that a 3D LES non-dissipative model is able to correctly capture most of the important aspects of lock-exchange gravity-driven flows at high Grashof numbers ($Gr>>10^8$) where DNS simulations are computationally too expensive. The validation study included not only qualitative comparisons with experimental visualizations of the evolution of a gravity current present in the three different types of lock-exchange configurations considered in the present work, but also a detailed quantitative study of these gravity currents. The main quantities that were compared with experimental data and theory were the front and bore velocities during the slumping phase, the position of the end of the slumping phase, the power coefficients in the expressions describing the evolution of the front velocity over the inviscid and viscous phases and the dependence with the local Reynolds number of the mean size of the lobes at the front of the current. For all these quantities the agreement with experiment and theory was found to be good.

It was demonstrated that 2D simulations at relatively low Grashof numbers ($Gr\sim10^6$) correctly predict the main aspects of the flow including the front speed and bed shear stress distribution. This is despite the fact that 2D simulations cannot account for vortex stretching phenomena or for the formation of lobes and clefts at the front of the gravity current. At high Grashof numbers ($Gr>10^8$), 2D LES was able to correctly predict the front speed of the intrusion and the general flow structure during most of the slumping phase for both infinite and finite volume lock-exchange flows. However, 2D simulations were unable to correctly capture the structure of the gravity current in the later stages of its evolution, specifically the break up of the large-scale Kelvin-Helmholtz billows into small-scale structures. This led the 2D LES simulations to underpredict the

front speed velocity during the self-similar phase. It also led to incorrect predictions of the bed shear stress distribution.

The flow structure of the head and tail regions was investigated for all the three types of lock exchange configurations considered in the present study. The main result is the fact that the formation of the lobe and cleft structure at the front of a gravity current is not dependent on the presence of a no-slip boundary if the Grashof number is high enough. Still, it was shown that the growth rates and characteristic sizes of the lobes are larger if the current propagates over a no slip surface. It was also shown that for $Gr>10^8$ high and low speed streaks are present in the near bed region some distance behind the front. As the local Reynolds number decays below levels at which turbulence can be maintained, the streaky structure was found to disappear. The streamwise velocity streaks were found to affect the distribution of the bed shear stress in the region behind the front and to promote mixing in the near-bed region. The effect of the Grashof number on the stretching and break up of the KH billows was studied. It was found that during the inviscid phase the lobes interact with the KH billows in the formation region and induce significant deformations of their cores in the spanwise direction. This makes the subsequent evolution of the KH billows to be highly three-dimensional. The flow structure in the tail region was correctly predicted by the 3D simulations over both the slumping and inviscid phases. This was in contrast to the results obtained from 2D simulations.

The present study provides the first qualitative and quantitative description of the bed shear stress distribution during the slumping and inviscid phases of the evolution of a turbulent bottom propagating gravity current ($Gr>10^8$). Qualitatively, it was shown that the large KH billows in the interface region and the presence of the streaks of high streamwise velocity behind the front are the main phenomena that affect the instantaneous distribution of the bed shear stress. It was also demonstrated that the effect of the Grashof number is important, including over a range of Grashof numbers where

the flow inside the head region is strongly turbulent (10^8<Gr<10^{12}). It was shown that for two GCs containing the same initial volume of lock fluid, the one at the higher Grashof number will be more effective in entraining sediment in the case in which the current propagates over a loose bed. This means that estimations of the amount of sediment entrained by gravity currents obtained from experiments/ simulations carried at lower Grashof numbers are lower than the real ones. For applications related to sediment entrainment induced by salinity currents forming at real lock facilities this is of great importance because the Grashof numbers of these gravity currents are much higher than the ones typically studied in laboratory experiments. The present model can be used toward estimating the amount entrained and the deposition patterns for lock exchange flows at Grashof numbers that are much closer to the ones encountered in these applications. In this case one expects scale effects to be much less important. I

Investigation of the global energy balance showed that for infinite volume bottom gravity currents, an equilibrium state is eventually attained in which the dissipation rate and the rates of change of the kinetic and potential energy are relatively constant. In the case of finite-volume lock exchange currents it was shown that, starting toward the end of the slumping phase, the variation of these quantities is logarithmic. The spatial distributions of the dissipation rate confirmed that most of the dissipation takes place inside the dissipative wake region due to the action of the interfacial vortices. However, it was shown that in the region situated just behind the front of the current, the dissipation inside the thin shear layers can be significant. For bottom propagating currents, the near bed region can also substantially contribute to the dissipation rate starting immediately behind the front. For bottom propagating currents it was found that the streamwise distribution of the dissipation rate changes significantly between the slumping and the self-similar phase. This information can be used toward developing simpler integral models that need to estimate the dissipation over the head and tail regions.

The following subsections summarize the major results of the 3D LES simulations of compositional Boussinesq gravity currents for each of the three generic lock-exchange configurations considered in the present work.

8.1.1 3D Infinite Volume Lock-Exchange Gravity Current Simulations

Good agreement was observed between the present 3D LES simulations and the results of previous experimental investigations and theory for the bulk flow quantities. The simulations successfully captured the development of the lobe-and-cleft structures at the front of the current and the shedding of interfacial vortices behind the head region. The presence of large-scale interfacial KH billows was found to strongly influence the instantaneous bed shear stress distribution. Consequently, the distribution of the friction velocity in the HGR simulation ($Gr=2\times10^9$) was found to be more uniform behind the front region compared to the LGR simulation ($Gr=1.25\times10^6$). In the HGR simulation it was observed that the rapid loss in the coherence of the KH billows was due to their interaction with small scale three-dimensional turbulent eddies, suggesting that part of the flow inside the gravity current was strongly turbulent. Consistent with this, vorticity contours near the top and bottom walls showed the presence of streaks of positive and negative vertical vorticity in the region corresponding to the heads of the two currents. These vorticity streaks are in fact induced by the formation of high and low streamwise-velocity wall streaks, similar to the ones observed in turbulent boundary layers and channel flows.

The analysis of the terms in the transport equation for the total kinetic energy showed that, in the later stages of the evolution of the current, the rates of change of the kinetic energy and potential energy, and the total dissipation rate become relatively constant suggesting that the gravity currents reach some sort of an equilibrium state.

8.1.2 3D Finite Volume Lock-Exchange Gravity Current Simulations

The 3D simulations correctly predicted a practically constant front velocity over the slumping phase and a front speed decrease proportional to $t^{-1/3}$ (the time t is measured from the release) over the inviscid phase, in agreement with theory and experiment. Additionally, a 2D simulation of a low Grashof number current (Gr=2.8×10^5) was found to directly transition from the slumping into the viscous phase, where the front speed decayed at a rate proportional to $t^{-1/5}$, consistent with experiment and theory (Rottman & Simpson, 1983).

In the 3D simulations the KH billows did not preserve their structure across the width of the channel and broke relatively rapidly into smaller 3D structures, similar to experimental observations. In the near-wall region beneath the upstream part of the current, the intensity of the turbulence was large enough to induce the formation of low and high streamwise velocity streaks, similar to the ones observed in turbulent constant-density channel flows. As the turbulence started to decay in the downstream part of the current, the streaky structure disappeared. A streaky distribution of the bed shear stress, that became finer as the Grashof number was increased, was observed in the region immediately behind the front. Beneath the remaining body of the current, several large spanwise bands of high and low bed shear stress were observed. The evolution in time of the balance among the potential energy, the kinetic energy and the integral of the total dissipation was compared for two simulations for which the only difference was the value of the Grashof number (Gr=2.3×10^9 vs. Gr=10^{12}). It was found that starting toward the end of the slumping phase, the variation of these quantities in time is proportional to $ln(t)^{\alpha}$, where the value of α is dependent on the variable.

8.1.3 3D Finite Volume Lock-Exchange Intrusive Gravity Current Simulations

The temporal evolution of lock-exchange intrusion currents developing into a two-layer ambient fluid was analyzed for two cases. In the first one (doubly-symmetric case), the depths of the two layers of ambient fluid were equal. In the second nonsymmetric case, the depths of the two layers were different. The agreement with the experimental data of Sutherland et al. (2004) was found to be satisfactory both qualitatively (structure of the intrusion current) and quantitatively (e.g., front velocity). The fact that the front velocity did not start to decay immediately after the end of the slumping phase in the doubly-symmetric case was due to the fact that lock fluid was still present behind the nose of the intrusion. However, the overall size of the wake and head region was found to decay significantly after the end of the slumping phase. Thus, it is expected that at a certain point mixing will become important in the nose region and the current will start decelerating.

Visualizations of the interface surface in the front region showed that, eventually, the 3D instabilities were strong enough to produce the formation of relatively large-scale deformations, similar to the lobes and clefts structures observed for gravity currents propagating over a no-slip boundary. The present simulation results appear to confirm the conclusions in the work of McElwaine & Patterson (2004) who provide evidence that the instability mechanism responsible for the development of lobes and clefts is not necessarily related to the presence of a no-slip surface, if the Reynolds numbers are high enough. The length scales of the structures in the front region were found to be smaller than the lobe dimensions observed in currents propagating over a no-slip boundary at similar Reynolds numbers.

Though most of the total dissipation was observed to occur in the dissipative wake region, the levels of the integral of the local dissipation rate at streamwise locations situated inside the head region were found to be comparable to those inside the wake

region. This is due to the dissipation taking place in the thin shear layers at the front of the intrusion interface.

8.2 Recommendations

The present simulations proved that LES can be successfully used to predict and investigate several flow features and quantities that are very difficult or impossible to determine or study experimentally. The model can be further enhanced to allow the study of other applications of fundamental or applied nature related to gravity current flows. These include:

- Study gravity currents propagating on constant or variable slope surfaces. This is important especially for applications in river engineering.
- Study interaction between a gravity current and an obstacle (e.g., submerged dams in rivers or reservoirs, oil pipelines on the bottom of a lake or ocean, etc.).
- Study evolution of particulate (turbidity) currents containing a non-uniform sediment size distribution. Study turbidity currents induced by the passage of a compositional gravity current over a loose bed (quantification of the amount of sediment entrained and carried each time a lock facility is operated is one of the main practical concerns).
- Study gravity currents propagating over rough surfaces. This is important especially in river engineering where the gravity currents typically propagate over a deformed bed surface containing ripples, dunes, etc.
- Study non-Boussinesq gravity currents in which the density differences between the lock and ambient fluid may be important. Especially at flood conditions, the differences between the concentration of a turbidity current and that of the water in the river or estuary can be substantially higher than 2-4% for which the use of the Boussinesq approximation is acceptable.

BIBLIOGRAPHY

Amen, R., and Maxworthy, T. 1980. The gravitational collapse of a mixed region into a linearly stratified fluid. *J. Fluid Mech.* 96: 65-80.

Benjamin, T.B. 1968. Gravity currents and related phenomena. *J. Fluid Mech.* 31: 209-248.

Birman, V.K., Martin, E., and Meiburg E. 2005. The Non-Boussinesq lock-exchange problem. Part 2. High resolution simulations. *J. Fluid Mech.* 537: 125-144

Blanchette, F., Piche, V., Meiburg E., and Strauss, M. 2005a Evaluation of a simplified approach for simulating gravity currents over slopes of varying angles. *Computers & Fluids,* 35(5): 492-500.

Blanchette, F., Strauss, M., Meiburg, E., Kneller, B., Glinsky, M. 2005b High-resolution numerical simulations of resuspending gravity currents: Conditions for self-sustainment. *J. Geophys. Res*. 110, C12022, doi:10.1029 2005JC002927

Britter, R.E., and Simpson, J.E. 1978. Experiments on the dynamics of a gravity current head. *J. Fluid Mech.* 88: 223-240.

Britter, R.E., and Simpson, J.E. 1981. A note on the structure of the head of an intrusive gravity current. *J. Fluid Mech.* 112: 459-

Chang, K.S., Constantinescu, G., Park, S-O. 2006. Analysis of the flow and mass transfer processes for the incompressible flow past an open cavity with a laminar and a fully turbulent incoming boundary layer. *J. Fluid Mech.* Accepted for publication.

Chen, G.Q, and Lee, J.H.W. 1999. Turbulent gravity current of lock release type: A numerical study. *Environmental Hydraulics*: 449-454.

Choi, S-U., and Garcia, M.H. 1995. Modeling of one-dimensional turbidity currents with a dissipative Galerkin finite-element method. *J. Hyd. Res.* 33(5): 623-648.

Choi, S-U., and Garcia, M.H. 2002. k-ε turbulence modeling of density currents developing two dimensionally on a slope. *J. Hyd. Eng.* 128(1): 55-63.

Fanneløp, T.K. 1994. *Fluid Mechanics for Industrial Safety and Environmental Protection.* Elsevier.

Faust, K.M., and Plate, E.J. 1984. Experimental investigation of intrusive gravity currents entering stably stratified fluids. *J. Hyd. Res.* 22:315-323.

Flynn, M.R., and Sutherland, B.R. 2004. Interfacial gravity currents and internal gravity wave generation in continuously stratified fluids. *J. Fluid Mech.* 514: 355-383.

Hacker, J., Linden, P.F., and Dalziel, S.B. 1996. Mixing in lock-release gravity currents. *Dynamics of Atmospheres and Oceans* 24: 183-195.

Hallworth, M.A., Huppert, H.E., Phillips, J.C., & Sparks, S.J. 1996. Entrainment into two-dimensional and axisymmetric turbulent gravity currents. *J. Fluid Mech*. 308: 289-311.

Härtel, C., Meiburg, E., and Necker, F. 2000. Analysis and direct numerical simulation of the flow at a gravity-current head. Part 1. Flow topology and front speed for slip and no-slip boundaries. *J. Fluid Mech*. 418: 189-212.

Härtel, C., Carlsson, F., and Thunblom, M. 2000b. Analysis and direct numerical simulation of the flow at a gravity-current head. Part 2: The lobe-and-cleft instability. *J. Fluid Mech.* 418: 213-229.

Holyer, J.Y. and Huppert, H.E. 1980. Gravity currents entering a two-layer fluid. *J. Fluid Mech.* 100:739-767.

Hoult, D.P. 1972. Oil spreading on the sea. *Ann. Rev. Fluid Mech.* 4: 341-68.

Huppert, H. 1982. The propagation of two-dimensional and axisymmetric viscous gravity currents over a rigid horizontal surface. *J. Fluid. Mech.* 121: 43-58.

Huppert, H., and Simpson, J.E. 1980. The slumping of gravity currents. *J. Fluid. Mech.* 99: 785-799.

Jacobsen, Ø. & Magnussen, B. F. 1987. 3D numerical simulation of heavy gas dispersion. J. Haz. Mater. 16: 215-230.

Kao, W.K., Park, C. and Pao, H.,-P. 1977. Buoyant surface discharge and small-scale oceanic fronts: a numerical study. *J. Geophys. Res.* 82: 1747-1752.

Keller, J.J., and Chyou, Y.-P. 1991. On the hydraulic lock-exchange problem. *Z. Angew. Math. Phys.* 42: 874-910.

Keulegan, G.H. 1957. An experimental study of the motion of saline water from locks into fresh water channels. *U.S. Natl. Bur. Stand. Rep.* 5168.

Keulegan, G.H. 1958. The motion of saline fronts in still waters. *U.S. Natl. Bur. Stand. Rep.* 5831.

Klemp, J.B., Rotunno, R., and Skamarock, W.C. 1994 The dynamics of gravity currents in a channel. *J. Fluid Mech.* 269: 169-198.

Kneller, B.C., Bennett, S.J., McCaffrey, W.D. 1997 Velocity and turbulence structure of density currents and internal solitary waves: potential sediment transport and the formation of wave ripples in deep water. *Sed. Geology* 112: 235-250

Lilly, D. K., 1992. A proposed modification of the Germano subgrid-sclale closure method. *Phys. Fluids A* 4.

Linden, P. F., and Simpson, J.E. 1986. Gravity driven flows in a turbulent fluid. *J. Fluid Mech*. 172: 481-497.

Lowe, R. J., Rottman, J. W. and Linden, P. F. 2005. The non-Boussinesq lock-exchange problem.Part 1. Theory and experiments. *J. Fluid Mech*. 537: 101–124.

Lowe, R.J., Linden, P.F., and Rottman, J.W. 2002. A laboratory study of the velocity structure in an intrusive gravity current. *J. Fluid Mech.* 456:33-48

McElwaine, J., and Patterson, M., 2004. Lobe and cleft formation at the head of a gravity current. Proceedings of the XXI International Congress of Theoretical and Applied Mechanics.

Maxworthy, T., Leilich, E., Simpson, J.E. and Meiburg, E. 2002. The propagation of a gravity current into a linearly stratified fluid. *J. Fluid Mech.* 453: 371-394.

Mehta, A., Sutherland, B.R., Kyba, P.J. 2002. Interfacial gravity currents: Part II – wave excitation. *Phys. Fluids* 14: 3558-3569.

Necker, F., Härtel, C., Kleiser and Meiburg, E. 2002. High resolution simulation of particle driven gravity currents. *Int. Journal of Multiphase Flows.* 28: 279-300.

Necker, F., Härtel, C., Kleiser, L. and Meiburg, E. 2005. Mixing and dissipation in particle-drive gravity currents. *J. Fluid Mech.* 545: 339-372.

Parsons, J. D. & Garcia, M. H. 1998 Similarity of gravity current fronts. *Phys. Fluids* 10: 3209-3213.

Pierce, C. D. & Moin, P. 2001. Progress-variable approach for large-eddy simulation of turbulent combustion. *Mech. Eng. Dept. Rep. TF-80*, Stanford University.

Pierce, C.D., and Moin, P. 2004. Progress-variable approach for large-eddy simulation of non-premixed turbulent combustion. *J. Fluid Mech.* 504: 73-97.

De Rooij, F., Linden, P.F., and Dalziel, S.B. 1999. Saline and particle-driven interfacial intrusions. *J. Fluid Mech.* 389: 303-334.

Rottman, J.W., and Simpson, J.E. 1983. Gravity currents produced by instantaneous releases of a heavy fluid in a rectangular channel. *J. Fluid Mech*. 135: 95-110.

Schmidt, W. 1911. Zur Mechanik der Boen. *Z. Meteorol.* 28: 355-362.

Shin, J.O., Dalziel, S.B., and Linden, P.F. 2004. Gravity currents produced by lock exchange. *J. Fluid Mech.* 521: 1-34.

Simpson, J.E. 1997. *Gravity Currents: in the Environment and the Laboratory*. 2nd Edition. Cambridge University Press.

Simpson, J.E., and Britter, R.E. 1979. The dynamics of the head of a gravity current advancing over a horizontal surface. *J. Fluid Mech.* 94: 477-495.

Simpson, J.E. 1972. Effects of the lower boundary on the head of a gravity current. *J. Fluid Mech.* 53: 759-768.

Sutherland, B.R., Kyba, P.J., and Flynn, M.R. 2004. Intrusive gravity currents in two-layer fluids. *J. Fluid Mech.* 514: 327-353.

Winters, K.B., Lombard, P.N., Riley, J.J., and D'Asaro, E.A. 1995. Available potential energy and mixing in density-stratified fluids. *J. Fluid Mech.* 289: 115-128.